Magnetic Fields in Protoplanetary Discs

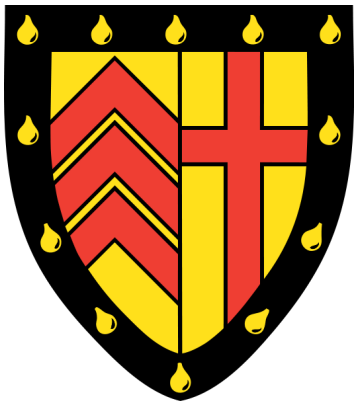

Kwong Ching Philip Leung

Department of Applied Mathematics and Theoretical Physics
University of Cambridge

This dissertation is submitted for the degree of
Doctor of Philosophy

Clare College June 2021

I would like to dedicate this Thesis to my mother
and to the memory of my father, who inspired me to pursue astrophysics.

The heavens declare the glory of God
and the firmament shows his handiwork.
(Psalm 19:1)

The Dust itself which is scattered so rare in Heaven, whereof all worlds, and the bodies that are not worlds, are made . . . waits not till created eyes have seen it or hands handled it, to be in itself a strength and splendour of Maleldil. Only the least part has served, or ever shall, a beast, a man or a god. But always, and beyond all distances, before they came and after they are gone and where they never come, it is what it is and utters the heart of the Holy One with its own voice. It is farthest from Him of all things, for it has no life, nor sense, nor reason; it is nearest to Him of all things for without intervening soul, as sparks fly out of fire, He utters in each grain of it the unmixed image of His energy. . . . Blessed be He!
(C. S. Lewis, *Perelandra*)

Preface

I hereby declare that except where specific reference is made to the work of others, the contents of this dissertation are original and have not been submitted in whole or in part for consideration for any other degree or qualification in this, or any other university. This dissertation is my own work and contains nothing which is the outcome of work done in collaboration with others, except as declared below and specified in the text.

Part I, 'Context and Framework', gives an overview of protoplanetary systems in general and introduces the background physics. Chapters 1 ('Origin and features of protoplanetary discs') and 2 ('Magnetohydrodynamics of protoplanetary discs') contain only background material and no new research. Chapter 3 ('Multi-scale radially local approach') represents original work, and outlines the local framework that will be adopted throughout the Thesis.

Part II, 'Magnetic flux transport in protoplanetary discs', is made up of five chapters. Chapter 4 introduces the flux transport problem in more detail, and is purely background material. Chapters 5 ('Flux transport model at the shearing box order'), 6 ('Flux transport model at Guilet & Ogilvie order') and 7 ('Effect of disc wind on flux transport rates) present original published research, while Chapter 7 is preliminary and unpublished work. Chapter 8 ('Conclusion to Part II') concludes Part II, with recommendations for future work in the area.

Part III, 'Symmetries of magnetised discs and winds', is made up of four chapters. Chapter 9 ('Introduction to symmetries of magnetic winds') introduces the wind symmetries problem in more detail, and is purely background material. Chapter 10 ('Wind-MRI interactions: Ohmic resistivity only') is original published research, while Chapter 11 ('Magnetic wind symmetries - full non-ideal MHD generality') contains original preliminary unpublished work. Chapter 12 ('Conclusion to Part III') summarises our findings, and again gives recommendations for future work in the area.

Regarding published work, parts of Chapters 3 to 6 and Chapter 8 make up Leung and Ogilvie (2019), while parts of Chapters 9, 10 and 12 make up Leung and Ogilvie (2020).

Kwong Ching Philip Leung
June 2021

Magnetic Fields in Protoplanetary Discs

Kwong Ching Philip Leung

Abstract

Protoplanetary discs are flattened discs of gas and dust surrounding young stars that are believed to be the sites of planet formation. They are believed to be threaded by large-scale magnetic fields, which significantly affect their dynamics through processes such as the magneto-rotational instability (MRI), or the launching of a magnetic wind. Understanding the interplay between magnetic fields and protoplanetary disc structure and dynamics is crucial to shedding light on the origin of the complex features uncovered in recent observations of these systems, as well as the processes that contribute to planet formation. The paradigm that has emerged over the past two decades is that protoplanetary discs are weakly ionised, so that non-ideal magnetohydrodynamic (MHD) effects such as Ohmic resistivity, Hall drift, and ambipolar diffusion have a major impact on both the activity of the MRI and the geometry of the magnetic wind. They also affect the long-term radial transport of the large-scale magnetic field threading the disc, which in turn determines the magnetic flux distribution of the disc and has a feedback on the behaviour of the magnetic processes. To date, there is no self-consistent model that can at the same time capture both the impact of magnetic processes on disc structure and dynamics, and the evolution of the magnetic flux distribution. This work makes a contribution towards the realisation of such a model, by exploring the impact of non-ideal MHD effects on the disc's magnetic flux transport, and how the interplay between magnetic processes under different conditions expected in protoplanetary discs influences the geometry of the magnetic field and disc dynamics.

The result from recent studies that protoplanetary discs are likely to be laminar in nature owing to the presence of non-ideal MHD makes it possible to simplify the problem to essentially one-dimensional vertical structure calculations based on radially local models. Although local models cannot capture the full properties of disc winds, they can nevertheless provide helpful insight into transport properties and geometry of the solutions that are found in global studies. To help gain understanding into the results and explore a large parameter space with potentially wide-ranging behaviour, I have invoked both semi-analytical techniques and numerical simulations in the investigation. I find that magnetic flux transport depends sensitively on both the inclination of the poloidal field and the non-ideal MHD effects that are present. In particular, the impact of Hall drift depends on whether the Hall parameter has the same sign as the scalar product between the magnetic field and disc rotation vector. The presence and profile of non-ideal MHD effects can lead to the excitation of large-scale

MRI channel modes that contribute to the eventual geometry of the magnetic field in the disc and subsequent wind launching, while the specific long-term outcome can also depend on the initial conditions used. The results obtained in this Thesis are consistent with the flux transport rates and geometries obtained in previous studies of protoplanetary discs, and contribute to a deeper understanding of the underlying physics that are at play in disc-magnetic field interactions. This work paves the way to an eventual self-consistent theory of magnetised protoplanetary disc evolution and its consequences for planet formation.

Acknowledgements

First, I would like to thank my supervisor, Gordon Ogilvie, for the unwavering support and guidance he has given me throughout the PhD. His expertise in and passion for astrophysics are beautifully adorned by the kindness and patience with which he communicates them. A better supervisor I could not have asked for, and the completion of this Thesis would not have been possible without him.

Second, I would like to thank my mother for her endless encouragements and prayers. The fresh perspectives she offered were crucial in helping me persevere through the hardest parts of the research. This Thesis is dedicated to her, and to the memory of my father, who first inspired me to explore the wonders of the universe when I was young.

For helpful conversations and making the workplace the friendly community I have been blessed to be part of, I would like to thank my research group and office mates, in particular Maria Christina Van Der Weele, Roger Dufresne, Janosz Dewberry, Cleo Loi, Loren Held, Callum Fairbairn, Antranik Sefilian and William Béthune. I also thank Jerome Guilet especially for helpful conversations about his previous work with Gordon on which parts of my work are based, as well as Geoffroy Lesur for providing the version of PLUTO I used for this Thesis. Many thanks are also owed to my examiners, Henrik Latter and Geoffroy Lesur, for patiently reading my Thesis and for the insightful comments they gave.

A PhD never happens in a vacuum, and it is right that I should also acknowledge the countless people who made life so full of colour for me during my time of research. Special thanks go to my friends over the years from Clare & Magdalene College Christian Unions, the communities at St Andrew the Great Church and Magdalene College Morning Chapel, fellow postgraduate students from the Christian Graduate Society, the team and guests of Friends International Cambridge, and the weekly prayer quartet I am part of with Chris Wiles, Gabor Igloi and David Willer.

The Croucher Foundation and the Cambridge Commonwealth, European & International Trust has been wonderful in their generous funding of my PhD studentship through a Cambridge Croucher International Scholarship. Pursuing a PhD degree in Cambridge would not have been possible financially without them, and I commend their goal of promoting the sciences among the people of Hong Kong.

All these wonderful people and opportunities are gifts from a kind and generous Creator God, whose ‘works are great, pondered by all those who delight in them’ (Psalm 111:2). So I end my thanks with the ancient Latin phrase: *Soli Deo gloria!*

Table of contents

List of figures

List of tables

Part I

Context and framework

Chapter 1

Origin and features of protoplanetary discs

1.1 Origin

Protoplanetary discs are flattened discs of gas and dust in orbit around young stars. They are believed to be the nurseries of planet formation. The idea of a protoplanetary disc was first proposed theoretically by Swedenborg (1734) and elaborated on by Kant (1755), who reasoned that the close alignment of the orbital planes of the planets of the Solar system points towards a common origin from a primordial disc. Over time, this was developed into the Nebular Hypothesis, where star systems form from the fragmentation of giant molecular clouds. These fragments then further collapse to form dense cores of protostellar nebulae, which evolve into stars and their surrounding discs. Each nebula has a certain amount of intrinsic angular momentum, and materials accelerate in their rotation as they fall towards the centre of the nebula to conserve angular momentum. Gas in the inner part of the nebula with lower angular momentum collapses to form the protostar, while gas in the outer part of the nebula settles into a flattened rapidly rotating disc where the gravitational pull inwards is balanced by a centrifugal force outwards. Planets are then believed to form during the disc's evolution, as the disc slowly deposits mass (accretes) onto the new protostar. Since their theoretical proposal, the existence of protoplanetary discs has been confirmed in observations of young stellar systems in the past few decades. Understanding protoplanetary discs and their evolution are therefore fundamental to understanding the processes that eventually led to the conditions of our own Solar system, and other planetary systems we see today.

Protoplanetary discs are a sub-class of accretion discs, which are ubiquitous objects in the Universe resulting from the conservation of angular momentum of material collapsing

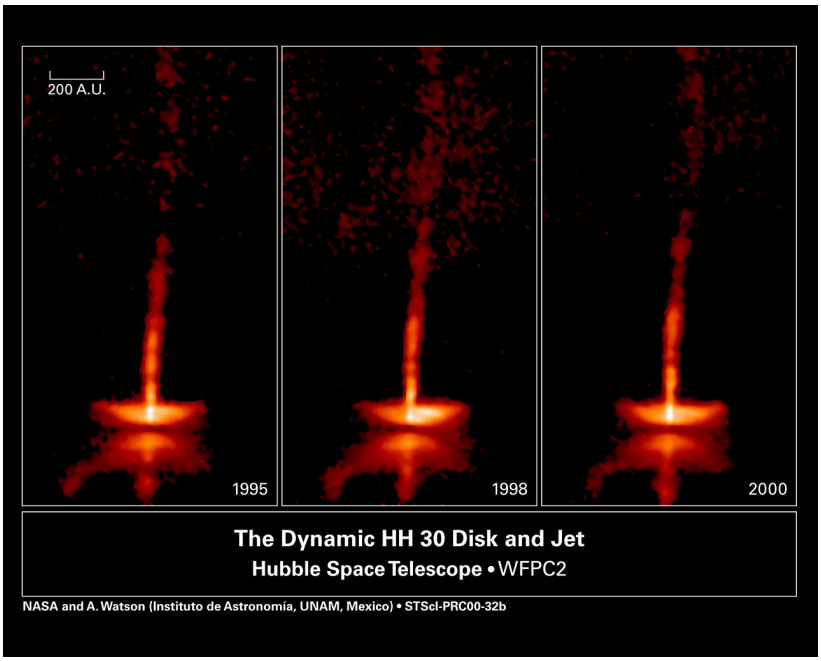

Fig. 1.1 Visible light image of the HH-30 protostellar disc as observed by Hubble. The diameter of the disc is 450 AU. Image credit: NASA, Watson, Stapelfeldt, Krist and Burrows.

under gravity. Accretion discs also occur in other contexts such as active galactic nuclei, and in the discs of close binary systems. Understanding protoplanetary disc dynamics therefore also has the scope of aiding our understanding of processes that may be at play in other astrophysical systems.

1.2 Observations

The first direct observation of a protoplanetary disc was in 1994 through the Hubble Space Telescope's images of HH-30 in the Orion nebula (O'dell and Wen, 1994) (see Figure 1.1). Beforehand, indirect observations from unresolved photometry only allowed for the inference of disc properties from theoretical models and comparison with generated synthetic observables, such as that of the expected infrared spectral energy density (SED) spectrum, which required assumptions about the discs' dust to gas ratio. These gave us coarse estimates of properties such as total disc mass (Beckwith et al., 1990) and the characterisation of disc types through their SEDs (Lada, 1987).

We place our work in the context of the discs of Class II Young Stellar Objects (YSOs), as categorised by Lada (1987). These are Classical T-Tauri systems, where the accreting envelope from the molecular clouds has all but dissipated, and the central star has been born. The disc at this stage is a few percent of the central stellar mass, and its evolution is

governed by dynamics such as accretion onto the central star, photoevaporation from stellar and cosmic radiation, formation of structures in the disc, and interactions with stellar or substellar companions (Williams and Cieza, 2011).

Hubble's side-on view of the HH-30 system showed the disc as a dark band along the mid-plane sandwiched between two bright curved regions, where light from the central protostar has been scattered from the dust at the disc's surface. A jet was also revealed to be emanating from the inner region of the disc, expanding for several billion kilometres from the star with a high level of collimation. Even though the spatial resolution was still coarse ($> 15-20$ AU) compared to current standards, these first direct images have led to new understanding of the structure of protoplanetary discs. Much progress has been made in the advancement of instrumentation since then, particularly with the commissioning of facilities like the Atacama Large Millimeter/submillimeter Array (ALMA). This has led to higher resolution images, down to 5 AU at typical distances to nearby star-forming regions of ~ 150 pc, revealing a whole range of other interesting features in the discs' substructure. Today, a range of observational tools are used to probe different regions and properties of protoplanetary discs. In order to have a better understanding of how these observations inform and constrain theoretical models, we present here a summary of the techniques used, and the disc regions and properties they probe:

- **UV Excess:** This measures the UV radiation emitted by the system in excess of that expected from the host star, and is a signature of the accretion shock. This measurement allows for the deduction of the accretion rate at the foot of the accretion column.

- **Scattered Light:** This observes light in the near and mid-infrared continuum, which comes from small $< \mu$m-sized dust grains in the disc atmosphere scattering and reflecting radiation from the central star. The dust disc is usually optically thick at these wavelengths, so scattered light probes the very surface of the dust layer (Andrews, 2020; Lesur, 2020). This tracer gives us the geometry of the dust component of the disc. Practical challenges for this probe are its dependence on contrast with the host star, which prevents measurements of the inner disc, and its need for stellar photons from the host star, which limits current measurements to discs with more luminous hosts at medium radii.

- **Continuum Emission:** This observes the (sub)-millimetre continuum, and probes the thermal emission from larger mm-sized dust grains in the disc. At low optical depths, which are traditionally expected in the sub-mm, the emissivity scales with the surface density of solids, and is also dependent on the temperature and particle properties. This tracer has the advantage of being bright, negating limitations due to

stellar contrast. It is also accessible at high resolution, hence most of our knowledge about disc structures is based on continuum emission data. Continuum emission from dust is used to determine disc masses and particle properties, though with large uncertainties due to the significant underlying assumptions required (Armitage, 2015).

- **Spectral Line Emission:** This probes specific rotational transition spectral lines in both the infrared and radio wavelengths of rare gas tracers, such as that of the $J = 3-2$ transition for the CO molecular gas. These lines are usually optically thick, and hence only trace the gas in the disc surface layer. Their intensities depend on the temperature of the atmosphere. At low optical depths, their intensities also depend on the gas density. If the relative abundance of the tracer species to H_2 is known, spatial maps of optically thin spectral line emission can be used to constrain the gas surface density, and also determine the disc velocity field (Andrews, 2020). Most of the information about disc kinematics, chemical composition and turbulence is obtained using this diagnostic (Armitage, 2015).

Figure 1.2, taken from Lesur (2020), summarises the different tracers and the disc regions they probe. For a more detailed review on the nature of protoplanetary disc observations, we refer to the recent review by Andrews (2020), which outlines the current state of the art in great detail. Measurements of disc properties such as disc mass, accretion rate, spatial profile of temperature, and gas and dust densities, provide valuable initial and boundary conditions for constraining theoretical models of protoplanetary disc evolution and planet formation processes.

1.3 Features of protoplanetary discs

Here, we summarise the key structural and dynamical properties of protoplanetary discs determined from observations that are crucial for the context of our work. Protoplanetary discs can be separated into two regions: a dust-free inner disc of hot gas from the disc inner edge at a few stellar radii to the dust sublimation radius, and an outer disc of dust and gas, with an outer edge ranging from 100 AU to 1000 AU. The typical dust to gas ratio in the outer disc is still a quantity poorly constrained by observation. It has been common for people to assume the dust content to be 1% of the total disc mass, the dust to gas ratio found in the interstellar medium (ISM), such as in the minimum mass Solar nebula model (MMSN) (Hayashi, 1981).

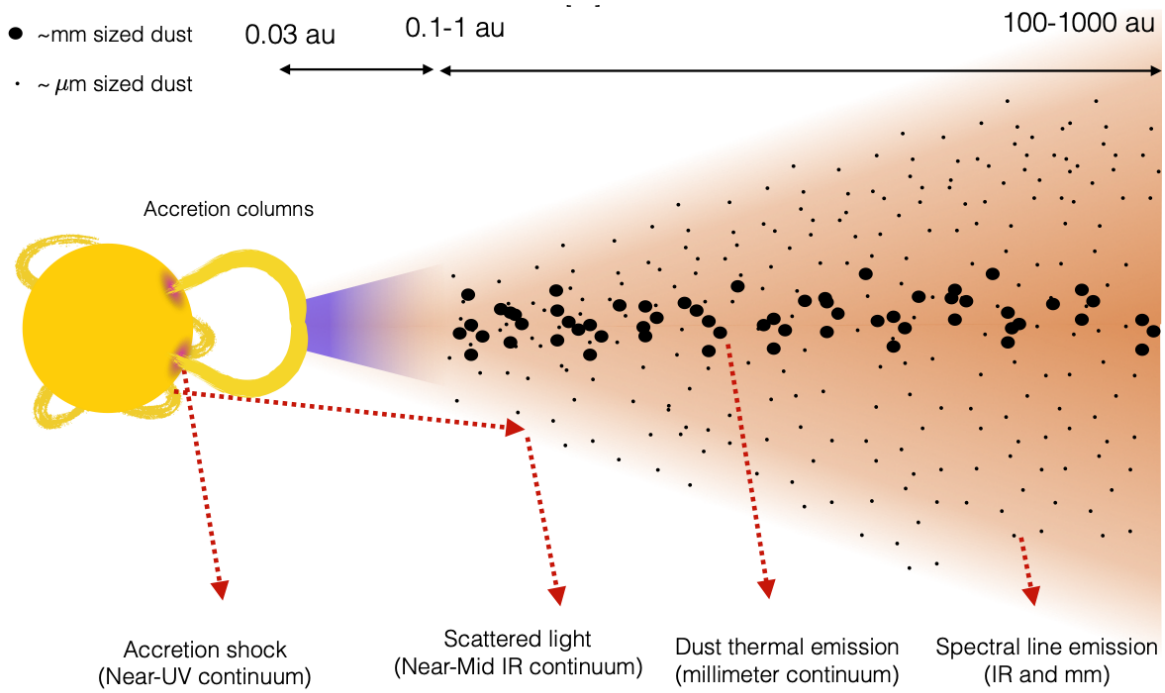

Fig. 1.2 Observational diagnostics of protoplanetary discs. For simplicity, only the disc and star are shown, and features such as disc wind and structure like rings and gaps are omitted. From Lesur (2020).

1.3.1 Temperature structure

Protoplanetary discs are distinguished from their stellar-mass black hole accretion disc counterparts by their relatively lower temperature profiles. While black hole accretion discs can reach a surface temperature ranging between $10^4 - 10^7$ K, a protoplanetary disc usually peaks at around 1000 K in the innermost region, before rapidly dropping off to several hundred Kelvin by 10 AU (Najita et al., 2003). The main source of heating is from radiative heating due to the central star, while secondary sources of heating such as external radiation (D'Alessio et al., 1997), radioactivity (Cleeves et al., 2013), viscous dissipation (D'Alessio et al., 1998), spiral shocks (Rafikov, 2016) and vertical structure perturbations (Dullemond and Dominik, 2004) may also be present. As a result, temperature is generally modelled as an increasing function of $T(z)$ and a decreasing function of $T(R)$, where z and R are the cylindrical vertical and radial coordinates respectively. This, coupled to the generally lower temperatures, lead to the lower ionisation fractions found in much of the disc, particularly in the central mid-plane regions, significantly affecting the nature of magnetic processes in those regions.

1.3.2 Accretion

There is no direct way of measuring the accretion rate in protoplanetary discs, and all current data come from two main indirect diagnostics: UV excess from the accretion shock at the stellar surface, and the fraction of stars showing disc features as a function of stellar age.

The UV excess results from material at the inner edge of the disc being disrupted and funnelled by the stellar magnetic field to the star's surface at a nearly free fall speed, forming an accretion shock that emits in the UV. Measurements of the UV excess translate to a typical accretion rate of $10^{-8} M_{\odot}$ yr^{-1}, with a variation of up to an order of magnitude on either side that is dependent on the particular system (Manara et al., 2016). However it should be noted that this only corresponds to the accretion rate at the foot of the accreting column, and does not take into account other processes such as vertical mass-loss due to a disc wind, or the overall mass flow in the disc itself. Typical outflow rates from low-mass classical T-Tauri stars have been found to be 10^{-9} to $10^{-7} M_{\odot}$ yr^{-1} (Frank et al., 2014).

The second diagnostic relies on estimating of the ages of T-Tauri stars, and analysing the decline of the fraction of systems with disc signatures (such as via the infrared excess resulting from dust surround the star or the UV excess) with stellar age. Using this method, Hernández et al. (2007) showed that typical disc fraction drops to 50% at around 3 Myr, while Fedele et al. (2010) measured a mass accretion timescale of 2.3 Myr for the whole system, and 3.0 Myr for the dust. Assuming a steady accretion and or wind mass loss rate throughout the lifetime of the discs, protoplanetary disc masses can be inferred to be in the range $10^{-3} - 10^{-1} M_{\odot}$, consistent with results obtained via observations of the total dust content of discs (Andrews et al., 2013).

1.3.3 Vertical outflows: winds and jets

As demonstrated in the case of HH-30, vertical outflows in the form of winds and jets are often found to be associated with protoplanetary discs. In fact, current observations point to most, if not all, young stellar systems having accretion-driven bi-polar outflows during their formation (Frank et al., 2014).

Jets are usually narrow and highly collimated, and have velocities of order $100 - 1000$ km s^{-1} (Frank et al., 2014). They consist of atomic and/or molecular gas, and are often observed in forbidden emission lines (Lesur, 2020). Jets are believed to originate from the innermost parts of the disc ($R < 5$ AU) due to their high velocity, and to be driven by dynamical interactions of accreted matter with magnetic fields from the star and/or threading the disc. Jets can propagate up to the parsec scale, significantly affecting the surrounding

interstellar environment. The outflow rate can also be up to 10% of the accretion rate in classical T-Tauri stars (Frank et al., 2014).

Winds are usually much slower, with velocities of order $1-30$ km s^{-1} (Frank et al., 2014), and observed via the emission lines of molecular gas evicted with the outflows. Winds are ejected from regions >1 AU, and their ejection radius can extend up to 10-100 AU from the central protostar (Bjerkeli et al., 2016; Lesur, 2020). They are believed to be either the result of material being “swept up" by the jet into the environment, or due to hydrodynamic or magnetohydrodynamic processes that drive a direct outflow from the disc (Frank et al., 2014; Lesur, 2020).

Understanding the nature and origin of outflows is important for understanding protoplanetary disc dynamics, as they can be significant sources of mass and angular momentum removal vertically, which in turn could drive processes such as accretion, or even substructure formation like that of rings and gaps (Riols and Lesur, 2019).

1.3.4 Turbulence

Turbulence can be an important driver for disc accretion, as given sufficient strength and the correct properties, it can act as an effective viscosity, transporting angular momentum radially outwards, and allowing mass to flow radially inwards. The presence of turbulence can also have a significant effect on planet formation processes, as it prevents the settling of dust to the disc mid-plane, and also affects the formation of planetesimals through collisions (Johansen et al., 2014), and the migration rate of low-mass planets (Kley and Nelson, 2012). Constraining the strength and nature of turbulence in protoplanetary discs is therefore crucial for theoretical work in understanding their dynamics.

Turbulence is indirectly estimated in two ways: through the broadening of molecular line profiles from turbulent motion of the gas (Armitage, 2015), and through measuring the level of dust settling in the disc which in turn gives an upper limit on the level of turbulence allowed (Pinte et al., 2016).

From theory, it is expected that turbulence in discs is subsonic. The contribution of small-scale fluid turbulence to the line width can be estimated as

$$\delta v = \frac{v}{c}\sqrt{\frac{2k_B T}{\mu m_H} + v_{\rm turb}^2}, \tag{1.1}$$

where v is the central frequency and c is the speed of light, T is the temperature, μ is the molecular weight of the observed species, and $v_{\rm turb}$ is the root-mean-square velocity estimator of the turbulence (Armitage, 2015). The low turbulent velocities expected therefore increases the difficulty in measuring turbulence levels using the spectral line broadening

method, and observations generally rely on the transitions of heavy molecules such as CO, CN and CS. Recent measurements by Flaherty et al. (2015) and Flaherty et al. (2017) using high resolution ALMA data have concluded negligible turbulence contribution to the line broadening in the disc around the star HD 163296, with an upper limit of $v_{\rm turb} < 0.1 c_s$. Other spectral line studies have also found that line broadening data for discs at large distances (> 30 AU) yielded an upper limit of $v_{\rm turb} < 0.03 c_s$ as best fit (Lesur, 2020). These results suggest that protoplanetary discs are largely laminar in nature, with a turbulence level that is insufficient in accounting for the accretion rates observed. This is further corroborated by direct measurements of the dust layer thickness of the HL-Tau system by Pinte et al. (2016), who found that 100 μm grains have settled towards the mid-plane with a vertical dust scale height 10 times smaller than the gas scale height, implying very low levels of turbulence present with $v_{\rm turb} \sim 10^{-2} c_s$. These results separate protoplanetary disc dynamics from other systems such as black hole accretion discs, where a high level of turbulence is expected, and points to other mechanisms such as wind-driven accretion and photoevaporation as mainly responsible for driving their evolution.

1.3.5 Structures

Perhaps the most fascinating and beautiful of protoplanetary disc features revealed by observations so far are the large variety of structures observed in recent high resolution studies. They show us that discs are not smooth and symmetrical as assumed in the past, but rather possess features varying on the scale of our own Solar System.

Morphologically, these structures can be categorised into four types:

- **Ring and cavity:** Discs with this feature are also known as transition discs, and account for between $5-25\%$ of observed discs, depending on the precise definition (Currie and Sicilia-Aguilar, 2011; Luhman et al., 2010). In these systems the outer disc is fairly normal compared with other discs, but the inner disc is truncated at some inner radius. However, most transition discs are also found to be accreting at rates comparable to other Classical T-Tauri stars (Manara et al., 2014), implying that the cavities, though devoid of dust, are not empty. These are usually gas-filled, and accretion onto the star continues.

- **Rings and gaps:** This category consists of discs with concentric, axisymmetric bands of brightness (rings) and darkness (gaps), reflecting the uneven radial distribution of the tracer. The most famous example of this is that of HL Tau, which has seven pairs of rings and gaps located between 20 AU and 100 AU (ALMA Partnership et al., 2015). It is the most common morphology that is identified in both scattered light and

mm-measurements (Andrews, 2020), and there exists a large variety of forms within this category.

- **Arcs:** Also known as the horseshoe morphology, these are non-axisymmetric structures organised as a crescent-shaped feature spanning a limited range of azimuth on one side of the disc. Interestingly, this feature is only observed in mm and sub-mm measurements of larger dust particles, and there is no observation of arcs in mid-IR imaging of gas or μm-sized dust (Armitage, 2015). This morphology type is also much rarer compared with the axisymmetric types (Andrews, 2020).

- **Spirals:** This morphology ranges from the large-scale symmetric two-armed spiral of the $m = 2$ mode, to tightly-wound asymmetric structures. Only six systems with spirals are currently known, three in mm measurements with the $m = 2$ mode (Huang et al., 2018; Pérez et al., 2016), and three in spectral line measurements with extended complex spirals (Christiaens et al., 2014; Tang et al., 2017, 2012; Teague et al., 2019).

Figure 1.3, taken from Andrews (2020), presents a gallery of images showing the four disc types observed in both mm and scattered light measurements.

Many of these features are observed in both scattered light images of discs in the near infrared using polarimetric differential imaging (e.g. in Benisty et al. (2015) and Ginski et al. (2016)), and mm and sub-mm interferometric observations (e.g. ALMA and the Submillimeter Array (SMA)). Interestingly, different morphologies are sometimes found to co-exist in the same disc, but for different tracers. For example, for the system MWC 758, spirals are observed in scattered light (Benisty et al., 2015), but rings, gaps and arcs are seen in mm measurements (Dong et al., 2018). This may be an indicator of different mechanisms simultaneously at work in the disc, and driving the evolution of different components of the disc. There are also cases where multiple features are observed in the same tracer for the same disc (Huang et al., 2018), and again may be an indicator of different physics being simultaneously at work in the system.

Theorists have proposed that these features could be the result of fluid dynamical processes in the disc, or of gravitational interactions of the disc with embedded planets. As of today, there is no clear consensus as to which may be the more common explanation (Lesur, 2020). Hence the origin of structures in discs remain an open question, prompting more theoretical research into mechanisms that can lead to their formation, and more detailed observations to constrain plausible models.

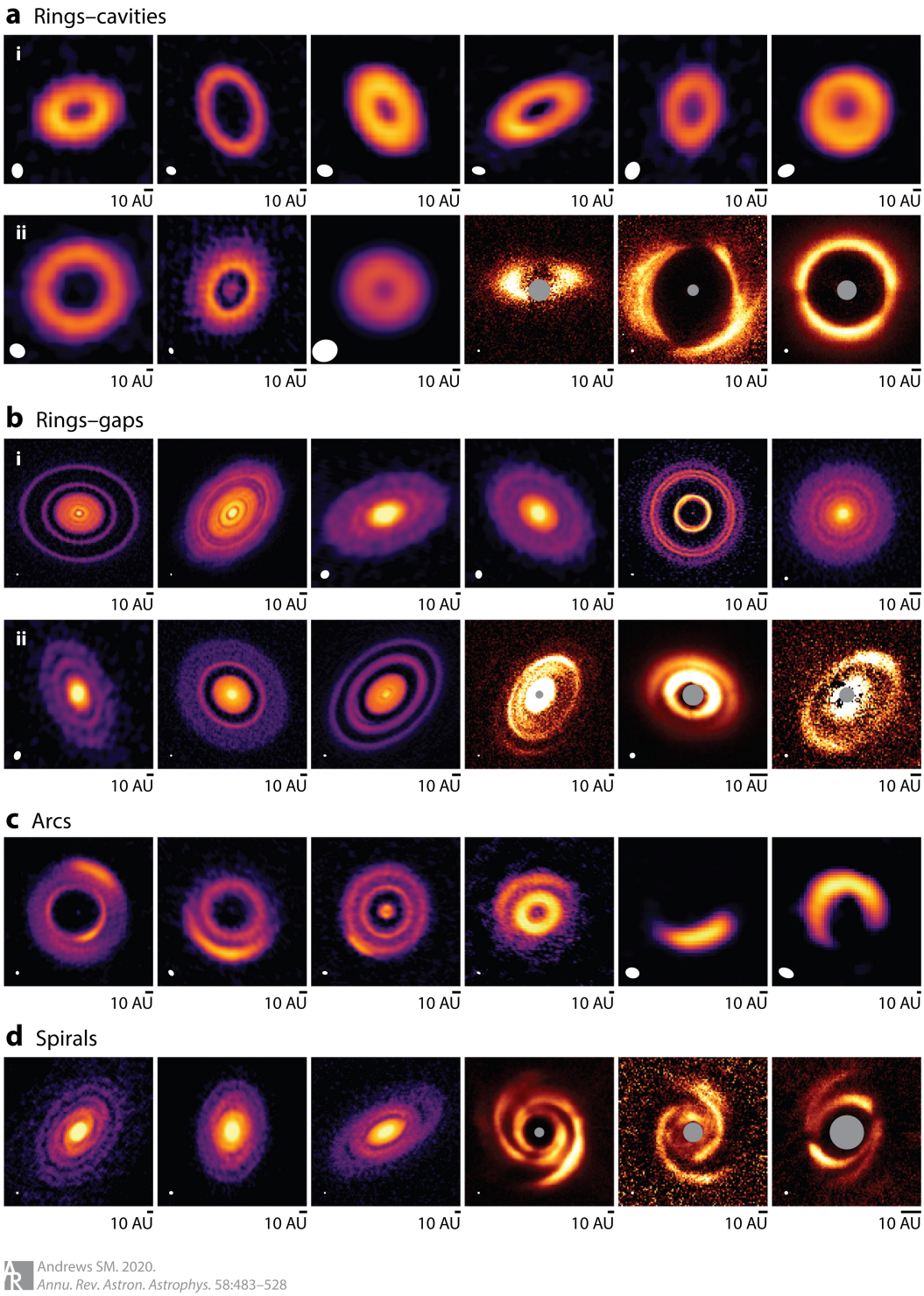

Fig. 1.3 A gallery of observations of protoplanetary discs grouped according to the four disc types discussed: a) ring and cavity, b) rings and gaps, c) arcs and d) spirals. All images are mm continuum measurements, with the exception of the bottom right three images of each of a), b) and c), which are scattered light observations. Figure used with permission from Andrews (2020). For full list of citations for each individual image, please see caption of figure 11 of Andrews (2020).

1.3.6 Magnetic fields

As we shall see in Chapter 2, magnetic fields are theorised to have a major impact on astrophysical gas dynamics, and in the disc context they may be responsible for mechanisms that lead to disc accretion, outflow, turbulence and structure formation. Magnetic fields are thought to be intrinsic to the molecular clouds from which star-disc systems form (Crutcher, 2012), and hence we should expect disc systems to have a certain degree of magnetisation. Constraining the field morphology and determining typical field strengths present are therefore crucial to understanding the feasibility and effectiveness of different magnetic mechanisms that may be at play in protoplanetary discs.

Sadly, to date, there are few observational constraints of magnetic fields in protoplanetary discs. Fields of sufficient strength and their topology can in theory be measured by the circular polarisation induced by Zeeman splitting of molecular emission lines. Measurements of magnetic fields in the inner disc using the Zeeman effect have yielded strong toroidal field strengths of a few kG (Donati et al., 2015), but there is no way of telling whether this field is from the host star or the disc. Theory has also predicted that field strengths could drop to a few mG at a few tens of AU (Wardle, 2007), and so far, all measurements at larger distances (>10 AU) using Zeeman splitting have only resulted in upper limits of $B_z < 0.8$ mG and $B < 30$ mG (Vlemmings et al., 2019).

In principle, field morphologies can also be determined from the linear polarisation of the dust thermal emission (mm continuum) (Bertrang et al., 2017; Cho and Lazarian, 2007). Here, dust is assumed to be aligned perpendicularly to magnetic field lines, leading to the preferential emission of thermal radiation with a specific polarisation that is 90° to the field as the particles vibrate. However, self-scattering by dust grains (Kataoka et al., 2015) and interplay from other grain alignment mechanisms (Kataoka et al., 2019; Tazaki et al., 2017) can also polarise the radiation, polluting the results and causing great uncertainty in their interpretation.

One final hint of the strength and orientation of protoplanetary disc field strengths comes from measuring the remnant magnetisation in meteorites and comets in our Solar System today, and assuming that the field was frozen into the objects during their formation in the disc stage, and that other protostellar systems have also formed in a similar environment. This has yielded field strengths of the order of 0.1 G around 1 AU from meteoric data (Fu et al., 2014), and upper limits of $B < 30$ mG at around $15-45$ AU from cometary observations (Biersteker et al., 2019).

1.4 The need for magnetohydrodynamics

For many years in accretion disc research, the processes that drive accretion to account for the observed rates have been a puzzle (Balbus and Hawley, 1998). How is angular momentum removed to allow for mass to be accreted?

1.4.1 Sources of radial angular momentum removal

Most accretion discs, including protoplanetary discs, can be approximated as fluids in Keplerian rotation around the central star. In this regime, the angular velocity of the fluid decreases with radial distance, leading to differential rotation and shear between the fluid elements at different radii. The presence of a shear viscosity could in theory lead to angular momentum transfer between these fluid elements, driving accretion. Indeed, the influential model of accretion disc evolution by Shakura and Sunyaev (1973) was based on this idea of the viscous spreading of the disc. Studies have shown that the standard microscopic viscosities expected in discs are too small to provide any significant angular momentum transfer that can account for the observed accretion rates (Clarke and Carswell, 2014; Spitzer, 1962). However, turbulent mixing might be a source of an effective viscosity that could facilitate the radially outward removal of angular momentum from the disc. We therefore turn to ask if there are any known processes that would cause the fluid flow to be destabilised, and for turbulence to develop.

The failure of pure barotropic hydrodynamics

First, we demonstrate the failure of pure barotropic hydrodynamics in accounting for instability in accretion discs. In the most simple and idealised case, we assume the disc to be a barotropic ideal hydrodynamic fluid. The linear stability of such an axisymmetric flow with a smoothly varying angular velocity profile, $\Omega(r)$, is given by the classic Rayleigh's criterion (Pringle and King, 2007):

$$\frac{\mathrm{d}l}{\mathrm{d}R} = \frac{\mathrm{d}}{\mathrm{d}R}(R^2\Omega) > 0 \rightarrow \text{stability}, \tag{1.2}$$

where R is the radial distance from the star, and l is the specific angular momentum of the fluid element. For a Keplerian disc, $l \propto R^{1/2}$ and $\Omega \propto R^{-3/2}$, leading to $\mathrm{d}l/\mathrm{d}R \propto R^{-1/2} > 0$, hence we should expect stability. In fact, as long as the specific angular momentum increases radially outward, which is the case in accretion discs, the differential rotation is always stable to linear axisymmetric perturbations.

There have been suggestions that the large Reynolds number ($\sim 10^{14}$) (Clarke and Carswell, 2014) expected in a primordial disc could lead it to be unstable to nonlinear perturbations such as in the pipe or Cartesian shear flow contexts. However, to date, there are no known instabilities in the rotating Keplerian shear flow context unique to astrophysical discs, and both analytic and numerical arguments (Lesur and Longaretti, 2009) have suggested that no non-linear instability could generate the levels of turbulence required for astrophysical significance. These are further supported by laboratory experiments which show that Keplerian rotation is hydrodynamically stable (Ji et al., 2006; Schartman et al., 2012).

Self-gravity

Other sources of instability have been proposed. Self-gravity can be important for discs or disc portions when the Toomre criterion

$$Q \equiv \frac{c_s \Omega}{\pi G \Sigma} < Q_{\rm crit} \sim 1 \tag{1.3}$$

is satisfied, where Σ is the disc surface density. This is usually the case in young, massive discs, when the surrounding envelope is still contributing significantly to disc transport. Self-gravity can lead to the generation of large-scale non-local features such as spiral density waves, which in turn can lead to angular momentum transport and accretion (Rafikov, 2016). However, self-gravity is more likely to be important during the earlier stages of star formation (Armitage, 2015), and is unlikely to be a significant factor in the evolution of Class II discs that our study is focused on when accretion from the envelope has largely ceased.

Entropy-driven instabilities

Another class of instabilities that may be present rely on the existence of non-trivial temperature gradients in the disc. These are called “entropy-driven" instabilities, and include examples like convection from vertical temperature gradients (Lesur and Ogilvie, 2010), the vertical shear instability from radial temperature gradients (Nelson et al., 2013), and the subcritical baroclinic instability (Petersen et al., 2007a,b), the last of which occurs when surfaces of constant density are not parallel to surfaces of constant pressure, and can be responsible for the generation of vortices. There have been numerous studies into each of these instabilities in recent years, and they are shown to be able to generate a low but noticeable level of transport ($\alpha \sim 10^{-4} - 10^{-3}$) that can account for disc dynamics where magnetohydrodynamic processes are suppressed.

Magnetohydrodynamic instabilities

This leaves us with the introduction of magnetohydrodynamic (MHD) instabilities, which have been the subject of much research over the last 30 years. The seminal paper by Balbus and Hawley (1991) noted that a weak magnetic field threading the disc can cause a linear instability, now known as the magneto-rotational instability (MRI), that transports angular momentum outwards. In its nonlinear stage, the MRI can lead to strong turbulence in the disc (Hawley et al., 1995) which in turn can drive significant accretion.

The MRI has been very effectively applied to account for the level of turbulence in well-ionised accretion disc systems such as black hole accretion discs, and discs in binary systems. However, the lower temperatures and high opacities of protoplanetary discs means that much of the disc is expected to be poorly ionised. In this regime, non-ideal MHD effects such as Ohmic resistivity, Hall drift and ambipolar diffusion significantly affect the nature and strength of MRI dynamics. The likely presence of non-ideal MHD dynamics in protoplanetary discs, and their impact on magnetic instabilities like the MRI, will be the subject of the next chapter.

1.4.2 Sources of vertical angular momentum removal

As noted in Section 1.3.3, outflows are commonly observed to be associated with protostellar systems. Two mechanisms have been proposed to account for these vertical mass losses: photoevaporation due to radiation from the central star, and magnetically driven winds. While photoevaporation removes mass vertically from the disc and is likely to be responsible for the inside-out clearing of discs that lead to the formation of transition discs (Haworth et al., 2016; Owen et al., 2012), it by itself does not remove angular momentum, and cannot account for accretion. Magnetically driven winds, on the other hand, can be an efficient mechanism for extracting angular momentum as well as mass from the disc, and provide another way for accretion in the disc to be driven (Blandford and Payne, 1982). This, coupled with the observation of disc winds emitted from regions well inside the gravitational radius[1] within which photoevaporation is inefficient (Ercolano and Pascucci, 2017), suggest that magnetically driven winds indeed have a major role to play in the evolution of protoplanetary discs. The exact mechanics and considerations of these magnetic winds in the protoplanetary disc context will be explored in the next Chapter.

[1]The gravitational radius is given by $R_g = GM_\star/c_s^2$, and is a characteristic length scale derived from balancing the gravitational potential energy and the thermal energy of the disc. Beyond R_g, particles can become sufficiently thermally excited from its gravitational potential to evaporate.

Chapter 2

Magnetohydrodynamics of protoplanetary discs

2.1 General concepts

2.1.1 Ideal MHD

The equations of magnetohydrodynamics (MHD) are obtained by combining Maxwell's equations with the equations of fluid mechanics. We begin by considering the case where the fluid is assumed to be perfectly conducting (ideal MHD), before moving on to the non-ideal MHD regime more common in protoplanetary discs.

Maxwell's equations are given by

$$\nabla \cdot \mathbf{E} = \frac{\rho_e}{\varepsilon_0}, \tag{2.1}$$

$$\nabla \cdot \mathbf{B} = 0, \tag{2.2}$$

$$\nabla \times \mathbf{E} = -\frac{\partial \mathbf{B}}{\partial t}, \tag{2.3}$$

$$\nabla \times \mathbf{B} = \mu_0 \left(\mathbf{J} + \varepsilon_0 \frac{\partial \mathbf{E}}{\partial t} \right), \tag{2.4}$$

where $\mathbf{E}$ and $\mathbf{B}$ are the electric and magnetic fields respectively, ρ_e is the electric charge density, ε_0 and μ_0 are the permittivity and permeability of free space respectively, and $\mathbf{J}$ is the electric current density. The equations of fluid dynamics are given by

$$\frac{\partial \rho}{\partial t} = -\nabla \cdot (\rho \mathbf{u}), \tag{2.5}$$

$$\rho\left(\frac{\partial \mathbf{u}}{\partial t}+\mathbf{u}\cdot\nabla\mathbf{u}\right)=-\nabla p-\rho\nabla\Phi+\mathbf{F}, \tag{2.6}$$

where ρ is the fluid mass density, $\mathbf{u}$ is the fluid velocity, p is the pressure, Φ is the combined gravitational and centrifugal potential, and $\mathbf{F}$ represents other forces that may be present in the system (e.g. from magnetic fields).

Consider the electric field in the fluid element's rest frame, $\mathbf{E}'$, given by:

$$\mathbf{E}'=\mathbf{E}+\mathbf{u}\times\mathbf{B}. \tag{2.7}$$

Since we are regarding the fluid as a perfect conductor in the ideal MHD limit, this rest frame electric field vanishes, resulting in

$$\mathbf{E}=-\mathbf{u}\times\mathbf{B}. \tag{2.8}$$

Combining this result with the third Maxwell equation, we arrive at the induction equation for ideal MHD:

$$\frac{\partial \mathbf{B}}{\partial t}=\nabla\times(\mathbf{u}\times\mathbf{B}). \tag{2.9}$$

Next, we compute the Lorentz force component of $\mathbf{F}$ in the momentum equation. We recognise that Lorentz force summed over all charged particles is

$$\mathbf{F}=\rho_e\mathbf{E}+\mathbf{J}\times\mathbf{B}. \tag{2.10}$$

We obtain an expression for $\mathbf{J}$ by noting that for fluid flow in the non-relativistic regime that we are considering, the displacement current (second term on the RHS) in Equation (2.4) can be neglected. This can be seen by considering motion on a characteristic length scale L and time scale τ, such that $u\sim L/\tau$. Noting that $\mu_0\varepsilon_0=1/c^2$, and substituting in Equation (2.8), the displacement current term has a magnitude $\sim uB/(c^2\tau)$. On the other hand, the LHS of Equation (2.4) has a magnitude $\sim B/l$. The ratio of their magnitudes is therefore $\sim u^2/c^2\ll 1$, justifying our neglect of the displacement current term in non-relativistic flows. Therefore, we arrive at

$$\mathbf{J}=\frac{1}{\mu_0}\nabla\times\mathbf{B}, \tag{2.11}$$

where $\mathbf{J}$ and $\mathbf{B}$ have a one-to-one correspondence.

Using the same argument based on characteristic scales, we can also show that the electric part of the Lorentz force can be neglected compared to the magnetic part. Gauss' law (Equation (2.1)) gives us $\rho_e\sim E/(\varepsilon_0 l)$. Hence the ratio of the electric to magnetic terms of

Equation (2.10) is $\sim [E^2/(\varepsilon_0 l)]/[B^2/(\mu_0 l)] \sim u^2/c^2 \ll 1$. Hence the Lorentz force is given by

$$\mathbf{F} = \mathbf{J} \times \mathbf{B} = \frac{1}{\mu_0}(\nabla \times \mathbf{B}) \times \mathbf{B}, \tag{2.12}$$

and the full set of ideal MHD equations are:

$$\frac{\partial \rho}{\partial t} = -\nabla \cdot (\rho \mathbf{u}), \tag{2.13}$$

$$\rho \left(\frac{\partial \mathbf{u}}{\partial t} + \mathbf{u} \cdot \nabla \mathbf{u} \right) = -\nabla p - \rho \nabla \Phi + \frac{1}{\mu_0}(\nabla \times \mathbf{B}) \times \mathbf{B}, \tag{2.14}$$

$$\nabla \cdot \mathbf{B} = 0, \tag{2.15}$$

$$\frac{\partial \mathbf{B}}{\partial t} = \nabla \times (\mathbf{u} \times \mathbf{B}). \tag{2.16}$$

These are known as the continuity equation, the momentum equation, the solenoidal condition and the induction equation respectively. We shall now discuss some of their properties that are crucial for understanding our work below.

2.1.2 Magnetic pressure and tension

First we look at the Lorentz force terms, which can be split using standard vector identities into two parts:

$$\frac{1}{\mu_0}(\nabla \times \mathbf{B}) \times \mathbf{B} = -\nabla \left(\frac{B^2}{2\mu_0} \right) + \frac{1}{\mu_0}(\mathbf{B} \cdot \nabla)\mathbf{B}. \tag{2.17}$$

The first term on the RHS is the magnetic pressure force, where $p_m = B^2/(2\mu_0)$ can be treated as a magnetic pressure resisting compression of field lines. In literature it is common to characterise the magnetisation of a disc by the dimensionless plasma beta parameter, which relates the thermal energy density (proportional to the gas pressure) to the magnetic energy density (equal to the magnetic pressure), and is defined as

$$\beta \equiv \frac{p}{p_m} = \frac{2\mu_0 p}{B^2}. \tag{2.18}$$

Mid-plane β values normally assumed to be characteristic of protoplanetary disc conditions lie in the range $10^4 - 10^6$ (Guilet and Ogilvie, 2014; Okuzumi et al., 2014; Takeuchi and Okuzumi, 2014), where a vertical field is assumed at the mid-plane, although observationally it is still largely unconstrained. A disc typically has a density profile that decreases rapidly at several scale heights above the mid-plane, and the height at which $\beta \sim 1$ is noted to

be the height from which magnetic winds are launched. The situation $\beta \approx 1$ is known as 'equipartition', and is the case when the magnetic and thermal energy densities are comparable to each other. It is often found to be a turning point in the behaviour of magnetic processes.

One physical significance of the magnetic pressure force is in understanding the launching of vertical outflows from a weakly magnetised disc. The disc's orbital motion can lead to the winding up of the poloidal field lines, causing a large toroidal field to develop over an extended range in z. The resultant magnetic pressure gradient can then lead to the launching of vertical outflows due to the magnetic pressure force, and is sometimes referred to as a magnetic tower flow (Lynden-Bell, 1996, 2003).

The second term on the right-hand side of Equation (2.18) is known as the curvature force/magnetic tension, and is best thought of as the same as the tension in a taut string. The term can be rewritten as

$$\frac{1}{\mu_0}(\mathbf{B}\cdot\nabla)\mathbf{B} = \frac{B^2}{2\mu_0}(\mathbf{b}\cdot\nabla)\mathbf{b} + \mathbf{b}\mathbf{b}\cdot\nabla\left(\frac{B^2}{2\mu_0}\right), \tag{2.19}$$

where $\mathbf{b} \equiv \mathbf{B}/|\mathbf{B}|$ is the unit vector along the magnetic field. The first term on the right-hand side is the magnetic pressure multiplied with $\mathbf{b}\cdot\nabla\mathbf{b}$, the vector curvature of the magnetic field, and implies that bent field lines would naturally resist the curvature and want to straighten up. The second term on the right-hand side is the component of the magnetic pressure gradient in the direction of the field lines, and acts as a negative stress along the field lines.

The magnetic tension force is important for the operation of the magnetorotational instability (see Section 2.2 for a more detailed discussion), as it gives rise to the return force between displaced fluid elements that is responsible for the spring-like nature of magnetised fluid elements. It is responsible for the driving of accretion or decretion flows in the disc depending on how the field bends in the azimuthal direction when viewed in the $z-\phi$ plane.

2.1.3 Magnetic flux

The ideal induction equation

$$\frac{\partial\mathbf{B}}{\partial t} = \nabla\times(\mathbf{u}\times\mathbf{B}). \tag{2.20}$$

has a simple and beautiful interpretation in that magnetic field lines are "frozen in" to the fluid, and therefore moves with the flow. This can be seen by rewriting the induction equation, using vector identities, into the form:

$$\frac{\mathrm{D}\mathbf{B}}{\mathrm{D}t} \equiv \left(\frac{\partial}{\partial t} + \mathbf{u}\cdot\nabla\right)\mathbf{B} = \mathbf{B}\cdot\nabla\mathbf{u} - \mathbf{B}\nabla\cdot\mathbf{u}, \tag{2.21}$$

where $\mathrm{D}/\mathrm{D}t \equiv \partial/\partial t + \mathbf{u}\cdot\nabla$ is the convective derivative that moves with the fluid flow. We can then note from the mass conservation equation that

$$\nabla\cdot\mathbf{u} = -\frac{1}{\rho}\frac{\mathrm{D}\rho}{\mathrm{D}t}. \tag{2.22}$$

Substituting this into the modified induction equation, and multiplying it by $1/\rho$, we arrive at

$$\frac{\mathrm{D}}{\mathrm{D}t}\frac{\mathbf{B}}{\rho} = \frac{\mathbf{B}}{\rho}\cdot\nabla\mathbf{u}. \tag{2.23}$$

This is the same equation satisfied by a material line element, $\delta\mathbf{x}$, defined as an infinitesimal line element that moves with the bulk velocity $\mathbf{u}$ of the fluid:

$$\frac{\mathrm{D}}{\mathrm{D}t}\delta\mathbf{x} = \mathbf{u}(\mathbf{x}+\delta\mathbf{x}) - \mathbf{u}(\mathbf{x}) \approx \delta\mathbf{x}\cdot\nabla\mathbf{u}. \tag{2.24}$$

Hence a magnetic field line is advected and distorted the same way as a material curve by fluid motion. This result is commonly known as Lundquist's theorem.

One corollary that follows from Lundquist's theorem is Alfvén's theorem, which states that the magnetic flux, which is a measure of the number of field lines passing through a given closed loop, is conserved through any loop moving with the fluid. We can see this in the case of a material surface element by considering the magnetic flux through it, given by $\delta\Phi = \mathbf{B}\cdot\delta\mathbf{S}$, where $\delta\mathbf{S}$ is the surface element. The convective derivative of the flux is then given by:

$$\begin{aligned}\frac{\mathrm{D}\delta\Phi}{\mathrm{D}t} &= \frac{\mathrm{D}\mathbf{B}}{\mathrm{D}t}\cdot\delta\mathbf{S} + \mathbf{B}\cdot\frac{\mathrm{D}\delta\mathbf{S}}{\mathrm{D}t} \\ &= \left(B_j\frac{\partial u_i}{\partial x_j} - B_i\frac{\partial u_j}{\partial x_j}\right)\delta S_i + B_i\left(\frac{\partial u_j}{\partial x_j}\delta S_i - \frac{\partial u_j}{\partial x_i}\delta S_j\right) \\ &= 0.\end{aligned} \tag{2.25}$$

Flux freezing means that fluid flow can change the magnetic field strength. This can be seen by considering the physical interpretation of the terms in Equation 2.21:

$$\frac{\partial\mathbf{B}}{\partial t} + \mathbf{u}\cdot\nabla\mathbf{B} = \mathbf{B}\cdot\nabla\mathbf{u} - \mathbf{B}\nabla\cdot\mathbf{u}. \tag{2.26}$$

The second term on the left-hand side represents the advection of the field by the flow, while the first and second terms on the right-hand side represent the effect of velocity gradients stretching (and hence amplifying) the field by elongating the fluid elements, and finally compression of the field by convergent or divergent fluid flows. This has a huge impact on the MHD of astrophysical fluids, as it means magnetic fields can be amplified or weakened and also have their geometry changed depending on the flow properties.

It is important to note at this point that flux freezing only strictly applies in ideal MHD. Once non-ideal MHD terms like resistivity, Hall drift and ambipolar diffusion are involved, such as in the protoplanetary disc context, the flux movement becomes much more complex. This will be explored in Section 2.4.2.

Magnetic flux in protoplanetary discs

One important diagnostic for protoplanetary discs is the poloidal magnetic flux threading it. Its strength and inclination has a direct impact on the feasibility of both the operation of the MRI and the launching of a magnetic wind. A large-scale axisymmetric poloidal magnetic field can be described with a magnetic flux function ψ in cylindrical coordinates (r, ϕ, z) by (Ogilvie, 1997)

$$\mathbf{B} = \nabla\psi \times \frac{\mathbf{e}_\phi}{r} \tag{2.27}$$

or

$$B_r = -\frac{1}{r}\frac{\partial\psi}{\partial z}, \qquad B_z = \frac{1}{r}\frac{\partial\psi}{\partial r}, \tag{2.28}$$

where $\mathbf{e}_\phi$ is the azimuthal unit vector, and B_r and B_z are the radial and vertical components of the magnetic field. The magnetic flux threading a disc of radius r is then given by

$$\int_0^r B_z(r', z) 2\pi r' \mathrm{d}r' = 2\pi\psi, \tag{2.29}$$

where we have set the integration constant to zero.

From its definition, $\mathbf{B} \cdot \nabla\psi = 0$, hence ψ is a useful label for magnetic field lines and defines their surfaces of revolution. It can be shown by integrating Faraday's law (Equation 2.3) with respect to r that the time-evolution of the magnetic flux function of the disc evolves in general as

$$\frac{\partial\psi}{\partial t} + r v_\psi B_z = \frac{\partial\psi}{\partial t} + v_\psi \frac{\partial\psi}{\partial r} = 0, \tag{2.30}$$

where

$$v_\psi = \frac{E_\phi}{B_z} \tag{2.31}$$

is the radial transport velocity of the vertical flux at a given height, with E_ϕ being the azimuthal component of the electric field (Guilet and Ogilvie, 2012). Calculating v_ψ is important for determining the long term evolution and consequent distribution of magnetic flux in the disc, and has been the subject of both semi-analytic (Guilet and Ogilvie, 2012, 2013, 2014) and numerical studies (Bai, 2017; Bai and Stone, 2017; Zhu and Stone, 2018).

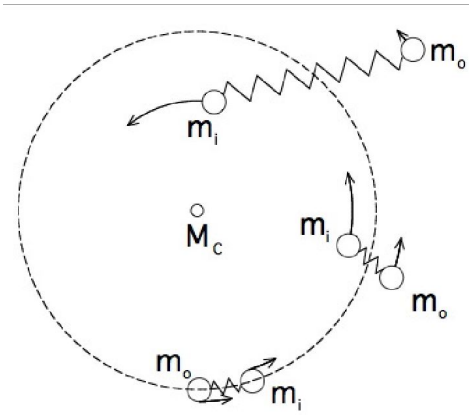

Fig. 2.1 Analogy of the MRI mechanism as masses (m_i and m_o) connected by springs in orbit at different radii around a central mass (M_c). The inner mass m_i has a higher angular velocity and gets 'ahead' in the orbit, transferring angular momentum to the outer mass m_o through the magnetic tension. This promotes m_o to a higher orbit while m_i loses angular momentum and moves to a lower orbit. This causes m_i to have an even higher angular velocity and be even further ahead in its orbit, and the process repeats and amplifies itself. Figure credit: H. Ji.

2.2 Magnetorotational Instability (MRI)

We begin our discussion of the MRI by qualitatively outlining the physical processes governing its operation. Magnetic fields in a disc connect fluid elements as though they were masses connected by a spring. Since a fluid element on an inner orbit rotates at a higher angular velocity than the outer one, their relative position increases, causing the magnetic tension binding the two elements together to also rise. This tension force slows down the inner element and speeds up the outer element, transferring angular momentum from the inner to the outer. As a result, the inner element moves to a lower orbit, while the outer element is promoted to a higher one. This process then repeats and amplifies, as represented by Figure 2.1. The MRI grows exponentially in the linear phase, followed by a nonlinear mixing of fluid elements, resulting in turbulence.

2.2.1 Linear MRI in unstratified discs

Quantitatively, we consider the linear MRI in a local framework rotating with the disc, where the characteristic length scale of motions is much shorter than the cylindrical radial distance from the star. In this local model, which will be derived and discussed in more detail in Chapter 3, x, y, and z correspond to the radial, azimuthal and vertical directions

respectively. We also assume a pure vertical background magnetic field of strength B_0, and that perturbations from equilibrium have the form

$$\mathbf{X} = \mathbf{X}_0 \exp(ikz), \tag{2.32}$$

where k is the wave number of the perturbation. The equations of motion for a fluid particle are then:

$$\frac{\mathrm{d}^2 X_x}{\mathrm{d}t^2} = 2q\Omega_0^2 X_x + 2\Omega_0 \frac{\mathrm{d}y}{\mathrm{d}t} - v_A^2 k^2 X_x, \tag{2.33}$$

$$\frac{\mathrm{d}^2 X_y}{\mathrm{d}t^2} = -2\Omega_0 \frac{\mathrm{d}X_x}{\mathrm{d}t} - v_A^2 k^2 X_y, \tag{2.34}$$

$$\frac{\mathrm{d}^2 X_z}{\mathrm{d}t^2} = -\Omega_0^2 X_z, \tag{2.35}$$

where Ω_0 is the orbital angular velocity at some reference radius r_0, defined as the centre of the box, $q \equiv -\partial \ln \Omega / \partial \ln r|_{r_0}$ is the shear parameter, and $v_A = B_0/\sqrt{\mu_0 \rho_0}$ is the Alfvén velocity.

The first term on the right-hand side of Equation (2.33) comes from the centrifugal force which acts radially outward, while the second term of the right-hand side of Equation (2.33) and the first term of the right-hand side of Equation (2.34) are the contributions from the Coriolis force, acting perpendicularly to the fluid motion. The final terms on the right-hand sides of Equations (2.33) and (2.34) are from the Lorentz force, and are restorative in nature. They arise from noticing that the magnetic perturbation can be obtained by integrating the induction equation with respect to time, giving us

$$\delta \mathbf{b} = ikB_0 \mathbf{x}, \tag{2.36}$$

and that only the magnetic tension term appears in the horizontal direction, hence

$$\begin{aligned} \frac{\mathbf{F}}{\rho} &= \frac{\mathbf{B} \cdot \nabla \delta \mathbf{b}}{\mu_0 \rho} \\ &= -\frac{k^2 B_0^2}{\mu_0 \rho} \mathbf{X} \\ &= -v_A^2 k^2 \mathbf{X}. \end{aligned} \tag{2.37}$$

Finally, the right-hand side term in Equation (2.35) arises from the vertical component of the gravitational acceleration towards the star once the fluid particle is displaced from the mid-plane.

The system of equations is separable in the vertical and horizontal directions. In the vertical direction, we recover simple harmonic motion about the mid-plane at the orbital frequency Ω_0.

The motion in the horizontal direction requires more thought. In the absence of magnetic fields, we can show that epicyclic motion ensues. To see this, we first integrate Equation (2.34) with respect to time. Without loss of generality, we can assume that the perturbation does not change the angular momentum of the fluid particle and set the constant of integration to zero, giving us

$$\frac{\mathrm{d}X_y}{\mathrm{d}t} = -2\Omega_0 X_x, \tag{2.38}$$

which can be interpreted as the conservation of angular momentum of the system, as $L = \frac{\mathrm{d}X_y}{\mathrm{d}t} + 2\Omega_0 X_x$ is the local angular momentum of the fluid particle. We then substitute this result into Equation (2.33) to give us a second order differential equation for X_x:

$$\frac{\mathrm{d}^2 X_x}{\mathrm{d}t^2} = -2\Omega_0^2(2-q)X_x. \tag{2.39}$$

This is simply a harmonic oscillator with frequency

$$\omega = \Omega_0^2\sqrt{2(2-q)} \equiv \kappa, \tag{2.40}$$

and is commonly known as the epicyclic frequency. In Keplerian discs such as protoplanetary systems, $q = 3/2$, hence κ is real, and the motion is an oscillation. Substituting the solution to X_x to Equation (2.34) then gives us an equivalent differential equation in X_y with the same epicyclic frequency. This is consistent with the result from Section 1.4.1 of Chapter 1 that pure Keplerian flows are linearly stable.

Next, we turn to the magnetised case. The azimuthal tension force now breaks angular momentum conservation, leading to instability. Let us assume the ansatz $\mathbf{X} \propto \exp \sigma t$ for the growth of this instability, where σ is the growth rate. The horizontal equations of motion then become

$$(\sigma^2 + v_A^2 k^2)X_x = 2q\Omega_0^2 X_x + 2\Omega_0 \sigma X_y, \tag{2.41}$$

$$(\sigma^2 + v_A^2 k^2)X_y = -2\Omega_0 \sigma X_x. \tag{2.42}$$

This is a linear eigenvalue problem, from which we can extract the dispersion from the determinant of the matrix $\mathbf{L}$ when the equations are cast into the form $\mathbf{LX} = 0$. Hence we obtain for the dispersion relation

$$\sigma^4 + \sigma^2(\kappa^2 + 2v_A^2 k^2) + v_A^2 k^2(v_A^2 k^2 - 2q\Omega_0^2) = 0. \tag{2.43}$$

We can check that the relation satisfies the behaviour we expect in different limits by noting that when $v_A = 0$, we recover pure epicyclic oscillations with $\sigma^2 = -\kappa^2$, while when $\Omega_0 = 0$,

we recover pure Alfvén waves with $\sigma^2 = -v_A^2 k^2$. A linear instability is present when $\sigma^2 > 0$, which is satisfied when

$$v_A^2 k^2 - 2q\Omega_0^2 < 0, \tag{2.44}$$

and can be recast as a criterion for the wavelength as

$$\frac{\lambda}{2\pi} > \frac{B_0}{\sqrt{2q\Omega_0^2 \mu_0 \rho}}. \tag{2.45}$$

This criterion shows us that the MRI is active when the magnetic tension is not too strong, as the minimum wavelength must fit in with the size of the box. The MRI is therefore a weak field instability, and can be stabilised by the presence of a strong magnetic flux.

Solving the dispersion relation (2.43) fully gives us further insights on the MRI in the ideal MHD limit. Figure 2.2, taken from Lesur (2020), plots the solutions for the Keplerian case $q = 3/2$. The maximum growth rate occurs at $\sigma_{\max} = q\Omega/2$ when $v_A k = \sqrt{\Omega_0^2 - \kappa^2/16}$, which for a Keplerian disc translates to $\sigma_{\max} = 0.75\Omega_0$. The value of the maximum growth rate is actually a more general result, and is the absolute limit for the growth rate of the MRI that is true even when non-ideal MHD effects are included (Desch, 2004). The stable branch connected to the unstable branch at the instability condition is that of an Alfvén wave, and shows that the MRI is an Alfvénic perturbation by nature. The two stable branches that are unconnected to the instability are epicyclic modes that are stable for all magnetisations, and take the classic frequency of κ when $v_A = 0$.

2.2.2 Effect of stratification

In practice, real discs are vertically stratified, with decreasing density as height increases. The effective wavenumbers become quantised, and the smallest possible wavenumber is set by the scaleheight H of the disc such that $kH = 1.1584$ for the lowest order mode (Latter et al., 2010). They are also found to satisfy the same dispersion relation as the non stratified case when v_A is set to be the value $v_A(z = 0)$ at the mid-plane. For an isothermal disc with B_z only, the maximum $v_A k$ condition leads to the further result that there is a mid-plane β value below which the disc would be stabilised, given by

$$\beta_0 < \frac{2(k_{\min} H)^2}{3} \simeq 0.89. \tag{2.46}$$

This again shows that the MRI is a weak field instability, which can be quenched by a strong magnetic field. This result will affect the way we formulate our investigation of the disc's vertical structure and magnetic flux transport rate in Part II of the Thesis.

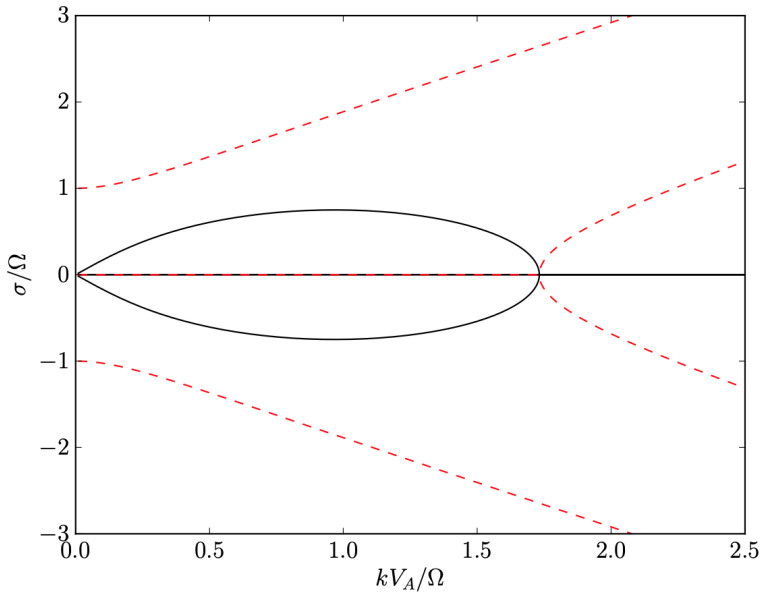

Fig. 2.2 Solutions for the dispersion relation (2.43) for the case $q = 3/2$. Black branches represent unstable modes, while red dashed lines are for stable modes. Figure from Lesur (2020).

2.2.3 Channel modes

The most unstable and fastest growing modes of the MRI are those that vary only with height, such that $\mathbf{k} = (0, 0, k_z)$. These are known as "channel modes" due to their lack of horizontal variation, and have the additional characteristic of being exact non-linear solutions of the full MHD equations in the incompressible limit (Goodman and Xu, 1994; Latter et al., 2009), which makes them both very robust and also significant as the disc saturates in the nonlinear regime. For stratified compressible discs, a link has also been found between large-scale MRI channel modes and the launching of magnetic winds from the disc surface (Lesur et al., 2013; Ogilvie, 2012; Riols et al., 2016), an effect which will be reviewed in more detailed in Chapter 9. In ideal MHD, channel modes take an "hourglass" ($B_x = -B_x$, $B_y = -B_y$, $u_x = u_x$, $u_y = u_y$) or "slanted" ($B_x = B_x$, $B_y = B_y$, $u_x = -u_x$, $u_y = -u_y$) symmetry in the vertical direction about the disc mid-plane. These symmetry properties will have particular significance as we examine the effect of the MRI on the magnetic wind profiles in Part III of the Thesis.

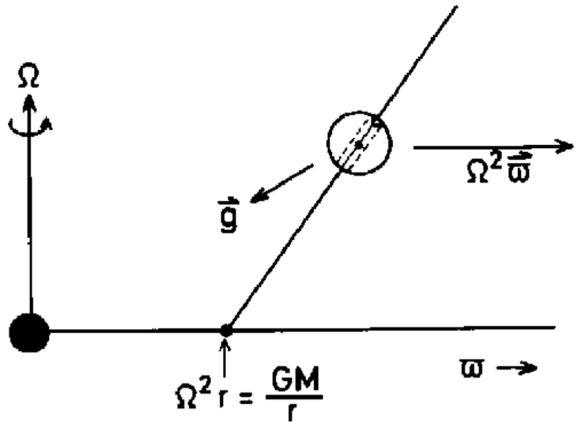

Fig. 2.3 Bead-on-a-wire analogy for centrifugal acceleration by a magnetic field. Figure from Spruit (1996).

2.3 Magnetically driven winds

In their seminal paper, Blandford and Payne (1982) applied the idea of the acceleration of gas tied to a rotating magnetic field (first noted by Henriksen and Rayburn (1971)) to the accretion disc context, proposing a mechanism for a disc driven magnetic wind. As with the MRI, we first give a qualitative description of the mechanism. Consider a large scale poloidal field anchored in the disc. Above the disc surface, gas density rapidly decreases so that the magnetic energy density becomes dominant over the thermal and rotational energies. As a result, the field in this region is approximately force-free, and rotates at the same angular velocity as the part of the disc to which it is attached (Ferraro (1937)'s law of isorotation). For a sufficiently ionised disc in the ideal MHD regime, the gas is tied to magnetic field lines (flux freezing). Hence as the field lines co-rotate with the disc, gas at the surface is flung out like beads on a wire when the component of the centrifugal force along the field line exceeds the gravitational force holding it down (see Figure 2.3). This centrifugal acceleration continues until the flow speed becomes comparable to the Alfvén speed. Beyond that point, the magnetic field is no longer strong enough to enforce co-rotation, and the field gets wound up. The outflow is then collimated into a jet parallel to the rotation axis by curvature forces due to the azimuthal magnetic field.

Quantitatively, we consider the dynamics of a steady axisymmetric magnetic wind. In ideal MHD, the induction equation gives us

$$\nabla \times (\mathbf{u} \times \mathbf{B}) = 0, \tag{2.47}$$

hence we can rewrite the electric field in terms of an electrostatic potential Φ_e where

$$\nabla\Phi_e = -\mathbf{E} = \mathbf{u}\times\mathbf{B}. \tag{2.48}$$

We now separate the velocity and magnetic field components into poloidal and toroidal parts denoted by the subscripts 'p' and 'ϕ' respectively:

$$\mathbf{u} = \mathbf{u}_p + u_\phi \mathbf{e}_\phi. \tag{2.49}$$

$$\mathbf{B} = \mathbf{B}_p + B_\phi \mathbf{e}_\phi. \tag{2.50}$$

We can then rewrite the right-hand side of Equation (2.48) as

$$\mathbf{u}\times\mathbf{B} = \left[\mathbf{e}_\phi \times (u_\phi \mathbf{B}_p - B_\phi \mathbf{u}_p)\right] + \left[\mathbf{u}_p \times \mathbf{B}_p\right], \tag{2.51}$$

where the first term of the right-hand side is the poloidal component and the second term is toroidal. Since Φ_e is axisymmetric, we expect $\partial\Phi_e/\partial\phi = 0$, and the poloidal component of Equation (2.51) must be zero. Hence the poloidal velocity field and magnetic field must also be parallel to each other, and can be written in the form

$$\rho\mathbf{u}_p = k\mathbf{B}_p, \tag{2.52}$$

where k is known in literature as the mass loading, and is the ratio of the mass flux to magnetic flux. This is simply a consequence of the flux freezing in the ideal MHD conditions, as well as the assumption that there is no flux transport - a common assumption but one that might be questioned.

We now recall the flux function, ψ, introduced back in Equation (2.27) of Section 2.1.3 for the poloidal component of magnetic fields. We also recall that by construction, $\mathbf{B}_p \cdot \nabla\psi = 0$, allowing us to use ψ to define magnetic surfaces of revolution. Similarly, it can be shown from the steady mass conservation equation that the mass loading, k, also obeys the same relation:

$$0 = \nabla\cdot(\rho\mathbf{u}) = \nabla\cdot(\rho\mathbf{u}_p) = \nabla\cdot(k\mathbf{B}_p) = \mathbf{B}_p\cdot\nabla k = 0, \tag{2.53}$$

hence we can rewrite k as a function of ψ, such that $k = k(\psi)$. This then allows us to write the steady induction equation in terms of k and ψ (replacing $\mathbf{u}_p$ and $\mathbf{B}_p$):

$$\begin{aligned}\nabla\times(\mathbf{u}\times\mathbf{B}) &= \nabla\times\left[\mathbf{e}_\phi\times(u_\phi\mathbf{B}_p - B_\phi\mathbf{u}_p)\right]\\ &= \nabla\times\left[\left(\frac{u_\phi}{r} - \frac{kB_\phi}{r\rho}\right)\nabla\psi\right]\\ &= \nabla\left(\frac{u_\phi}{r} - \frac{kB_\phi}{r\rho}\right)\times\nabla\psi,\end{aligned} \tag{2.54}$$

giving us another function that is constant on magnetic surfaces of revolution:

$$\omega(\psi) = \frac{u_\phi}{r} - \frac{kB_\phi}{r\rho}. \tag{2.55}$$

This has units of time^{-1}, and can be interpreted as the angular velocity of the magnetic surface. Combining the definitions of Equations (2.52) and (2.55) then allows us to rewrite the full velocity as

$$\mathbf{u} = \frac{k\mathbf{B}}{\rho} + r\omega\mathbf{e}_\phi, \tag{2.56}$$

showing us that the velocity field is parallel to the magnetic field in a frame corotating with the magnetic field at ω.

2.3.1 Angular momentum removal

We now consider the mechanism by which angular momentum is removed by the magnetic wind. It can be shown by substituting Equation (2.56) into the azimuthal component of the equation of motion that another invariant along magnetic surfaces is present known as the angular momentum invariant (see section 9.5 of Ogilvie (2016) for derivation):

$$l = l(\psi) = ru_\phi - \frac{rB_\phi}{\mu_0 k}. \tag{2.57}$$

l is the angular momentum removed in the outflow per unit mass, with the first term on the right-hand side being the angular momentum intrinsic to the outflowing mass, while the second term represents angular momentum removed by the torque exerted by the magnetic field on the disc.

The efficiency of angular momentum removal from the disc is given by the magnetic lever arm, defined as

$$\frac{r_A^2}{r_0^2}, \tag{2.58}$$

where r_0 and r_A are the radii of the footpoint and the Alfvén point (where $u_p = u_{Ap}$ the poloidal Alfvén velocity) of the wind. This arises by recognising that u_ϕ can be rewritten using Equations (2.56) and (2.57) (see section 9.6 of Ogilvie (2016)) as

$$u_\phi = \frac{r^2\omega - A^2 l}{r(1-A^2)} = \left(\frac{1}{1-A^2}\right) r\omega + \left(\frac{A^2}{A^2-1}\right)\frac{l}{r}, \tag{2.59}$$

where

$$A = \frac{u_p}{v_{Ap}} = \frac{u_p\sqrt{\mu_0\rho}}{B_p} = k\sqrt{\frac{\mu_0}{\rho}} \tag{2.60}$$

is the ratio of the poloidal velocity to the poloidal Alfvén velocity, and is known as the poloidal Alfvén number. The footpoint azimuthal velocity can then be shown to be $\approx r_0\omega$, while at the Alfvén point, in order for u_ϕ to be continuous, the numerator of Equation (2.59) must also be zero, giving us $l = r_A^2\omega$ there. As the outflow is accelerated far beyond the Alfvén point ($A \ll 1$), $u_\phi \approx 1/r \to 0$, hence for a mass outflow rate $\dot{M}$, angular momentum is lost at a rate $\dot{M}l = \dot{M}r_A^2\Omega_0$ in a magnetised disc wind, compared with $\dot{M}r_0^2\Omega_0$ in a purely hydrodynamic outflow.

The magnetic lever arm increases if r_A is significantly larger than r_0, indicating more efficient angular momentum loss. It is also a measure of the mass accreted compared with the mass lost in the outflow, since the accretion of a unit of mass $\Delta M_{\rm acc}$ requires its angular momentum $r_0^2\Omega_0\Delta M_{\rm acc}$ to be removed, while the angular momentum in the outflow removed by mass $\Delta M_{\rm jet}$ from r_0 is $r_A^2\Omega_0\Delta M_{\rm jet}$, giving us $\Delta M_{\rm acc}/\Delta M_{\rm jet} = r_A^2/r_0^2$.

2.3.2 The Bernoulli equation and the nature of the magnetic wind

The nature of the wind can be examined by looking at the Bernoulli invariant, which measures the energy content of the flow, and is obtained by the scalar product of the equation of motion with $\mathbf{u}$. The three components of the equation of motion in cylindrical coordinates are

$$\rho\mathbf{u}_p\cdot\nabla u_r = \frac{\rho u_\phi}{r} - \frac{\partial p}{\partial r} - \rho\frac{\partial\psi_G}{\partial r} + J_\phi B_z - J_z B_\phi, \tag{2.61}$$

$$\frac{1}{r}\rho\mathbf{u}_p\cdot\nabla(ru_\phi) = \frac{1}{r\mu_0}\nabla\cdot(r\mathbf{B}_p B_\phi), \tag{2.62}$$

$$\rho\mathbf{u}_p\cdot\nabla u_z = -\frac{\partial p}{\partial z} - \rho\frac{\partial\psi_G}{\partial z} - \frac{\partial}{\partial z}\left(\frac{B_r^2+B_\phi^2}{2\mu_0}\right) + \frac{B_r}{\mu_0}\frac{\partial B_z}{\partial r}, \tag{2.63}$$

where $\psi_G = -GM/\sqrt{r^2+z^2}$ is the gravitational potential due to the central star. Dotting the equation of motion with $\mathbf{u}$ therefore yields

$$\mathbf{u}_p\cdot\nabla\left(\frac{u^2}{2}+\psi_G\right) = -\mathbf{u}_p\cdot\frac{\nabla p}{\rho} + \mathbf{u}\cdot\frac{\mathbf{J}\times\mathbf{B}}{\rho}. \tag{2.64}$$

We follow Lesur (2020) in recasting the work done due to the Lorentz force in terms of variables that are invariant on magnetic surfaces using Equations (2.56) and (2.52):

$$\begin{aligned}\mathbf{u}\cdot\frac{\mathbf{J}\times\mathbf{B}}{\rho} &= r\omega\frac{\mathbf{J}_p\times\mathbf{B}_p}{\rho}\\ &= \omega\frac{\mathbf{B}_p\cdot\nabla(rB_\phi)}{\rho}\\ &= \mathbf{u}_p\cdot\nabla\left(\frac{r\omega B_\phi}{k}\right).\end{aligned} \tag{2.65}$$

The work due to pressure is also re-expressed in terms of the enthalpy per unit mass H and a heating term, $\dot{Q}$, which in the disc context would be mainly due to radiative processes:

$$\mathbf{u}_p \cdot \frac{\nabla p}{\rho} = \mathbf{u}_p \cdot \nabla H - \dot{Q}. \tag{2.66}$$

Since the velocity field is parallel to the magnetic field in a frame corotating with it at ω, streamlines coincide with surfaces of constant ψ, and we can integrate along a streamline a to yield the Bernoulli energy budget on poloidal field lines and streamlines (equation 11.16 in (Lesur, 2020)):

$$\mathscr{B} \equiv \frac{u^2}{2} + \psi_G + H - \int_{s(a)} \dot{Q} \mathrm{d}s - \frac{r\omega(a)B_\phi}{k(a)}, \tag{2.67}$$

where s represents the distance along the streamline , and a labels the chosen streamline. It is worth noting that $\mathscr{B}$, though a constant, is no longer the classical Bernoulli function, as it takes into account the heating. For the wind to accelerate matter to $z \to \infty$, we require $\mathscr{B} > 0$. This can be achieved in three ways: (1) a thermally driven wind due to a hot disc, which corresponds to a high initial H in the disc, (2) photoevaporative heating from stellar and cosmic radiation as the gas accelerates along the streamline, which corresponds to the integral term with $\dot{Q}$, and (3) a wind driven by interactions between the magnetic field and the disc rotation, which corresponds to the final term in the equation. Winds that are mainly driven by the first two processes are known as "thermal winds", while winds driven solely by magnetic effects are known as "cold MHD winds".

Recent works have shown that winds from protoplanetary discs are most likely driven by a combination of both thermal and magnetic effects (Bai, 2017; Bai et al., 2016; Béthune et al., 2017). These are known as "magneto-thermal" winds, where strong external heating on the coronal regions can aid in the acceleration of the disc wind which is launched by magnetic effects at the wind base. Compared to pure cold MHD wind solutions, magneto-thermal winds are warmer, denser and slower, and can have high wind mass loss to mass accretion ratios, while having moderate values of the magnetic lever arm (Lesur, 2020).

Magnetically driven winds can in turn be characterised into two regimes:

1. Magnetocentrifugal winds, where strong poloidal fields enforce approximate corotation of the fluid with the wind base, and the picture of beads centrifugally accelerated on rigid rotating wires is the appropriate way to describe their mechanics.

2. Magnetic pressure gradient driven winds, where corotation is not a good approximation in the observer's frame due to weak poloidal fields, and the acceleration is more appropriately interpreted as due to the magnetic pressure gradient of the toroidal field that results from the winding up of the poloidal field.

Mathematically, both the centrifugal and magnetic viewpoints of acceleration are equally valid, and as explained in Spruit (1996), depends on the frame of reference in which we are working. On the one hand, in the frame corotating with the wind base, magnetic forces 'disappear' and the flow seems to be purely centrifugal, although it is actually the magnetic forces that mediate the rotational energy to the flow. On the other hand, in the inertial frame, the acceleration can be seen to be magnetic, where the poloidal Lorentz force is given by

$$\begin{aligned}\mathbf{F}_p &= \frac{1}{\mu_0}(\nabla \times \mathbf{B})_p \times \mathbf{B}_\phi \\ &= -\nabla \frac{B_\phi^2}{2\mu_0} - \frac{B_\phi^2}{\mu_0}\mathbf{e}_r,\end{aligned} \tag{2.68}$$

and the pressure gradient and tension force from the toroidal field are seen as the main drivers of the outflow. Net outward acceleration requires B_ϕ^2 to decrease sufficiently rapidly along the field line to overcome the axis-directed tension force, and it is more physically intuitive to describe the wind as being driven by a magnetic pressure gradient. Recent works have placed protoplanetary disc winds to lie in the magnetic pressure gradient driven regime, with a smaller Alfvén radius ($r_A/r_0 \sim 1$) and more heavy mass loading than winds in the centrifugally driven wind regime (Lesur, 2020). This is due to the weakly magnetised (mid-plane $\beta \ll 1$) nature of protoplanetary disc outflows, which is required by observational constraints that discs are generally massive with an average accretion velocity much smaller than the sound speed (Lesur, 2020). Stronger field models launching magnetocentrifugal winds would have led to much larger accretion velocities that are sonic with the same disc surface density estimates, making them incompatible with observations.

2.3.3 Minimum poloidal magnetic field inclination for wind-launch

For the launching of a cold outflow from a thin accretion disc, a famous result of Blandford and Payne (1982) is that a minimum inclination of 30° of the poloidal magnetic field to the vertical is required. This can be seen by examining the contours of the effective potential $\Phi_{\rm cg}$ along a streamline, where both gravitational and centrifugal terms are included:

$$\Phi_{\rm cg}(s) = -\frac{GM}{\sqrt{r^2+z^2}} - \frac{1}{2}\Omega^2 r^2. \tag{2.69}$$

Here, Ω is the rotation of the gas, which would normally be nearly Keplerian if the footpoint of the wind is in the disc and corotation is enforced by the magnetic field. Rewriting $\Omega \approx \Omega_0 = \sqrt{GM/r_0^3}$, where the subscript 0 denotes the footpoint of the wind, we can then find the contours of equipotential passing through the footpoint through equating

$$\Phi_{\rm cg}(s_0) = -\frac{GM}{r_0} - \frac{1}{2}\Omega_0^2 r_0^2 \tag{2.70}$$

with

$$\Phi_{\rm cg}(s) = -\frac{GM}{\sqrt{r^2+z^2}} - \frac{1}{2}\Omega_0^2 r^2. \tag{2.71}$$

We follow Ogilvie (2016) by renomalising the equation using units such that $r_0 = 1$. After some algebra, this gives us the result (Ogilvie, 2016)

$$z = \sqrt{\frac{(2-r)(r-1)^2(r+1)^2(r+2)}{(3-r^2)^2}}. \tag{2.72}$$

A plot showing the contour lines of $\Phi_{\rm cg}$ is shown in Figure 2.4, taken from Ogilvie (2016). In order for a wind to be launched by centrifugal acceleration alone without thermal assistance, its streamline must always be crossing contours of lower $\Phi_{\rm cg}$, which require a minimum launch angle from the vertical whether the wind is directed towards or away from the star. This angle can be found by taking the limit $r \to 1$, $z \to 0$ in Equation 2.72, which gives us

$$z \approx \pm\sqrt{3}(r-1), \tag{2.73}$$

translating to a minimum launch angle of 30°. This result would bear relevance to our work later when we consider 1D isothermal disc models, and in whether we need to model the launching of a wind for the range of poloidal magnetic field inclinations explored.

2.3.4 Critical points in the outflow

We end our current discussion of the magnetic wind with a consideration of the critical points that the outflow must pass through, and which together with a given value of ρ_0 at the mid-plane, would constrain the wind solution. These critical points are derived by rewriting the Bernoulli equation as $\mathscr{B}(s,\rho;k,r_A)$, where the solution curve $\rho(s)$ is a contour line of the Bernoulli function in the $s-\rho$ plane. In this scenario, we assume that there is no explicit heating, and that we have an isothermal equation of state where $p = c_s^2\rho$. Critical points are stationary points of the saddle type, and must satisfy

$$\frac{\partial\mathscr{B}}{\partial s} = 0, \qquad \frac{\partial\mathscr{B}}{\partial\rho} = 0. \tag{2.74}$$

It can then be shown that (Spruit, 1996)

$$\rho\frac{\partial\mathscr{B}}{\partial\rho} = -\frac{(u_p^2-u_{sp}^2)(u_p^2-u_{fp}^2)}{u_p^2-u_{Ap}^2}, \tag{2.75}$$

where u_{sp} and u_{fp} are the slow and fast poloidal magnetosonic speeds given by

$$u_{s,f;p} = \sqrt{\frac{c_s^2+u_A^2 \pm \sqrt{(c_s^2+u_A^2)^2 - 4c_s^2u_{Ap}^2}}{2}}, \tag{2.76}$$

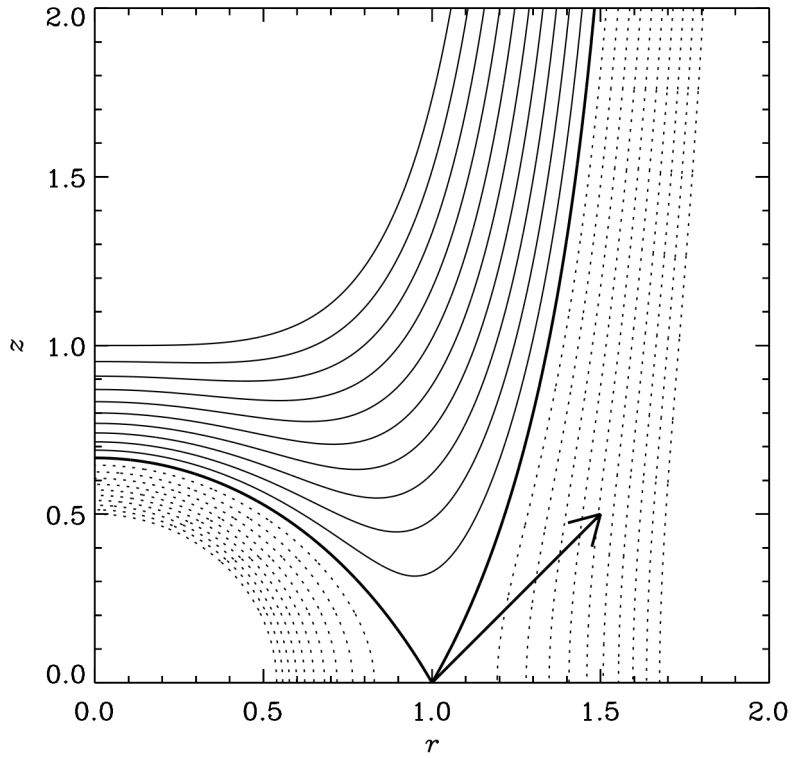

Fig. 2.4 Plot showing the contour lines of $\Phi_{\rm cg}$, as defined by Equation (2.69), in units where $r_0 = 1$. Downhill directions are denoted by dotted contours, while uphill directions are denoted by solid contours. The bold arrow from the footpoint shows a possible wind trajectory which crosses contour lines of lower potential in its path. For a centrifugal wind to be launched without thermal assistance from a thin disc, its inclination at its footpoint must be at least 30° to the vertical. Figure from Ogilvie (2016).

with

$$u_A = \frac{B}{\sqrt{\mu_0 \rho}}, \qquad u_{Ap} = \frac{B_p}{\sqrt{\mu_0 \rho}} \tag{2.77}$$

being the Alfvén speeds based on the total and poloidal field strengths respectively. The critical points can be interpreted as the points at which the flow matches the speed of a magnetosonic wave propagating opposite to the flow, and are known as the slow and the fast point where $u_p = u_{sp}$ and $u_p = u_{fp}$ respectively. There is an additional critical point at the Alfvén point, where $u_p = u_{Ap}$. This comes not from Equation (2.75), where the Alfvén point is simply a node in the family of solutions, but rather from considering the Grad-Shafranov cross-field balance equation of motion for stationary axisymmetric flow. As the Grad-Shafranov equation is beyond the scope of this discussion, we refer the reader to the detailed arguments presented in Sakurai (1985) for understanding the nature of the Alfvén critical point.

For a wind solution to be fully constrained, it must pass through all three critical points, otherwise boundary effects can significantly alter the solution. Most radially local shearing box wind solutions to date (see Chapter 3 for a description of the shearing box formalism), including our own in this Thesis, pass through only the slow point and Alfvén point but are not super-fast. It is therefore important to test their robustness by varying the boundary conditions (Bai, 2015; Lesur et al., 2014).

2.4 Non-ideal MHD

2.4.1 Origin and key features

As mentioned in Section 1.3.1 of Chapter 1, protoplanetary discs are usually 'cold' discs that are poorly ionised. In this regime, the ideal MHD approximation is insufficient to describe the magnetic processes involved, and non-ideal MHD effects become important. We derive here the generalised Ohm's law and discuss the nature and key properties of each of the non-ideal effects (Ohmic resistivity, Hall drift and ambipolar diffusion), before discussing their regions of influence in protoplanetary discs, and their effect on both the MRI and magnetic winds in later subsections.

There are two approaches to modelling non-ideal effects: through a conductivity tensor taking into account the different ionised species present (Norman and Heyvaerts, 1985; Wardle and Ng, 1999), or through the dynamical multifluid model (Balbus and Terquem, 2001). The two can be shown to be mathematically equivalent and are closely related (Königl et al., 2010).

The former approach was used in the vertical structure models of Königl et al. (2010); Salmeron et al. (2011); Teitler (2011) because of its terseness and mathematical economy. The non-ideal effects are incorporated through a modified Ohm's law:

$$\mathbf{J} = \sigma \cdot \mathbf{E}' = \sigma_O \mathbf{E}'_{\parallel} + \sigma_H \mathbf{b} \times \mathbf{E}'_{\perp} + \sigma_P \mathbf{E}'_{\perp}, \tag{2.78}$$

where $\mathbf{b} = \mathbf{B}/|\mathbf{B}|$, $\mathbf{E}'$ is the electric field in the frame comoving with the neutrals, $\mathbf{J}$ is the current density, $\parallel$ and $\perp$ indicate the components of the electric field parallel and perpendicular to $\mathbf{b}$ respectively, and the tensor

$$(\sigma)_{ij} = \begin{pmatrix} \sigma_P & \sigma_H & 0 \\ -\sigma_H & \sigma_P & 0 \\ 0 & 0 & \sigma_{\parallel} \end{pmatrix}, \tag{2.79}$$

where σ_P and σ_H are the Pedersen and Hall conductivities respectively, describes the conductivity of the multi-component fluid. These conductivities are directly related to the chemistry of the disc and evolve accordingly (Wardle, 1999).

The latter multifluid approach is used in studies that are more concerned with understanding the different dynamical behaviour of the three non-ideal mechanisms (Balbus and Terquem, 2001; Wardle and Koenigl, 1993). This approach explicitly draws out the physics of the coupling between the magnetic field and the disc. Numerical simulations in particular often use this approach, having first computed the diffusivities from the full conductivity tensor, as it bears more correlation with disc phenomenology (Bai and Stone, 2014).

Derivation using the multifluid approach

As dynamical behaviour, rather than complex chemistry, is also what our study is primarily concerned with, we follow Balbus (2011) in our derivation of the non-ideal terms in its multi-fluid model. We assume the fluid to be composed of neutrals, ions and electrons, and that it is locally overall neutral. We ignore the effect of dust grains for now, and defer their discussion to later. We denote ions and electron flow quantities by the subscripts 'i' and 'e' respectively, while we leave the neutral quantities which are dominant in the fluid without any subscripts, or where it is necessary to distinguish them, with the subscript 'n'. We assume that each species is separately conserved, and that collisions are elastic in nature.

The equations of motion for the three species are then given by

$$\rho \frac{\partial \mathbf{u}}{\partial t} + \rho(\mathbf{u} \cdot \nabla)\mathbf{u} = -\nabla P - \rho \nabla \Phi - \mathbf{p}_{ni} - \mathbf{p}_{ne}, \tag{2.80}$$

$$\rho_i \frac{\partial \mathbf{u}_i}{\partial t} + \rho_i(\mathbf{u}_i \cdot \nabla)\mathbf{u}_i = -\nabla P_i - \rho_i \nabla \Phi + Zen_i\,(\mathbf{E} + \mathbf{u}_i \times \mathbf{B}) - \mathbf{p}_{in}, \tag{2.81}$$

$$\rho_e \frac{\partial \mathbf{u}_e}{\partial t} + \rho_e (\mathbf{u}_e \cdot \nabla)\mathbf{u}_e = -\nabla P_e - \rho_e \nabla \Phi - e n_e (\mathbf{E} + \mathbf{u}_e \times \mathbf{B}) - \mathbf{p}_{en}, \tag{2.82}$$

where $\mathbf{p}_{ab}$ denotes the rate of momentum transfer per unit volume from species a to species b, Z is the ionisation number per ion, and e is the charge of a proton. By Newton's Third Law, it is worth noting that $\mathbf{p}_{ab} = -\mathbf{p}_{ba}$. Only the ion and electron equations have the Lorentz force term (second last terms on the right-hand side of Equations (2.81) and (2.82)) in addition to the momentum transfer terms (the $\mathbf{p}$ terms), as only these species are charged and under the influence of electric and magnetic fields. We ignore $\mathbf{p}_{ie}$ and $\mathbf{p}_{ei}$ in Equations (2.81) and (2.82) because they are proportional to $n_i n_e$, where n denotes the number density of a species, which is minuscule in comparison to the other terms present.

We first derive expressions for the momentum exchange terms from properties of the species. From conservation of energy and momentum, it can be shown that $\mathbf{p}_{ni}$ is given by

$$\mathbf{p}_{ni} = n\mu_{ni}(\mathbf{u} - \mathbf{u}_i)\nu_{ni} \tag{2.83}$$

where n is the neutral number density, $\mu_{ni} \equiv m_i m_n/(m_i + m_n)$ is the reduced mass of the ion and neutral particles, with m denoting the mass of each particle, and ν_{ni} is the collision frequency between a neutral particle with the ion population (Morse, 1963; Reed, 2018). The collision frequency is then derived from the kinetic theory of gases (see e.g. Blundell and Blundell (2009)), and takes the form

$$\nu_{ni} = n_i \langle \sigma_{ni} w_{ni} \rangle, \tag{2.84}$$

where n_i is the ion number density, σ_{ni} is the effective cross section for neutral-ion collisions, w_{ni} is the relative velocity between neutrals and ions, and the angle brackets denote averaging over a Maxwell-Boltzmann distribution for the relative velocity. This then gives us

$$\mathbf{p}_{ni} = n n_i \mu_{ni} \langle \sigma_{ni} w_{ni} \rangle (\mathbf{u} - \mathbf{u}_i), \tag{2.85}$$

allowing us to determine the momentum transfer from the fluid properties of the species involved. Using similar considerations, the neutral-electron momentum transfer is given by

$$\mathbf{p}_{ne} = n n_e \mu_{ne} \langle \sigma_{ne} w_{ne} \rangle (\mathbf{u} - \mathbf{u}_e) \simeq n n_e m_e \langle \sigma_{ne} w_{ne} \rangle (\mathbf{u} - \mathbf{u}_e), \tag{2.86}$$

where the $\simeq$ comes about because $m \gg m_e$, hence $\mu_{ne} \simeq m_e$. As noted before, $\mathbf{p}_{in}$ and $\mathbf{p}_{en}$ are simply given by $-\mathbf{p}_{ni}$ and $-\mathbf{p}_{ne}$ respectively.

We next note that for a weakly ionised gas, as is the case in protoplanetary discs, Equations (2.81) and (2.82) would be dominated by the Lorentz force terms and the momentum transfer terms. This can be seen by considering the typical dynamical timescale involved with the Lorentz force terms, given by the ion and the electron gyroperiods respectively, which are

much smaller than the macroscopic flow crossing time associated with the inertial force terms for the ions and electrons when the ionisation is low (Balbus, 2011). This allows us to approximate to a high level of accuracy that

$$Zen_i\,(\mathbf{E}+\mathbf{u}_i\times\mathbf{B})-\mathbf{p}_{In}=0, \tag{2.87}$$

$$-en_e\,(\mathbf{E}+\mathbf{u}_e\times\mathbf{B})-\mathbf{p}_{en}=0. \tag{2.88}$$

We note that because of our charge neutrality assumption, $Zen_i = en_e$. Summing the two expressions and rearranging, we obtain

$$en_e(\mathbf{u}_i-\mathbf{u}_e)\times\mathbf{B} \;=\mathbf{p}_{in}+\mathbf{p}_{en}, \tag{2.89}$$

$$\mathbf{J}\times\mathbf{B} \;=\mathbf{p}_{in}+\mathbf{p}_{en}, \tag{2.90}$$

where in going from line (2.89) to (2.90), we noted that $en_e(\mathbf{u}_i-\mathbf{u}_e)$ simply gives us the current density $\mathbf{J}$ of the overall fluid. We can then use Newton's Third Law to substitute this expression back into the neutrals' momentum equation, yielding the same momentum equation as we had in ideal MHD:

$$\rho\frac{\partial\mathbf{u}}{\partial t}+\rho(\mathbf{u}\cdot\nabla)\mathbf{u}=-\nabla P-\rho\nabla\Phi+\mathbf{J}\times\mathbf{B}. \tag{2.91}$$

This shows us that while the fluid may be weakly ionised, the neutral component still behaves under the Lorentz force as though it was fully ionised due to momentum transfer with ions and electrons. Indeed, it is in the induction equation that non-ideal MHD makes a difference, which we shall derive now.

We first note that the Lorentz force acting on the neutrals through collisional coupling can be rewritten as

$$\mathbf{J}\times\mathbf{B}=n_i n\mu_{in}\langle\sigma_{ni}w_{ni}\rangle(\mathbf{u}_i-\mathbf{u})+n_e n m_e\langle\sigma_{ne}w_{ne}\rangle[(\mathbf{u}_e-\mathbf{u}_i)+(\mathbf{u}_i-\mathbf{u})]. \tag{2.92}$$

We then consider the ratio of the electron-neutral to ion-neutral collision cross section, which can be assumed to be

$$\frac{\langle\sigma_{ni}w_{ni}\rangle}{\langle\sigma_{ne}w_{ne}\rangle}=\left(\frac{m_e}{\varepsilon\mu_{in}}\right)^{1/2}, \tag{2.93}$$

where the approximately geometrical nature of σ_{ni} and σ_{ne} leads to the $\mu_{ne}^{-1/2}\simeq m_e^{-1/2}$ and $\mu_{ni}^{-1/2}$ dependencies, while $\varepsilon<1$ reflects the larger ion-neutral cross section that results from long range induced dipole interactions for ions, and which are much less present for the electrons. Equation (2.92) can then be rearranged as

$$(\mathbf{u}_I-\mathbf{u})\left[1+\frac{1}{Z}\left(\frac{\varepsilon m_e}{\mu_{in}}\right)^{1/2}\right]=\frac{\mathbf{J}\times\mathbf{B}}{\gamma\rho\rho_i}+\sqrt{\frac{\varepsilon m_e}{\mu_{ni}}}Z(\mathbf{u}_i-\mathbf{u}_e), \tag{2.94}$$

where

$$\gamma \equiv \frac{\langle \sigma_{ni} w_{ni} \rangle}{m_i + m_n} \tag{2.95}$$

is known as the drag coefficient, and comes from a common way to rewrite the ion-neutral momentum transfer in astrophysical literature as

$$\mathbf{p}_{In} = \rho \rho_i \gamma (\mathbf{u}_i - \mathbf{u}). \tag{2.96}$$

The second term in the square brackets in Equation (2.94) is much smaller than 1 due to the $(\varepsilon m_e/\mu_{in})^{1/2}$ dependence, and hence can be neglected, while the second term on the right-hand side of the same equation can also be neglected for the same reason, provided $(\mathbf{u}_i - \mathbf{u}_e)$ is comparable to $(\mathbf{u}_i - \mathbf{u})$.

Let us consider again Equation (2.88), with the expression for $\mathbf{p}_{en}$ from Equation (2.86) substituted in. We can rewrite the equation as:

$$\mathbf{E} + [\mathbf{u} + (\mathbf{u}_e - \mathbf{u}_i) + (\mathbf{u}_i - \mathbf{u})] \times \mathbf{B} + \frac{n m_e \langle \sigma_{ne} w_{ne} \rangle}{e} [(\mathbf{u}_e - \mathbf{u}_i) + (\mathbf{u}_i - \mathbf{u})] = 0. \tag{2.97}$$

Substituting Equation (2.94) into Equation (2.97), and neglecting the terms that are insignficant as per the discussion above, we have

$$\mathbf{E} + \mathbf{u} \times \mathbf{B} - \frac{\mathbf{J} \times \mathbf{B}}{e n_e} \left[1 - \frac{m_e \nu_{en} n_e}{\gamma \rho \rho_i} \right] + \frac{(\mathbf{J} \times \mathbf{B}) \times \mathbf{B}}{\gamma \rho \rho_i} - \frac{\mathbf{J}}{\sigma_{\text{cond}}} = 0, \tag{2.98}$$

where

$$\sigma_{\text{cond}} \equiv \frac{e^2 n_e}{m_e \nu_{en}} \tag{2.99}$$

is the electrical conductivity. Again, the second term in the square brackets in Equation (2.98) can be neglected, as it is equal to $(1/Z)(\varepsilon m_e/\mu_{in})^{1/2} \ll 1$. This leaves us with a modified Ohm's law for a non-ideal fluid

$$\mathbf{E} + \mathbf{u} \times \mathbf{B} - \frac{\mathbf{J}}{\sigma_{\text{cond}}} - \frac{\mathbf{J} \times \mathbf{B}}{e n_e} + \frac{(\mathbf{J} \times \mathbf{B}) \times \mathbf{B}}{\gamma \rho \rho_i} = 0, \tag{2.100}$$

which is the inverse of Equation (2.78). This can then be incorporated into the induction equation via the normal procedure using Maxwell's equations and the relation $\mathbf{J} = \nabla \times \mathbf{B}/\mu_0$ (see Section 2.1.1) to give us

$$\frac{\partial \mathbf{B}}{\partial t} = \nabla \times [\mathbf{u} \times \mathbf{B} - \eta_O \nabla \times \mathbf{B} - \eta_H (\nabla \times \mathbf{B}) \times \mathbf{b} + \eta_A ([\nabla \times \mathbf{B}] \times \mathbf{b}) \times \mathbf{b}], \tag{2.101}$$

where $\mathbf{b} = \mathbf{B}/|\mathbf{B}|$, and we have substituted the coefficients for the non-ideal diffusivities given by

$$\eta_O = \frac{1}{\mu_0} \frac{m_e n}{e^2 n_e} \nu_{en}, \tag{2.102}$$

$$\eta_H = \frac{1}{\mu_0}\frac{|\mathbf{B}|}{en_e}, \tag{2.103}$$

$$\eta_A = \frac{1}{\mu_0}\frac{|\mathbf{B}|^2}{\gamma\rho\rho_i}, \tag{2.104}$$

for Ohmic resistivity, Hall drift, and ambipolar diffusion respectively.

2.4.2 General properties of the non-ideal terms

At this point, it is worth noting some of the key features of the three non-ideal effects from their form in the induction equation.

Ohmic resistivity

For constant diffusivity, the Ohmic contribution in Equation 2.101 can be rewritten using vector identities and the $\nabla \cdot \mathbf{B} = 0$ condition as $\eta_O \nabla^2 \mathbf{B}/\mu_0$, which is simply a diffusion term for $\mathbf{B}$. The presence of Ohmic resistivity breaks flux freezing, and can be interpreted as the slippage of field lines across fluid elements when viewed in the rest frame of the fluid. The strength of Ohmic resistivity is often characterised by the nondimensional magnetic Reynolds number:

$$R_m = \frac{LV}{\eta_O}, \tag{2.105}$$

where L and V are the characteristic lengthscale and velocity of the system. Astrophysical plasmas often have high R_m, allowing ideal MHD to be a suitable approximation. However, in protoplanetary discs, as we shall see later, there is a region where $R_m < 10^3$ known as the "dead zone", and Ohmic resistivity can no longer be neglected. Ohmic resistivity is isotropic and linear, and dissipative in nature. Given the right conditions, it can contribute to electric heating that can generate significant heat transport in protoplanetary discs (Béthune and Latter, 2020).

Hall drift and ambipolar diffusion

Hall drift and ambipolar diffusion become important when the mean velocities of neutrals, ions and electrons differ from each other significantly. The Hall drift term can be rewritten in terms of a drift velocity in the form

$$\mathbf{u}_\mathrm{H} \equiv \mathbf{u}_e - \mathbf{u}_i = -\frac{\eta_H}{\mu_0|\mathbf{B}|}\nabla \times \mathbf{B} = -\frac{\mathbf{J}}{en_e}, \tag{2.106}$$

where it can be seen that it is the electron-ion drift that is responsible for this effect, whereas the ambipolar diffusion term can be rewritten in terms of the ambipolar drift velocity

$$\mathbf{u}_{\rm AD} \equiv \mathbf{u}_i - \mathbf{u} = \frac{\eta_A}{\mu_0 |\mathbf{B}|^2} (\nabla \times \mathbf{B}) \times \mathbf{B} = \frac{\mathbf{J} \times \mathbf{B}}{\gamma \rho \rho_i}, \tag{2.107}$$

where it can be seen that it is the ion-neutral drift that is responsible for this effect. The non-ideal MHD induction equation then has the form

$$\frac{\partial \mathbf{B}}{\partial t} = \nabla \times [(\mathbf{u} + \mathbf{u}_{\rm H} + \mathbf{u}_{\rm AD}) \times \mathbf{B} - \eta_O \nabla \times \mathbf{B}]. \tag{2.108}$$

The ambipolar diffusion term has a component which acts like Ohmic diffusion with a tendency to straighten up field lines, but it also has an anisotropic nonlinear element which can in some situations act as an anti-diffusion mechanism (Bai and Stone, 2014; Béthune et al., 2016). The Hall effect, on the other hand, should not really be thought of as a diffusive mechanism at all, as it is dispersive in character, and conserves magentic energy (it is non-dissipative) (Polygiannakis and Moussas, 2001). Its behaviour is strongly dependent on the geometry of the magnetic field present, as the Hall term behaves oppositely to the other terms in the induction equation when the sign of $\mathbf{B}$ is reversed.

Figure 2.5, taken from Wurster (2017), illustrates the movement of field lines with respect to fluid elements in regimes where each of the three non-ideal MHD effects dominate. In the pure Ohmic case, neutrals, ions and electrons have similar mean velocities, and field lines simply drift with respect to the fluid background to diffuse and straighten out. For the Hall regime, field lines are tied to the electrons, and drift with respect to the ion background whose contribution to the current can be neglected due to the ratio m_e/m_i being negligible. Finally, in the ambipolar diffusion dominated regime, field lines are tied to ions, while electrons are tied to the field lines in turn. They drift with respect to the neutral fluid as the ions move at a different mean velocity to the neutral particles.

2.4.3 Non-ideal regimes in protoplanetary discs

We now turn to consider the strength of each non-ideal effect in the protoplanetary disc context. It customary in the literature to assess and compare the non-ideal effects using the non-dimensional Elsasser numbers given by:

$$\Lambda_{O,H,A} \equiv \frac{v_A^2}{\eta_{O,H,A} \Omega}, \tag{2.109}$$

where the subscripts O, H, A denote Ohmic, Hall and ambipolar diffusion respectively, $v_A \equiv |\mathbf{B}|/\sqrt{\mu_0 \rho}$ is the Alfvén speed, and Ω is the (usually assumed Keplerian) angular velocity of the disc. The Elsasser number is an inverse measure of the diffusivity, and as will be

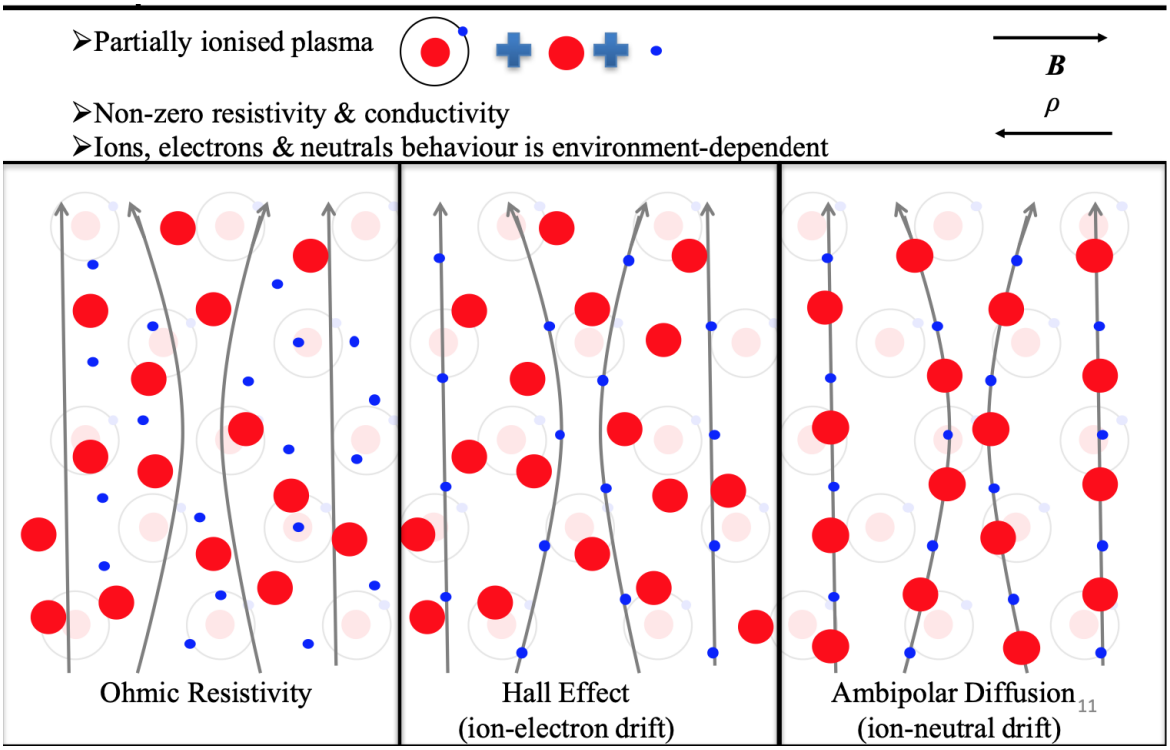

Fig. 2.5 Schematic showing the movement of field lines with respect to fluid elements in regions where each of the three non-ideal MHD regimes dominates. Red filled circles denote ions, while blue dots denote electrons. The neutral particles with bound ion and electron are shown in the background. Field lines are indicated by grey lines with arrows. Figure taken from Wurster (2017).

discussed in Section 2.5, is a useful quantity to determine whether the MRI is expected to be active in the region, with any of the Elsasser numbers falling below unity usually leading to stabilisation of the linear MRI.

Since both the Ohmic and Hall Elsasser numbers depend on the magnetic field strength, with $\Lambda_O \propto B^2$ and $\Lambda_H \propto B$, it is customary to use two other dimensionless numbers without field strength dependence to characterise the two effects, the first of which we have already seen in the magnetic Reynolds number, which when put into the disc context becomes

$$R_m \equiv \frac{\Omega H^2}{\eta_O}, \tag{2.110}$$

where H is the disc scale-height, while the other is the Hall Lundquist number, given by

$$\mathscr{L}_H \equiv \frac{v_A H}{\eta_H}. \tag{2.111}$$

As these two numbers have no dependence on field strength, they are used to characterise different regimes of nonlinear MRI saturation in the disc. The Hall Lundquist number is closely related to the Hall length, given by $l_H = H/\mathscr{L}_H$, which is also independent of the magnetic field strength. It is the characteristic length scale below which the Hall effect becomes important, and is given by the ratio of the Hall diffusivity to the Alfvén speed (Kunz and Lesur, 2013).

We can assess the varying and comparative strengths of the non-ideal effects in the disc by writing them in terms of the ionisation fraction and the density, while assuming a constant value of 10^{-3} Gauss for the field strength (Wardle, 1997). We reference Fromang (2013), who took typical values expected of protoplanetary disc mid-planes at 1 AU, with $n \sim 10^{14}$ cm^{-3}, $\gamma_i = 2.810^{13}$ cm^3 s^{-1} g^{-1}, $m_i = 39 m_H$ and $T \sim 100$ K. They then yielded the following expressions for the diffusivities:

$$\eta_O \sim \left(\frac{10^3}{x_e}\right) \text{cm}^2\ \text{s}^{-1}, \tag{2.112}$$

$$\eta_H \sim \left(\frac{50}{x_e}\right)\left(\frac{10^{14}\text{cm}^{-3}}{n}\right) \text{cm}^2\ \text{s}^{-1}, \tag{2.113}$$

$$\eta_A \sim \left(\frac{2.6\times 10^{-3}}{x_e}\right)\left(\frac{10^{14}\text{cm}^{-3}}{n}\right)^2 \text{cm}^2\ \text{s}^{-1}, \tag{2.114}$$

where $x_e \equiv n_e/n$ is the ionisation fraction. It is worth noting that all three non-ideal effects have the same inverse dependence on ionisation fraction, indicating we should expect each effect to weaken in strength as we move away vertically from the mid-plane, as the disc goes from weakly to significantly ionised in the disc atmosphere due to less shielding from

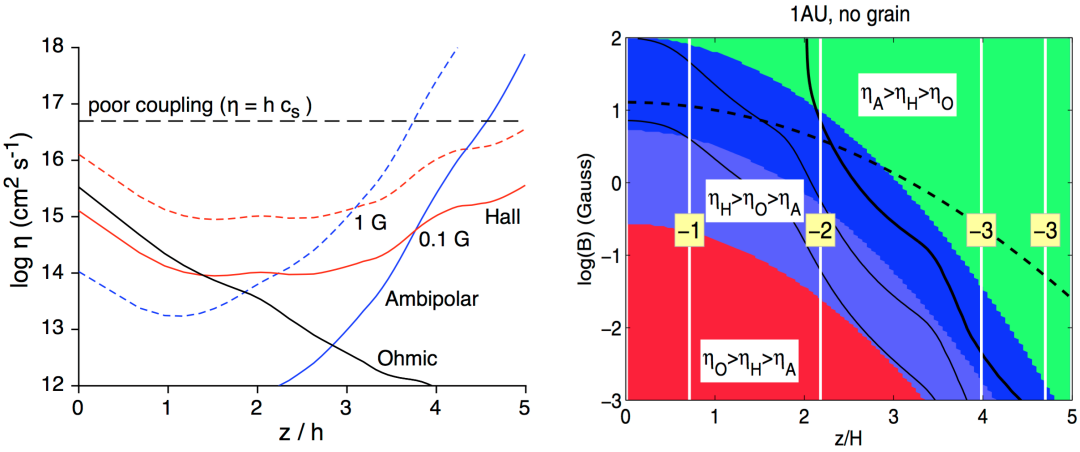

Fig. 2.6 Left: diffusivity profile from Wardle (2007) of a vertical slice of a MMSN model disc at 1 AU for magnetic field strengths of 0.1 and 1 G (*solid* and *dashed curves* respectively). Right: plot from Bai (2011) showing the regions where different diffusivities would dominate for different field strengths in a vertical slice of a disc at 1 AU.

radiation. $\eta_H \propto n^{-1}$, while $\eta_A \propto n^{-2}$, hence we would expect the disc to pass from first an Ohmic resistivity dominated region, followed by a Hall dominated region, and finally to an ambipolar diffusion dominated region as we move towards lower density regions up from the disc mid-plane. This is indeed the picture given by Wardle (2007) and Bai (2011), shown in the two panels of Figure 2.6, in their detailed ionisation model calculations of the non-ideal diffusivities in a disc at 1 AU, with no dust grains present.

As protoplanetary discs decrease in density as the radius increases, traditional models predict the disc mid-plane itself to be Ohm-dominated in the innermost region, and to be Hall-dominated beyond ($R > 1$ AU), before eventually ambipolar diffusion takes over at the disc outer edge ($R \sim 100$ AU). However, it should be noted with caution that these estimates can be drastically affected by the various factors contributing to disc ionisation, as discussed in the next subsection. The traditional assumption that discs can be divided neatly into regions where each non-ideal MHD effect is assumed to be dominant has been subject to question by recent analytical, semi-analytical and numerical studies which show that this picture is likely to be an oversimplification (Wurster, 2021). They showed that the Hall effect and ambipolar diffusion are more likely of comparable importance throughout most of the outer disc ($R > 1$ AU), and when expressed in dimensionless numbers correspond to $10^{-1} < \mathscr{L}_H < 10$ in most of the disc mid-plane region increasing abruptly at the disc surface, while $\Lambda_A \simeq 1$ throughout most of the disc (Lesur, 2020).

Factors contributing to the ionisation fraction

A key parameter determining the various non-ideal strengths is the ionisation fraction, and its variation in the disc, about which there is still much uncertainty and no general consensus in the protoplanetary disc community. In Chapter 11 we present in detail two ionisation models used by Lesur et al. (2014) and Béthune and Latter (2020) in calculating the different non-ideal contributions in different parts of the disc. Here however, we will limit ourselves to simply outlining the different factors that contribute to disc ionisation, and why there are still great uncertainties in our understanding of their extent in discs.

Sources of ionisation come mainly in five forms: X-rays from the central star, cosmic rays, radioactive nuclei present in the protostellar cloud, FUV ionisation from the central star, and thermal ionisation. Here we discuss each of them in turn.

- X-ray ionisation arises from the Bremsstrahlung emission from the corona around the central star (Bai and Goodman, 2009; Igea and Glassgold, 1999), and depends hugely on its X-ray flux, which can lead to variations of up to an order of magnitude in the ionisation fraction near the disc surface (Lesur, 2020).

- The ionisation rate due to cosmic rays can vary up to 6 orders of magnitude, due to them both being possibly shielded by the stellar wind, which drastically reduces their effect (Cleeves et al., 2015), or being accelerated in shocks surrounding the protostar produced by the protostellar jet, which leads to drastic enhancement (Padovani et al., 2018). Cosmic rays are responsible for most of the ionisation in the disc below two scale heights, and can lead to 3 orders of magnitude of uncertainty in the ionisation fraction.

- Radioactive decay ionisation is determined from current data from meteorites in the Solar System, and estimating their abundance in the era of the Solar System formation. The study most commonly quoted in the literature gives an radioactive ionisation rate of $\zeta_{\rm rad} = 10^{-19}$ s^{-1} (Umebayashi and Nakano, 2009).

- Stellar FUV photons arise from the stellar accretion shock and the stellar chromosphere. They ionise carbon and sulfur atoms in the surface layers of the disc, and for the disc composition and chemistry commonly assumed, lead to a floor value of $x_e > 10^{-5}$ at column densities $< 10^{-2}$ g cm^{-2} (Perez-Becker and Chiang, 2011).

- Thermal ionisation due to collisions between molecules may be present for inner parts of the protoplanetary disc ($R < 0.5$ AU), as $T > 300$ K. However, as our work mostly focuses on the outer parts of discs, we will neglect the discussion of thermal ionisation

in those regions. The coronal region of the disc surface on the other hand is also expected to be heated by stellar X-rays to temperatures in excess of $8,000$ K (Aresu et al., 2011), hence we should expect the fluid beyond around four scale-heights above the mid-plane to be fully ionised due to thermal collisions.

Disc structure plays a significant role in how much the ionising sources affect the ionisation fraction. Vertical column density determines both the penetration depth of X-rays, cosmic rays and FUV radiation, as well as the recombination rate (which decreases with decreasing density), and the height above which we expect X-ray heating to have fully ionised the fluid. The temperature structure of the disc affects both the vertical density structure and microphysics, while the disc surface density distribution can significantly change the ionisation fraction by 2 orders of magnitude when varied between the commonly used denser minimum mass solar nebula (MMSN) model, which leads to lower ionisation fractions, and ones that are more observationally motivated. Disc surface densities generally decrease with increasing radius, hence we expect ionisation to also increase accordingly.

Finally, disc metallicity as well as the presence of dust grains can also significantly affect the ionisation fraction. The presence of metal atoms significantly modifies the reaction network of ionisation and recombination, as metals recombine with electrons at a much lower rate than molecular ions, and can lead to a dramatic increase in the ionisation fraction by up to 3 orders of magnitude (Fromang et al., 2002). Grains on the other hand not only affect the reaction network by typically reducing the ionisation fraction by 2-3 orders of magnitude, but can also change the dependence of the diffusivities on the ionisation rate, as grains absorb the charges present and become the dominant charge carriers instead near the mid-plane. The latter effect could even change the sign of the Hall coefficient, as the dominant heavier charge carrier becomes negatively charged instead. Overall, dust grains can increase diffusivities by 2-4 orders of magnitude, while the detailed microphysics depends on factors such as grain size and abundance (Ilgner and Nelson, 2006; Salmeron and Wardle, 2008). This is also affected by grain evolution from processes such as vertical settling that changes their spatial distribution, and coagulation that changes their size. It is still unclear what dust abundances and sizes are to be expected in protoplanetary discs, hence there is an overall uncertainty of ± 3 orders of magnitudes of uncertainty in the diffusivities (Lesur, 2020). For most of our study, we will be considering the "intermediate" case of a metal-free dust-free environment, while at times we may arbitrarily change the diffusivities by a few orders of magnitudes to mimic the effect of including metals and dust.

2.5 Non-ideal effects on the MRI

The presence of non-ideal MHD significantly affects the operation of the MRI in discs, and has been the subject of much investigation over the past two decades. Here, we limit ourselves to sketching out the derivation and implications of non-ideal MHD on the linear MRI in 1-D vertical variations that are most relevant to our Thesis. Our sketch largely follows the more detailed discussion in the excellent review by Lesur (2020), which the reader can consult for completeness.

Let us consider the linearised equations of small axisymmetric perturbations of a disc with a background mean vertical and azimuthal magnetic field

$$\mathbf{B}_0 = B_{0,y}\mathbf{e}_y + B_{0,z}\mathbf{e}_z. \tag{2.115}$$

For simplicity, we consider the unstratified case in which there is no vertical gravity, and the flow is incompressible ($\nabla \cdot \mathbf{u} = 0$). As before, we work in the radially local model, where Cartesian x, y, z coordinates correspond to the R, ϕ, z directions in the disc respectively. Writing the perturbations from equilibirum as

$$\mathbf{u} = \mathbf{v}\exp(i\mathbf{k}\cdot\mathbf{x} + \sigma t), \tag{2.116}$$

$$\mathbf{B} = \mathbf{B}_0 + \mathbf{b}\exp(i\mathbf{k}\cdot\mathbf{x} + \sigma t), \tag{2.117}$$

where $\mathbf{k} = k_z\mathbf{e}_z$ is the wave vector, assumed to be purely vertical, σ the linear growth rate, and $\mathbf{b}$ here is the initial perturbation amplitude of the perturbation (here $\mathbf{b} \neq \mathbf{B}/|\mathbf{B}|$), we obtain the linearised equations

$$\sigma\mathbf{v} = i\frac{\mathbf{k}\cdot\mathbf{B}_0}{\mu_0\rho}\mathbf{b} + 2\Omega v_y\mathbf{e}_x - (2-q)\Omega v_x\mathbf{e}_y, \tag{2.118}$$

$$\begin{aligned}\sigma\mathbf{b} = \; & i\mathbf{k}\cdot\mathbf{B}_0\mathbf{v} - q\Omega b_x\mathbf{e}_y - \eta_O k^2\mathbf{b} + \eta_H(\mathbf{k}\cdot\hat{\mathbf{B}}_0)\mathbf{k}\times\mathbf{b} \\ & - \eta_A\{(\mathbf{k}\cdot\hat{\mathbf{B}}_0)^2\mathbf{b} - (\mathbf{b}\cdot\hat{\mathbf{B}}_0)([\mathbf{k}\cdot\hat{\mathbf{B}}_0]\mathbf{k} - k^2\hat{\mathbf{B}}_0)\},\end{aligned} \tag{2.119}$$

$$\mathbf{k}\cdot\mathbf{v} = 0, \tag{2.120}$$

$$\mathbf{k}\cdot\mathbf{b} = 0. \tag{2.121}$$

We can see from Equation (2.119) that the Ohmic diffusion term, as mentioned before, acts purely as a linear dampener for the growth, with a greater effect on modes that have shorter wavelengths. The Hall term on the other hand rotates the magnetic perturbation around the wave vector while keeping its magnitude constant. The direction of rotation is dependent on

the signs of $\mathbf{B}$ and η_H. Finally, the first ambipolar diffusion term acts as another pure linear dampener, while the second term introduces anisotropic complexity to its behaviour.

Using Equations (2.120) and (2.121), we can reduce this set of equations into a fourth order problem involving only horizontal components. This can then be solved using standard matrix methods (we refer the reader to Lesur (2020), Kunz and Balbus (2004) and Desch (2004) for details) to yield the well known dispersion relation:

$$\sigma^4 + \mathscr{C}_3\sigma^3 + \mathscr{C}_2\sigma^2 + \mathscr{C}_1\sigma + \mathscr{C}_0 = 0, \tag{2.122}$$

where the $\mathscr{C}$ coefficients are given by

$$\mathscr{C}_3 = 2\eta_O k_z^2 + \tau_A(k_z^2 v_A^2 + \omega_A^2), \tag{2.123}$$

$$\mathscr{C}_2 = \kappa^2 + 2\omega_A^2 + \eta_O^2 k^4 + \tau_A^2\omega^2 k_z^2 v_A^2 + l_H k_z \omega_A(l_H k_z \omega_A - q\Omega), \tag{2.124}$$

$$\mathscr{C}_1 = \mathscr{C}_3(\omega_A^2 + \kappa^2), \tag{2.125}$$

$$\begin{aligned}\mathscr{C}_0 = {} & \omega_A^2(\omega_A^2 - 2q\Omega^2) + \kappa^2 k_z^4 \eta_O^2 + l_H\omega_A k_z[(4-q)\Omega\omega_A^2 - q\Omega\kappa^2 + l_H\omega_A k_z^3] \\ & + \kappa^2\tau_A^2\omega_A^2 k_z^2 v_A^2,\end{aligned} \tag{2.126}$$

with $\mathbf{v}_A = \mathbf{B}_0/\sqrt{\mu_0\rho}$ being the Alfvén velocity, and we have defined $\omega \equiv \mathbf{k}\cdot\mathbf{v}_A$ to be the Alfvén frequency, $l_H \equiv \eta_H/v_A$ the Hall length, $\tau_A \equiv \eta_A/v_A^2$ the ambipolar time, the timescale at which neutral particles collide with ions, and $\kappa^2 \equiv 2\Omega^2(2-q)$ is the square of the epicyclic frequency as before. In the vicinity of $\sigma = 0$, the necessary and sufficient condition for stability is $\mathscr{C}_0 > 0$, because $\mathscr{C}_1 > 0$. We now turn to examine this condition for regimes where different non-ideal effects dominate.

2.5.1 Ohmic diffusion and damping of the MRI

In the case of pure Ohmic resistivity, the $\mathscr{C}_0 > 0$ condition leads to

$$\frac{2q\Omega^2}{k_z^2 v_{Az}^2} - \kappa^2\frac{\eta_O^2}{v_{Az}^2} < 1 \tag{2.127}$$

for a disc to be stable. For a Keplerian disc with $\kappa^2 = \Omega^2$, the general condition for modes in the disc to be stabilised is

$$\frac{3\Omega^2}{k_z^2 v_{Az}^2} - 1 < \Lambda_O^{-2}, \tag{2.128}$$

showing us that there is a minimum wave-number $k_{z,\min}$ (hence largest wavelength that can be fitted in the disc vertical domain) above (below) which the disc would always be stable.

This shows that Ohmic resistivity preferentially stabilises the smaller wavelength modes of the MRI, while increasing η_O increases the range of wavelengths that are fully stabilised. Noting from Section 2.2 that the most unstable mode in ideal MHD has $\omega_A = 3\Omega/4$, this leads to the condition

$$\Lambda_O^2 < \frac{1}{3} \tag{2.129}$$

for the most unstable ideal MRI mode to be stabilised.

In real discs where stratification is present, the condition $\Lambda_O < 1$ tends to be sufficient in suppressing the MRI locally, leading to a region known as the 'dead zone' in the disc mid-plane in the inner disc where the MRI is quenched. The presence of Ohmic resistivity significantly alters the shape of the MRI eigenmode, flattening it in regions where Λ_O is low, as well as reducing the growth rate from its ideal MHD value. Strong resistivity at the mid-plane also restricts communication between the two sides of the disc through the quenching of Alfvén waves. This results in modes that are localised on one side of the disc with identical growth rates to those located on the other (Lesur, 2020), and may be combined to give overall "hourglass" or "slanted" modes. This can also be interpreted as the "hourglass" and "slanted" modes becoming degenerate, as the localised modes can be obtained through a linear combination of degenerate "hourglass" and "slanted" modes. The effect of Ohmic resistivity on the shape and growth rate of the MRI modes will be explored more fully in Chapter 10 as we consider Ohmic resistive only disc wind solutions.

2.5.2 Ambipolar diffusion and nonlinear dampening of the MRI

We follow the same procedure as for the pure Ohmic resistivity case, but now for pure ambipolar diffusion. The $\mathscr{C}_0 > 0$ condition leads to

$$\frac{2q\Omega^2}{k_z^2 v_{Az}^2} - 1 < \kappa^2 \tau_A^2 \left(\frac{v_A}{v_{Az}}\right)^2 \tag{2.130}$$

for stability, recalling our definition of the ambipolar time as $\tau_A \equiv \eta_A / v_A^2$. Considering the Keplerian case of $\kappa^2 = \Omega^2$, the condition for general disc stability over all modes is given by

$$\frac{3\Omega^2}{k_z^2 v_{Az}^2} - 1 < \Lambda_A^{-2} \left(\frac{v_A}{v_{Az}}\right)^2, \tag{2.131}$$

which is essentially the same result as Equation (2.128) for the Ohmic resistivity case when $v_A = v_{Az}$ (pure vertical field), showing that ambipolar diffusion also preferentially stablises the smaller wavelength modes of the MRI, while increasing η_A increases the range of wavelengths that are fully stabilised. It is also worth noting that when $v_A \neq v_{Az}$, an overall

background magnetic field tilted from the vertical axis, which in the case of discs would usually result from a strong v_{Ay} arising from the winding up of the poloidal field, acts to increase the stability of the system. Examining the most unstable ideal MRI mode where $\omega_A = 3\Omega/4$ then leads to the condition

$$\Lambda^2 < \frac{1}{3}\left(\frac{v_A}{v_{Az}}\right)^2 \tag{2.132}$$

for its stabilisation, which again is exactly the same result as Equation (2.129) for Ohmic resistivity when $v_A = v_{Az}$.

These results show while ambipolar diffusion affects the MRI in much the same way as Ohmic resistivity when the magnetic field is near vertical, key differences arise in cases where $B_y \gg B_z$, as it can lead to a stable disc even when $\Lambda_A > 1$. This can be understood by the fact that η_A increases quadratically with the overall magnetic field strength $|\mathbf{B}|$, while the MRI depends only on the magnetic tension due to B_z. An increase in B_y therefore increases the diffusivity, but does not change the mechanics of the feedback loop as described in Section 2.2, resulting in greater dampening on the MRI.

2.5.3 Hall drift and Hall driven linear waves

For the pure Hall case, and in the absence of disc rotation ($\Omega = 0$), the dispersion relation can be rewritten as

$$\sigma^4 + \sigma^2(2\omega_A^2 + l_H^2\omega_A^2 k_z^2) + \omega_A^2 = 0, \tag{2.133}$$

which corresponds to two waves with frequency $\omega \equiv i\sigma$ given by

$$\omega = \omega_A\left[\pm\frac{l_H k_z}{2} + \sqrt{\frac{l_H^2 k_z^2}{4} + 1}\right]. \tag{2.134}$$

The two branches become degenerate and reduce to Alfvén waves when $k_z \to 0$, but when $k_z \to \infty$ they take on different behaviours. The positive solution corresponds to the whistler, also known as electron-cyclotron modes, since for as $k_z \to \infty$, $\omega \to \omega_A l_H k_z = \omega_H$, the whistler wave frequency. The negative solution corresponds to ion-cyclotron modes, and as $k \to \infty$, $\omega \to \omega_A/l_H k_z = \omega_{IC}$, the ion-cyclotron frequency . Both positive and negative solutions introduce helicity to the magnetic field, and when $l_H > 0$, correspond to right-handed and left-handed polarised waves respectively. When disc rotation is reinserted, these two waves lead to two Hall-specific instabilities, known as the Hall shear instability (HSI) for the positive case, and the ion-cyclotron instability (ICI) for the negative case.

Hall shear instability

The Hall shear instability (HSI) (Kunz, 2008) occurs for the positive solution of Equation (2.134), and arises from the action of the disc shear on whistler waves. It amplifies horizontal fields, and its action can be seen by considering the Hall and shear terms for the horizontal components of the induction equation, which are

$$\frac{\partial B_x}{\partial t} = \cdots + \frac{B_z}{\mu_0}\frac{\partial}{\partial z}\eta_H \frac{\partial}{\partial z} B_y, \tag{2.135}$$

$$\frac{\partial B_y}{\partial t} = \cdots - \left(\frac{B_z}{\mu_0}\frac{\partial}{\partial z}\eta_H \frac{\partial}{\partial z} + q\Omega\right) B_x. \tag{2.136}$$

When $\eta_H B_z \Omega$ is positive (aligned configuration), the Hall effect rotates the azimuthal magnetic field into the radial direction such that Keplerian shear then generates from the radial field an azimuthal magnetic field component of the same sign as before, and the process repeats itself to amplify the overall horizontal field strength. On the other hand, when $\eta_H B_z \Omega$ is negative (anti-aligned configuration), the radial field that results from rotation of the azimuthal field is of the opposite sign, and Keplerian shear generates from the radial field a correspondingly opposite-signed azimuthal contribution to the azimuthal field, leading to a negative feedback loop that weakens the horizontal fields. The action of the HSI, and its amplifying or dampening nature due to the aligned or anti-aligned configuration, is shown diagrammatically in Figure 2.7, which is taken from Lesur (2020).

The HSI comes from oscillations of the electron (or lighter) fluid, and Lesur (2020) obtained a criterion for instability by examining the low magnetisation limit that allows us to decouple the ions from the electrons. In this regime, where $\omega_A \to 0$, while keeping $l_H \omega_A > 0$, the dispersion relation becomes

$$(\sigma^2 + \kappa^2)[\sigma^2 + l_H \omega_A k_z (l_H k_z \omega_A - q\Omega)] = 0. \tag{2.137}$$

The condition for the HSI to be unstable for a Keplerian disc is then

$$l_H v_{Az} k_z^2 (l_H k_z^2 v_{Az} - q\Omega) < 0, \tag{2.138}$$

provided the configuration is aligned, which translates to the additional condition that $q l_H v_{Az} > 0$. The inequality shows us that when $k_z^2 l_H v_{Az} > q\Omega$, in other words when the whistler frequency becomes too large, the HSI vanishes. The HSI is susceptible to small scale quenching, and in a given system has a maximum k_z (minimum wavelength) below (above) which it can operate. Like the MRI, the maximum growth rate of the HSI is $\sigma_{\max} = q\Omega/2$, when $k_z^2 l_H v_{Az} = q\Omega/2$, and the fastest growing modes vary in the vertical direction only, manifesting themselves as channel-like modes.

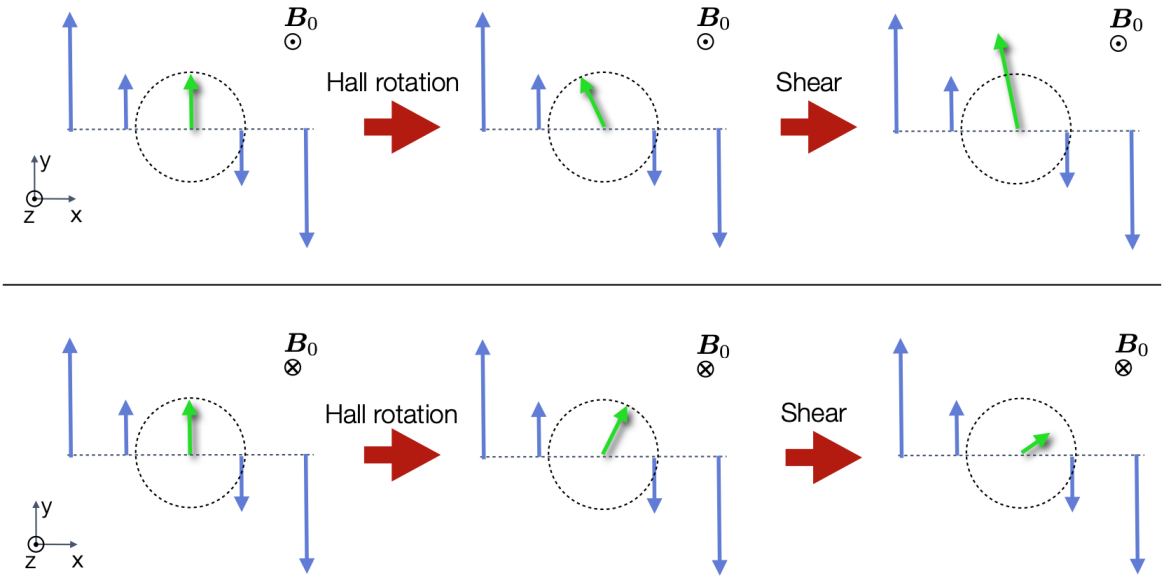

Fig. 2.7 Diagram illustrating the action of the HSI in amplifying/weakening fields in the aligned/anti-aligned configuration (top/bottom). For a positive η_H, the direction of Hall rotation of the field depends on the sign of $B_z = B_0$. For positive $B_0 > 0$, the rotated field is amplified by shear, while for negative $B_0 > 0$ it is damped. Figure taken from Lesur (2020).

Ion-cyclotron instability

The ion-cyclotron instability (ICI), also called 'diffusive MRI' by Pandey and Wardle (2012), occurs only for anti-aligned configurations, and corresponds to the negative solution of Equation (2.134). The instability arises from the coupling of the left handed Hall wave to the epicyclic motion (Wardle and Salmeron, 2012). Lesur (2020) derived an instability condition for the ICI by setting $k_z \to \infty$ to filter out the whistler wave (as the HSI becomes quenched), while assuming that σ remains finite, and keeping only the highest $O(k_z^4)$ terms in the dispersion relation. Equation (2.122) then becomes

$$\sigma^2 l_H^2 k_z^2 \omega_A^2 + [\omega_A^2 + (2-q)\Omega l_H \omega_A k_z][\omega_A^2 + 2\Omega l_H \omega_A k_z] = 0. \tag{2.139}$$

We see that in the limit $\Omega \to 0$, $\sigma \to \omega_{IC}$, confirming to us that we are dealing with ion-cyclotron modes here. The condition for these modes to be unstable is then

$$\frac{v_{Az}^2}{(2-q)\Omega} > -l_H v_{Az} > \frac{v_{Az}^2}{2\Omega}, \tag{2.140}$$

which naturally requires the anti-aligned configuration. There is no constraint on k_z in the instability condition, hence the ICI can operate on any sufficiently short length scale for the approximation to be valid. However, it is only active within a restricted range of field

strengths. Physically, these modes behave like the standard MRI picture, with δB_ϕ generated from δB_r, except that here it is not differential shear of the radial field that is responsible for the generation, but the Hall effect (Pandey and Wardle, 2012). This means δB_r can lead to generation of δB_ϕ of the same sign, rather than of the opposite sign as in the shear-driven case.

The left hand panel of Figure 2.8, taken from Lesur (2020), plots the Hall-MRI mode growth rates in 2D plane characterised by a modified Hall Lundquist number,

$$\mathscr{L}_H^* = \frac{1}{l_H k_z} = \frac{v_A}{\eta_H k_z}, \tag{2.141}$$

which gives us a measure of the strength of the Hall effect, against ω_A the Alfvén frequency. In the limit of low $\mathscr{L}_H^*$, the regions when $\sigma > 0$ are bounded by the HSI and ICI instability conditions calculated in our limiting cases, which are represented by the solid and dashed white curves respectively. As $\mathscr{L}_H^* \to \infty$, we simply recover ideal MHD as expected. This shows us that in the presence of the Hall effect, the behaviour of the MRI can vary drastically depending on whether it is in the aligned or anti-aligned configuration. In the aligned configuration, Hall drift has a stabilising effect on the MRI, while Hall drift has a destabilising effect in the anti-aligned configuration. In the aligned configuration, Hall-MRI has a lower mode frequency at which σ is maximum than the MRI in ideal MHD. This is because the HSI is most efficient when ω_A is comparable to the whistler wave, while for the MRI this happens when it is comparable to the Alfvén wave. Since the whistler frequency is proportional to $l_H k_z$ and decreases as Hall strength is increased, the HSI leads to a higher growth rate at lower ω_A.

Ohm-Hall MRI

Ohmic resistivity can drastically affect the behaviour of Hall-MRI, and vice versa when considered in the other sense of the impact of Hall drift on resistive-MRI. The effect of Ohmic resistivity on Hall MRI was examined in detail by Wardle and Salmeron (2012) and Pandey and Wardle (2012). Here we will only give an overview of the major results, while sketching out the reasoning behind them.

Generally, resistivity stabilises Hall-MRI modes, starting from those with highest ω_A down to lower ω_A as Λ_O decreases. The ICI is first to be stabilised due to its higher $|\omega_A|$ values, while the HSI is also heavily damped. We can see this in the right hand panel of Figure 2.8, which plots the growth rates in the $\mathscr{L}_H^* - \omega_A$ plane for a disc with $\Lambda_O = 0.1$. The ICI branch is completely quenched, while the HSI is heavily damped from the pure Hall-MRI case (compare with the left hand panel which is pure Hall-MRI). Interestingly, the unstable region grows as $\mathscr{L}_H^*$ is decreased, showing us that Hall drift can reinvigorate regions that

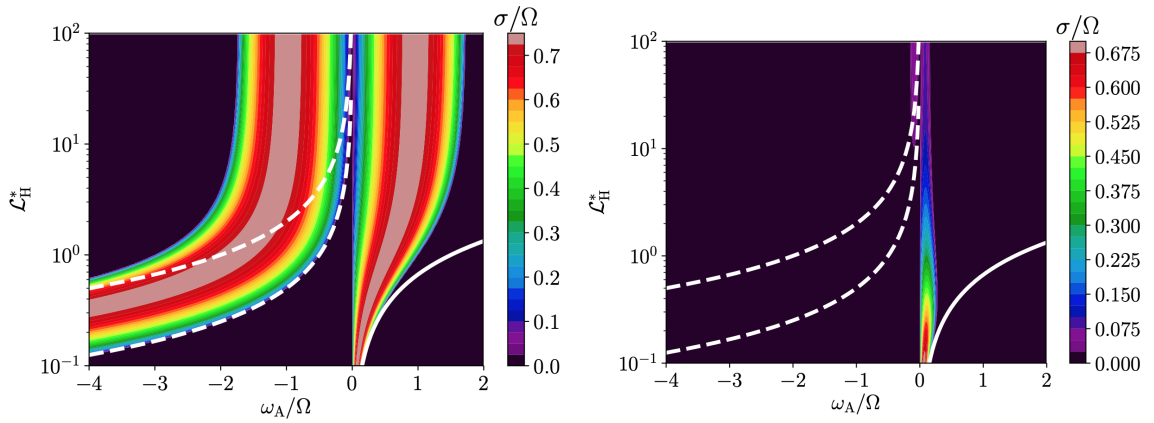

Fig. 2.8 Plots of the Hall-MRI growth rate σ in a 2D plane characterised by the modified Hall Lundquist number $\mathscr{L}_H^*$ and Alfvén frequency ω_A. The left hand plot is for the pure Hall-MRI case, while the right hand plot has an Ohmic resistivity such that $\Lambda_O = 0.1$. The dotted white lines are the analytic bounds of Equation (2.139) for the ICI in the high $|k_z|$ limit, while the white line is the analytic bound of Equation (2.138) for the HSI in the $\omega_A \to 0$ limit. Both plots are taken from Lesur (2020).

would normally have been rendered inactive by resistive stabilisation. The stabilising effect of the HSI mode under the effect of resistivity is examined by Lesur (2020) taking the limits $\omega_A \to 0$ with $l_H \omega_A > 0$ in the dispersion relation, giving

$$(\sigma^2 + \kappa^2)[(\sigma + \eta_O k_z^2)^2 + l_H \omega_A k_z (l_H k_z \omega_A - q\Omega)] = 0. \tag{2.142}$$

This gives the criterion

$$\Lambda_O^2 < \frac{1}{2}\Lambda_H^2 \tag{2.143}$$

for stabilising the most unstable HSI mode. However, if the reverse is true, then the HSI can in theory revive regions in the disc that have been thought to have been rendered 'dead' by resistivity. These perturbations would be mostly magnetic in nature with minimal effect on the velocity fields, as the HSI is ultimately an unstable whistler mode amplifying the horizontal fields, but which leaves the main mass carriers of ions and neutrals unperturbed. However, as we shall see in Section 2.6, they can lead to drastic changes in the overall magnetic field geometry threading the disc, which can in turn affect the discs' transport properties. In the anti-aligned case on the other hand, the effects of Ohm Hall-MRI are similar to that of the purely resistive case, but with slightly reduced growth rates for the MRI modes compared with the purely resistive case.

2.6 Non-ideal MHD effects on disc structure and magnetic wind launch

The effect of non-ideal MHD on protoplanetary disc structure and the launching of the magnetic wind has been studied in both semi-analytic models (Königl et al., 2010; Nolan et al., 2017; Teitler, 2011; Wardle and Koenigl, 1993) and numerical simulations (Bai, 2017; Béthune et al., 2017; Gressel et al., 2020, 2015; Riols et al., 2020). On the one hand, semi-analytic models, such as the 1-D vertical structure models based on the work of Wardle and Koenigl (1993), often require gross assumptions about the disc geometry, such as assuming a standard "hourglass" symmetry of the large-scale magnetic field threading the disc (see Figure 3.1 in Section 3.2). They also constrained the vertical flux radial transport rate to zero, and they used simplified diffusivity profiles that are set to be constant throughout the vertical extent of the disc. Although they demonstrate that diffusive discs can indeed launch magnetic winds driving mass accretion under the gross conditions expected in protoplanetary discs, and are indeed a useful first step towards eventually realising a global framework for modelling the structure and evolution of wind-driven non-ideal MHD protoplanetary discs, they are also limited by their construction as stationary steady-flow solutions, as well as arbitrary restrictions on disc geometry and the requirement of self-similarity on radial scales (Teitler, 2011). Numerical simulations, on the other hand, allow for the study of discs in a time dependent manner and can explore different geometries under more realistic conditions. However, they are limited by computing power, which in turn leads to insufficient integration time for determining the long term outcome of solutions, and lower resolution than semi-analytic studies. To gain insight into the effect of non-ideal MHD on protoplanetary disc structure and wind launching therefore requires complementary studies by both semi-analytical and numerical methods.

Recently, both radially local shearing box simulations (Bai, 2015; Lesur et al., 2014) and global simulations (Bai, 2017; Béthune et al., 2017; Gressel et al., 2015) have shown that when realistic prescriptions of all three non-ideal MHD effects are included, we should expect turbulent activity from the MRI to be quenched throughout most of the disc, resulting in a mostly laminar disc with steady flow. This is particularly the case when ambipolar diffusion is included, which quenches MRI turbulence in the disc surface layers due to η_A's dependence on B^2 quenching the surface modes before they develop into turbulence due to the enhanced diffusivity from magnetic perturbation growth, and allows a weakly magnetised outflow to be launched (Bai and Stone, 2013b; Lesur et al., 2014). On the other hand, the presence of Hall drift in the aligned configuration leads to the generation of a strong laminar stress in the disc through the action of the HSI, which enhances angular momentum and mass

transport (Bai, 2015, 2017; Simon et al., 2015). This laminar stress is polarity dependent, and is not present when the configuration is anti-aligned. The mostly laminar nature of the flow recovered in both local and global simulations stretches from the inner disc (down to 0.3 AU) to the outer disc region (up to 30 AU) (Bai, 2013, 2015), and shows that protoplanetary discs are most likely wind-driven, rather than MRI turbulence-driven as in traditional pictures of accretion disc transport. It also justifies the use of 1-D vertical structure models in modelling radially local regions of protoplanetary discs, and is a simplification that will be employed in the work of this Thesis.

Another important effect non-ideal MHD have on protoplanetary discs is in the overall geometry of the large-scale magnetic field threading the disc, which also affects the vertical variation of the velocity profile about the mid-plane and the overall geometry of the magnetic wind. Bai and Stone (2013b) first noted in their local shearing box simulations that both the traditional "hourglass" and less common "slanted" geometries can result from discs with Ohmic and ambipolar diffusion prescriptions. They initially dismissed the "slanted" symmetry as unphysical solutions resulting from the limitations of the shearing box formalism, which neglects curvature terms and does not distinguish which direction the star is in, hence the requirement that field lines should eventually bend to the same direction away from the central object is not enforced. However, the repeated occurrence of the "slanted" symmetry in subsequent shearing box simulations (Bai, 2014, 2015; Lesur et al., 2014), and most strikingly the emergence of "slanted"-like solutions in global simulations where the inward-directed field only bends away from the star high up in the coronal region (Bai, 2017; Béthune et al., 2017) (see also Figure 2.9), have led to the conclusion that "slanted"-like solutions are indeed a robust feature of protoplanetary discs, and are closely linked with the presence of non-ideal MHD.

The origin of the "slanted" symmetry has never been clearly demonstrated, although there have been various hypotheses. Bai (2017) suggested that in aligned cases where Hall drift is included, the development of "slanted" regions in the disc may be a result of the HSI strongly amplifying the horizontal field, particularly in the inner disc (< 10 AU). Lesur et al. (2014) in their local simulations have similarly suggested that the HSI spontaneously saturates into a "slanted" configuration. This is supported by the observation in both Béthune et al. (2017) and Bai (2017) that "slanted" symmetries are more prevalent for discs in the aligned configuration, and that anti-aligned cases or weak field conditions ($\beta_{\rm mid} \gtrsim 10^4$) lead to more "hourglass" discs. On the other hand, "slanted"-like configurations have also been seen in global simulations with both Ohmic resistivity and ambipolar diffusion (Gressel et al., 2020; Riols et al., 2020), as well as simulations where only Ohmic resistivity is present (Rodenkirch et al., 2020). The HSI therefore cannot be the sole explanation of this phenomenon, and it

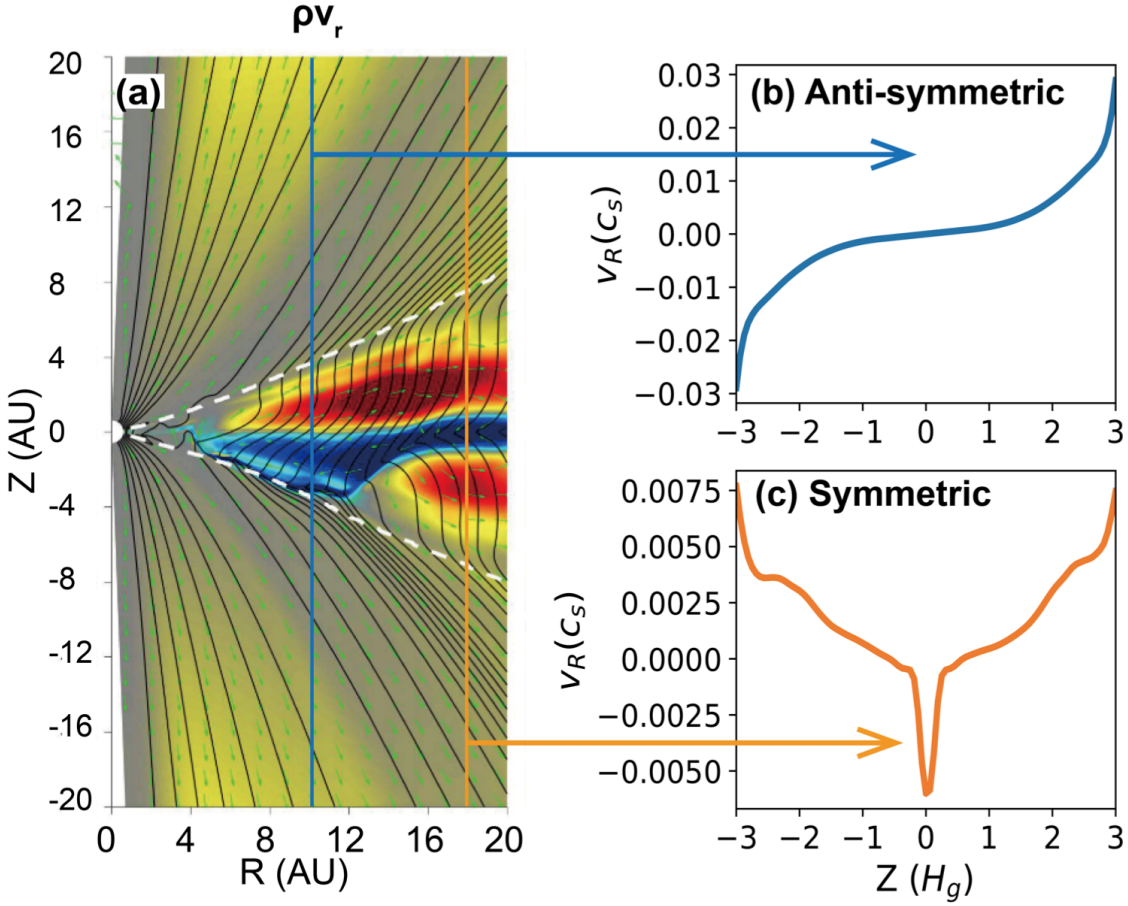

Fig. 2.9 Radial gas flow and poloidal field profile from one of the simulations (figure 7) in Bai (2017), where the Hall effect is in the aligned configuration, and all three non-ideal MHD effects are included with realistic prescriptions. Notice that at 10 AU, the poloidal field has a "slanted" symmetry in the disc region before bending back away from the star in the coronal region, resulting in an anti-symmetric radial velocity profile in the disc about the mid-plane. On the other hand, at 18 AU, the poloidal field has an "hourglass" symmetry throughout, and the resulting radial velocity profile is symmetric about the mid-plane.

has been suggested that the "slanted" symmetry could be the result of explusion of the strong mid-plane current layer required by the "hourglass" configuration, by strong diffusive effects from Ohmic and ambipolar diffusion in the disc which render the sustenance of a strong mid-plane current layer to be unstable (Bai and Stone, 2013b). Béthune et al. (2017) and Bai (2017) have also noted that the eventual disc symmetry may be affected by the initial conditions of the simulation, and this will be one of the areas we will be investigating in Part III of the Thesis.

The changing of the geometry of the disc vertical profile and magnetic wind has important consequences on its dynamics and long term transport properties. In local models, the "slanted" symmetry leads to overall zero horizontal transport of mass and magnetic flux due to the opposite directions of the horizontal flow above and below the mid-plane. Although in global models the magnetic field eventually bends away from the star high up in the corona, the "slanted"-like asymmetric solutions nonetheless have much reduced overall radial transport properties than the "hourglass" symmetric solutions for the same disc parameters (Bai, 2017). The different horizontal flow profiles resulting from the two symmetries also have an impact on dust transport in discs governed by wind-driven accretion, with the radial drift of small dust modestly enhanced in the presence of a mid-plane accretion flow in the "hourglass" case compared with the asymmetric "slanted"-like case (Hu and Bai, 2021). The question of the global outflow configuration is therefore an important one, and remains open for further investigation.

2.7 Current paradigm and key questions

The current paradigm for protoplanetary disc structure and dynamics can be summarised as follows. Protoplanetary discs are relatively cold and weakly ionised discs where non-ideal MHD effects are prominent in shaping disc dynamics, most notably in suppressing turbulent activity caused by the MRI, which is the dominant mechanism of disc accretion and angular momentum removal expected in other accretion disc systems. Instead, protoplanetary discs are expected to be threaded by a weak large-scale magnetic field, which, when coupled with thermal heating of the disc surface layers from the central star, leads to the launching of magneto-thermal winds from the disc surface. The magnetic nature of these winds means that they remove angular momentum vertically, driving accretion through the mostly laminar disc. While Ohmic resistivity acts as a simple diffusivity of the magnetic field suppressing the MRI, Hall drift and ambipolar diffusion are anisotropic and nonlinear, leading to a whole variety of effects on the disc vertical structure and transport properties. Under certain conditions, the disc may adopt a "slanted" symmetry close to the disc mid-plane instead of the traditional

"hourglass" symmetry where the poloidal field bends away from the star above and below the disc. In a global setting, the "slanted"-like solution leads to an overall asymmetric profile about the mid-plane, which can have significant effects on the overall disc dynamics.

One of the key questions that remains to be addressed is the long-term transport of the large-scale magnetic field through the disc, as the behaviour of the magnetic processes in the disc is highly sensitive to the amount of vertical magnetic flux threading the disc. Understanding this is particularly crucial for the formulation of any secular theory of disc evolution where the flux distribution is expected to change over time. Part II of this Thesis is devoted to addressing this problem, and particularly the contribution of non-ideal MHD effects to the long term radial transport of the vertical magnetic field.

Another key question flagged up by recent studies on protoplanetary discs is on the origin of the "slanted" symmetry state and the factors that contribute to the disc adopting one symmetry over another. As we have already seen, the symmetry adopted by the disc can have a significant impact on long term transport and short term dynamical properties of the disc, and is an important problem to address. Part III of the Thesis is devoted to the study of this problem, and the proposal of a new mechanism that could be partly responsible for the development of the "slanted" symmetry profiles we find in many studies of late.

In addition to the simplification of the problem to studying 1-D vertical slices of radially local regions of a protoplanetary disc, we also adopt the isothermal assumption throughout this Thesis. Although we will not be able to explore the detailed thermodynamics of the disc or capture the "thermal" nature of the magneto-thermal wind launch, this simplification allows us to simplify the physics and explore in a more systematic manner over a wider parameter space the interaction between non-ideal effects, the MRI and magnetic winds. Recent models of protoplanetary discs are often of such great complexity that it is often very difficult to separate the physics and note what is the primary cause of an observed phenomenon. Our aim in this work is to find the bare-bone essentials in what governs the long-term magnetic flux transport, as well as the geometry of the disc profile and magnetic wind configuration. Our goal is that our study will shed light on the interpretation of current and future investigations where more physics is put back in to simulate protoplanetary discs as realistically as possible, and to pave the way to a unified understanding of disc structure and evolution.

Chapter 3

Multi-scale radially local approach

In this Chapter, we derive the radially local equations that will form the basis of the rest of the Thesis. Guilet and Ogilvie (2012) were distinctive in using a multiscale asymptotic approach in deriving their 1D radially local vertical structure equations, allowing radial gradients of various quantities to be placed on the same footing as inclination and outflow in driving flux transport. This approach is often employed in the study of warped discs where processes vary at different spatial and time scales (Ogilvie, 1999). We follow the same multiscale asymptotic approach, but here derive a more general formalism. All our subsequent work is based on the equations derived using this formalism, and here we also use the equations derived to make some general observations on the interplay between various source terms and the angular momentum transport and magnetic flux evolution.

3.1 Governing equations

The continuity equation is given by

$$\frac{\partial \rho}{\partial t} + \nabla \cdot (\rho \mathbf{u}) = 0, \tag{3.1}$$

and the conservation of momentum by

$$\rho \left(\frac{\partial \mathbf{u}}{\partial t} + \mathbf{u} \cdot \nabla \mathbf{u} \right) = -\rho \nabla \Phi - \nabla p + \frac{1}{\mu_0} (\nabla \times \mathbf{B}) \times \mathbf{B} + \nabla \cdot \mathbf{T}, \tag{3.2}$$

where ρ is the density, $\mathbf{u}$ is the velocity, Φ is the gravitational potential, p is the pressure, $\mathbf{B}$ is the magnetic field, and $\mathbf{T}$ is the viscous stress. The full viscous stress is given by

$$\mathbf{T} = \rho \nu \left[\nabla \mathbf{u} + (\nabla \mathbf{u})^{\mathrm{T}} - \frac{2}{3} (\nabla \cdot \mathbf{u}) \mathrm{I} \right], \tag{3.3}$$

where ν is the kinematic viscosity and I is the unit tensor of second rank. We neglect self-gravity and do not consider a thermal energy equation. For thermodynamic closure, we assume an isothermal relation such that

$$p = c_s^2 \rho. \tag{3.4}$$

We recall the full non-ideal MHD induction equation:

$$\frac{\partial \mathbf{B}}{\partial t} = \nabla \times \left(\mathbf{u} \times \mathbf{B} - \eta_O (\nabla \times \mathbf{B}) - \eta_H (\nabla \times \mathbf{B}) \times \mathbf{b} + \eta_A \left[(\nabla \times \mathbf{B}) \times \mathbf{b} \right] \times \mathbf{b} \right), \tag{3.5}$$

where $\mathbf{b} = \mathbf{B}/|\mathbf{B}|$, and η_O, η_H, η_A are the Ohmic, Hall and ambipolar diffusivities respectively. Ohmic and ambipolar diffusivities are always positive. The Hall coefficient, on the other hand, can have either sign, depending on whether the more massive charge carrier in the disc is positively ($\eta_H > 0$) or negatively ($\eta_H < 0$) charged. Ideal, Ohmic and/or ambipolar diffusive-only discs are insensitive to the polarity of alignment of the large scale field with the rotation of the disc. The Hall effect, on the other hand, does depend on the polarity of the magnetic field. Reversing the sign of $(\mathbf{B} \cdot \Omega\mathbf{x})$, where $\Omega\mathbf{x}$ is the angular velocity vector, has the same effect as reversing the sign of η_H on the equations. In this paper, we define the positive (negative) polarity case as when $\eta_H (\mathbf{B} \cdot \Omega\mathbf{x}) > (<)\ 0$.

We consider the problem in cylindrical polar coordinates (r, ϕ, z), and assume an axisymmetric potential $\Phi(r,z)$ that is symmetric about the midplane $z = 0$, given by

$$\Phi(r,z) = -\frac{GM}{\sqrt{r^2 + z^2}}. \tag{3.6}$$

The orbital angular velocity $\Omega(r)$ is then defined via

$$-r\Omega^2 = -\frac{\partial \Phi_{\rm m}}{\partial r}, \tag{3.7}$$

where

$$\Phi_{\rm m}(r) = -\frac{GM}{r} \tag{3.8}$$

is the midplane potential. We also define the residual velocity as

$$\mathbf{v} = \mathbf{u} - r\Omega\, \mathbf{e}_\phi, \tag{3.9}$$

which is the departure from Keplerian motion.

3.1.1 Asymptotic expansion

We perform an asymptotic expansion for the fluid variables, using an ordering scheme that is well understood for thin discs. The characteristic angular semi-thickness of the disc is given by the disc aspect ratio $H/r = \mathscr{O}(\varepsilon)$, where $0 < \varepsilon \ll 1$ is a small dimensionless parameter. The sound speed to orbital velocity ratio in an isothermal disc is then of $\mathscr{O}(\varepsilon)$.

For a magnetised disc, the ordering scheme of the magnetic field depends on the strength and orientation of the field (Ogilvie, 1997). We consider here a situation where the magnetic energy density is comparable to the thermal energy density, and set both the Alfvén speed and the adiabatic sound speed at $\mathscr{O}(\varepsilon)$ compared with the orbital velocity. For specific field configurations, such as vertical field dominance in the Guilet & Ogilvie model described in Chapter 6, we might set some of the asymptotic terms to zero for that particular situation. Instead of including a viscous stress, which is normally intended to represent a turbulent or eddy viscosity, we set the viscosity to zero to give us a laminar disc, as recent protoplanetary disc simulations have shown them to be.

We assume axisymmetry and so neglect all $\partial/\partial\phi$ terms. The internal structure of the thin disc and its slow evolution in time are resolved through rescaled spatial and time coordinates

$$\xi = \frac{r}{\varepsilon}, \qquad \zeta = \frac{z}{\varepsilon}, \qquad t_1 = \varepsilon t, \qquad t_2 = \varepsilon^2 t,$$

where ζ is a scaled vertical variable, t_1 is the flux evolution timescale and t_2 is the accretion timescale. To incorporate the multiscale nature of our approach, we separate the radial lengthscale into small variations of order H within a small radial region of the disc ($\xi \sim \mathscr{O}(1)$) and global radial variations of order r ($r \sim \mathscr{O}(1)$). Timescales are also separated into a fast dynamical timescale of order Ω^{-1} ($t \sim \mathscr{O}(1)$), an intermediate magnetic flux transport timescale ($t_1 \sim \mathscr{O}(1)$), and a slow accretion timescale ($t_2 \sim \mathscr{O}(1)$). The coordinate transformations are hence given by

$$\partial_r \mapsto \varepsilon^{-1}\partial_\xi + \partial_r, \qquad \partial_z \mapsto \varepsilon^{-1}\partial_\zeta,$$
$$\partial_t \mapsto \partial_t + \varepsilon\partial_{t_1} + \varepsilon^2\partial_{t_2},$$

where we have introduced the shorthand $\partial_r \equiv \partial/\partial r$, etc.

We then use the following expansion of fluid variables (each of the terms in the expansion is a function of $r, \xi, \zeta, t, t_1, t_2$):

$$\rho = \rho_0 + \varepsilon\rho_1 + \cdots, \tag{3.10}$$

$$p = \varepsilon^2 [p_0 + \varepsilon p_1 + \cdots], \tag{3.11}$$

$$\mathbf{v} = \varepsilon [\mathbf{v}_0 + \varepsilon \mathbf{v}_1 + \cdots], \tag{3.12}$$

$$\mathbf{B} = \varepsilon [\mathbf{B}_0 + \varepsilon \mathbf{B}_1 + \cdots], \tag{3.13}$$

$$\eta_O = \varepsilon^2[\eta_{O0} + \varepsilon\eta_{O1} + \cdots], \tag{3.14}$$

$$\eta_H = \varepsilon^2[\eta_{H0} + \varepsilon\eta_{H1} + \cdots], \tag{3.15}$$

$$\eta_A = \varepsilon^2[\eta_{A0} + \varepsilon\eta_{A1} + \cdots]. \tag{3.16}$$

We can see that $p/\rho \sim \mathscr{O}(\varepsilon^2)$, giving us $c_s \sim \mathscr{O}(\varepsilon)$ as we would expect. We consider departures from Keplerian motion comparable to the sound speed, and a similar order for the Alfvén speed, hence set both $\mathbf{v}$ and $\mathbf{B}$ to be of $\mathscr{O}(\varepsilon)$. Variations across the disc height due to diffusive effects are assumed to occur on the dynamical timescale, hence $\eta_{O,H,A} \sim \mathscr{O}(\varepsilon^2 r^2/t) \sim \mathscr{O}(\varepsilon^2)$. Finally, within the thin disc, the gravitational potential has the Taylor expansion

$$\Phi = \Phi_{\mathrm{m}}(r) + \varepsilon^2 \Psi(r) \frac{1}{2}\zeta^2 + O(\varepsilon^4), \tag{3.17}$$

where

$$\Psi = \Omega^2 \tag{3.18}$$

for the point-mass potential we have chosen.

At leading order ($\mathscr{O}(1)$ for mass conservation and $\mathscr{O}(\varepsilon)$ for the momentum equation), we recover the standard shearing box equations. The next order equations can be thought of as linear equations with source terms given by the solution of the leading order equations. We give the expansion of these equations at the first two leading orders below.

3.1.2 Mass and momentum equations

The mass and momentum equations, assuming axisymmetry, can be rewritten as:

$$\mathrm{D}\rho = -\rho\Delta, \tag{3.19}$$

$$\mathrm{D}u_r - \frac{u_\phi^2}{r} = -\partial_r\Phi - \frac{1}{\rho}\partial_r p + \frac{1}{\rho}\left(J_\phi B_z - J_z B_\phi\right), \tag{3.20}$$

$$\mathrm{D}u_\phi + \frac{u_r u_\phi}{r} = \frac{1}{\rho}\left(J_z B_r - J_r B_z\right), \tag{3.21}$$

$$\mathrm{D}u_z = -\partial_z\Phi - \frac{1}{\rho}\partial_z p + \frac{1}{\rho}\left(J_r B_\phi - J_\phi B_r\right), \tag{3.22}$$

where

$$\mathrm{D} = \partial_t + u_r\partial_r + u_z\partial_z, \tag{3.23}$$

$$\Delta = \frac{1}{r}\partial_r(ru_r) + \partial_z u_z, \tag{3.24}$$

and the current is given by

$$\mathbf{J} = \frac{1}{\mu_0}\nabla\times\mathbf{B}. \tag{3.25}$$

We introduce the following operators:

$$\mathrm{D} = \mathrm{D}_0 + \varepsilon\mathrm{D}_1 + \varepsilon^2\mathrm{D}_2 + \cdots, \tag{3.26}$$

with

$$\mathrm{D}_0 = \partial_t + v_{r0}\partial_\xi + v_{z0}\partial_\zeta, \tag{3.27}$$

$$\mathrm{D}_1 = \partial_{t_1} + v_{r1}\partial_\xi + v_{r0}\partial_r + v_{z1}\partial_\zeta, \tag{3.28}$$

$$\mathrm{D}_2 = \partial_{t_2} + v_{r2}\partial_\xi + v_{r1}\partial_r + v_{z2}\partial_\zeta. \tag{3.29}$$

Also

$$\Delta = \Delta_0 + \varepsilon\Delta_1 + \cdots, \tag{3.30}$$

with

$$\Delta_0 = \partial_\xi v_{r0} + \partial_\zeta v_{z0}, \tag{3.31}$$

$$\Delta_1 = \partial_\xi v_{r1} + \frac{1}{r}\partial_r(rv_{r0}) + \partial_\zeta v_{z1}. \tag{3.32}$$

Assuming the potential of Equation (3.8), the leading-order equations are then

$$\mathrm{D}_0\rho_0 = -\rho_0\Delta_0, \tag{3.33}$$

$$\mathrm{D}_0 v_{r0} - 2\Omega v_{\phi 0} = -\frac{1}{\rho_0}\partial_\xi p_0 + \frac{1}{\mu_0}\left[\left(\partial_\zeta B_{r0} - \partial_\xi B_{z0}\right)B_{z0} - B_{\phi 0}\partial_\xi B_{\phi 0}\right], \tag{3.34}$$

$$\mathrm{D}_0 v_{\phi 0} + \frac{1}{r}\partial_r(r^2\Omega)v_{r0} = \frac{1}{\mu_0}\left[\partial_\xi(B_{r0}B_{\phi 0}) + B_{z0}\partial_\zeta B_{\phi 0}\right], \tag{3.35}$$

$$\mathrm{D}_0 v_{z0} = -\Psi\zeta - \frac{1}{\rho_0}\partial_\zeta p_0 + \frac{1}{\mu_0}\left[\left(-\partial_\zeta B_{\phi 0}\right)B_{\phi 0} - \left(\partial_\zeta B_{r0} - \partial_\xi B_{z0}\right)B_{r0}\right], \tag{3.36}$$

At the next order, we have

$$\mathrm{D}_1\rho_0 + \mathrm{D}_0\rho_1 = -\rho_1\Delta_0 - \rho_0\Delta_1, \tag{3.37}$$

$$\begin{aligned}\mathrm{D}_1 v_{r0} + \mathrm{D}_0 v_{r1} - \frac{v_{\phi 0}^2}{r} - 2\Omega v_{\phi 1} \\ = -(\partial_r\Psi)\frac{1}{2}\zeta^2 + \frac{\rho_1}{\rho_0^2}\partial_\xi p_0 - \frac{1}{\rho_0}(\partial_r p_0 + \partial_\xi p_1) \\ + \frac{1}{\mu_0}\left(J_{\phi 1}B_{z0} - J_{z1}B_{\phi 0} + J_{\phi 0}B_{z1} - J_{z0}B_{\phi 1}\right),\end{aligned} \tag{3.38}$$

$$\begin{aligned}\mathrm{D}_1 v_{\phi 0} + \mathrm{D}_0 v_{\phi 1} + \frac{v_{r0}v_{\phi 0}}{r} + \frac{1}{r}\partial_r(r^2\Omega)v_{r1} \\ = \frac{1}{\mu_0}\left(J_{z1}B_{r0} - J_{r1}B_{z0} + J_{z0}B_{r1} - J_{r0}B_{z1}\right),\end{aligned} \tag{3.39}$$

$$\begin{aligned}\mathrm{D}_1 v_{z0} + \mathrm{D}_0 v_{z1} = \frac{\rho_1}{\rho_0^2}\partial_\zeta p_0 - \frac{1}{\rho_0}\partial_\zeta p_1 \\ + \frac{1}{\mu_0}\left(J_{r1}B_{\phi 0} - J_{\phi 1}B_{r0} + J_{r0}B_{\phi 1} - J_{\phi 0}B_{r1}\right),\end{aligned} \tag{3.40}$$

with

$$\mu_0 J_{r0} = -\partial_\zeta B_{\phi 0}, \tag{3.41}$$

$$\mu_0 J_{r1} = -\partial_\zeta B_{\phi 1}, \tag{3.42}$$

$$\mu_0 J_{\phi 0} = \partial_\zeta B_{r0} - \partial_\xi B_{z0}, \tag{3.43}$$

$$\mu_0 J_{\phi 1} = \partial_\zeta B_{r1} - \partial_\xi B_{z1} - \partial_r B_{z0}, \tag{3.44}$$

$$\mu_0 J_{z0} = \partial_\xi B_{\phi 0}, \tag{3.45}$$

$$\mu_0 J_{z1} = \partial_\xi B_{\phi 1} + \frac{1}{r}\partial_r(rB_{\phi 0}). \tag{3.46}$$

3.1.3 Induction equation

Again we assume axisymmetry throughout this analysis. The full induction equation is then given by

$$\begin{aligned}\frac{\partial \mathbf{B}}{\partial t} + (\mathbf{u}\cdot\nabla)\mathbf{B} = \ & (\mathbf{B}\cdot\nabla)\mathbf{u} - \mathbf{B}(\nabla\cdot\mathbf{u}) - \nabla\times[\eta_O\mathbf{J}] \\ & - \nabla\times[\eta_H\mathbf{J}\times\mathbf{b}] + \nabla\times\{\eta_A[\mathbf{J}\times\mathbf{b}]\times\mathbf{b}\},\end{aligned} \tag{3.47}$$

where $\mathbf{b} = \mathbf{B}/|\mathbf{B}|$, and η_O, η_H, η_A are the Ohmic, Hall and ambipolar diffusivities respectively.

We define

$$\mathbf{B}\cdot\nabla = \mathrm{M}_B = \mathrm{M}_{B0} + \varepsilon\mathrm{M}_{B1} + \varepsilon^2\mathrm{M}_{B2} + \cdots, \tag{3.48}$$

with

$$\mathrm{M}_{B0} = B_{r0}\partial_\xi + B_{z0}\partial_\zeta, \tag{3.49}$$

$$\mathrm{M}_{B1} = B_{r1}\partial_\xi + B_{r0}\partial_r + B_{z1}\partial_\zeta, \tag{3.50}$$

$$\mathrm{M}_{B2} = B_{r2}\partial_\xi + B_{r1}\partial_r + B_{z2}\partial_\zeta. \tag{3.51}$$

Note that this is of the same form as D with the exception of $\partial_t, \partial_{t_1}, \partial_{t_2}$ terms.

At zeroth order, all the terms cancel out. The first order equations are of order ε, and they are:

$$\mathrm{D}_0 B_{r0} = \mathrm{M}_{B0} v_{r0} - B_{r0}\Delta_0 \tag{3.52}$$

$$\mathrm{D}_0 B_{\phi 0} + \Omega B_{r0} = \mathrm{M}_{B0} v_{\phi 0} + B_{r0}\partial_r(r\Omega) - B_{\phi 0}\Delta_0 \tag{3.53}$$

$$\mathrm{D}_0 B_{z0} = \mathrm{M}_{B0} v_{z0} - B_{z0}\Delta_0 \tag{3.54}$$

The next order ε^2 equations are:

$$\begin{aligned}\mathrm{D}_0 B_{r1} + \mathrm{D}_1 B_{r0} - \frac{B_{\phi 0} v_{\phi 0}}{r} - \Omega B_{\phi 1} \\ = \mathrm{M}_{B0} v_{r1} + \mathrm{M}_{B1} v_{r0} - \frac{v_{\phi 0} B_{\phi 0}}{r} - B_{r1}\Delta_0 - B_{r0}\Delta_1\end{aligned} \tag{3.55}$$

$$\begin{aligned}\mathrm{D}_0 B_{\phi 1} + \mathrm{D}_1 B_{\phi 0} + \frac{B_{r0} v_{\phi 0}}{r} + \Omega B_{r1} \\ = \mathrm{M}_{B0} v_{\phi 1} + \mathrm{M}_{B1} v_{\phi 0} + \frac{v_{r0} B_{\phi 0}}{r} + B_{r1}\partial_r(r\Omega) - B_{\phi 1}\Delta_0 - B_{\phi 0}\Delta_1\end{aligned} \tag{3.56}$$

$$\mathrm{D}_0 B_{z1} + \mathrm{D}_1 B_{z0} = \mathrm{M}_{B0} v_{z1} + \mathrm{M}_{B1} v_{z0} - B_{z1}\Delta_0 - B_{z0}\Delta_1 \tag{3.57}$$

We also have the zero divergence condition

$$\nabla\cdot\mathbf{B} = 0, \tag{3.58}$$

which when written in cylindrical coordinates, gives:

$$\partial_z B_z = -\partial_r(rB_r). \tag{3.59}$$

The resulting relations in increasing order are therefore:

$$\partial_\zeta B_{z0} = -\partial_\xi B_{r0}, \tag{3.60}$$

$$\partial_\zeta B_{z1} = -\partial_\xi B_{r1} - \frac{1}{r}\partial_r(rB_{r0}). \tag{3.61}$$

3.2 Angular momentum and magnetic flux transport

Of particular interest to us are the leading terms for angular momentum and magnetic flux transport rates. We consider the case where there is no wind-driven accretion. Assuming that disc variables are periodic in ξ, we simplify the equations by averaging over the horizontal directions. We note that with no mass loss vertically through the disc, the surface density can only evolve because of radial mass fluxes, which are only possible because of angular momentum removal. The lowest order at which angular momentum flux through the disc allows an evolution of the surface density occurs at the classic viscous timescale t_2. Therefore, we proceed to average over the fast dynamical timescale t as well as the intermediate magnetic flux transport timescale t_1. The leading order angular momentum transport equation is then recovered by combining the $\mathscr{O}(\varepsilon)$ ϕ-component of the momentum equation with the $\mathscr{O}(\varepsilon^2)$ mass equation, and integrating over the vertical extent with a vertical boundary condition which forbids incoming or outgoing fluxes in ζ to give

$$\partial_{t_2}\Sigma_0 = \frac{1}{r}\partial_r\left\{\left[\partial_r(r^2\Omega)\right]^{-1}\left[\partial_r\left(r^2\left\{\langle\rho_0 v_{\phi 0}v_{r0}\rangle - \frac{1}{\mu_0}\langle B_{r0}B_{\phi 0}\rangle\right\}\right)\right]\right\}, \tag{3.62}$$

where $\langle\rangle$ from here onwards denote both the spatial and temporal averagings and the vertical integration mentioned, and Σ_0 is the first order disc surface density. We recover the well known 'diffusion equation' for an accretion disc, where mass transport is facilitated through 'viscous' stresses arising from a Reynolds component associated with internal motions ($\langle\rho_0 v_{\phi 0}v_{r0}\rangle$) and a Maxwell component associated with the horizontal magnetic field components ($-\langle B_{r0}B_{\phi 0}\rangle$).

The vertical flux evolution is calculated from the z component of the induction equation and using the condition $\nabla\cdot\mathbf{B}=0$:

$$\begin{aligned}\partial_{t_1}\langle B_{z0}\rangle + \frac{1}{r}\partial_r\Bigg(r\Bigg[&\langle v_{r0}B_{z0}\rangle - \langle v_{z0}B_{r0}\rangle + \left\langle \eta_{O0}\partial_\zeta B_{r0}\right\rangle \\ &+ \left\langle \eta_{H0}\frac{1}{B_0}\left\{B_{r0}\partial_\xi B_{\phi 0} + B_{z0}\partial_\zeta B_{\phi 0}\right\}\right\rangle \\ &+ \Bigg\langle \eta_{A0}\frac{1}{B_0^2}\Bigg\{B_{r0}B_{\phi 0}\partial_\zeta B_{\phi 0} + \left(B_{r0}^2 + B_{z0}^2\right)\left(\partial_\zeta B_{r0} - \partial_\xi B_{z0}\right) \\ &\quad + B_{\phi 0}B_{z0}\left(\partial_\xi B_{\phi 0}\right)\Bigg\}\Bigg\rangle\Bigg]\Bigg) = 0.\end{aligned} \tag{3.63}$$

The terms within the square brackets give us the vertical magnetic flux radial transport rate. The first term describes advection with the radial flow, while the second term comes from $\mathbf{B}$ being an advected solenoidal vector. Standard accretion disc models assume the large scale

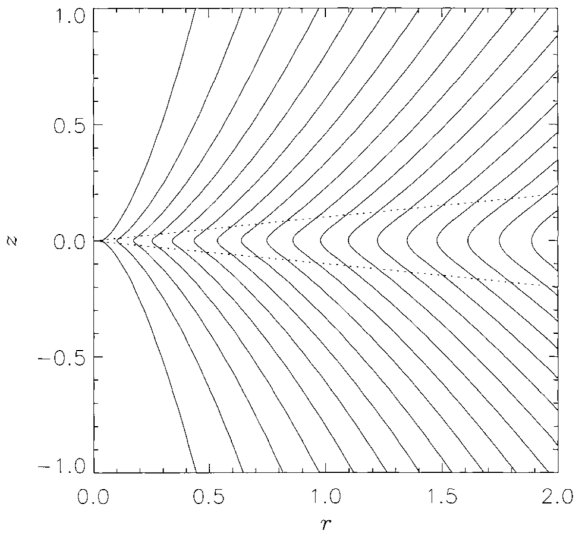

Fig. 3.1 General form of the open disc magnetic field geometry assumed in standard accretion disc models. Magnetic field lines are shown in the meridional plane, while the dotted lines indicate the surfaces of the disc. Figure taken from Ogilvie (1997).

magnetic field to have an open field geometry with the poloidal component bending outward from the star (Ogilvie, 1997) (see Figure 3.1). In this configuration (where we have assumed $B_z > 0$), flux transport comes from poloidal motion across the field lines, and drive radially inward accretion of the flux ($-\langle v_{z0} B_{r0} \rangle < 0$). For the Ohmic term, we expect $\langle \partial_\zeta B_{r0} \rangle > 0$ in the standard disc magnetic configuration. This means an overall effect of transporting the magnetic field radially outwards, in agreement with other studies of the effect of Ohmic resistivity in the presence of an inclined field (Guilet and Ogilvie, 2012).

The Hall and ambipolar terms are more complicated. We further simplify the problem by assuming that only large scale radial gradients and vertical variations are present (in other words we set $\partial_\xi = 0$). Then the Hall term,

$$\left\langle \eta_{H0} \left(\frac{B_{z0}}{B_0} \right) \partial_\zeta B_{\phi 0} \right\rangle, \tag{3.64}$$

depends on the vertical gradient of the azimuthal field. The sign of the Hall term, and consequently the direction of the flux transport induced by it, are also dependent on the sign of the Hall coefficient and the vertical magnetic field, reversing if one of them changes. Its effect is strongest when there is a strong vertical field threading the disc. From simulations (Bai and Stone, 2017; Béthune et al., 2017), typically $\partial_\zeta B_{\phi 0} < 0$ near the midplane and > 0 at the disc surface, hence we would expect the Hall flux transport to switch direction as we go up from the disc midplane. For $\eta_H (\mathbf{B}_z \cdot \boldsymbol{\Omega} \mathbf{x}) > (<) \, 0$, we expect this transport to be

radially inward (outward) near the midplane. This is indeed what is found in recent Hall global simulations (Bai and Stone, 2017).

The ambipolar term on the other hand has both an 'Ohm-like' and a 'Hall-like' component. The 'Ohm-like' component,

$$\left\langle \eta_{A0} \left(\frac{B_{r0}^2 + B_{z0}^2}{B_0^2} \right) \partial_\zeta B_{r0} \right\rangle, \tag{3.65}$$

is outwardly directed assuming the standard configuration, and is strongest and equivalent in form to Ohmic diffusion when **B** is purely poloidal. The 'Hall-like' component,

$$\left\langle \eta_{A0} \left(\frac{B_{r0} B_{\phi 0}}{B_0^2} \right) \partial_\zeta B_{\phi 0} \right\rangle, \tag{3.66}$$

depends on the correlation between the horizontal components of the magnetic field. Normally, we expect the sign of B_ϕ to be opposite to that of B_r because of Keplerian shear, and $B_{r0}B_{\phi 0} < 0$. Hence the 'Hall-like' ambipolar term would act in the opposite (same) direction as the Hall term for $\eta_H(\mathbf{B}_z \cdot \Omega\mathbf{x}) > (<)\ 0$.

It is worth noting that Section 2 (and Figure 1) of Bai and Stone (2017) also provides an analytic explanation on why the Hall term drives magnetic flux transport when a surface toroidal field accompanied by a wind is present, with Equation 9 of Bai and Stone (2017) essentially the same as our Equation (3.64). Although our analysis is more rigorous, the essence of the Hall-mediated magnetic flux transport is the same.

Part II

Magnetic flux transport in protoplanetary discs

Chapter 4

Introduction to the magnetic flux transport paradigm

As discussed in Chapter 2, the strength and geometry of a large-scale magnetic field threading the disc can drastically affect the operation of magnetic processes within it, such as the MRI and magnetic wind launching. So far, two possible origins for this large-scale magnetic field have been proposed: it is either created locally by a dynamo process (Brandenburg et al., 1995; Hawley et al., 1996), or it arises from the concentration of the flux that is intrinsic to the accreting gas (Lubow and Spruit, 1995; Spruit et al., 1995). It is yet unclear whether the former can generate a significant magnetic field coherent over a scale comparable to the radius (Spruit, 2010).

The latter case, where magnetic flux of the accreting gas is concentrated as it accumulates in the inner regions of the disc, has been subject to increasing study. Semi-analytic work such as carried out by Lovelace et al. (2009) and Guilet and Ogilvie (2012, 2013) studied the competing effects of inward accretion due to advection with an accreting flow, and outward diffusion due to a turbulent resistivity, in what is known as the 'advection-diffusion' paradigm. The disc is assumed to be turbulent due to processes like the MRI. This, as mentioned before in Section 1.4.1, leads to an effective viscosity, ν, which drives accretion of the material towards the star, also advecting magnetic flux radially inwards. However, the same turbulence also mixes up fluid parcels and their magnetic flux, driving reconnection processes on small scales. This leads to an effective resistivity, η, which allows the magnetic field to diffuse, and in the presence of an outwardly bending global poloidal field, results in an outward transport of flux. The turbulent viscosity and diffusivity are linked via the effective magnetic Prandtl number $\mathscr{P} \equiv \nu/\eta$. For MHD turbulence, $\mathscr{P}$ is expected to be of order unity (Fromang and Stone, 2009; Guan and Gammie, 2009; Lesur and Longaretti, 2009).

The first studies by van Ballegooijen (1989), Lubow et al. (1994), Heyvaerts et al. (1996) concluded that outward diffusion would significantly outweigh any accretion for thin discs with significant field bending. These subsequent studies, however, neglected the vertical structure of the disc, which, as subsequently pointed out (Guilet and Ogilvie, 2012; Ogilvie and Livio, 2001; Rothstein and Lovelace, 2008), has a significant impact on the averaging procedure used in the calculations. These studies examined the impact of disc structure using quasi-steady state radially local models, and found that for weak magnetic fields, the contribution of the accretion flow to the flux transport velocity is much larger than the mass transport velocity. This is due to larger radial velocities away from the mid-plane, which barely affect mass flow but do affect flux transport. Further work by Guilet and Ogilvie (2014); Okuzumi et al. (2014) and Takeuchi and Okuzumi (2014) applied the results from these local models to the global evolution of large-scale magnetic fields, and verified that an equilibrium is reached and that the maximum attainable field strength and a rough estimation of its associated Maxwell stress are compatible with the steady-state accretion rate observed in actual systems. Hence a possible solution to the too-efficient-diffusion problem of an inclined magnetic field is provided.

This flux transport paradigm, however, is more relevant to well ionised discs such as around black holes and compact stars, where turbulence can readily occur. Recent studies and global simulations have shown that protoplanetary discs are likely to be laminar in most parts, and therefore should not be modelled as turbulent (Bai and Stone, 2017; Béthune et al., 2017; Suriano et al., 2017, 2018). Current advection-diffusion models also do not account for the non-ideal effects of Hall drift and ambipolar diffusion, which are likely to be significant throughout much of the protoplanetary discs. Recently numerical simulations have begun examining the flux transport problem globally in the non-ideal MHD protoplanetary disc context (Bai and Stone, 2017) and in the ideal MHD weak field regime (Zhu and Stone, 2018). However, they still suffer from current computational limitations of evolving a disc for long enough to determine its long term global flux evolution (G. Lesur, priv. comm.). A new model addressing these concerns and including all three non-ideal MHD contributions is required for modelling the flux transport problem for the protoplanetary disc context, which is what we seek to address here.

In this Part, we investigate the flux transport problem in the protoplanetary disc context through 1D radially local semi-analytic models similar to that of Guilet and Ogilvie (2012), but where non-ideal effects also have a significant role in the flux evolution (Fromang, 2013). However, as many of the same principles can be applied to accreting discs in general, it is hoped that the framework could be extended to the study of stellar mass black hole accretion and AGN discs as well.

The structure of this Part is as follows. Chapter 5 discusses the shearing box equations vertical structure model, where we estimate flux transport rates due to an inclined B field or a magnetic torque at the disc surface. Chapter 6 extends the Guilet and Ogilvie (2012) model (hereafter GO model) to include all three non-ideal effects. It also examines the flux transport driven by large scale radial gradients, in addition to that by a surface inclined field or magnetic torque. The implications and limitations of our semi-analytic results are discussed there, along with directions for future study. Both Chapters 5 and 6 are restricted to cases where a magnetic wind is not explicitly present, and where the poloidal magnetic field inclination is set below the wind launching threshold (see Section 2.3.3). In Chapter 7, we extend our study of the flux transport problem to discs with winds using numerical simulations. We first confirm the steady state solutions of Chapter 5 by evolving discs with the same parameters and boundary conditions. We then explore regimes where the poloidal magnetic field inclination angle allows for magnetic wind launching and the presence of v_z is important, and sketch out an semi-analytic framework to help us interpret the results. Finally, we summarise and conclude our findings in Chapter 8.

Chapter 5

Flux transport model at the shearing box order

In our first investigation, we develop a semi-analytic radially local 1D vertical model that includes all non-ideal MHD effects for the flux transport problem. Our first model is essentially a local shearing box, where we solve the leading order equations, and assume variations only in the vertical direction. This assumption is motivated by global non-ideal MHD simulations such as those of Bai and Stone (2017), where quasi-steady states were achieved and the 1D vertical disc profiles were measured. The goal of our approach is to gain insight into the interpretation of their results.

We begin by examining the case with no magnetic wind present by restricting the range of field inclinations explored to below the wind launching threshold, but then mimic the presence of a vertical outflow by setting a non-zero azimuthal field, hence magnetic torque, at the boundary. In our model, flux transport is driven by the interplay between the bending of the poloidal field and the diffusivities present, as well as advection by the accretion flow driven by the applied magnetic torque. We also restrict ourselves to discs that have the traditional "hourglass" symmetry (see Sections 2.2.3 and 2.6) in its variables, allowing us to solve for only the upper half of the disc.

5.1 Method

5.1.1 Leading order equations

We use the thin disc approximation ($J_z = 0$, see Equation (5.4)), and consider a Keplerian rotating frame. We want to find the quasi-steady state equilibrium profiles, so the disc is set

to be steady on the dynamical timescale (i.e. $\partial_t = 0$). As before, we assume an isothermal and inviscid flow. For now, there is also no vertical outflow, so we set $v_z = 0$.

Without loss of generality, we use units such that $B_z, \Omega, c_s, \mu_0 = 1$, with B_z being a constant in this model. The vertical coordinate z is then in units of the isothermal scaleheight, $H = c_s/\Omega$, while diffusivities are given in units of $H^2\Omega$. The ratio of the Alfvén speed and the sound speed (a measure of the field strength) is then defined by our choice of the midplane ($z = 0$) density, $\rho(0)$:

$$c_s = 1 \implies v_a/c_s = v_a, \tag{5.1}$$

$$v_a = \frac{B}{\sqrt{\mu_0 \rho}} = \sqrt{\frac{B_x^2 + B_y^2 + 1}{\rho}}, \tag{5.2}$$

$$v_a(0) = \sqrt{\frac{1}{\rho(0)}}, \tag{5.3}$$

where Equation 5.3 comes from recognising that the field is vertical at the mid-plane in the hourglass symmetry. $\rho(0) \gg 1$ therefore corresponds to a weak magnetic field and $\rho(0) \ll 1$ to a strong one. When $\rho(0) = 1$, $v_a = c_s$ at the midplane. For an isothermal disc profile, $\rho(z)$ decreases as z increases, so we expect magnetic effects to become stronger compared to hydrodynamic effects as we move away from the midplane.

The local equations are identical to the shearing box equations, and correspond to the leading order equations of the multiscale asymptotic approach of Chapter 3. We consider only vertical variations, setting $\partial_x = 0$. To incorporate non-ideal effects, we use the modified electric field in the rest frame of the multi-component fluid ($\mathbf{E} + \mathbf{v} \times \mathbf{B}$), with $\mathbf{E}$ being the electric field in the shearing-box frame:

$$\mathbf{E} + \mathbf{v} \times \mathbf{B} = \eta_O \mathbf{J} + \eta_H \mathbf{J} \times \mathbf{b} - \eta_A (\mathbf{J} \times \mathbf{b}) \times \mathbf{b}, \tag{5.4}$$

where $\mathbf{J} = \nabla \times \mathbf{B}$ is the current density, $\mathbf{v}$ is the Keplerian-shear subtracted velocity, and the other variables are as before. This is another way of writing the modified induction equation, since $\partial_t \mathbf{B} = -\nabla \times \mathbf{E}$. In our scheme here, the positive (negative) polarity configuration for the Hall effect is achieved when $\eta_H > (<)\ 0$.

We then have the following governing equations:

$$-2\rho\Omega v_y = J_y B_z, \tag{5.5}$$

$$\frac{1}{2}\rho\Omega v_x = -J_x B_z, \tag{5.6}$$

$$0 = -\rho\Omega^2 z - \frac{\mathrm{d}p}{\mathrm{d}z} + J_x B_y - J_y B_x. \tag{5.7}$$

$$0 = \frac{\mathrm{d}E_y}{\mathrm{d}z}, \tag{5.8}$$

$$0 = -\frac{3}{2}\Omega B_x - \frac{\mathrm{d}E_x}{\mathrm{d}z}, \tag{5.9}$$

$$\frac{\mathrm{d}B_z}{\mathrm{d}z} = 0, \tag{5.10}$$

with currents given by

$$J_x = -\frac{\mathrm{d}B_y}{\mathrm{d}z}, \tag{5.11}$$

$$J_y = -\frac{\mathrm{d}B_x}{\mathrm{d}z}, \tag{5.12}$$

$$J_z = 0, \tag{5.13}$$

where x, y, z denotes the radial, azimuthal and vertical directions respectively, and we have removed the ordering subscripts. Equations (5.5) to (5.7) are the three components of the equation of motion, while the horizontal components of the induction equation are given by Equations (5.8) and (5.9). These terms on the RHS of Equations (5.5) and (5.6) indicate that the departure from Keplerian motion are driven by the Maxwell terms. We can also see that the density structure is determined by the effects of gravity, pressure balance, and magnetic compression, which are represented by the first, second and final pair of terms respectively of Equation (5.7).

5.1.2 Flux transport

The flux transport rate is given by the azimuthal electric field E_y, which is constrained to be a constant with varying disc height in our model. In Section 2.1.3 we saw that it measures the flux transport rate by examining the equation governing the evolution of the poloidal magnetic flux function $\Psi(r,z)$. Ψ, and equivalently B_z (see Equation (2.29)), evolves on the long accretion time-scale $\tau_a \equiv r/|v_r|$ as the poloidal field drifts radially through the disc, and we can define a radial flux transport rate to be given by

$$v_\Psi = E_y/B_z \tag{5.14}$$

(Guilet and Ogilvie, 2012; Königl et al., 2010; Ogilvie and Livio, 2001). E_y is found in our model as an eigenvalue of the solution, with $E_y > (<)\ 0$ implying a radially outward (inward) transport of flux.

5.1.3 Boundary conditions and numerical method

We use the standard assumption that the disc is antisymmetric about the midplane in B_x and B_y, and symmetric in v_x and v_y. Give that $B_z = 1$, the value of $B_x(z \to \infty)$ sets the inclination of the poloidal field, which is one of the parameters we vary. In a real disc, the inclination would be determined by the global magnetic field geometry. For the case where there is no wind, we expect no external magnetic torque to be acting on the disc, and set $B_y = 0$ as $z \to \infty$. In the case where we mimic the presence of a wind, we set B_y to be non-zero as $z \to \infty$, since there is now an external magnetic torque acting on the disc removing angular momentum vertically. For an actual outflow, we would expect $B_y(\infty) < 0$. The value of $\rho(0)$ is another parameter we vary and sets the field strength (from here on, we use the shorthand ρ_0 to denote the midplane density). In our units, ρ_0 is equivalent to $\beta_0/2$, where $\beta = p_{\text{thermal}}/p_{\text{magnetic}}$ is the plasma beta. A large value of ρ_0 would therefore indicate a weak midplane magnetic field.

We recast Equations (5.5)−(5.9) into a fourth order ordinary differential system with variables ρ, B_x, B_y and E_x by algebraically eliminating horizontal velocities through Equations (5.5) and (5.6) to obtain currents in terms of electric fields. The resulting equations are:

$$\rho' = c_s^{-2}[-\rho\Omega^2 z + J_x B_y - J_y B_x], \tag{5.15}$$

$$B_x' = \mu_0 J_y, \tag{5.16}$$

$$B_y' = -\mu_0 J_x, \tag{5.17}$$

$$E_x' = -\frac{3}{2}\Omega B_x, \tag{5.18}$$

where the prime denotes differentiation with respect to z. We define the diffusion constants as the following:

$$C_H = \frac{\eta_H}{|\mathbf{B}|}, \tag{5.19}$$

$$C_A = \frac{\eta_A}{|\mathbf{B}|^2}, \tag{5.20}$$

such that

$$\mathbf{E} + \mathbf{v} \times \mathbf{B} = C_O \mathbf{J} + C_H \mathbf{J} \times \mathbf{B} - C_A (\mathbf{J} \times \mathbf{B}) \times \mathbf{B}. \tag{5.21}$$

Then the currents are given by

$$\begin{pmatrix} J_x \\ \\ J_y \end{pmatrix} = \frac{1}{\rho^2 \det(\mathbf{R})} \begin{pmatrix} A_{11} & A_{12} \\ \\ A_{21} & A_{22} \end{pmatrix} \begin{pmatrix} E_x \\ \\ E_y \end{pmatrix}, \tag{5.22}$$

with

$$\begin{aligned} \rho^2 \det(\mathbf{R}) = {} & [C_O + C_A(B_z^2 + B_y^2)][C_O + C_A(B_z^2 + B_x^2)]\rho^2 \\ & + [(C_H B_z - C_A B_x B_y)\rho + (2\Omega)^{-1} B_z^2][(C_H B_z + C_A B_x B_y)\rho + 2\Omega^{-1} B_z^2], \end{aligned} \tag{5.23}$$

$$A_{11} = [C_O + C_A(B_z^2 + B_x^2)]\rho^2, \tag{5.24}$$

$$A_{12} = (-C_H B_z + C_A B_x B_y)\rho^2 - (2\Omega)^{-1}\rho B_z^2, \tag{5.25}$$

$$A_{21} = (C_H B_z + C_A B_x B_y)\rho^2 + 2\Omega^{-1}\rho B_z^2, \tag{5.26}$$

$$A_{22} = [C_O + C_A(B_z^2 + B_y^2)]\rho^2. \tag{5.27}$$

E_y now becomes an eigenvalue of the problem, and we solve Equations (5.15) to (5.18) using the shooting method. We integrate upwards from the midplane with values determined by the boundary conditions and guessed midplane values for E_x and E_y. The ODE system is integrated using a fourth-order Runge-Kutta method up to a sufficient height to mimic the solution as $z \to \infty$ (we set $z_{\text{end}} = 10H$ in our case, where H is the isothermal scale height. Extending z_{end} beyond this value is found to yield no significant variation in our results). There, boundary conditions at infinity are applied. This is followed by Newton-Raphson iterations to adjust the guessed solution until the variables converge to the desired upper boundary conditions.

5.1.4 Diffusivity profiles

We used two different diffusivity profiles in our calculations. The first profile, 'Uniform', assumes uniform η_O, η_H and η_A across all scale heights, and is useful for determining the general behaviour of the disc due to each diffusivity. The second scheme, 'CstIon', tries to capture PPD vertical diffusivity profiles more accurately by assuming only constant ionisation across the vertical extent, leading to $\eta_O = \text{constant}$, $\eta_H \propto B/\rho$ and $\eta_A \propto B^2/\rho^2$ (Balbus, 2011; Wardle, 2007). We also impose a rapid transition to the ideal MHD regime

above a certain scale-height for each diffusivity to model the effect of photoionisation of the disc surface from the star. Mathematically, this is given by:

$$\eta_O = \begin{cases} \eta_{O,0}, & z \leq z_{O,\mathrm{cut}} \\ \eta_{O,0} \exp\left(-\dfrac{\chi_O}{(z-z_{O,\mathrm{cut}})^2}\right), & z > z_{O,\mathrm{cut}} \end{cases} \tag{5.28}$$

$$\eta_H = \begin{cases} \eta_{H,0}\left(\dfrac{B}{\rho}\Big/\dfrac{B_0}{\rho_0}\right), & z \leq z_{H,\mathrm{cut}} \\ \eta_{H,0}\left(\dfrac{B}{\rho}\Big/\dfrac{B_0}{\rho_0}\right) \exp\left(-\dfrac{\chi_H}{(z-z_{H,\mathrm{cut}})^2}\right), & z > z_{H,\mathrm{cut}} \end{cases} \tag{5.29}$$

$$\eta_A = \begin{cases} \eta_{A,0}\left(\dfrac{B}{\rho}\Big/\dfrac{B_0}{\rho_0}\right)^2, & z \leq z_{A,\mathrm{cut}} \\ \eta_{A,0}\left(\dfrac{B}{\rho}\Big/\dfrac{B_0}{\rho_0}\right)^2 \exp\left(-\dfrac{\chi_A}{(z-z_{A,\mathrm{cut}})^2}\right), & z > z_{A,\mathrm{cut}} \end{cases} \tag{5.30}$$

where B_0 and ρ_0 are the vertical magnetic field strength and density respectively at the disc mid-plane. In all the plots that follow, the labelled values of η are true for the whole disc in the 'Uniform' case, whereas for the 'CstIon' case, they are the values of the midplane diffusivities $\eta_{O,0}$, $\eta_{H,0}$ and $\eta_{A,0}$. We also set

$$\begin{pmatrix} \chi_O & z_{O,\mathrm{cut}} \\ \chi_H & z_{H,\mathrm{cut}} \\ \chi_A & z_{A,\mathrm{cut}} \end{pmatrix} = \begin{pmatrix} 1 & 1 \\ 3 & 2 \\ 5 & 2 \end{pmatrix} \tag{5.31}$$

to reflect the regions above which we expect the different non-ideal effects to be reduced rapidly to zero. It is worth noting that even the 'CstIon' profile is only a rough mimicking of what diffusivity profiles in real discs are like, and a more thought-through prescription will be used in the later simulations of Chapter 11.

5.1.5 Marginal stability analysis

According to Ogilvie (1998), steady state solutions where field lines bend several times as they pass through the disc indicate their instability to the MRI in the ideal MHD regime. Although it yet remains to be rigorously proven, we follow Ogilvie and Livio (2001) and Guilet and Ogilvie (2012) in assuming that this to be true when non-ideal effects are included as well. The multiple bending corresponds to the "channel mode" of the MRI for a vertical field. The lowest order "$n = 1$" mode, which determines the overall marginal stability,

has opposite symmetry in the disc to the fluid variables. There, ΔB_x and ΔB_y, where Δ denotes a perturbation, would be symmetric about the midplane, while Δu_x and Δu_y would be antisymmetric. Hence we can compute the level of magnetisation (in our case given by $\rho_0 = \beta_0/2$) that leads to a marginally stable state to the MRI by solving for a set of linearised equations of small perturbations on top of the nonlinear equations, with the appropriate symmetry conditions.

This was done for a range of diffusivity coefficients using the shooting method described in Section 5.1.3. Midplane values of ΔB_y and ρ were guessed along with E_x and E_y as before (ΔE_x is calculated as an output, while ΔE_y is zero due to the symmetry of the perturbation). The mid-plane value of ΔB_x determines the amplitude of the marginal mode, and was arbitrarily set to 10. Boundary conditions for the unperturbed variables were the same as before. For the perturbed variables, mid-plane values are derived from the symmetry conditions ($\Delta u_x = \Delta u_y = 0$), while the upper boundaries are set to enforce the fixed inclination ($\Delta B_x = 0$) and magnetic torque ($\Delta B_y = 0$) conditions. Threshold field strengths are then computed, which mark the field strengths below which the disc would be unstable to the MRI, and where we would expect multiple bending in the vertical structure solutions.

5.2 Results

5.2.1 Disc vertical structure profiles

We found disc vertical structure profiles to be divided into stable and unstable solutions (see Figure 5.1, more profiles are also presented in Figures 7.2 and 7.3) when the field is aligned with the rotation. Weak field solutions with small non-ideal contributions show multiple bending of the poloidal field lines, indicating an unstable configuration due to the MRI or other instabilities (Ogilvie, 1998). Strong field solutions or those with large non-ideal contributions, on the other hand, share the same general shape with a single bend and are stabilised by the strong field and/or diffusive effects present. When the field is anti-aligned with the rotation and the Hall effect is present, almost all solutions have multiple bends, and the solver often failed to converge. This is interpreted as indicating that there are no stable solutions in the anti-aligned case with the Hall effect in our 1D equilibrium model.

Qualitatively, we find that the ‘Uniform’ and ‘CstIon’ diffusivity profiles give us similarly shaped vertical structures for the same set of midplane diffusivities. Differences lie in the magnitude of the horizontal **B** field, which may contrast by up to an order of magnitude (with those under ‘Uniform’ being larger than those under ‘CstIon’) due to the ‘CstIon’ profile allowing η_H and η_A to take significantly larger values away from the mid-plane as ρ

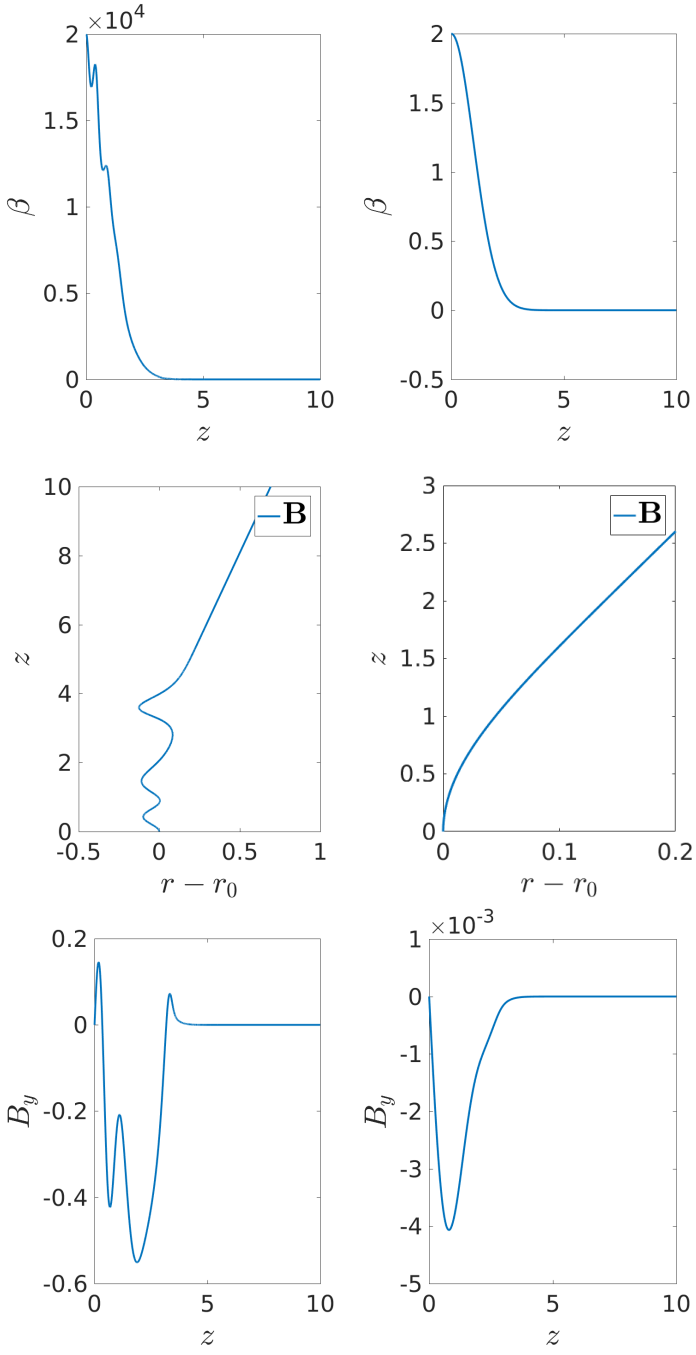

Fig. 5.1 Vertical profiles for weak field (left three) and strong field (right three) cases, $B_x(\infty) = 0.1$, with midplane diffusivities of $[\eta_O, \eta_H, \eta_A] = [0.01, 0.02, 0.002]$ & $[1, 2, 0.2]$ respectively. In our units, $B_z = 1$. The top and bottom panels of each triplet plot plasma $\beta = p/p_{mag}$ and B_y respectively, while the central panel plots the **B** field in the rz plane. In all these plots, the 'CstIon' diffusivity profile is used.

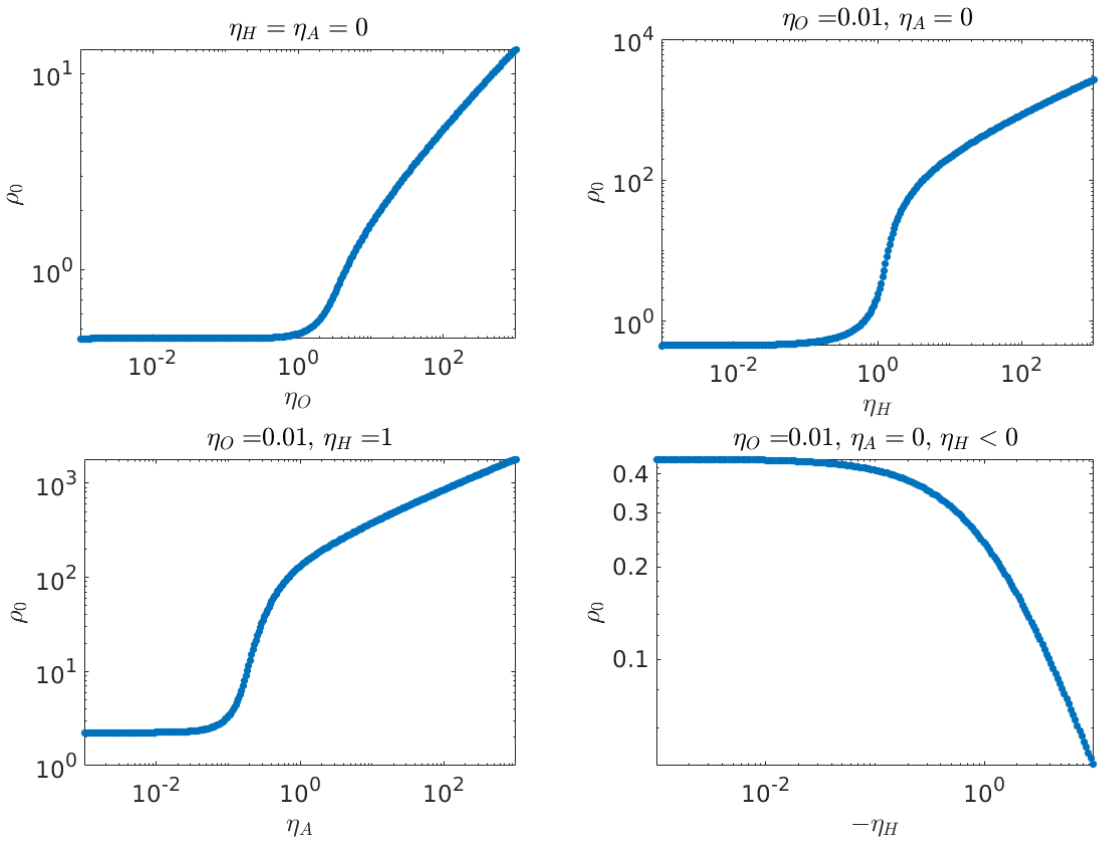

Fig. 5.2 Plots of threshold midplane densities against midplane values of the various non-ideal effects with fixed non-ideal backgrounds characterised by their midplane values. In all these plots, the 'CstIon' diffusivity profile is used, while the boundary conditions are $B_x(\infty) = 0.05$ and $B_y(\infty) = 0$.

decreases. Another difference is that the 'CstIon' solutions have less smooth features in their vertical profiles at $z \sim 3-4$, when the diffusivity profile rapidly drops off to the ideal MHD regime, than their 'Uniform' counterparts. However, overall, their trends in the stability of solutions and dependence on diffusivities and field strength are the same. In all the figures that follow, we plot the solutions for the more realistic 'CstIon' diffusivity profile.

5.2.2 Threshold magnetisation for marginal stability and variation with diffusive effects

We conducted the marginal stability analysis described in Section 5.1.5 to find the transition field strength between stable and unstable configurations. Some representative plots of our results are shown in Figure 5.2. As diffusive effects tend towards zero, the threshold mid-

plane ρ_0 for marginal stability tends towards the value of 0.4474, giving us a corresponding $\beta_0 \approx 0.89$. This agrees with the value found in other studies[1] for the largest value of B_z allowing the MRI to operate in the ideal MHD regime (Gammie and Balbus, 1994a; Paris and Ogilvie, 2018).

When $\eta_H > 0$ (positive polarity configuration), all three non-ideal effects help stabilise the disc - the threshold mid-plane ρ_0 increases (i.e. critical field strength decreases) with increasing strength of each non-ideal effect. On the other hand, for negative polarity (which in our case is when $\eta_H < 0$), increasing the magnitude of the Hall diffusivity decreases the threshold ρ_0 (critical field strength increases), showing that the Hall term has the effect of destabilising the disc[2].

Multiple branches are observed when we varied the strength of ambipolar diffusivity under certain backgrounds. These were also observed as we varied the initial guessed value of ρ_0. We interpret these branches to correspond to the excitation of different modes of instability, with higher modes giving multiple bends in the disc. Marginal stability should therefore be given by the branch with the lowest ρ_0 values giving us the lowest order mode, where only one bend occurs.

5.2.3 Flux transport rate and variation with diffusive effects

The variation of E_y with parameters was calculated by solving for a particular set of diffusivities, then iterating to either higher/ lower diffusivities using the previous solution. This procedure allows us to identify different branches (if any) of solutions, which occur when the disc is in an unstable configuration.

We studied most extensively the positive polarity case when $\eta_H > 0$. When $\eta_H < 0$ (negative polarity case), the solver failed to converge for the majority of cases. This may be indicative of the destabilising effect a negative polarity coupled with η_H has, as found by Balbus and Terquem (2001).

[1] In Paris and Ogilvie (2018), a value of $B_{z'} = 0.94$ is found, where $B_{z'} = B_z/\sqrt{\mu_0 \Sigma \Omega c_s}$ and $\Sigma = \int_\infty^\infty \rho \mathrm{d}z$. For an isothermal disc with small magnetic compression, $\rho(z)$ follows a Gaussian profile and $\rho_0/\Sigma = 1/\sqrt{2\pi}$, giving us $\beta = p/p_{\mathrm{mag}} \approx 0.894$.

[2] The "stability" here refers to the threshold magnetisation for marginal stability, or in terms of local analysis, to the critical wavenumber for instability. However, the Hall term also has the effect of enhancing the maximum growth rate for $\eta_H(\mathbf{B}_z \cdot \Omega\mathbf{x}) > 0$ (e.g., Figure 6 of Wardle and Salmeron (2012)), the phenomenon called the Hall-shear instability (Kunz, 2008). For this reason, some authors, e.g., Wardle and Salmeron (2012), describe the Hall effect for $\eta_H(\mathbf{B}_z \cdot \Omega\mathbf{x}) > 0$ as "destabilising", which is true for our disc model as well if the disc is already in the unstable regime, but irrelevant if our disc is in the regime stable to the MRI.

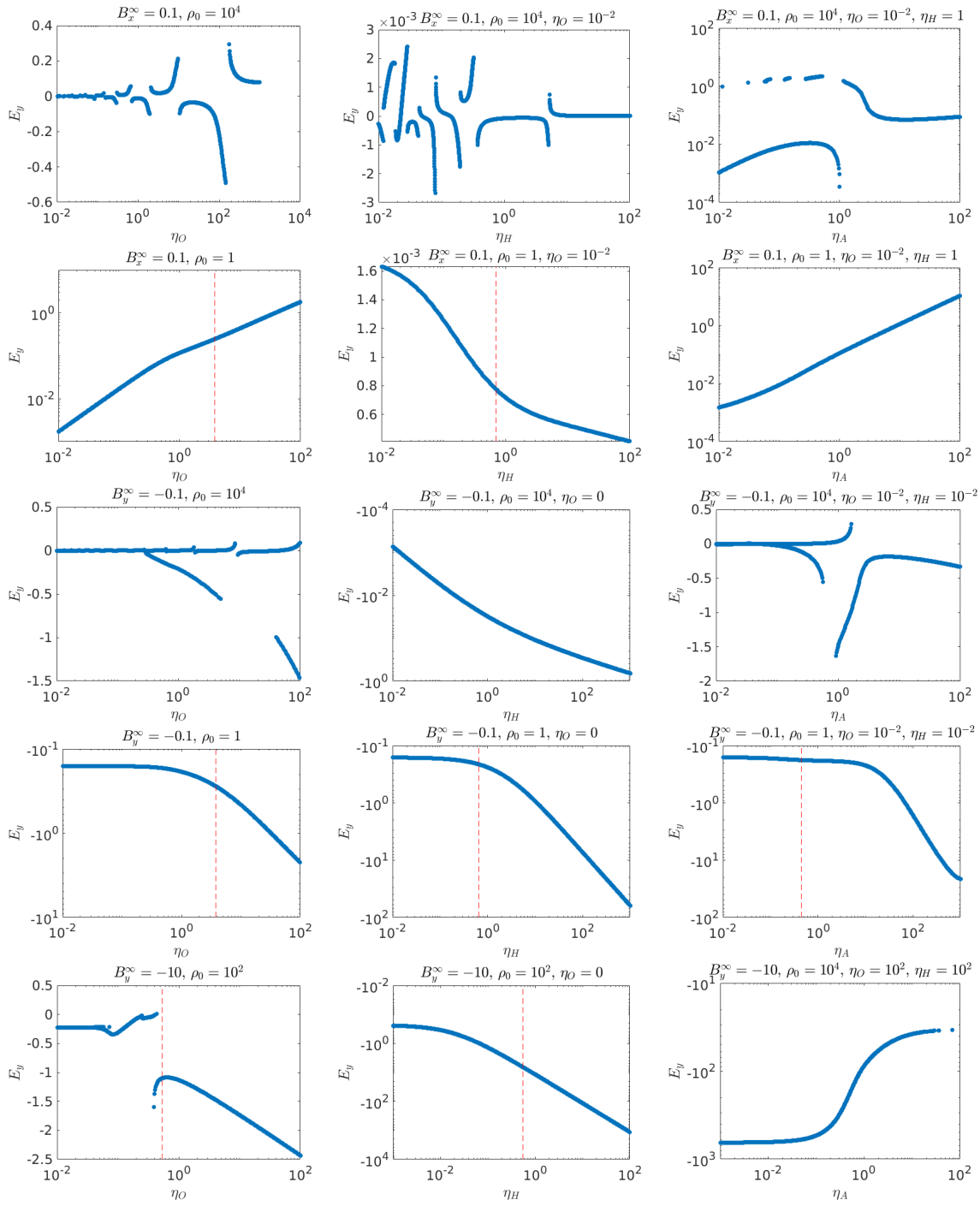

Fig. 5.3 E_y and its variation with midplane diffusivities. E_y gives the radial flux transport velocity in units of the sound speed c_s. The flux transport of the top two rows are inclination ($B_x(\infty)$) driven with $B_x(\infty) = 0.1$, while those of the bottom three rows are outflow ($B_y(\infty)$) driven, with $B_y(\infty) = -0.1$ for rows 3 and 4, and $B_y(\infty) = -10$ for row 5. Red vertical dashed lines mark the threshold diffusivity for marginal stability calculated using the model in Section 5.1.5. Rows 1 and 3 show the weak field case ($\rho_0 = 10,000$) while rows 2 and 4 plot the strong field case ($\rho_0 = 1$). Row 5 plots the case for an intermediate field strength ($\rho_0 = 100$) except the rightmost on which has a weak field ($\rho_0 = 10,000$). Background non-ideal effects are characterised by their mid-plane values. For rows 1 and 3, points of marginal stability are not plotted as they exist at higher diffusivity values than the range explored, whereas for the rightmost plots of both rows 2 and 5, the discs are already stable due to the background diffusivities. In all these plots, the 'CstIon' diffusivity profile is used.

Unstable solutions and bifurcations

In all cases, weak field solutions with low background non-ideal effects show multiple branches when the direction of iteration is varied, indicative of unstable configurations. From the marginal stability analysis, we expect the point of bifurcation at the largest value of the varied diffusivity to correspond to an equivalent point there, or at least occur at a lower diffusivity than the critical one calculated. Currently our study is not fully conclusive on this, as not all branches have been exhaustively identified using our method. However, we do find that all points of bifurcation occur at lower diffusivities than the critical points calculated. On the other hand, strong field solutions with large diffusivities appear to be stable, and solutions calculated by referencing in both directions agree.

Inclination driven flux transport

First, we explore the flux transport driven by inclination alone by setting the inclination through the value of $B_x(\infty)$. We eliminate the effect of outflow driven flux transport by setting $B_y(\infty)$ to zero.

In unstable configurations (top row of Figure 5.3), we find that the value of E_y flips between positive and negative, with asymptotes in the diffusivity space where $E_y \to \pm\infty$. This may be indicative of collective effects such as the presence of MRI channel modes.

In stable configurations (second row of Figure 5.3), both Ohmic resistivity and ambipolar diffusion result in significant roughly linear increases in E_y, and facilitate radially outward diffusion ($E_y > 0$) of the **B** field when $B_x(\infty) > 0$ (i.e. field bends outwards) as in Figure 5.1. This agrees with the prediction from our simple analysis in Section 3.2 for the Ohmic case. For the ambipolar case, we expect the variation of E_y with η_A to follow the same pattern as that with η_O as long as the 'Ohm-like' term in Equation (3.65) is significantly larger than the 'Hall-like' term in Equation (3.66). This condition is indeed met for the profiles considered, as both B_x and B_y throughout the disc are significantly smaller than 1, leading the disc to be largely dominated by the poloidal field component.

The Hall effect gives no flux transport ($E_y = 0$) when it is the only non-ideal effect present, but reduces the magnitude of E_y when Ohmic and/or ambipolar diffusion are present, tending to a limit as η_H becomes very large. When the Hall effect is the only non-ideal term present, $B_y = 0$ throughout the disc, and there is a solution with a purely poloidal field, so that the current and Hall drift are purely in the azimuthal direction.

Outflow driven flux transport

Next, we explore the flux transport driven by outflow alone through setting a non-zero negative value for $B_y(\infty)$. This provides a crude way of mimicking the effect of angular momentum lost vertically in an outflow. We eliminate the effect of inclination driven flux transport by setting $B_x(\infty)$ to zero.

Again, in the unstable configurations (third row of Figure 5.3), we find that the value of E_y flips between positive and negative, with asymptotes in the diffusivity space where $E_y \to \pm\infty$ indicative of collective effects such as the presence of MRI channel modes.

In stable configurations (bottom two rows of Figure 5.3), there is radially inward flux transport even when all diffusive effects disappear. This is due to flux being dragged in with the accreting gas as angular momentum is lost vertically through the disc. When $|B_y(\infty)| < 1$ (fourth row of Figure 5.3), both Ohmic resistivity and ambipolar diffusion lead to roughly linear but small increases in the magnitude of the flux transport, keeping the same radially inward direction. This is expected as the "Ohm-like" component of the ambipolar term would dominate since the disc field is largely poloidal in nature. The Hall effect, on the other hand, contributes significantly to radially inward flux transport when coupled with the outflow, with roughly linear increases between $|E_y|$ and η_H. When $|B_y(\infty)| > 1$ (bottom row of Figure 5.3), variations with Ohmic and Hall coefficients remain the same as before, but the trend with ambipolar diffusivity is reversed. Increasing the ambipolar effect now leads to a marked decrease in the inward flux transport, tending to a limiting value at high ambipolar diffusivities. This agrees with the picture described in Equation (3.5) when the "Hall-like" component (3.66) of the ambipolar term dominates because of the large poloidal field now present in the disc. This component operates in the opposite direction to the Hall effect in the aligned polarity configuration, hence leads to a dampening of the inward flux transport when present.

5.3 Analytic models

5.3.1 Incompressible limit - constant density profile

To help us understand and interpret the results, we examined solutions of the same set of equations in the incompressible limit for two density profiles: (i) a constant density profile with prescribed disc height, and (ii) a Gaussian density profile that takes into account the hydrostatic balance in the disc, but ignores the effect of magnetic compression. Here, we present the results of (i), which admit approximate analytic solutions, and how they inform the relations between flux transport, diffusive effects and inclination/outflow.

Approximate analytic solutions

We solve the same system of Equations (5.5)−(5.9) and set $\rho =$ constant. The permeability of free space, μ_0 is set to 1. We assume a Keplerian disc and set the orbital parameter $q = -\partial \ln \Omega / \partial \ln r$ to $3/2$. For simplicity and the possibility of admitting analytic solutions, we also assume that $\eta_O =$ constant, and constant ionisation fractions in the disc. This means $\tilde{\eta}_H, \tilde{\eta}_A =$ constant, where they are field-independent coefficients given by

$$\tilde{\eta}_H = \eta_H / |\mathbf{B}|, \tag{5.32}$$

$$\tilde{\eta}_A = \eta_A / |\mathbf{B}|^2. \tag{5.33}$$

This leads to the following form of the modified Ohm's law including the non-ideal effects:

$$E_x = -v_y B_z + \eta_O J_x + \tilde{\eta}_H J_y B_z + \tilde{\eta}_A [J_x B_z^2 + (J_x B_y - J_y B_x) B_y], \tag{5.34}$$

$$E_y = v_x B_z + \eta_O J_y - \tilde{\eta}_H J_x B_z + \tilde{\eta}_A [J_y B_z^2 - (J_x B_y - J_y B_x) B_x], \tag{5.35}$$

with

$$J_x = -\frac{\mathrm{d}B_y}{\mathrm{d}z}, \tag{5.36}$$

$$J_y = \frac{\mathrm{d}B_x}{\mathrm{d}z}. \tag{5.37}$$

The ODE system is linear in the Ohmic and Hall only cases, and can be reduced to give us the following wave equation:

$$\frac{\mathrm{d}^2 B_x}{\mathrm{d}z^2} + k^2 B_x = 0, \tag{5.38}$$

with k^2 given by

$$k^2 = \frac{3\Omega^2}{v_{az}^2} \left[1 + \frac{\eta_O^2 \Omega^2}{v_{az}^4} \left(\frac{1}{1 + \tilde{\eta}_H B_z \Omega / 2 v_{az}^2} \right) + \frac{2 \tilde{\eta}_H B_z \Omega}{v_{az}^2} \right]^{-1}, \tag{5.39}$$

where $v_{az} = B_z / \sqrt{\rho}$ is the vertical component of the Alfvén velocity.

If we expect the disc to satisfy the symmetry and boundary conditions described in Section 5.1.3, then the relevant solution is

$$B_x = B_x(\infty) \frac{\sin kz}{\sin kH}, \tag{5.40}$$

where the surfaces of the disc are at $z = \pm H$, and above and below the disc we have $B_x = \pm B_x(\infty)$ respectively.

The other variables can be deduced from B_x and the boundary conditions. If $B_y = \pm B_y(\infty)$ at the upper and lower boundaries (where $B_y(\infty)$ can be zero), we have

$$B_y = \frac{\Omega\eta_O}{2v_{az}^2}\left(\frac{1}{1+\Omega\tilde{\eta}_H B_z/2v_{az}^2}\right)B_x(\infty)\left(\frac{z}{H}-\frac{\sin kz}{\sin kH}\right)+B_y(\infty)\frac{z}{H}. \tag{5.41}$$

The ambipolar contribution, on the other hand, has both a linear and a nonlinear part. The linear part behaves as an additional Ohmic resistivity. The nonlinear part is of order $B^2_{\text{horizontal}}$, which is small if the surface value of $B_{\text{horizontal}}$ is also small. We limit our analysis here to the cases when $B_y(\infty) < 1$, and therefore only the "Ohm-like" component of the ambipolar term contributes significantly to the flux transport. The system can hence be roughly solved as the same set of linear equations with a modified Ohmic resistivity $\eta_{O,\text{mod}} = \eta_O + \tilde{\eta}_A B_z^2$ when ambipolar diffusion is also included.

Relation to Balbus and Terquem (2001)

Equation (5.39), which gives us the wavenumber of the field solution, is mathematically identical to the wavenumber formula (Equation (46)) of a marginally stable Ohm and Hall only MRI mode derived in Balbus and Terquem (2001). The problem they examined, however, is different from the one investigated here. They determined the local stability of a differentially rotating disc threaded by a weak vertical field and were looking at plane wave disturbances of the form $\exp(ikz - i\omega t)$. The Boussinesq limit was used as it corresponds to fluid displacements within a local approximation in z, rendering vertical structure unimportant. Our work, on the other hand, solves for the disc vertical structure, but deliberately makes the physically unrealistic uniform density approximation to simplify the equations. Our solution therefore must obey the boundary conditions determined by field inclination and symmetry criteria, which are not required in the problem examined by Balbus and Terquem (2001).

Marginal stability and variation with magnetisation and diffusivities

As in Section 5.1.5, we examine the case of a disc at marginal stability to the MRI. In our approximate analytic model, because the equations are already linear, we solve the same set of equations for the perturbed fluid variables. As before, these perturbations have opposite symmetry about the mid-plane to the fluid variables, which in our case means that $\delta B_x \propto \cos kz$. The boundary condition at $z \pm H$ is now $\delta B_x = 0$ and $\delta B_y = 0$, to meet the fixed inclination and outflow conditions. We expect the marginally stable mode to allow just one bend of the field through the disc, hence we require the corresponding critical wavenumber to satisfy $k_{\text{crit}}H = \pi/2$. The condition for marginal stability then becomes:

$$2q\Omega^2 = \frac{\pi^2 v_{az}^2}{4H^2}\left[1+\frac{\eta_O^2\Omega^2}{v_{az}^4}\left(\frac{1}{1+\tilde{\eta}_H B_z\Omega/2v_{az}^2}\right)+\frac{2\tilde{\eta}_H B_z\Omega}{v_{az}^2}\right]. \tag{5.42}$$

We can recast this in terms of a dimensionless magnetisation parameter:

$$\mu = \frac{B_z}{\sqrt{\Sigma H \Omega^2}}, \tag{5.43}$$

where $\Sigma = 2\rho H$ is the disc surface density, giving us

$$\frac{4q}{\pi^2} = \mu^2 + \left(\frac{\eta_O}{2H^2\Omega}\right)^2 \left(\frac{1}{1+\tilde{\eta}_H\sqrt{\rho}/2\sqrt{2}H\mu}\right)\frac{1}{\mu^2} + \frac{\sqrt{2\rho}\Omega}{\tilde{\eta}_H}\mu. \tag{5.44}$$

Magnetisations that give us a stable solution can be determined when the left hand side of Equation (5.44) is larger than the right hand side. We rearrange the terms in the equation to give us the following quartic, with the inequality giving us the condition for a stable solution as:

$$f(\mu) = \mu^4 + 5\mathscr{H}\mu^3 + (4\mathscr{H}^2 - \mathscr{Q})\mu^2 - \mathscr{Q}\mathscr{H}\mu + \mathscr{R}^2 \geq 0, \tag{5.45}$$

where we have defined the following dimensionless parameters:

$$\mathscr{R} = \frac{\eta_O}{2H^2\Omega}, \tag{5.46}$$

$$\mathscr{H} = \frac{\tilde{\eta}_H}{2H}\sqrt{\frac{\rho}{2}} = \frac{\tilde{\eta}_H}{2\sqrt{2}H}\frac{\sqrt{\rho}}{B_z} = \frac{\eta_H}{2\sqrt{2}H}\frac{1}{v_{az}}, \tag{5.47}$$

$$\mathscr{Q} = \frac{4q}{\pi^2}. \tag{5.48}$$

The shape of $f(\mu)$ vs. μ (see Figure 5.4) is determined by the Hall diffusivity only, while Ohmic diffusivity stabilises the entire profile by adding a constant term to $f(\mu)$. At high magnetisations, the disc is always stabilised whether the field is aligned with the rotation or not. In the intermediate region, a large Hall parameter extends the region for instability when the polarity is negative, but has a stabilising effect when the polarity is positive. This agrees with our previous result that the Hall effect is responsible for destabilising the disc in the anti-aligned case, while it is stabilising in the aligned case. In Appendix A, we explore in more detail the consequences of Hall drift and Ohmic resisitivity on an incompressible disc's stability, and identify the criteria for different regimes and their behaviour.

Flux transport

For flux transport, the constant density model gives us this simple relation:

$$\begin{aligned} E_y &= \left(\frac{2B_z^2}{\Omega\rho} + \tilde{\eta}_H B_z\right)\frac{\mathrm{d}B_y}{\mathrm{d}z} + \eta_O\frac{\mathrm{d}B_x}{\mathrm{d}z} \\ &= \frac{\eta_O}{H}B_x(\infty) + \left(\frac{2B_z^2}{\Omega\rho} + \eta_H\right)\frac{B_y(\infty)}{H}, \end{aligned} \tag{5.49}$$

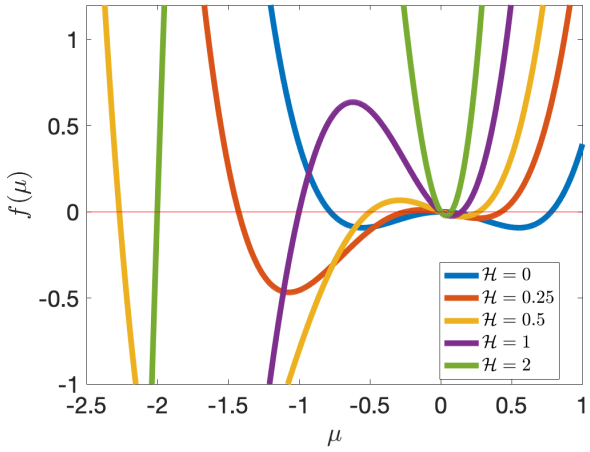

Fig. 5.4 Plot of $f(\mu)$ vs. μ for various Hall parameters $\mathscr{H}$, with $\mathscr{R} = 0$. The red line marks $f = 0$, the boundary between stable and unstable disc configurations. Solutions below the line are unstable, while solutions above the line are stable. Increasing $\mathscr{R}$ does not alter the shape of the plot but shifts f up by $\mathscr{R}^2$. As $\mathscr{H}$ increases, the unstable ($f < 0$) region expands when $\mu < 0$, while it contracts when $\mu > 0$. $f \to \infty$ as $\mu \to \pm\infty$ for all values of $\mathscr{H}$.

with the radial flux transport velocity given by E_y/B_z.

We can see that flux transport is directly proportional to the inclination and Ohmic diffusivity, which is also the case in the numerical solutions of the compressible model. When no diffusive effects are present, the relation suggests that the presence of an outflow would still drive inward flux accretion, with a large magnetisation (small ρ) giving the fastest rate. This is indeed what we observed in the compressible model, and can be interpreted to be a result of the loss of angular momentum driving inward gas accretion, which in turn advects the flux frozen into the gas along with it. A larger magnetisation would mean a higher degree of flux freezing, hence advection with the accretion flow.

The flux transport rate modification due to the Hall effect coupled with inclination is not explained here, but the constant density model predicts that the Hall effect coupled with a non-zero B_y at infinity would also lead to a non-zero flux transport. A positive η_H coupled with the negative B_y^+ expected for a wind would therefore lead to a negative E_y proportional to η_H and B_y^+, signifying a radially inward accretion of flux. This is indeed what we find in the solutions of Section 5.2.3. Such an effect has been noted before in passing in Hall-wind shearing box simulations (Bai, 2014) and also in the global simulations of Bai and Stone (2017). It is also noteworthy that the η_H term in our flux transport equation is essentially of the same form as Equation 10 of (Bai and Stone, 2017), although our analytic model is more rigorous and would therefore provide a more accurate estimate.

5.3.2 Incompressible limit - Gaussian density profile

For our second incompressible limit, we imposed a Gaussian density profile that takes into account the balance between pressure and gravity in an isothermal disc, but ignores the effect of magnetic compression from the horizontal field components. Solutions are calculated numerically using the same method as the compressible case, but with the density profile fixed. Comparing the solutions of this model to that of the compressible model allows us to determine whether magnetic compression has a significant effect on the flux transport observed.

The Gaussian density profile imposed is the following:

$$\rho = \rho_0 \exp\left(-z^2/2\right), \tag{5.50}$$

where ρ_0 is the mid-plane density value.

We found that solutions from the Gaussian incompressible model are very similar both in form and magnitude to those of the compressible model. Figure 5.5 plots a selection of E_y and its variation with mid-plane diffusivities for both compressible discs (top two rows) and incompressible Gaussian discs (bottom two rows) with the same diffusivity paramters between them under the 'Uniform' diffusivity scheme. The only significant differences arise where bifurcations in the E_y-diffusivity space occur in the compressible model. There, the Gaussian incompressible model yields vertical asymptotes on either side of the point of divergence instead. This can be explained by the fact that as the instability encounters a point of resonance, magnetic compression can provide the required change in density structure to dampen its effect, hence allowing the solution branches to diverge rather than tend towards a vertical asymptote. Therefore we can conclude that magnetic compression has no significant effect on the flux transport, in the parameter space we have explored.

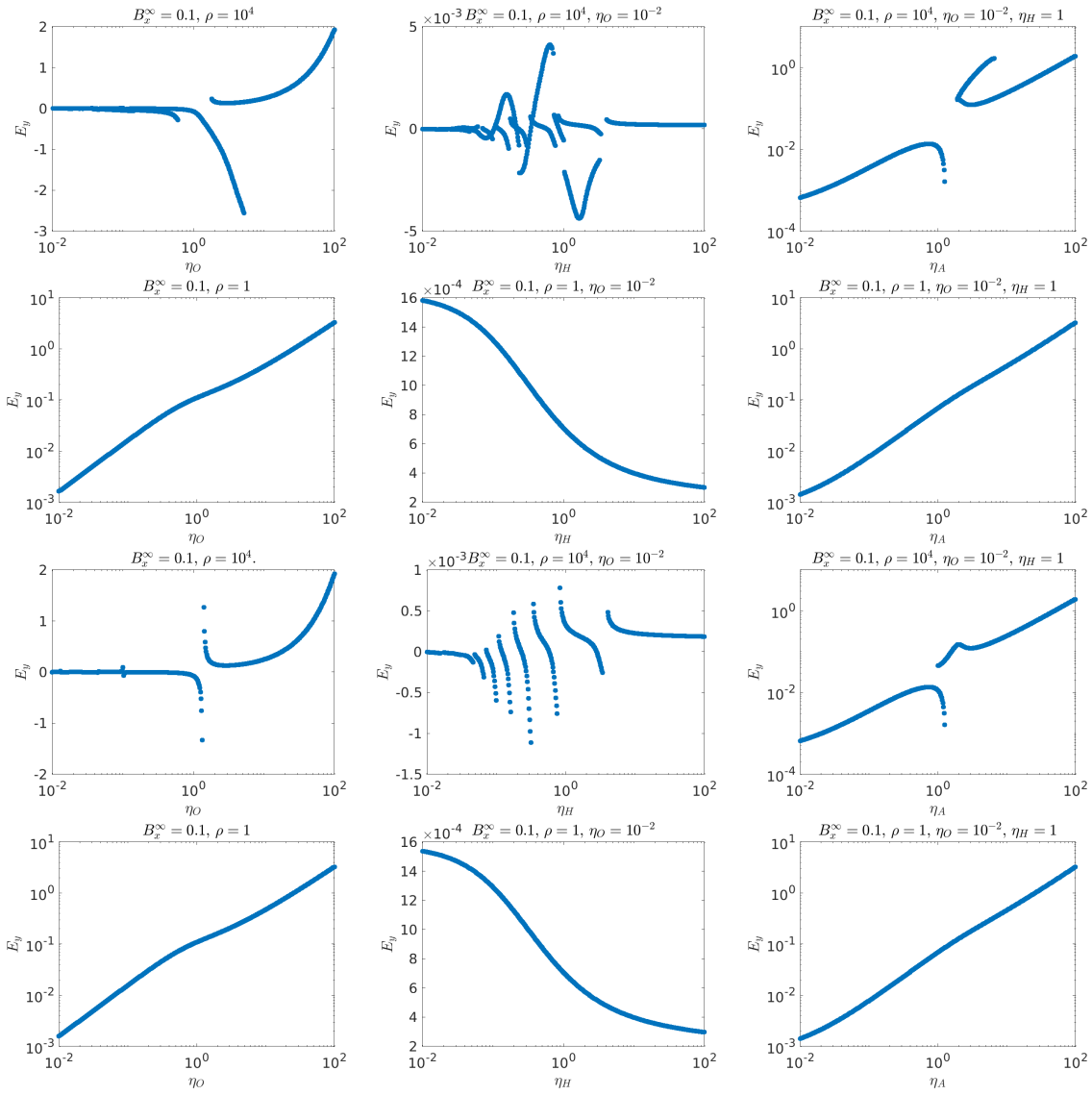

Fig. 5.5 E_y and its variation with midplane diffusivities. E_y gives the radial flux transport velocity in units of the sound speed c_s. The flux transport is inclination ($B_x(\infty)$) driven with $B_x(\infty) = 0.1$. The top two rows are for a compressible disc, while the bottom two rows are for the Gaussian incompressible case. Rows 1 and 3 show the weak field case ($\rho_0 = 10,000$), rows 2 and 4 plot the strong field case ($\rho_0 = 1$). Background non-ideal effects are characterised by their mid-plane values. In all these plots, the 'Uniform' diffusivity profile is used. To be compared with rows 1 and 2 of Figure 5.3.

Chapter 6

Flux transport model at Guilet & Ogilvie order

Our second semi-analytic model follows the scalings used in Guilet and Ogilvie (2012) (hereafter GO1). This scheme considers the case when the vertical field B_z dominates over B_r and B_ϕ by a factor of ε^{-1}. The motivation for this is to put the effects from large scale radial gradients (the ∂_r terms) on the same footing as inclination and outflow. Again, instead of using the residual velocity $\mathbf{v} = \mathbf{u} - r\Omega\hat{\mathbf{e}}_\phi$, we use the full velocity $\mathbf{u}$ (we do not relabel it as $\mathbf{v}$ here). Compared to the multiscale approach in Chapter 3, we make the following adjustments:

$$B_{r0}, B_{\phi 0}, B_{z1}, u_{r0}, u_{\phi 0}, u_{z0}, u_{z1} = 0, \tag{6.1}$$

The next order terms are assumed to be dominant, and the higher order terms are neglected. We extend the analysis of GO1 to derive the case for a laminar disc with all non-ideal diffusivities present.

6.1 Governing equations

6.1.1 Leading order equations

The leading order radial component of the equation of motion is

$$-\rho_0 r\Omega^2 = -\rho_0 \partial_r \Phi_m, \tag{6.2}$$

which describes the centrifugal force balance against the inward gravitational pull. For a Keplerian disc this gives us $\Omega_0 = (GM/r^3)^{1/2}$.

The vertical component of the equation of motion at leading order gives us the hydrostatic equilibrium between the vertical gravitational force and the vertical pressure gradient:

$$0 = -\rho_0 \Psi \zeta - \partial_\zeta p_0. \tag{6.3}$$

For an isothermal disc, we have the familiar solution

$$\rho_0 = \frac{\Sigma_0}{\sqrt{2\pi} H_0} \exp\left(-\frac{\zeta^2}{2H_0^2}\right), \tag{6.4}$$

where $H_0 = c_s/\Omega_0$ is the isothermal scaleheight and $\Sigma_0(r,\tau)$ is the surface density.

The horizontal components of the equation of motion and the induction equation come at the next order, due to the terms that we set to zero in Equation (6.1). They are identical to the equations in GO1 except for the addition of the Hall and ambipolar terms:

$$-2\rho_0\Omega_0 u_{\phi 1} = -\rho_0 \partial_r \Psi \frac{1}{2}\zeta^2 - \partial_r\left(p_0 + \frac{B_{z0}^2}{2\mu_0}\right) + \frac{B_{z0}}{\mu_0}\partial_\zeta B_{r1}, \tag{6.5}$$

$$\rho_0 u_{r1} \frac{1}{r}\partial_r(r^2\Omega_0) = \frac{B_{z0}}{\mu_0}\partial_\zeta B_{\phi 1}, \tag{6.6}$$

$$0 = B_{z0}\partial_\zeta u_{r1} + \partial_\zeta[(\eta_{O0} + \eta_{A0})\left(\partial_\zeta B_{r1} - \partial_r B_{z0}\right) + \eta_{H0}\partial_\zeta B_{\phi 1}], \tag{6.7}$$

$$0 = B_{z0}\partial_\zeta u_{\phi 1} + B_{r1} r \partial_r \Omega_0 + \partial_\zeta\left[(\eta_{O0} + \eta_{A0})\partial_\zeta B_{\phi 1} - \eta_{H0}\left(\partial_\zeta B_{r1} - \partial_r B_{z0}\right)\right]. \tag{6.8}$$

Under these scalings, we can see that Ohmic and ambipolar diffusivities have the same effect on the disc dynamics. The Hall term comes in at $\pi/2$ phase difference with the Ohmic and ambipolar terms in the induction equation. This reflects the nature of the Hall term being the magnetic field cross multiplied once with the Ohmic term, while the ambipolar term is crossed twice with the magnetic field, and has the $\pi/2$ phase difference applied twice from geometric rotation with respect to the Ohmic term, hence acts in the same direction at leading order.

This analysis yields four linear equations for the unknowns u_{r1}, $u_{\phi 1}$, B_{r1} and $B_{\phi 1}$. The linearity is a result of the assumption that we are examining the case of small deviations from orbital motion and a vertical magnetic field.

6.1.2 Non-dimensionalisation

We follow the same approach as GO1 in non-dimensionalising our equations. We used the following definitions:

$$\tilde{\rho} \equiv \frac{\rho_0 H}{\Sigma}, \tag{6.9}$$

$$u_r \equiv \frac{r}{H}\frac{v_{r1}}{c_s}, \tag{6.10}$$

$$u_\phi \equiv \frac{r}{H}\frac{v_{\phi 1}}{c_s}, \tag{6.11}$$

$$b_r \equiv \frac{r}{H}\frac{B_{r1}}{B_{z0}}, \tag{6.12}$$

$$b_\phi \equiv \frac{r}{H}\frac{B_{\phi 1}}{B_{z0}}. \tag{6.13}$$

A dimensionless vertical spatial coordinate is also defined as

$$\zeta \equiv z/H. \tag{6.14}$$

This ζ is different from the rescaled dimensional variable ζ defined earlier in Section 3.1.1. We can then define dimensionless laminar diffusivities:

$$\tilde{\eta}_O = \frac{\eta_{O,l}}{c_s H}, \tag{6.15}$$

$$\tilde{\eta}_H = \frac{\eta_H}{c_s H}, \tag{6.16}$$

$$\tilde{\eta}_A = \frac{\eta_A}{c_s H}. \tag{6.17}$$

We assume a point-mass potential and circular Keplerian orbital motion at leading order. An isothermal equation of state is also employed for simplicity.

The density profile in dimensionless form is

$$\tilde{\rho} = \frac{1}{\sqrt{2\pi}} \exp\left(-\zeta^2/2\right), \tag{6.18}$$

and the differential equations (6.5)−(6.8) are rewritten as

$$-2u_\phi - \frac{1}{\beta_0 \tilde{\rho}}\partial_\zeta b_r = \frac{3}{2} + D_H - D_{v\Sigma} + \left(\frac{3}{2} - D_H\right)\zeta^2 - \frac{D_B}{\beta_0 \tilde{\rho}}, \tag{6.19}$$

$$\frac{1}{2}u_r - \frac{1}{\beta_0 \tilde{\rho}}\partial_\zeta b_\phi = 0, \tag{6.20}$$

$$-\partial_\zeta\left(\left[\tilde{\eta}_O + \tilde{\eta}_A\right]\partial_\zeta b_r + \tilde{\eta}_H \partial_\zeta b_\phi\right) - \partial_\zeta u_r = -D_B \partial_\zeta\left(\tilde{\eta}_O + \tilde{\eta}_A\right), \tag{6.21}$$

$$-\partial_\zeta\left(-\tilde{\eta}_H \partial_\zeta b_r + \left[\tilde{\eta}_O + \tilde{\eta}_A\right]\partial_\zeta b_\phi\right) - \partial_\zeta u_\phi + \frac{3}{2}b_r = D_B \partial_\zeta \tilde{\eta}_H, \tag{6.22}$$

where

$$\beta_0 \equiv \frac{\mu_0}{B_z^2}\frac{\Sigma c_s^2}{H}, \tag{6.23}$$

$$D_H \equiv \frac{\partial \ln H}{\partial \ln r}, \tag{6.24}$$

$$D_{v\Sigma} = 2D_H - \frac{3}{2} + \frac{\partial \ln \Sigma}{\partial \ln r}, \tag{6.25}$$

$$D_B \equiv \frac{\partial \ln B_z}{\partial \ln r}. \tag{6.26}$$

A key thing to note here is that the LHS of Equations (6.19)-(6.22) forms the differential system, while the RHS are source terms that drive the advection and diffusion of flux. These equations are in many ways similar to those we obtained in Section 5.1.1. The first two terms on the LHS of Equation (6.19) correspond to the two terms in Equation (5.5), with the only difference being the addition of large scale radial gradient and Keplerian source terms on the RHS. Equation (6.20) is identical to Equation (5.6), while Equations (6.21) and (6.22) are linearised versions of Equations (5.8) and (5.9) respectively.

6.2 Set-up and method of solution

6.2.1 Boundary conditions

We use the same boundary conditions as determined in Section 3.2 of GO1, which come from analysing the same expected symmetry of the solutions as Section 5.1.3, with v_{r1} and $v_{\phi 1}$ being even functions of ζ, while B_{r1} and $B_{\phi 1}$ are odd. The following quantities can then be determined to vanish exponentially fast as $\zeta \to \pm\infty$:

$$\rho u_r \to 0, \tag{6.27}$$

$$\rho u_\phi \to 0, \tag{6.28}$$

$$b_r - (D_B\zeta \pm b_{rs}) \to 0, \tag{6.29}$$

$$b_\phi - (\pm b_{\phi s}) \to 0. \tag{6.30}$$

The symmetry of the solutions also constrain the following mid-plane ($\zeta = 0$) values to be the following:

$$\partial_\zeta u_r = 0, \tag{6.31}$$

$$\partial_\zeta u_\phi = 0, \tag{6.32}$$

$$b_r = 0, \tag{6.33}$$

$$b_\phi = 0. \tag{6.34}$$

A non-vanishing $b_{\phi s}$, the value of b_ϕ at $\zeta \to \infty$, is again included for mimicking the effect of angular momentum removal by a magnetic wind or magnetic braking due to interaction with an external medium. As noted in GO1, the boundary conditions are homogeneous, except for the linear source terms proportional to D_B, b_{rs} and $b_{\phi s}$ in Equations (6.29) and (6.30).

6.2.2 Form of the solution for a laminar inviscid disc

The linearity of the equations means that the general solution is a linear combination of the solution vectors corresponding to each source term, which appear either on the right hand side of equations (6.19)−(6.22), or as a non-vanishing boundary condition at infinity in the form of b_{rs} and $b_{\phi s}$. We can thus write the general solution $\mathbf{X} = \{u_r, u_\phi, b_r, b_\phi\}$ as:

$$\mathbf{X} = \mathbf{X}_{\rm K} + \mathbf{X}_{\rm DH} + \mathbf{X}_{\rm D\nu\Sigma} D_{\nu\Sigma} + \mathbf{X}_{\rm DB} D_{\rm B} + \mathbf{X}_{\rm brs} b_{rs} + \mathbf{X}_{\rm b\phi s} b_{\phi s}, \tag{6.35}$$

where $\mathbf{X}_{\rm DH}$ is the solution vector corresponding to the source term proportional to D_H and so on. $\mathbf{X}_K$ corresponds to the solution vector when $D_H, D_{\nu\Sigma}, D_B, b_{rs}, b_{\phi s} = 0$, where the source terms arise only from the radial derivatives of the leading order Keplerian, gravitational and geometric terms. Following GO1, we also define

$$\mathbf{X}_{\rm hyd} = \mathbf{X}_{\rm K} + \mathbf{X}_{\rm DH}, \tag{6.36}$$

as the solution with hydrodynamic ('Hydro') source terms $D_H = 1$ (corresponding to a disc with a constant aspect ratio H/r) and $D_{\nu\Sigma} = 0$ (for a steady accretion flow far from the inner boundary). Under these definitions, we have

$$\mathbf{X} = \mathbf{X}_{\rm hyd} + \mathbf{X}_{\rm D\nu\Sigma} D_{\nu\Sigma} + \mathbf{X}_{\rm DB} D_{\rm B} + \mathbf{X}_{\rm brs} b_{rs} + \mathbf{X}_{\rm b\phi s} b_{\phi s}. \tag{6.37}$$

The solution depends in a non-linear way only on the parameters β_0, η_O, η_H and η_A (we drop the ˜ in the text from this point onwards in this Chapter but refer to the non-dimensionalised diffusivities). Since we consider a laminar inviscid disc, we set α to zero, and can neglect the $\mathscr{P}$ dependence. η_O and η_A have the same effect at the order we are considering, so we only need to examine one of them, which we choose to be η_O. For each triplet of values of the three parameters β_0, η_O and η_H, one needs to compute the six solution vectors for each of the terms on the right hand side of Equation (6.35). The general solution is then given by a linear combination of these solution vectors with the appropriate coefficients.

6.2.3 Numerical method

To solve the system of ODEs, we employ the same pseudo-spectral method of GO1 using a decomposition on a basis of Whittaker cardinal functions (see Appendix C for a description of the method). These functions are well suited to problems on an infinite interval (Boyd, 2001; Latter et al., 2010). The use of Whittaker cardinal functions implicitly imposes the condition that the variables have to vanish exponentially fast at infinity. Following GO1, we replace b_r and b_ϕ with the following variables:

$$\tilde{b}_r \equiv b_r - D_B\zeta - b_{rs}\tanh(\zeta^3), \tag{6.38}$$

$$\tilde{b}_\phi \equiv b_\phi - b_{\phi s}\tanh(\zeta^3). \tag{6.39}$$

to satisfy this condition. We can then see that these new variables do vanish exponentially fast at infinity from the boundary conditions given in equations (6.29) and (6.30).

6.3 Flux transport for uniform diffusivities

Flux transport is again calculated by integrating the radial component of the induction equation:

$$u_\Psi = u_r + \tilde{\eta}_O(\partial_\zeta b_r - D_B) + \tilde{\eta}_H\partial_\zeta b_\phi = \text{constant}, \tag{6.40}$$

where

$$u_\Psi \equiv \frac{r}{H}\frac{v_\Psi}{c_s} \tag{6.41}$$

is the dimensionless magnetic flux transport velocity, same as the one defined in equation (5.14).

For simplicity, we used constant diffusivity profiles where η_O, η_H, η_A are each uniform in the vertical extent in our calculations. We present here only results from the positive polarity case of $\eta_H(\mathbf{B}_z \cdot \Omega\mathbf{x}) > 0$, as most solutions for the negative polarity case failed to converge, indicative of unstable configurations. Representative plots of the variation of u_Ψ with diffusivities can be found in Figure 6.1. For all our solutions, we isolate a particular source term and set its coefficient to 1. The case for $b_{\phi s} = 1$ corresponds to a torque that spins the disc up, leading to decretion rather than the normal accretion. To examine the case for $b_{\phi s} = -1$, which mimics the effect of a magnetic wind, we simply need to reverse the sign of u_Ψ when interpreting the plots.

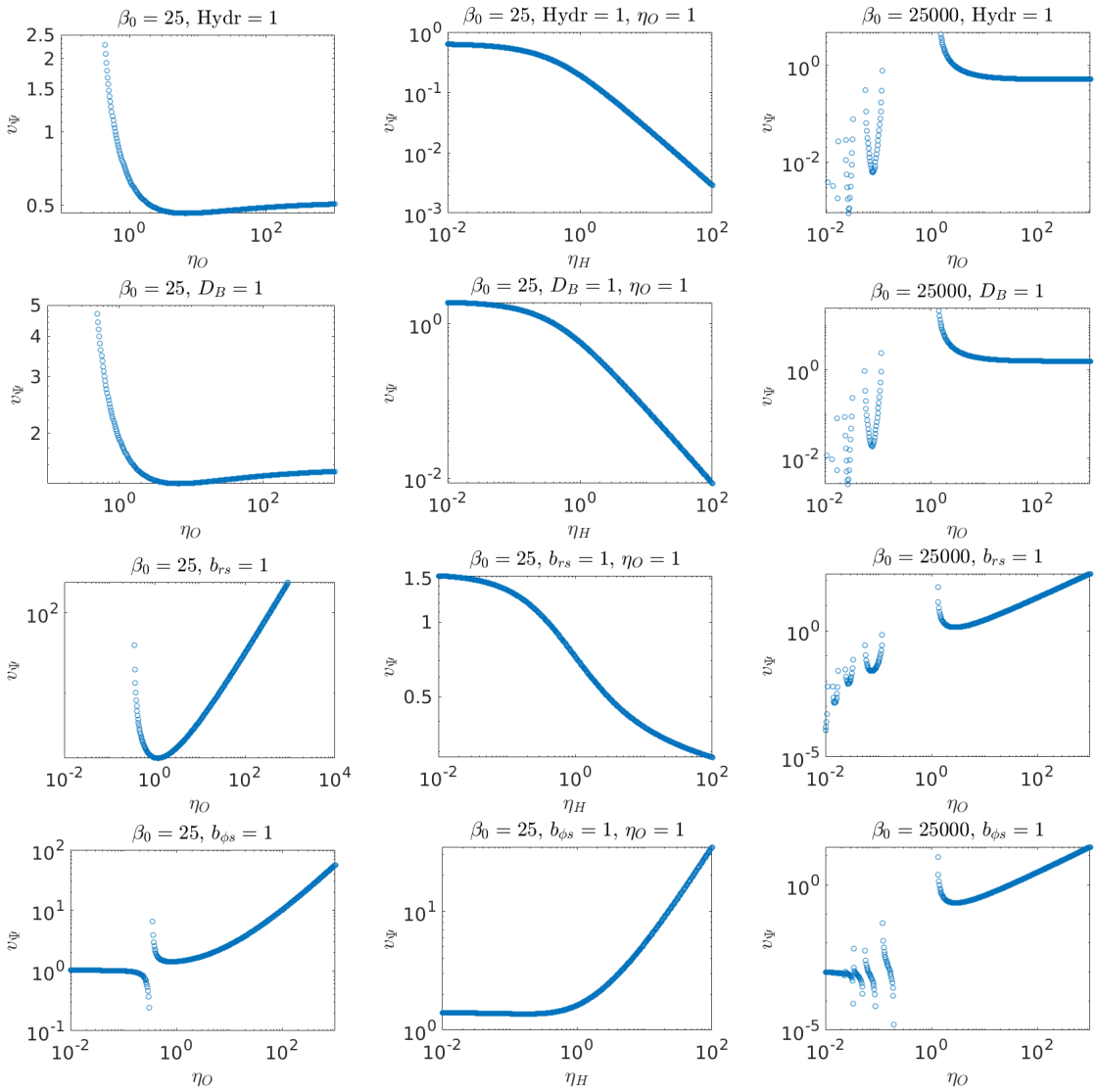

Fig. 6.1 Plots of u_Ψ (in the plots they are labelled as v_Ψ) variation with diffusivities. Each column corresponds to a specific mid-plane β_0, with $\beta_0 = 25, 25, 2.5 \cdot 10^4$ from left to right respectively. The first row shows the contribution due to the 'Hydro' source term, while the rows below show the contributions due to the D_B, b_{rs} and $b_{\phi s}$ source terms as we go down. Values where $u_\Psi < 0$ are not plotted due to the logarithmic scales used, but they exist in the unstable regions which are marked by the presence of multiple asymptotes.

6.3.1 Variation with Ohmic resistivity

Characteristic plots of the variation of u_Ψ with η_O are displayed in the left and right columns of Figure 6.1. We found that qualitatively, the 'Hydro' and D_B source terms share the same trend, while the b_{rs} and $b_{\phi s}$ source terms follow a different trend. As the mid-plane field strength is decreased (β_0 increased), solutions change from a single smooth curve, to multiple curves separated by asymptotes in η_O. The multiple curves signify the onset of instabilities, and this result is in agreement with the picture given by our model in Section 5, with instabilities setting in below a critical field strength. The same is observed for when η_O increases. Beyond a threshold diffusivity, the solution is stable and has only one branch.

In the stable configurations, both 'Hydro' and D_B source terms contribute to radially outward flux transport ($u_\Psi > 0$). Away from the asymptote, which appears to indicate a region of instability, the flux transport velocity increases fractionally ($< 10\%$) as η_O is increased.

On the other hand, for both b_{rs} and $b_{\phi s}$ source terms, an increase in η_O leads to a similar order of magnitude increase in u_Ψ, which is positive in the stable region. This confirms both the picture in our previous model (see Section 5.2.3) that a positive inclination of the poloidal field away from the star when coupled with diffusivity drives outward flux transport, and also that the rate at which it does so correspond to roughly linear increases. Remembering to reverse the sign for an actual wind, the results for $b_{\phi s}$ show us that a wind, coupled with resistivity, leads to an accretion of flux ($u_\Psi < 0$), again in agreement with our results from the shearing box model.

6.3.2 Variation with Hall diffusivity

When the Hall term was the only non-ideal MHD effect present, the solver did not converge. Analytically, we can determine that we would have iso-rotation and no flux transport. We therefore examined the cases where a background Ohmic resistivity was also present.

The variation of u_Ψ with η_H is found to share the same trend between the 'Hydro', D_B and b_{rs} source terms, while those for the $b_{\phi s}$ source term follow a different trend. Again, as the mid-plane field strength is decreased, solutions go from a single smooth curve, to multiple curves separated by asymptotes in η_H. The same is observed for when η_H increases. Beyond a threshold diffusivity, the solution is stable and only has one branch.

In the stable configurations, 'Hydro', D_B and b_{rs} source terms contribute to a radially outward flux transport ($u_\Psi > 0$). Away from the final asymptote that marks the region of instability, the flux transport velocity decreases to zero as η_H is increased. This is similar to the picture in our previous shearing box model that indicates a decrease in the inclination

driven flux transport rate with an increase in the Hall coefficient, with the only difference being that the nonlinear Hall term in our previous model leads only to a minor correction of the flux transport rate, whereas the linearised Hall term here reduces it to zero. On the other hand, for the $b_{\phi s}$ source term, an increase in η_H leads to a similar order of magnitude increase in u_Ψ. u_Ψ is positive in the stable region. Therefore for $b_{\phi s} = -1$, mimicking the effect of a magnetic wind, increasing the Hall contribution leads to a significant accretion of flux ($u_\Psi < 0$), which is again in agreement with our results from the shearing box model.

6.4 Analytic models

To help us interpret the trends in flux transport, we developed three approximate analytic models following the same procedure as Section 4.1 and Appendix A of GO1. Full mathematical details of how these three models were calculated can be found in Appendix D, but here we give a brief qualitative description of the procedure and assumptions used to derive these models.

We split the disc into two regions: a passive field region with weak (passive) magnetic field ($\beta \gg 1$) around the mid-plane where hydrodynamic effects dominate over magnetic effects; then further up the disc, we have a region with strong magnetic field ($\beta \ll 1$) where magnetic effects are dominant and the field is approximately force-free. The transition point between the regions is where the magnetic pressure is equal to the thermal pressure, and is given by:

$$\zeta_B = \sqrt{\ln\left(\frac{2}{\pi}\beta_0^2\right)}. \tag{6.42}$$

We can see from this that the lower the field strength, the larger the value of ζ_B, and the better the approximation of the mid-plane region as under a 'passive' field.

The models are constructed by first calculating the general forms of the approximate analytic profiles in each of the two regions, constrained by the given mid-plane and disc surface ($\zeta \to \infty$) boundary conditions. We assume that the Lorentz force is negligible in the passive field region hence ignore the effect of the magnetic field in the velocity profile there. In the force-free region, nothing can compensate the Lorentz force, and the fluid is frozen into the magnetic field lines, with iso-rotation being enforced as in the ideal MHD case. The two regions are then connected across the transition region, which is assumed to be infinitesimally thin about ζ_B. When connecting the regions, we assumed continuity of the magnetic field components across the transition, and integrated the horizontal components of the induction equation over the transition region to find the appropriate boundary conditions.

The first two of the models represent different diffusivity regimes: the first assumes only the presence of a constant Ohmic diffusivity, while the second addresses the situation when the disc is dominated by Hall drift but with a small Ohmic contribution. Our third model improves on the first model by using better boundary conditions that more appropriately address the presence of the intermediate transition region, and is derived using the description outlined in Appendix A of GO1.

6.4.1 Source terms and disc vertical profiles

Figures 6.2 and 6.3 show the vertical structure profiles in the case of a disc with only Ohmic diffusion and a Hall dominated disc with small Ohmic contribution respectively. The red lines are from the simple two-zone models that use the boundary condition of continuous magnetic fields, while the purple lines in the Ohm only case are from the improved two-zone model that take into account the intermediate region, and modifies the jump condition in the magnetic fields at the transition point. They both provide good qualitative descriptions of the solution, with the improved model matching very well to the actual numerical solution.

By analysing the mathematical forms of the analytic solutions (see Appendix D), we can deduce how the various source terms affect the shape of the disc vertical profile in the different variables. The radial magnetic gradient D_B provides the background gradient in ζ for the profile of b_r, while b_{rs} sets the limit of $b_r(\infty)$ when D_B is absent, defining the surface inclination of the poloidal field. Similarly, $b_{\phi s}$ sets the value of $b_\phi(\infty)$, and hence the magnetic torque acting on the disc. Ohmic resistivity causes bends to occur in the passive field region for the b_ϕ profile, while the Hall drift, which operates at $\pi/2$ phase to Ohmic diffusion, causes the bends to happen in b_r instead. u_r tends towards the flux transport value as $\zeta \to \infty$, but is largely zero in the passive field region. u_ϕ is similarly very small in the disc, but increases drastically in the force-free region as a result of iso-rotation with the magnetic fields.

6.4.2 Flux transport rates

Here, we analyse only the flux transport driven by inclination and outflow, while we leave those due to large scale radial gradients to a future investigation. Analytically, we find that the flux transport is given by these simple expressions:

$$u_\Psi = \eta_O \frac{b_{rs}}{\zeta_B} \tag{6.43}$$

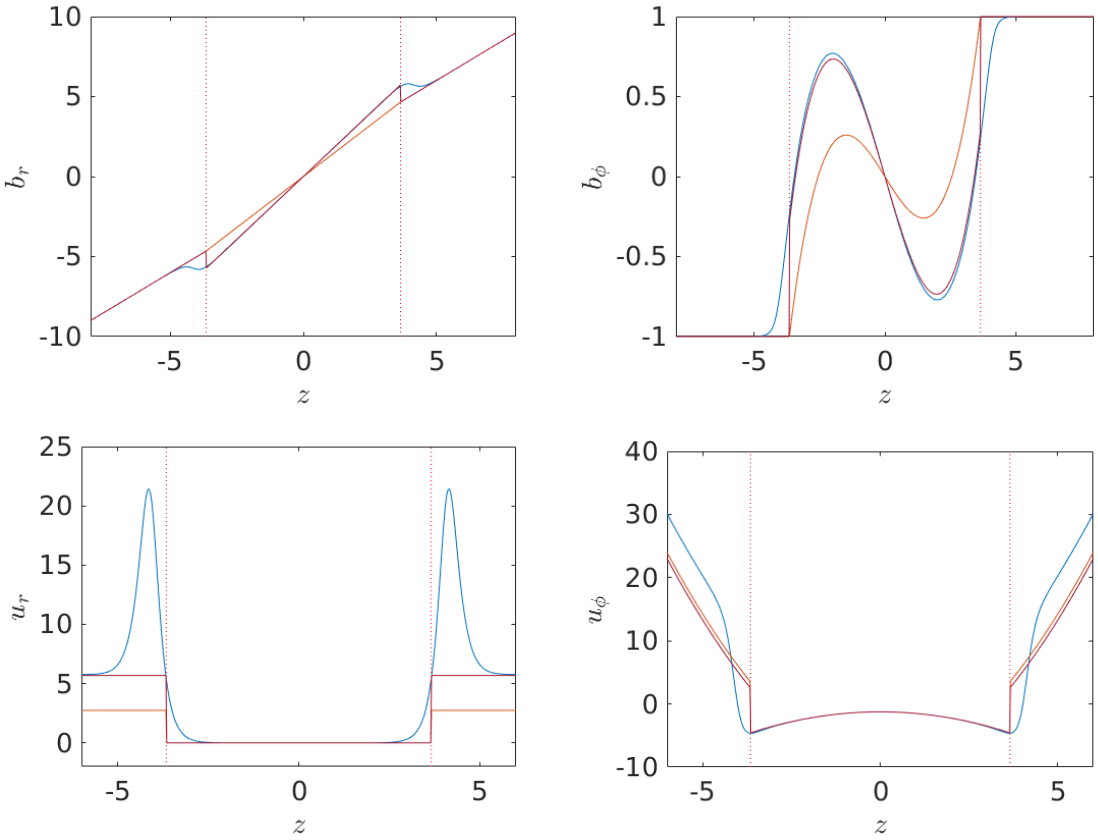

Fig. 6.2 Vertical structure profiles of the radial (left-hand panels) and azimuthal (right-hand panels) magnetic field (top panels) and velocity (bottom panels) for the Ohm only case with $\eta_O = 10$ and $\beta_0 = 1000$. We used the 'Hydro' source terms, and also set b_{rs}, $b_{\phi s}$ and D_B to 1. Red lines correspond to the simple two-zone analytic model (see Appendix D.1), while purple lines include improved boundary conditions accounting for the transition region (see Appendix D.3). The vertical dotted lines mark the height ζ_B where the transition between passive and force-free field regions take place.

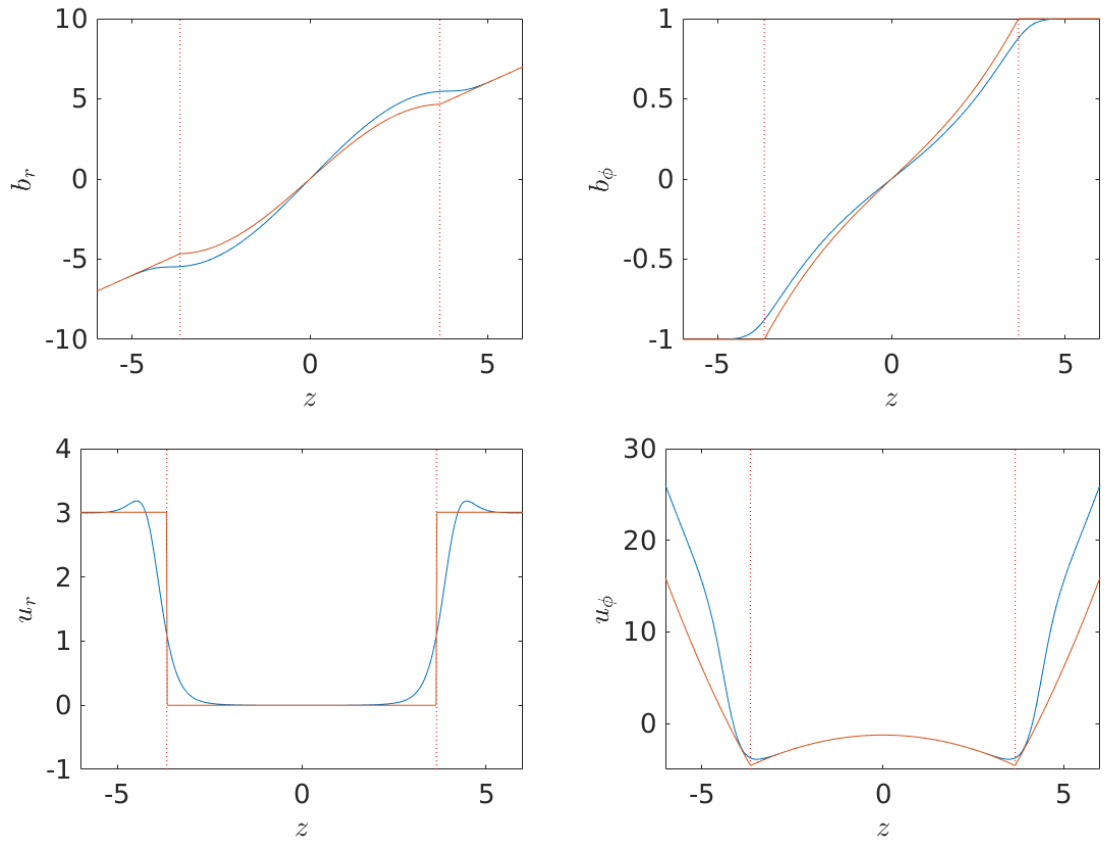

Fig. 6.3 Same as Figure 6.2 but for the Hall dominated case with $\eta_O = 1$, $\eta_H = 10$. Red lines correspond to the two-zone analytic model (see Appendix D.2).

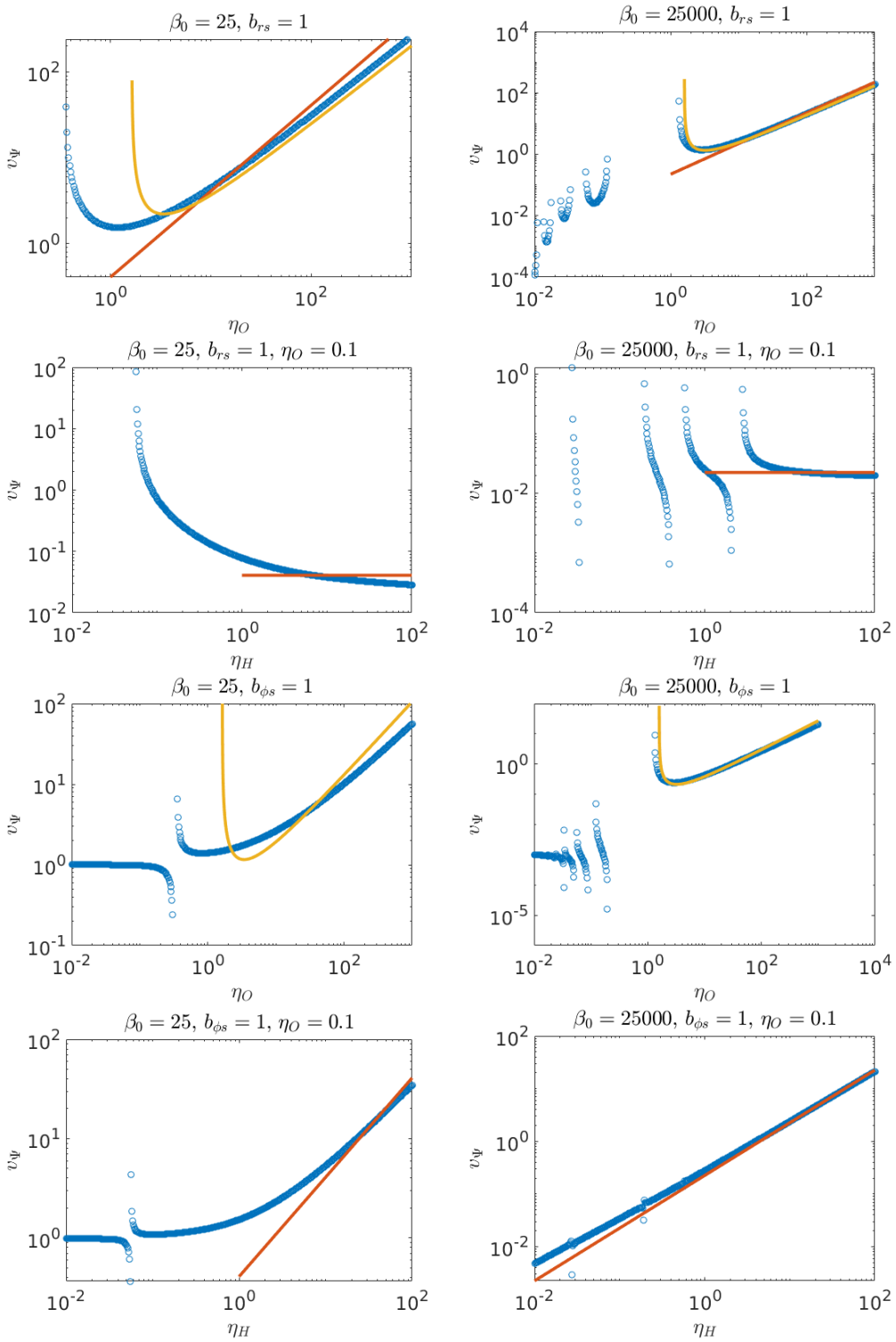

Fig. 6.4 Plots of radial flux transport rates given by u_Ψ and their variation with Ohmic (first and third rows) and Hall (second and fourth rows) diffusivities, coupled with $b_{rs} = 1$ (top two rows) and $b_{\phi s} = 1$ (bottom two rows) source terms, at strong ($\beta_0 = 25$, left hand column) and weak ($\beta_0 = 25000$, right hand column) magnetisations. Red lines correspond to the two-zone analytic models for Ohm only (first row) and Hall dominated (second and fourth rows) cases, while orange lines include improved boundary conditions accounting for the transition region (first and third rows).

for the Ohm only case,

$$u_\Psi = \eta_H \frac{b_{\phi s}}{\zeta_B} + \eta_O \frac{b_{rs}}{\zeta_B} \tag{6.44}$$

for the Hall dominated case, and

$$u_\Psi = \frac{\eta_O}{\zeta_B \left(1 - \dfrac{\pi}{2\eta_O}\right) - \dfrac{1}{\zeta_B} \ln\left(\dfrac{2}{\eta_O}\right)} \left(b_{rs} + \frac{\pi b_{\phi s}}{\zeta_B^2}\right) \tag{6.45}$$

for the Ohm only case with improved boundary conditions accounting for the transition region.

These expressions do not involve the radial advection velocity in the ideal MHD limit like second term in Equation (5.49) because of the separation of the disc into two zones, with the flux transport value determined by the expression in the passive field region where the only non-diffusive contribution, u_r, is approximated to be zero. In the absence of any diffusivity, it can be easily shown (see Appendix D.4) that the original equations admit an analytic solution with uniform u_r throughout the disc, and the flux transport is simply due to advection via the wind torque, with $u_\Psi = u_r = 4b_{\phi s}/\beta_0$. Hence our simple two-zone analytic models should only be used in the high diffusivity regime, as is common in protoplanetary discs.

As in the uniform density shearing box model (see Section 5.3.1), we find Ohmic diffusivity to be linked with inclination, and Hall diffusivity with outflow, in driving flux transport. Again, it is worth noting that the η_H term in Equation (6.44) is essentially of the same form as Equation 10 of (Bai and Stone, 2017). In the modified analytic model where jump conditions in the magnetic fields are calculated by taking the transition region into account, we have a modified flux transport rate which also couples Ohmic resistivity with outflow.

Figure 6.4 shows how these analytic predictions fit the actual flux transport rates calculated. We first look at the inclination cases which are the top two rows of the figure. Here the red lines are from the simple two zone models, while the orange lines in the Ohm only cases are from the third model that includes the modified boundary conditions. We see that the analytic models offer good descriptions in the limit of weak field (β_0 large) and high diffusivity. This is because under these conditions, the passive field region is extended and better matched by the assumptions used in the analytic model. Particularly, the asymptotes of the modified analytic model appears to be able to predict the transition point to instability, which occurs when the denominator of Equation (6.45) is equal to zero. It would be worth investigating in the future how the region of instability is influenced by the balance between diffusive effects (from η_O) and the field strength (from ζ_B).

Next, we turn to the outflow cases, which are displayed in the bottom two rows of Figure 6.4. The orange lines in the top two Ohm only plots are from the modified analytic model, while the red lines in the bottom two Hall dominated panels are from the simple analytic model. We can see that again they predict the outflow driven flux transport fairly well in the high diffusivity, weak field (β_0 large) regime. The simple two zone models are unable to describe the presence of the asymptote and transition to the unstable regime, but the model with modified boundary condition matches the first asymptote in the Ohm-only case in the weak field limit.

The relative success of the analytic models so far (though with limitations, such as in the outflow case) in matching the numerical solutions suggest that it is also possible to understand the flux transport driven by other source terms similarly, and we will be looking at constructing these models and examining their interpretations in the future.

6.5 Discussion

6.5.1 Comparing the shearing box and Guilet & Ogilvie models

Both the shearing box and the GO models share the same qualitative trends of how diffusivities, coupled with inclination and outflow, can be effective in driving flux transport. In particular, approximate analytic solutions for both models under simplified schemes show how Ohmic resistivity (and the 'Ohm-like' term of ambipolar diffusivity) is coupled with inclination to drive radially outward flux transport, while Hall drift with $\eta_H(\mathbf{B}_z \cdot \Omega\mathbf{x}) > 0$ is coupled with outflow in facilitating radially inward flux transport. The similarity between the expressions in Equations (5.49), (6.43) and (6.44) suggest that we can identify ζ_B, the height at which magnetic pressure equals thermal pressure, as the relevant value for the disc height H to be used in the constant density shearing box model of Section 5.3.1. Both models also show similar trends and behaviour in how the stability of solutions vary with diffusivity and magnetisation values. The large similarities between the results of the two models may be due to the fact that horizontal magnetic field components are largely relatively small compared with the vertical field for the parameter space explored, hence the effects due to the nonlinearity of the Hall and ambipolar terms are less significant overall.

6.5.2 Comparison with current global simulations

While outward inclination coupled with Ohmic resistivity has long been known to facilitate outward flux transport, the possibility of Hall drift coupled with an outflow driving significant flux transport has only been briefly noted (Bai, 2014) in the past, and never extensively

investigated. Only recently have global simulations (Bai and Stone, 2017; Béthune et al., 2017; Suriano et al., 2017, 2018) begun exploring the flux transport problem in laminar protoplanetary discs where all three non-ideal effects are accounted for. In Bai and Stone (2017), the mechanism governing flux evolution can be described as a competition between the Hall effect, ambipolar diffusion, and the magnetic wind driven accretion. In the positive (negative) polarity configuration, the Hall effect transports flux (out)inwards rapidly in the mid-plane regions and (in)outwards slowly in the disc upper layers. Ambipolar diffusion, on the other hand, always transports flux outward, whereas magnetic wind driven accretion advects flux inwards. In the aligned case, there is a cancellation effect between the inward flux transport due to Hall drift and the magnetic wind and outward due to ambipolar diffusion, while all three effects work to transport flux outward in the negative polarity case. Our calculations also found a similar picture in that Hall drift reduces the effect of outward flux transport due to ambipolar/Ohmic diffusion in the positive polarity case. However, it is unclear from the results of Bai and Stone (2017) whether there is any specific coupling between Hall drift and the wind that further enhances flux transport inwards. Our models also agree with Béthune et al. (2017) and Bai and Stone (2017) that the polarity of the magnetic field is a significant parameter on disc dynamics and flux transport when Hall drift is present. However, we are not able to confirm the flux transport trends in the negative polarity cases due to the breakdown of stable solutions in our models. Our model restricts the overall flux transport rate in a radially local region to be constant across all scale-heights, which is indeed what is found in global simulations (Bai, 2017; Bai and Stone, 2017).

A significant proportion of the parameter space explored yielded unstable solutions characteristic of MRI channel modes, and it would be interesting to see in future studies if they might relate to flux transport mechanisms reported in global simulations that are cyclic in nature, such as those in Suriano et al. (2017, 2018, 2019).

Chapter 7

Effect of disc wind on flux transport rates

The work up to this point has been concerned with flux transport in discs where the inclination of the poloidal magnetic field to the vertical is small, and insufficient for modelling the launching of a magnetic wind. In this chapter, we use the PLUTO code to extend our analysis to solutions where the inclination is large, a magnetic wind is naturally launched, and v_z can no longer neglected. We first verify the validity of our flux transport calculations and accompanying simplifications in Chapter 5 by performing shearing box simulations with identical parameters. We then investigate the effect of a non-zero v_z and wind launching in the extended parameter space on the flux transport dependence on non-ideal effects uncovered in the last two chapters. Finally, we sketch out an analytic framework to help us interpret some of the results, before summarising.

7.1 The PLUTO numerical code

We introduce the PLUTO numerical code (Mignone et al., 2007), which is a widely-used and well-documented compressible finite-volume MHD code. It is built on modern Godunov-type shock-capturing schemes, which solves the relevant fluid equations by integrating a system of conservation laws. The code is built as a multiphysics, multialgorithm modular environment, allowing for the incorporation of additional physical effects with advances in computational fluid dynamics. It also comes with an in-built standard shearing box module (Balbus and Hawley, 2003; Hawley et al., 1995; Regev and Umurhan, 2008), which we use for computing our radially local solutions.

In this Thesis, we use a modified version of PLUTO 4.0, developed by Geoffroy Lesur, where Hall drift and ambipolar diffusion are included (Lesur et al., 2014), in addition to the Ohmic resistivity module which is part of the standard release of the code. The implementation in PLUTO of ambipolar diffusion, and Hall drift in particular, is a difficult task. This is due to the non-hyperbolic nature of the terms in the induction equation, while the Godunov scheme is designed for solving hyperbolic conservation laws. The numerical implementation of the Hall effect is quite involved, and we refer the reader to Appendix A of Lesur et al. (2014) for details of the approximations used. The ambipolar module on the other hand is included as a source term in a similar way to the Ohmic resistivity module, with shearing sheet boundary conditions applied to the current density to prevent the occurrence of spurious instabilities from the radial boundaries. We tested the validity of the Hall and ambipolar modules by comparing the numerical growth rate and shape of MRI modes with their predicted semi-analytic values (see Section 7.2), as well as confirming the steady state solutions of the semi-analytic approach of Chapter 5 (see Section 7.3).

7.2 Comparing MRI modes between PLUTO and the semi-analytic model

First, we verify the numerical implementation of Hall drift and ambipolar diffusion in PLUTO by computing 1D MRI linear modes in a vertically stratified disc. These are tested by conducting four simulations with uniform η_A and η_H profiles in the vertical extent initialised at their predicted MRI modes, which were found along with their predicted growth rates by a pseudospectral method solving for the full set of linearised equations (see Appendix E for details). Their growth rates and mode shapes are then observed over the course of the simulations to see if they correspond to those predicted. We used discs with $\beta = 10$ for all our runs. It is worth noting that we artificially imposed $v_z = 0$ in the simulation domain, otherwise spurious instabilities grow in the upper disc regions. The resolution used was 1000 grid cells in the z direction over the extent $|z| \leq 5$. Each simulation was run for $4\Omega^{-1}$, and the amplitude of the initial mode in $b_x = B_x/B_z$ and $b_y = B_y/B_z$ was set to be of order 10^{-3}.

Table 7.1 gives a list of the simulations and the measured growth rates of the MRI modes being investigated, as well as their predicted growth rates from the semi-analytic model. The runs are named such that the numerics after the letters 'H' and 'A' and before the hyphens give the values of η_H and η_A used in code units respectively, with 'p' replacing decimal points. The column 'Mode (initial)' indicates the mode obtained from the semi-analytic calculation that was used to initialise each simulation, with the symmetry of the mode ('Even'

Table 7.1 Table showing the simulations run to test the implementation of Hall and ambipolar terms in PLUTO. Runs are initialised with the profile indicated in 'Mode (initial)' while 'Mode (final)' indicates the dominant mode at the end of each run. 'σ (SAM)' and 'σ (sim)' gives the predicted and measured growth rates of the modes respectively. See text for more details, and for an explanation of the nomenclature of the simulations.

Name	Mode (initial)	Mode (final)	σ (SAM)	σ (sim)
H0-A0p2-E1	Even (1)	Even (1)	0.5746	0.5743
H0-A0p2-O2	Odd (2)	Odd (2)	0.5264	0.5264
H1-A0p2-E1	Even (1)	Even (1)	0.6900	0.6896
H0-A0p2-Spec	Special	Even (1)	NA	NA

or 'Odd' for b_x and b_y in z) followed by the a number in brackets that gives its ranking in growth rate among available modes with 1 indicating the fastest growing mode. Similarly, 'Mode (final)' gives the final mode that was dominant in the simulation at the end of the run. 'σ (SAM)' gives the growth rate predicted for the initial mode from the pseudospectral calculation, while 'σ (sim)' gives the growth rate measured through fitting the simulation data over time with an exponential model.

Overall, we found the correspondence between simulation and prediction to be very good. Runs initialised with modes specific to the diffusivity profile and background field strength of the vertically stratified disc remain dominated by the same modes throughout the simulations, with their growth in amplitude over time being exact exponential fits as would be expected for the MRI, and measured growth rates that agree within 0.5% of the predicted values. An example of this is shown in Figure 7.1, where the left hand plot shows a comparison between the initial and final mode shapes of δB_x and δB_y (normalised such that $\max(\delta B_x) = 1$) for the run 'H0-A0p2-E1', while the plot on the right shows the growth of b_x at $z = 0$ from $t = 0$ to $t = 4\Omega^{-1}$ and its exponential fit for the same run. The final simulation 'H0-A0p2-Spec' is initialised using the 'Even (1)' profile of 'H1-A0p2-E1', which has notable differences to its own 'Even (1)' profile in shape and growth rate. We found that over time, the mode shape is altered from its initial profile to fit that predicted by the linear model for its own diffusivity profile. This gives us further proof that the ambipolar and Hall modules in the PLUTO code indeed accurately capture the behaviour of the MRI in 1D vertically stratified discs.

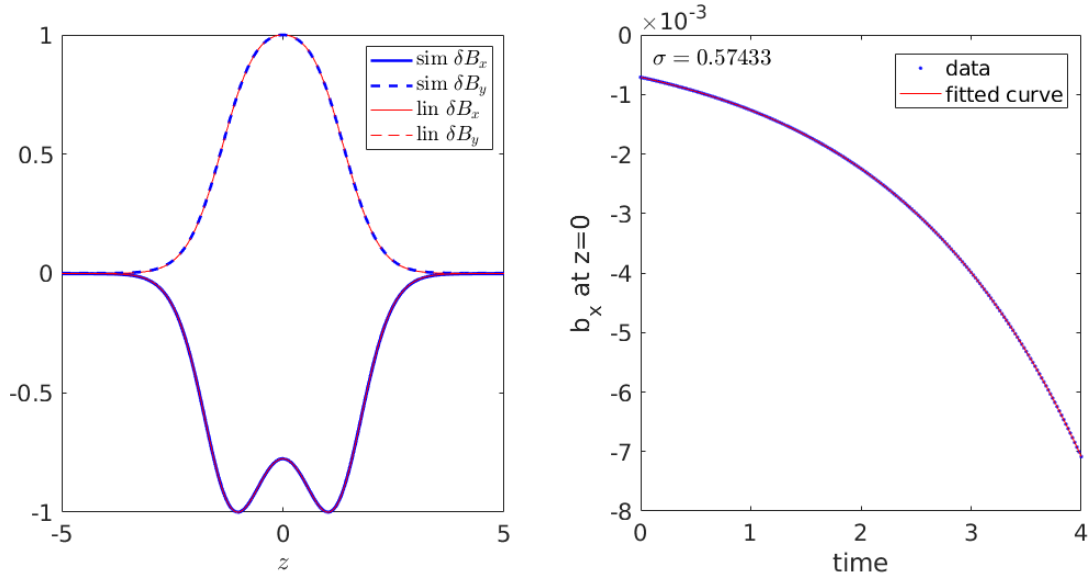

Fig. 7.1 Left: Mode shapes between the final state of δB_x (blue solid) and δB_y (blue dashed) of the simulation 'H0-A0p2-E1', and the predicted shape of δB_x (red solid) and δB_y (red dashed) of the linear model prediction. Right: plot of the growth of b_x at $z = 0$ over time of the same simulation (blue dots), with best exponential fit (red curve) plotted alongside, as well as the measured growth rate σ displayed.

7.3 Confirming the steady state solutions of the semi-analytic approach

To both verify the validity of the semi-analytic solutions in Chapter 5, as well as further confirm that the numerical implementation of the non-ideal terms in our version of `PLUTO` is correct, we perform shearing box simulations for a selection of field strengths and background diffusivities to see if steady states are achieved, and how they compare with the solutions from our semi-analytic model. To simplify our testing, we consider only the 'Uniform' diffusivity profile where η_O, η_H and η_A are constant throughout the whole vertical extent of each simulation.

7.3.1 Set-up

Units

We set $\Omega = 1$, $c_s = 1$, and also the initial mid-plane density $\rho_0 = 1$. The simulation time is then a scaled time given in units of the dynamical timescale $\tau_{\rm dyn} = \Omega^{-1}$. The length-scale on

the other hand is given in terms of the vertical scale height $H = c_s/\Omega = 1$. The vertical field strength B_z is calculated from the β_0 parameter of the disc, and is given by

$$B_z = c_s\sqrt{\frac{2\rho_0}{\beta}} = \sqrt{\frac{2}{\beta}}. \tag{7.1}$$

Grid

We work in a shearing box of dimension $\mathbf{L} = (L_x, L_y, L_z)$ divided into $\mathbf{N} = (N_x, N_y, N_z)$ grid points in the respective directions. We run full disc simulations with the vertical box extending from $z = -L_z/2$ to $z = L_z/2$, and horizontal extents of $x = -L_x/2$ to $x = L_x/2$ and $y = -L_y/2$ to $y = L_y/2$. For our 1D simulations, $L_x = L_y = 1$ and $N_x = N_y = 1$, while $L_z = 10$, and $N_z = 512$, with a resolution of 51.2 cells per H in the vertical direction.

Boundary conditions

For the shearing box to be valid, shearing periodic boundary conditions must always be applied along the x-boundaries such that boxes are sliding with respect to each other at relative velocity $w = |q\Omega_0 L_x|$, where $q = -3/2$ is the shear parameter for a Keplerian disc. The boundary condition in the x-direction is therefore given by:

$$\begin{cases} q(-L_x/2, y, z, t) = q(L_x/2, y - wt, z, t), \\ v_y(-L_x/2, y, z, t) = v_y(L_x/2, y - wt, z, t) + w, \end{cases} \tag{7.2}$$

where q here denotes all variables apart from v_y.

For the y-direction, we use normal periodic boundary conditions, where

$$q(x, -L_y/2, z, t) = q(x, +L_y/2, z, y, t) \tag{7.3}$$

is true for all variables q.

For the z-direction, we use outflow boundary conditions for the fluid velocities such that

$$\frac{\partial \mathbf{v}}{\partial z} = 0. \tag{7.4}$$

However, we fix the values of the magnetic fields at the upper and lower z boundaries as we did in Chapter 5, where

$$\begin{cases} B_x(x, y, \pm L_z/2, t) = \pm B_{xs}, \\ B_y(x, y, \pm L_z/2, t) = \pm B_{ys}, \\ B_z(x, y, \pm L_z/2, t) = B_z, \end{cases} \tag{7.5}$$

and B_{xs}, B_{ys} and B_z are set by the parameters of the problem.

Solvers

For all runs, we used the modified HLL Riemann solver of Lesur et al. (2014) and the constrained transport (CT) method of Evans and Hawley (1988), which by design maintains the $\nabla \cdot \mathbf{B} = 0$ condition to machine precision. The CT method updates the face-centred magnetic field of grid cells by treating it as an area-weighted average on the zone face and updating it using Stokes' theorem. This requires computing the electromotive force at zone edges by averaging the face-centred electromotive forces. We follow Lesur et al. (2014) by using arithmetic averaging to achieve this. We then advance the equations in time using a third-order-accurate Runge-Kutta scheme.

Initial conditions and time evolution

We initialise all our simulations with a purely vertical magnetic field, and random velocity fluctuations of maximum amplitude of 0.1 in code units. We evolve each simulation for at least $300\Omega^{-1}$, by which time most have settled into a steady solution.

7.3.2 Results

Our results are summarised in Table 7.2. Simulations are named in the following manner: btα-Oγ-Hδ-Aε-bxξ-byχ, where α denotes the value of β_0 used in setting the vertical magnetic field of the simulation, $\gamma, \delta, \varepsilon$ are the strengths of η_O, η_H, η_A in code units respectively, and ξ and χ give the values of $b_x = B_x/B_z$ and $b_y = B_y/B_z$ respectively at the upper boundary. In cases where a value is 0, we omit the Latin alphabet indicator beforehand as well as the numeric 0. For all numerics, to avoid special symbols, we replace negative signs with the letter 'n', and decimal points with the letter 'p'. The simulation named 'bt10-H5-A2-byn0p1' for example would then denote a run done with the parameters $\beta_0 = 10$, $\eta_O = 0$, $\eta_H = 5$, $\eta_A = 2$, $b_x(L_z/2) = 0$ and $b_y(L_z/2) = -0.1$. β_0 is the plasma β parameter used to set the initial vertical field strength, while $\beta_{0,\mathrm{thres}}$ is the threshold mid-plane plasma β calculated using the method of Section 5.1.5, above which we expect the disc to be unstable to the MRI. The column v_b (SAM) is the flux transport velocity in units of c_s calculated using the same parameters as the simulation from the semi-analytic model of Chapter 5. The v_b (sim) and $\dot{m}_w/10^{-6}$ (sim) columns give the flux transport and upper boundary mass outflow values from the simulations averaged over the times when steady "hourglass" states have been achieved respectively. The definition of v_b is the same as that of v_Ψ in Equation (5.14) of Chapter 5.

We found that all runs initially settle into steady "hourglass" symmetry (see Section 2.2.3 and 2.6) solutions of the type investigated in Chapters 5 and 6, and most solutions persisted

Table 7.2 Table showing the flux transport velocities v_b and mass loss rates through the upper boundary $\dot{m}_w$ for our low inclination simulation runs (denoted by sim), compared to the flux transport velocities v_b obtained using the semi-analytic method of Chapter 5 (denoted by SAM). β_0 is the plasma β parameter used to set the initial vertical field strength, while $\beta_{0,\mathrm{thres}}$ is the threshold mid-plane plasma β calculated using the method of Section 5.1.5, above which we expect the disc to be unstable to the MRI. For an explanation of the nomenclature of the runs, see the first paragraph of Section 7.3.2, and how it relates to the diffusivity profiles and boundary conditions used.

Name	β_0	$\beta_{0,\mathrm{thres}}$	v_b (SAM)	v_b (sim)	$\dot{m}_w/10^{-6}$ (sim)
bt1-O2-bx0p1	1	1.17	0.144	0.145	0.430
bt1-A2-bx0p1	1	1.17	0.144	0.145	0.430
bt1-O2-H5-bx0p1	1	18.6	0.0963	0.0967	0.304
bt1-H5-A2-bx0p1	1	18.5	0.0963	0.0974	0.304
bt10-O2-bx0p1	10	1.17	0.186	0.187	1.46
bt10-A2-bx0p1	10	1.17	0.186	0.186	1.46
bt10-O2-H5-bx0p1	10	18.6	0.0792	0.0794	0.871
bt10-H5-A2-bx0p1	10	18.5	0.0792	0.0794	0.871
bt1-O2-byn0p1	1	1.19	-0.348	-0.345	0.310
bt1-A2-byn0p1	1	1.18	-0.348	-0.345	0.305
bt1-O2-H5-byn0p1	1	18.5	-0.584	-0.580	0.272
bt1-H5-A2-byn0p1	1	18.5	-0.584	-0.580	0.272
bt10-O2-byn0p1	10	1.19	-0.0946	-0.0945	1.03
bt10-A2-byn0p1	10	1.18	-0.0952	-0.0941	1.03
bt10-O2-H5-byn0p1	10	18.5	-0.242	-0.242	0.783
bt10-H5-A2-byn0p1	10	18.5	-0.242	-0.242	0.783

for the duration of the runs. However, we found that the runs with $\beta_0 > \beta_{0,\text{thres}}$ gradually transit to overall unsteady asymmetric profiles with a "slanted" character while satisfying the boundary conditions for the horizontal magnetic fields which are anti-symmetric about $z = 0$. This is in line with the prediction from our marginal stability analysis that discs with β_0 above the threshold β values would be unstable to the MRI. It is interesting to note here that the onset of the MRI is linked to the changing of the overall symmetry of the disc, and this effect will be investigated in more detail in Chapters 10 and 11.

For the (quasi-)steady "hourglass" solutions that all runs initially settle into, we found that the flux transport rates obtained via the numerical simulations agree with the rates calculated using the semi-analytic method to a high degree of precision, differing by no more than 1% in the worst case, and often with a much smaller difference. Similarly, we found that the magnetic field profiles between the numerical steady states and semi-analytic solutions match up almost exactly. These are plotted in Figure 7.2 for the $b_x(L_z/2) = 0.1$ cases, and in Figure 7.3 for the $b_y(L_z/2) = -0.1$ cases. v_z is sub-Alfvénic throughout the simulation domain, and are orders of magnitude smaller than v_x and v_y in the disc region $|z| < 3H$, before becoming comparable to the horizontal velocities near the boundaries at the vertical extremes of the box. The total mass loss rate in each simulation is $\sim 10^{-6}$ in code units, and cause negligible changes in the density profile and wind structure compared with the $v_z = 0$ semi-analytic models. These results all point to our semi-analytic models of Chapter 5 being adequate for estimating the flux transport rates as well as computing the vertical structures of discs with small inclinations and no natural wind-launching. They also confirm that the implementation of the non-ideal MHD terms in the PLUTO code indeed capture the behaviour expected, particularly with regard to their effects on the shape and properties of the steady state solutions.

When discs have settled into steady state solutions for their magnetic field profiles, we found that this is often accompanied by a periodic oscillation in the absolute values of the horizontal velocity profiles. These oscillations have a period of $2\pi\Omega^{-1}$, and translate the horizontal velocity profiles in their values without changing their shape. This likewise causes a corresponding oscillation in the value of v_b in the simulation while keeping its flat profile in the vertical domain. This periodic oscillation, a case of which is shown in Figure 7.4, can be understood as that of a horizontal epicyclic oscillation, which is an intrinsic property of the shearing box formalism. These epicycles (see also discussion in Section 2.2.1) can be interpreted physically as describing a slightly elliptical orbit (Ogilvie, 2012). Locally, they cause the horizontal velocities to oscillate sinusoidally from the equilibrium profile, but do not alter the equilibrium or the magnetic field profile. The equilibrium values of v_b are obtained

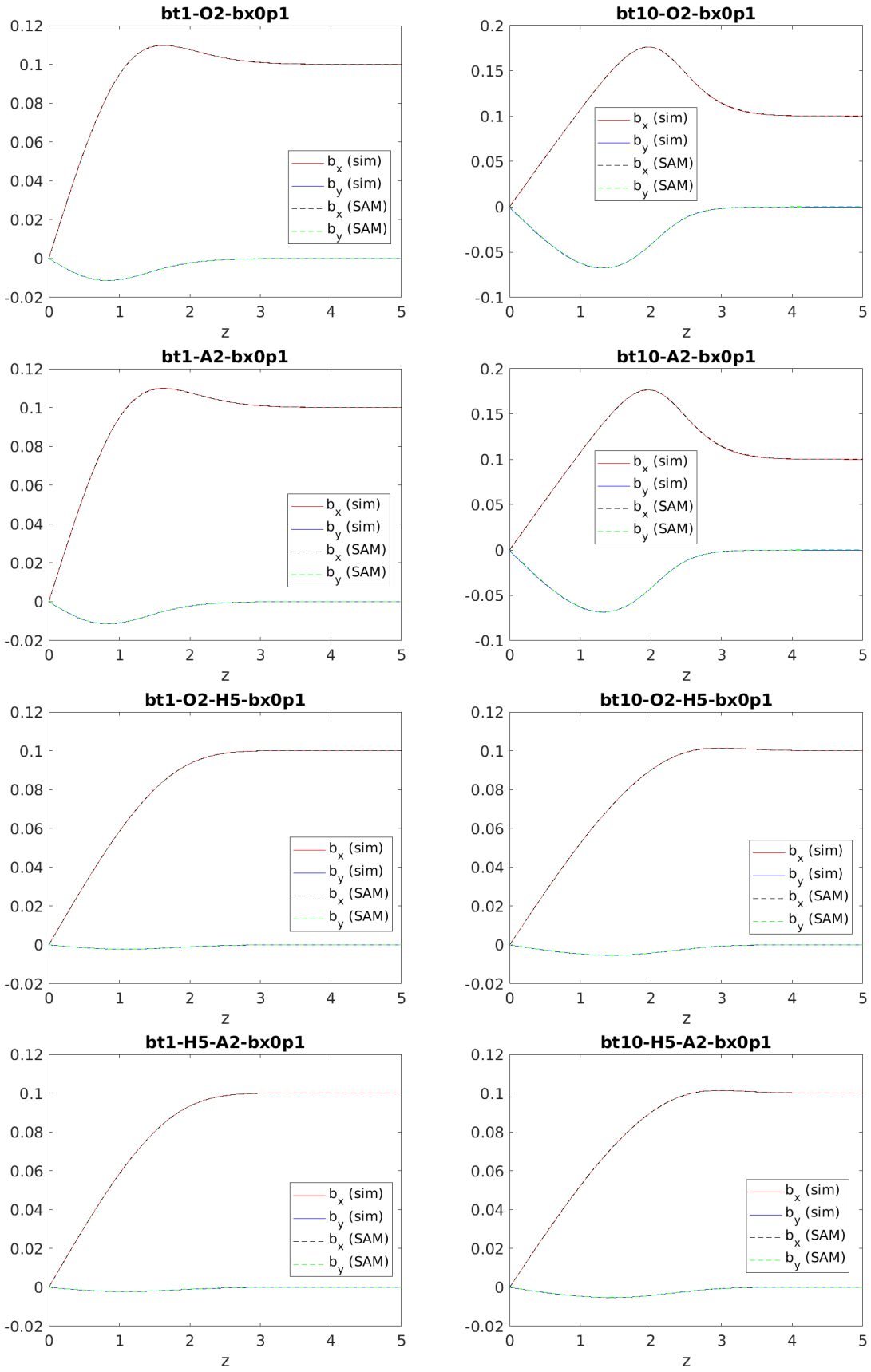

Fig. 7.2 Profiles of b_x and b_y, plotted against z for the $z > 0$ half of the hourglass symmetric (quasi-) steady solutions in the $b_x(L_z/2) = 0.1$ cases. The name of the simulation is displayed in the title of each plot. Red and blue solid lines are for the profiles obtained for b_x and b_y respectively in the simulations, while black and green dashed lines are for the profiles obtained for b_x and b_y respectively in the semi-analytic model of Chapter 5.

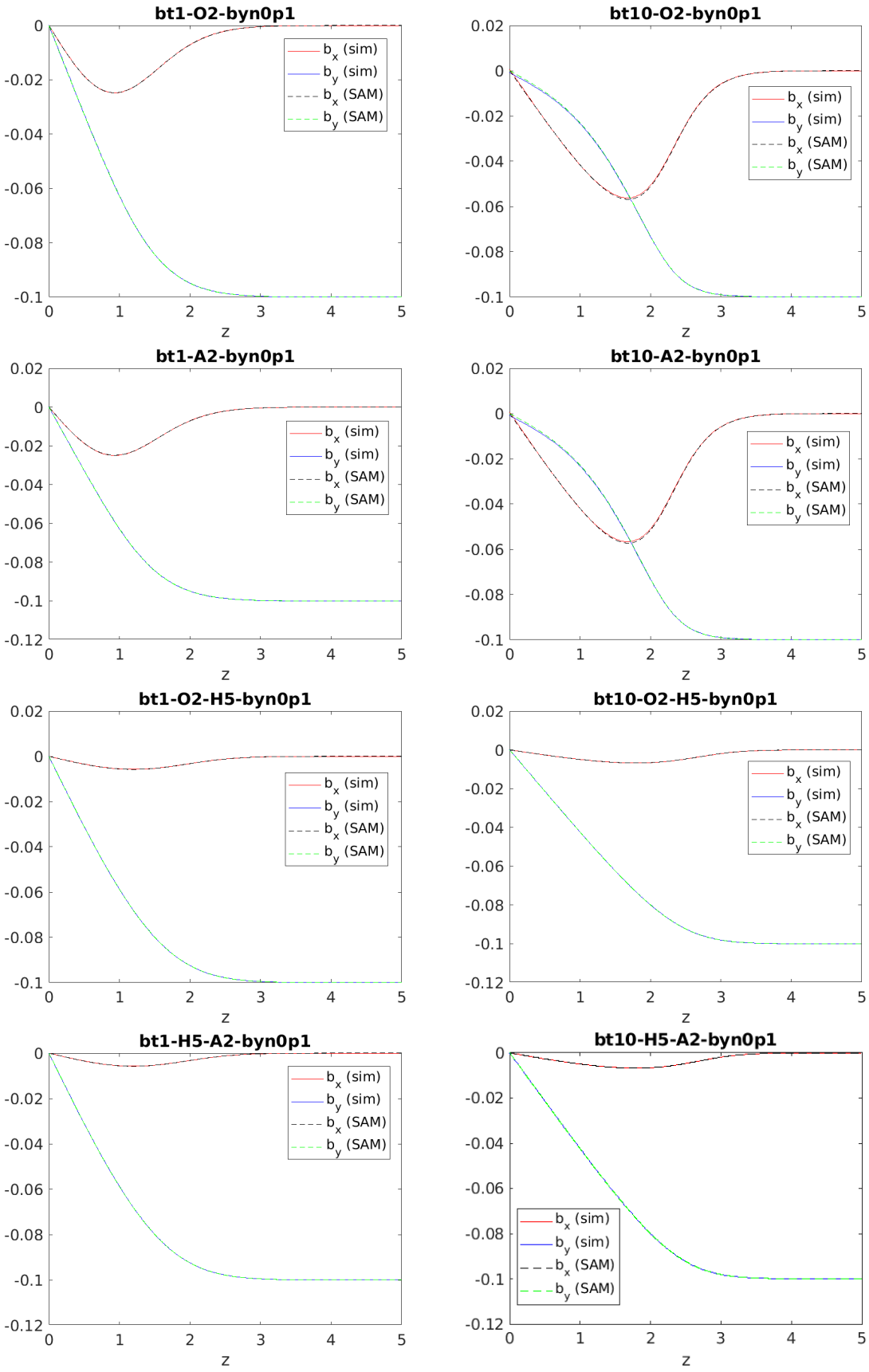

Fig. 7.3 Same as Figure 7.3, but for cases where $b_y(L_z/2) = -0.1$.

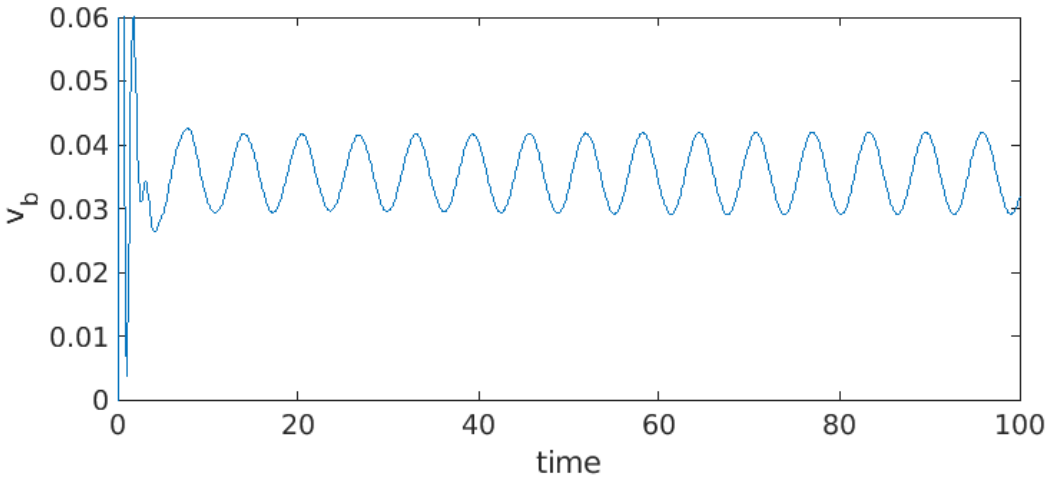

Fig. 7.4 Variation of v_b given in units of c_s with time give in units of Ω^{-1}, for simulation run bt10-O2-H5-bx0p1. Note that the period of the oscillation from $t = 20\Omega^{-1}$ onwards is $2\pi\Omega^{-1}$, and that the oscillation is sinusoidal in nature, indicative of it being an epicyclic oscillation intrinsic to the shearing box (Ogilvie, 2012).

by averaging over the values of v_b over complete cycles of the epicyclic oscillation, and as shown in Table 7.2, agree with the semi-analytic predictions with remarkable precision.

7.4 Wind solutions

We now extend our investigation to cases with $b_x(\infty) > 1/\sqrt{3}$, where wind-launching needs to be properly included in the disc model and our semi-analytic model fails to describe it adequately.

7.4.1 Set-up

We use the same simulation set-up as Section 7.3.1, but now include a mass replenishment scheme to account for the more significant mass losses expected from the outflows and allow a steady state to exist. We ran two different mass replenishment schemes: 'wide' and 'narrow'. The 'wide' scheme keeps the total mass in the simulation domain constant by computing the total mass within the simulation at the end of each time-step, and multiplying the density everywhere by a constant factor to make up for the deficit. The 'narrow' scheme operates similarly, but instead of multiplying the density everywhere by a constant factor, we add a narrow Gaussian density function of the form $\rho_{\rm add} \propto \exp\left(-z^2/2z_i^2\right)$, where $z_i = 0.1H$, to the density to make up for the deficit. Both schemes technically break the conservation of

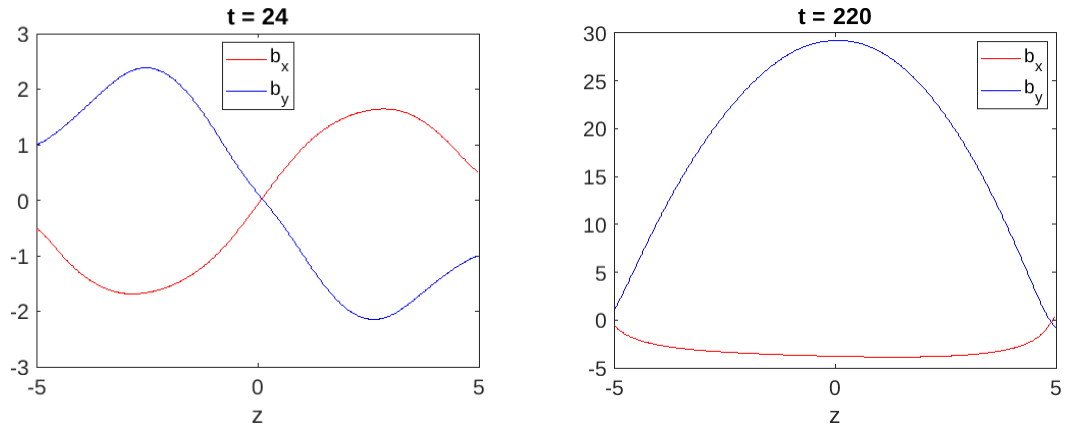

Fig. 7.5 b_x (red) and b_y (blue) profiles plotted against z for the simulation bt1000-O2-H2-bx0p5-byn1 at $t = 24\Omega^{-1}$ (left) and $t = 220\Omega^{-1}$ (right).

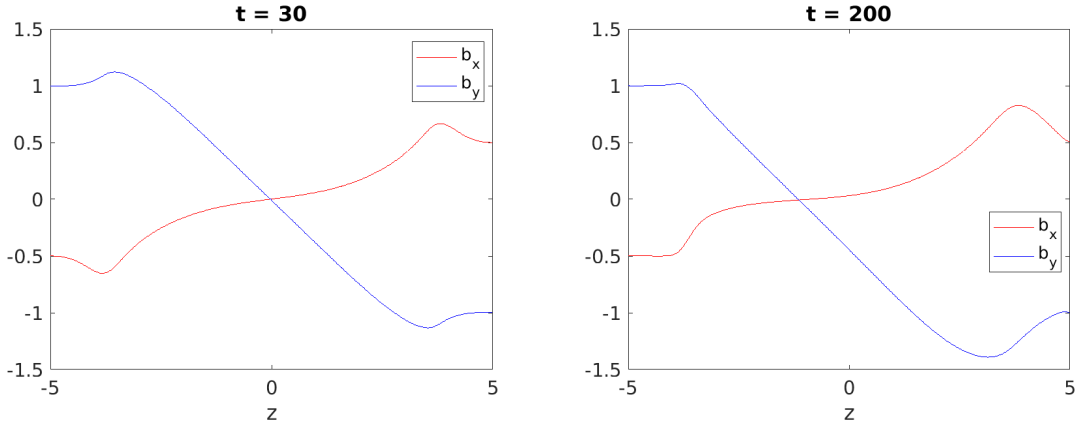

Fig. 7.6 b_x (red) and b_y (blue) profiles plotted against z for the simulation bt1000-O2-Hn2-bx0p5-byn1 at $t = 30\Omega^{-1}$ (left) and $t = 200\Omega^{-1}$ (right).

momentum, as the added mass adopts the velocity profile of the disc, but are commonly used in shearing box simulations where outflows are significant (Bai, 2014; Lesur et al., 2014; Ogilvie, 2012; Riols et al., 2016). We ran simulations under both schemes for the Ohmic resistive discs to see if the method of mass replenishment significantly alters the results, and under the 'narrow' scheme only for ambipolar diffusive discs. All our simulations are done with either Ohmic and Hall terms only, or ambipolar and Hall terms only, to allow us to compare the effects between Ohmic resistivity and ambipolar diffusion on the solutions. We also used a higher β_0 value of 1000 in all the runs in this Section.

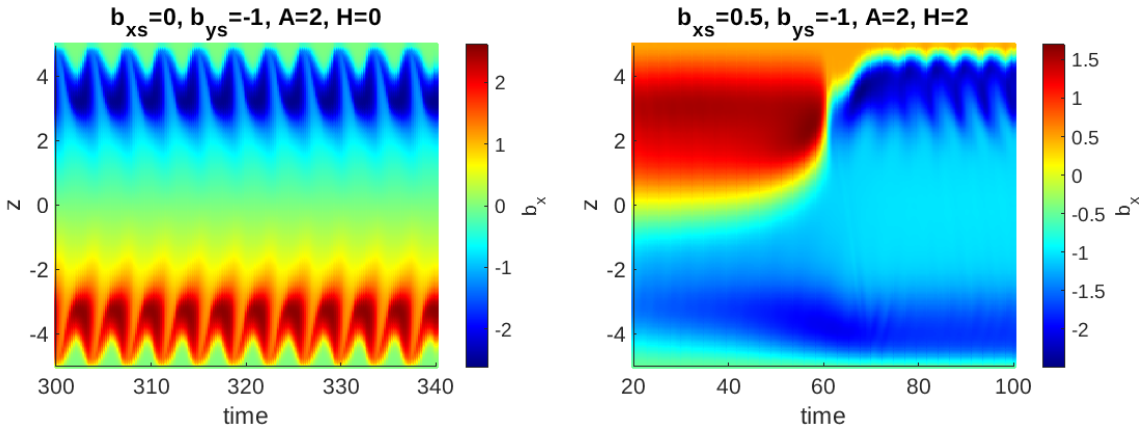

Fig. 7.7 Space-time plots of b_x for the simulations bt1000-A2-byn1 (left) and bt1000-A2-H2-bx0p5-byn1 (right). The left-hand plot shows an unsteady hourglass symmetric state with cyclic behaviour, while the right-hand plot shows a disc that transits from its initial hourglass steady state ($t \sim 0-40\Omega^{-1}$) to an unsteady asymmetric state with slanted character ($t > 80\Omega^{-1}$).

7.4.2 Results

We found that similar to our results from Section 7.3.2, most discs initially settle into hourglass symmetry (quasi-)steady states (e.g. the left panels of Figures 7.5 and 7.6). A small subset of discs then transit to asymmetric states with "slanted" symmetry character for the long term. These asymmetric profiles are either steady (e.g. the right panels of Figures 7.5 and 7.6), or vary in shape periodically (e.g. for $t > 80\Omega^{-1}$ of the right-hand plot of Figure 7.7). We also found that some discs never settle into any (quasi-)steady states, but instead have periodic asymmetric solutions with "hourglass" symmetry character (e.g. the left-hand plot of Figure 7.7). All solutions are sub-Alfvénic in their v_z profiles, and the b_x and b_y boundary conditions which are anti-symmetric about $z = 0$ are always satisfied.

The epicyclic oscillations affecting v_x, v_y and v_b profiles are present in all solutions, but are generally of much smaller magnitude than their counterparts in Section 7.3.2. They also decay in magnitude rapidly over time. We attribute this to the presence of a more significant mass outflow (100-fold of those in Section 7.3) from the disc. Since our mass replenishment scheme does not conserve the angular momentum of the box, if the box is gaining or losing angular momentum due to mass loss and replenishment, then the epicyclic oscillations would be affected. Further evidence for this can be obtained if it can be shown that the decay timescale of the oscillations is related to the mass loss timescale, given by $1/\dot{m}_w$.

Our flux transport velocity and mass outflow rate results are shown graphically in the plots of Figures 7.8, 7.9 and 7.10. The vertical axes of the left hand plots denote the flux transport velocity in units of c_s, while the vertical axes of the right hand plots denote the

mass loss rate from one side of the disc averaged over the top and bottom boundaries in units of $\rho_0 c_s$. The horizontal axes for all plots denote the variables that are changed between simulations. The title of each plot shows the parameters which are kept the same between simulations in the plot, with b_{xs} and b_{ys} being the b_x and b_y boundary conditions on the upper boundary respectively, O or A being the value of η_O or η_A respectively, and H being the value of η_H. Cyan and blue markers and lines are for runs done with Ohmic and Hall effects only, with cyan for runs under the 'wide' mass replenishment scheme, and blue for runs under the 'narrow' scheme. Red markers and lines denote runs done with ambipolar and Hall effects only under the 'narrow' scheme. v_b values are calculated by averaging out the epicyclic oscillations over time for each disc at its (quasi-)steady state(s), or over a representative period of time for the case of unsteady discs. m_w values are taken from both the upper and lower boundaries of the disc, and averaged over the same time periods as for calculating the v_b values. Circle markers are for hourglass steady states, asterisks for cyclical hourglass-like asymmetric states, triangle markers for asymmetric slanted-like steady states, and square markers for cyclical asymmetric slanted-like steady states. Results of the initial or persistent hourglass steady states are connected by solid lines, while results of final asymmetric slanted-like steady states are connected by dashed lines. To avoid cluttering the diagrams too much, we only plot the hourglass steady solutions of the runs done under the 'wide' mass replenishment schemes, but note that in actuality, these discs exhibit similar behaviour as discs done under the 'narrow' scheme, with some persisting in hourglass steady states, and others transitioning to asymmetric slanted-like states for the long term.

For most runs, we find that using the 'wide' and 'narrow' mass replenishment schemes do no significantly affect the flux transport velocities or mass outflow rates of the discs, with results differing by no more than 10%. For the rest of the discussion we will restrict ourselves to the results from the 'narrow' scheme, which was applied to both Ohmic and ambipolar diffusive discs.

7.4.3 Discussion

Flux transport for (quasi-)steady hourglass discs

We first discuss the flux transport trends for the (quasi-)steady hourglass configurations of the type explored in Chapters 5 and 6.

For inclination-driven only flux transport, we found that a positive value of b_{xs} coupled with Ohmic and/or ambipolar diffusion leads to radially outward flux transport (top left plot of Figure 7.8), with a roughly linear increase in flux transport rate with diffusivity, in agreement with the trend uncovered in Chapters 5 and 6. Adding a Hall term with positive

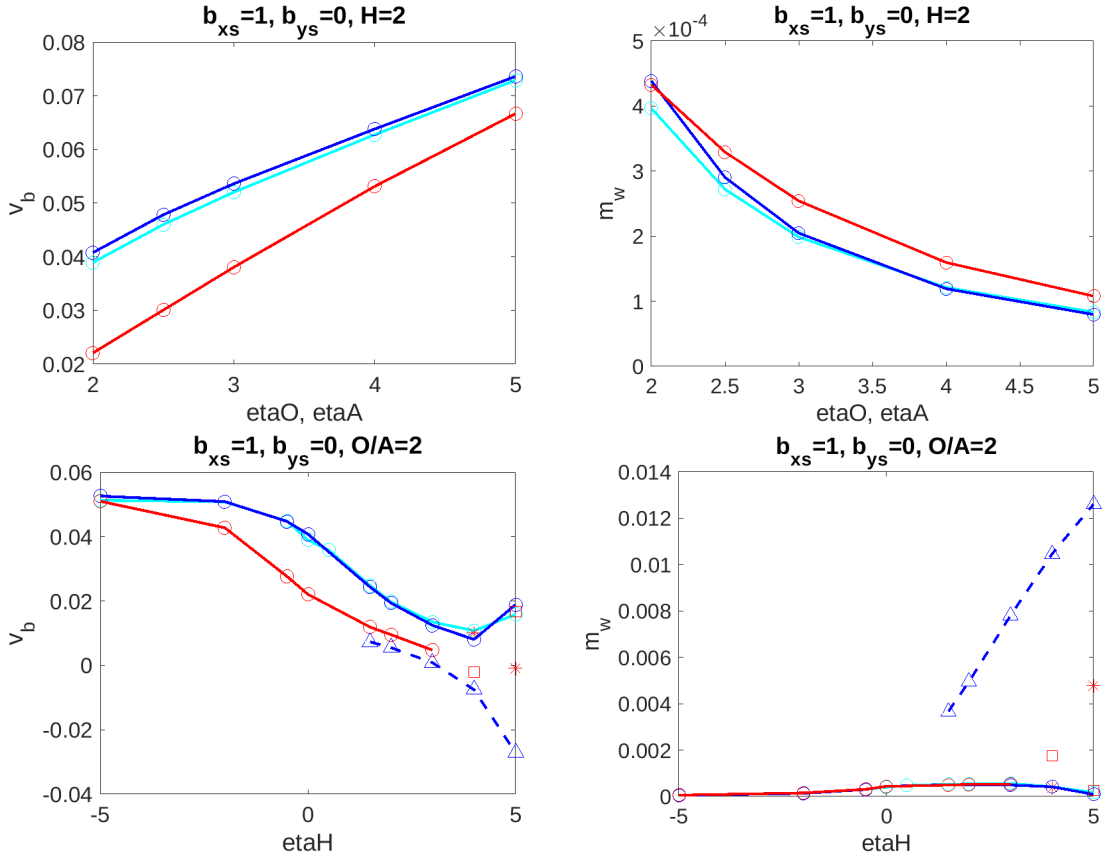

Fig. 7.8 Plots of time-averaged flux transport velocities (left) and similarly time-averaged mass loss rates from one side of the disc averaged over the upper and lower boundaries (right) against diffusivity coefficients used in the simulations. Other parameters for the simulations are indicated in the title, with more detailed explanation in the text. Circles (connected by solid lines) are for simulation data taken for the hourglass symmetry (quasi-) steady states, while triangles (connected by dashed lines) are for the subset of runs which ended in asymmetric slanted-like steady states. Asterisks are for hourglass-like unsteady solutions, while squares are for asymmetric slanted-like unsteady states. Cyan and dark blue are for Ohmic resistivity and Hall drift only discs done under the 'wide' and 'narrow' mass replenishment schemes respectively, while red is for ambipolar diffusivity and Hall drift only discs done under the 'narrow' scheme.

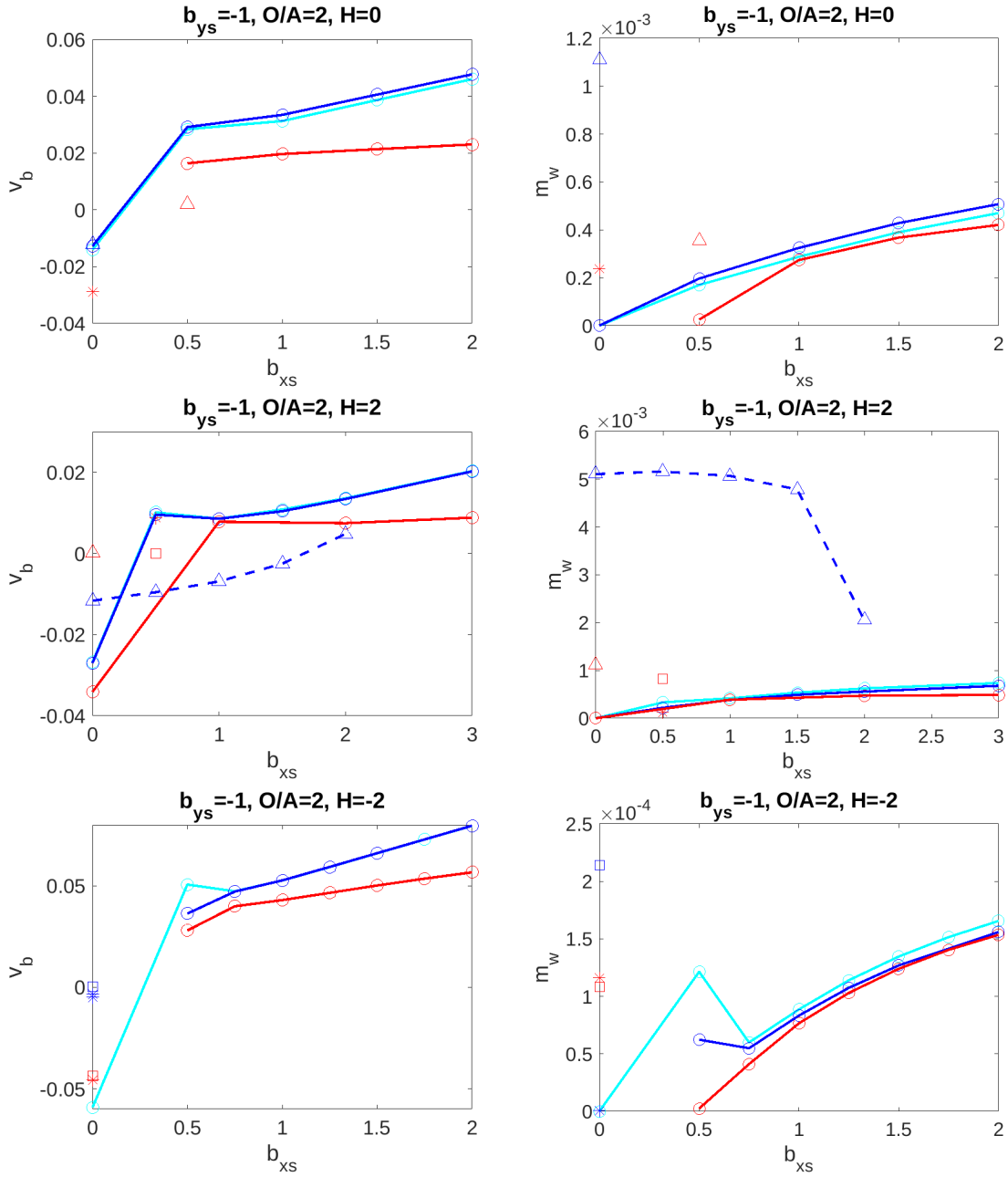

Fig. 7.9 Same as Figure 7.8, except the parameter varied within each plot on the x axis is now b_{xs}.

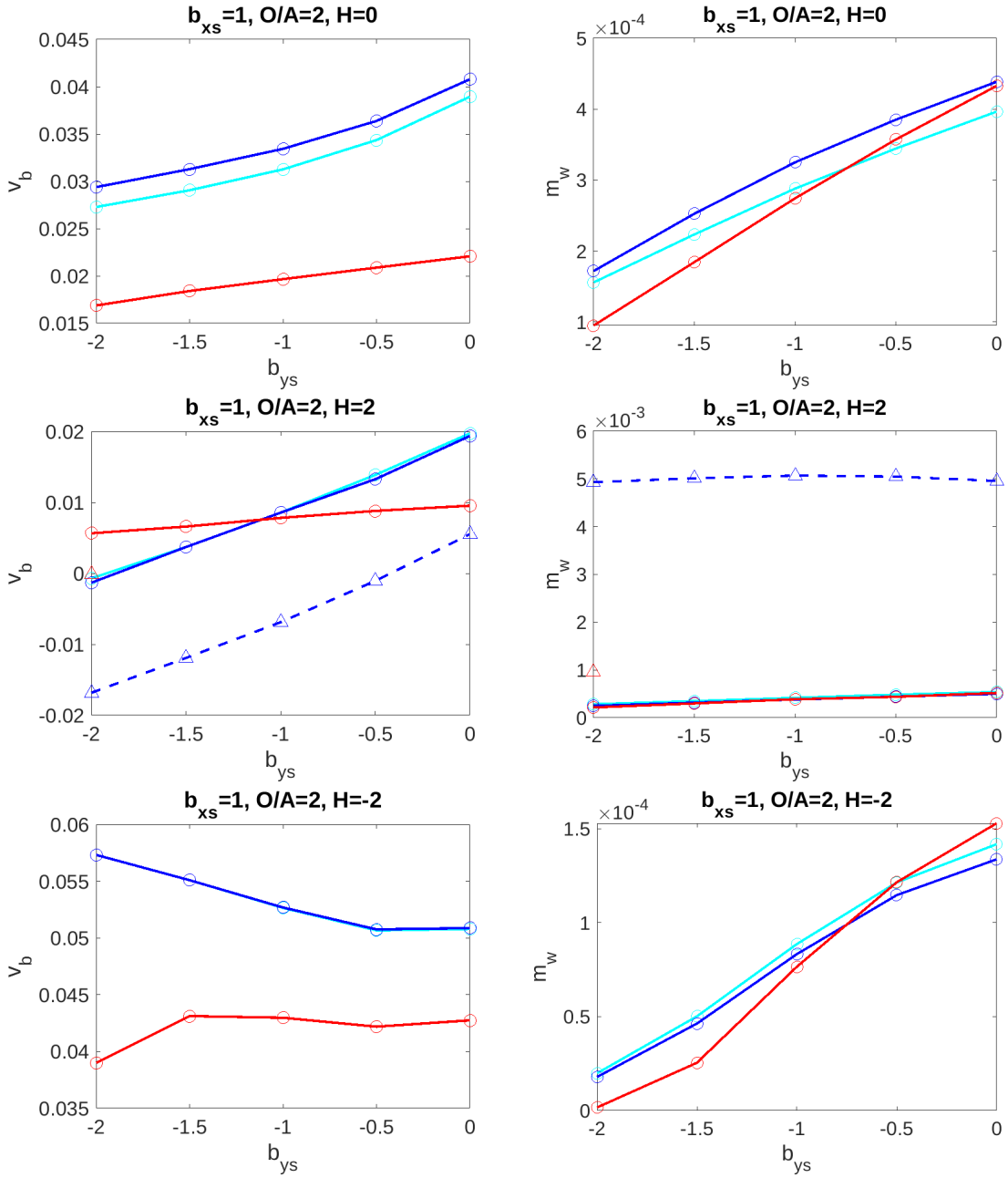

Fig. 7.10 Same as Figure 7.8, except the parameter varied within each plot on the x axis is now b_{ys}.

Hall coefficient reduces the radially outward flux transport rate but does not reverse the direction for discs in the hourglass (quasi-)steady symmetric state, while a negative Hall coefficient increases the radially outward flux transport (bottom left plot of Figure 7.8), again in agreement with the predictions of the flux transport models of the previous two Chapters.

For B_y torque-driven flux transport, a negative value of b_{ys} coupled with Ohmic and/or ambipolar diffusion contributes to radially inward flux transport. On the other hand, a positive Hall coefficient coupled with a negative b_{ys} increases (decreases) the inward (outward) flux transport rate compared to a disc with the same parameters but with no Hall drift, while a negative Hall coefficient coupled with a negative b_{ys} decreases (increases) the inward (outward) flux transport rate, with both even reversing the direction of flux transport if the coupling is strong enough. These results are again in agreement with the findings of the last two Chapters, confirming to us that the presence of an outflow does not modify the flux transport trends uncovered there, as long as the hourglass symmetry of the solution is preserved. We are also able to explore the flux transport trends with the Hall effect for cases with a negative Hall coefficient (which in our model translates to the anti-aligned configuration), and show that they contribute in an opposite way to that of the aligned configuration.

It is worth noting here that for most of the hourglass (quasi-)steady solutions, ambipolar diffusive only discs have lower magnitude flux transport rates than Ohmic resistive only discs with equal values of η_A and η_O. We attribute it to the way we have parameterised the problem, such that η_A, which in normal circumstances is proportional to B^2, is set to be constant instead in the disc. As a result, we eliminated the B_y^2 effect (see Section 2.5.2) which would normally have significantly increased the ambipolar diffusivity when $b_y \gg 1$. Our current prescription does the opposite to the normal situation whereby we reduce the B-independent parts of the ambipolar coefficient when b_x and b_y are large to keep η_A constant, resulting in a smaller diffusive contribution to the flux transport than for the Ohmic resistive case. Real discs are more likely to have $\eta_A \propto B^2/\rho^2$, which would result in more complex differences between Ohmic and ambipolar diffusive-driven flux transport than those presented here.

Trends in $\dot{m}_w$ for hourglass steady solutions

For hourglass (quasi-)steady solutions, increasing b_{xs} for the range explored generally leads to a larger outflow rate. This is expected as increasing the inclination of the poloidal field away from the vertical means a larger contribution of the centrifugal force in accelerating gas outwards along poloidal field lines. Increasing the magnitude of $-b_{ys}$ on the other hand decreases the outflow rate. We rule out magnetic compression of the disc as the reason for this decrease in outflow rate, as the density profiles between the discs in our weak field regime

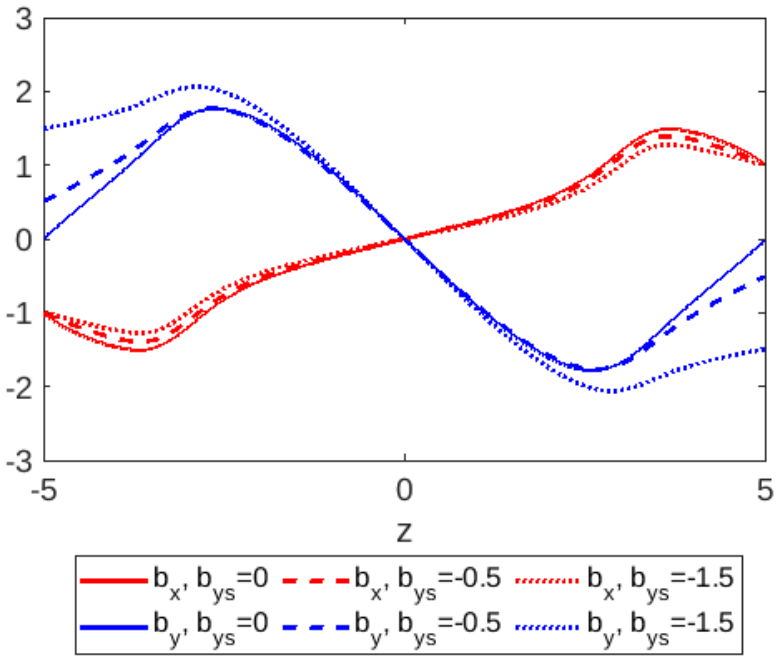

Fig. 7.11 b_x (red) and b_y (blue) profiles of the runs bt1000-O2-bx1 (solid lines), bt1000-O2-bx1-byn0p5 (dashed lines) and bt1000-O2-bx1-byn1p5 (dotted lines).

in the hourglass states all have negligible alterations from the hydrostatic Gaussian profile for $|z| < 3H$. Instead, we speculate the decrease in $\dot{m}_w$ with increasing $-b_{ys}$ is due to the smoothing the peaks in the b_y profiles as $-b_{ys}$ increases, which far outweights the steepening of the peaks in the b_x profiles (see Figure 7.11). The decreasing magnetic pressure gradient $\mathrm{d}(B_x^2 + B_y^2)/\mathrm{d}z$ from the peaks beyond $|z| > 3H$ contributes to the vertical acceleration of matter out of the disc, hence the weakening of the overall gradient leads to a lower overall outflow rate.

Increasing η_O and η_A decreases the overall outflow rate (top right plot of Figure 7.8). This is again due to weakening of the magnetic pressure gradient from beyond $|z| > 3H$ that contributes to the vertical acceleration of matter out of the disc. This results from the smoothing of the peaks in the magnetic profile, this time in both b_x and b_y, due to the higher diffusive effects.

Increasing η_H when it is positive increases the overall outflow rate (right-hand side of the bottom right plot of Figure 7.8), and may be attributed to increasing b_x and b_y and their peaks in the solution through the HSI, leading to greater mass loss vertically. Having an increasingly negative η_H on the other hand results in a smaller outflow rate (left-hand side of the bottom right plot of Figure 7.8), and may be attributed to their much flatter b_x and b_y profiles, drastically reducing the magnetic pressure gradient contribution to the outflow.

Stability and symmetry of solutions

Next, we turn to examine the cases where the hourglass steady solutions do not persist, but transition to asymmetric slanted-like solutions.

It is interesting to note that when we calculated the threshold β_0 values using our marginal stability method (see Section 5.1.5) for discs with the same parameters in diffusivity as those used in this Section, we generally obtained $\beta_{0,\text{thes}} \sim \mathcal{O}(1) - \mathcal{O}(10)$, with little dependence on the values of b_{xs} and b_{ys} used. The fact that many of our simulations settled into steady hourglass solutions despite their much larger $\beta_0 = 1000$ suggests that the much stronger outflows we have in this Section, with $\dot{m}_w \sim 10^{-4}$, may be responsible for increasing the stability of the discs here compared to the ones in the semi-analytic model where v_z is arbitrarily set to zero, or the simulations in Section 7.3.2 with a much smaller $\dot{m}_w \sim 10^{-6}$.

Discs where Ohmic resistivity and Hall effect only are present are more susceptible to transitioning to the asymmetric slanted-like solutions than discs where ambipolar diffusivity and Hall effect only are present. This is evidenced by the more numerous blue dashed lines in our plots, which denote the former, than the red dashed lines, which denote the latter. This may be due to the nonlinear anisotropic nature of the ambipolar term being better at supporting the mid-plane current sheets present in the hourglass steady solution than Ohmic resistivity (Brandenburg and Zweibel, 1994), leading to greater resilience of ambipolar diffusive discs to transitioning away from the hourglass steady state. The effect of ambipolar diffusivity on stabilising the mid-plane current sheet will be investigated in more detail in Section 11.4 of this Thesis.

Discs where the Hall coefficient is positive are more likely to transition to the asymmetric slanted-like states than those with no Hall drift present, or where the Hall coefficient is negative (compare the middle left plots of Figures 7.9 and 7.10 with the top and bottom left plots, as well as the right half of the bottom left plot of Figure 7.8 with the left half). This is likely due to the HSI (see Section 2.5.3) being active when the Hall coefficient is positive, amplifying horizontal fields, as we see in the left hand plot of Figure 7.5 compared with the left hand plot of Figure 7.6, where all other parameters are the same with the exception of the sign of the Hall coefficient being reversed. The amplified hourglass profile then has a sharper current sheet at the mid-plane, which is less well supported when strong diffusivities are present, leading to greater likelihood for its expulsion and transition to the asymmetric slanted-like states. The HSI may also enhance the growth rate of the lowest order MRI channel mode with slanted symmetry, which eventually takes over the disc profile. The second effect and its possible role in transitioning discs from the hourglass symmetry to a slanted-like configuration will be explored in more detail in Chapter 10 for Ohmic

resistive-only discs, before application to discs where all three non-ideal effects are present in Chapter 11.

Asymmetric slanted-like steady solutions generally have outflow rates $\dot{m}_w$ that are one or two orders of magnitudes larger than their hourglass (quasi-)steady counterparts, while asymmetric periodic solutions have larger but similar magnitude outflow rates to the hourglass (quasi-)steady solutions. This might again suggest a link between strong outflows and the saturation of solutions to steady states, and will be further explored in Section 10.6.2. Asymmetric slanted-like steady solutions also have b_x and b_y profiles that are orders of magnitude larger than their hourglass (quasi-)steady counterparts (compare the right-hand plot of Figure 7.5 with the left-hand plot), providing the reason for the much greater outflow rates of these solutions, as the stronger horizontal magnetic pressure gradient contributes to the driving of the vertical outflow. The possible effects they have on the saturation and stability of the solution will also be further explored in Section 10.6.2.

Flux transport and mass outflow trends for asymmetric steady solutions

In the cases examined in this Section, all asymmetric steady states have lower v_b than their hourglass steady counterparts. The differences become more pronounced with increasing η_H and $-b_{ys}$, even leading to the switching of signs and hence the direction of flux transport, while the differences become less pronounced with increasing b_{xs}. The mass outflow rate on the other hand increases sharply with increasing η_H, most likely due to the enhanced horizontal fields resulting from the HSI creating larger magnetic pressure gradients for driving vertical outflows. Increasing b_{xs} and $-b_{ys}$ on the other hand has little effect on $\dot{m}_w$, except for the sudden drop in magnitude for $b_{xs} = 2$ in the middle right plot of Figure 7.9. $\dot{m}_w$ can also be drastically different between the two sides of the disc due to the asymmetric nature of the solutions, while v_b is the same across the full vertical extent, as it is only dependent on the steady-state nature of the solutions. Normally, for fully slanted symmetry solutions in the shearing box, we would expect $v_b = 0$. However, this is not the case in our simulations, as the hourglass symmetric b_x and b_y boundary conditions are still satisfied, forcing the fields to bend back near the boundary, similar to what would need to occur in a global symmetry where the fields must eventually bend away from the star. However, given the limited ability of the shearing box formalism in exploring global geometries, we relegate any further exploration of the flux transport and mass outflow trends of asymmetric steady solutions to a future study where a more appropriate global formalism will be used.

Overall, it is interesting to note here that asymmetric slanted-like steady solutions have significantly different flux transport velocities to those of the hourglass steady states they have evolved. This points to the sensitivity of the flux transport process to the geometry of

the solution, and the need to further investigate the conditions for a disc to transition between states.

A comment on the cyclic nature of the unsteady solutions

Finally, we note that the cyclic nature of the unsteady solutions, as displayed in Figure 7.7 for both hourglass and slanted-like states, may be a manifestation of the MRI in the upper atmospheric regions of the disc. We will explore this effect more fully in Chapter 10.

Chapter 8

Conclusion to Part II

In this Part, we have developed a formalism to compute the radially local effects of non-ideal MHD effects coupled with inclination, the B_y torque of an outflow and large scale radial gradients on disc dynamics through the use of a multiscale asymptotic approach. Using semi-analytic methods, we investigated the flux transport due to inclination and outflow first at the shearing box order, and then at the Guilet & Ogilvie order (Guilet and Ogilvie, 2012), which also allows the computation of the additional contributions from large scale radial gradients. Our findings from both models are qualitatively similar, and we examined the trends of inclination and outflow driven flux transport and their variation with the three non-ideal MHD effects. By developing approximate analytic models, we gained insights into how diffusivities are coupled with the various other parameters in facilitating flux transport, and derived simple relations for estimating this. We then confirmed the validity of the solutions of our semi-analytic models in the small mass outflow regimes they were meant to represent using numerical shearing box solutions in PLUTO, before using the same numerical method in extending our investigation to regimes where a mass outflow is significant.

Our main findings include:

1. Stable disc configurations arise from having a strong field (low β_0) and high diffusivity values, while weak field and low diffusivities give rise to unstable configurations characteristic of MRI channel modes.

2. In the positive polarity case, where $\eta_H(\mathbf{B}_z \cdot \Omega\mathbf{x}) > 0$, all diffusivities are stabilising, while the Hall effect becomes destabilising in the anti-aligned case.

3. Outward inclination of the poloidal field coupled with Ohmic and ambipolar diffusion both drive radially outward flux transport which increases roughly linearly with diffusivity, while the Hall effect coupled with outward inclination reduces the flux transport rate but does not reverse its direction.

4. When the toroidal field in the disc is small compared to the overall field, B_y torque-driven flux transport is not significantly affected by the presence of Ohmic and ambipolar diffusion, but is significantly enhanced when the Hall effect is present. In the high β_0, high diffusitivity limit common to protoplanetary discs, this scales roughly linearly with η_H and the surface toroidal field strength. All B_y torque-driven flux transport is radially inward, as would be expected from advection due to the accretion flow caused by vertical removal of angular momentum in the outflow. When the toroidal field in the disc is large, the flux transport behaviour with Ohmic and Hall coefficients remain the same, while it is reversed in the ambipolar case, as the "Hall-like" component of the ambipolar term dominates over the "Ohm-like" component, and acts in the opposite direction to the Hall term.

5. When a vertical mass outflow is significant, discs with parameters that are predicted to lead to instability by the $v_z = 0$ semi-analytic models may instead have stable solutions. This points to a possible link between strong mass outflows as a stabilising factor for otherwise unstable discs.

6. A vertical mass outflow does not alter the overall trends in flux transport for the hourglass (quasi-)steady states uncovered in our semi-analytic models, while Hall drift in the negative polarity case contributes in an opposite way to the flux transport of the positive polarity case.

7. Most discs initially settle into the standard hourglass configuration assumed in our semi-analytic models. Discs that are unstable in the hourglass configuration eventually transition to asymmetric states with slanted character that are either stable or have periodic variations. The stable slanted solutions have much larger outflow rates than their quasi-steady hourglass counterparts, while the flux transport rates are also drastically different.

8. Discs with Ohmic resistivity and significant Hall drift in the positive polarity configuration are more prone to transitioning to asymmetric slanted-like steady states, while discs with ambipolar diffusion instead of Ohmic resistivity are more likely to remain in the hourglass steady solution.

8.1 Implications, model limitations and future directions

One important implication of our results is the need to further investigate the interplay between Hall drift and a wind outflow in facilitating flux transport. Bai (2016), who attempted

to present a framework of global protoplanetary disc evolution incorporating the latest advances in protoplanetary disc research, found disc evolution to be largely dominated by wind-driven processes, while viscous spreading is suppressed. He noted that the timescale of disc evolution is largely governed by the global flux evolution in the disc, and admitted that an understanding of this and in particular of how the Hall effect affects magnetic flux evolution is still lacking. To bridge this gap, a more detailed way of modelling the wind outflow in the presence of the Hall effect than our simple prescription of a non-zero surface B_ϕ would be required, where disc boundary conditions are formally matched to the Blandford & Payne solutions. Our current work also separates out the different effects contributing to the flux transport rate as if they were independent of and isolated from each other, when in a real disc, they are likely to be present in varying degrees, and also are connected with each other. Modelling the combined outcome from the various effects will therefore require a self-consistent way of determining their presence and relation with each other. The feasibility of an approach taking into account these concerns, tailored for the flux transport problem, should be examined in future work.

The question of how to model asymmetrical solutions both numerically and semi-analytically should also be looked into. In addition to the asymmetric solutions we uncovered in Chapter 7, disc solutions with vertical symmetry breaking have also been observed in many recent local (Bai and Stone, 2013b; Lesur et al., 2014; Simon et al., 2015) and global (Bai, 2017; Béthune et al., 2016, 2017) disc simulations. They have drastic contrasts in their overall flux transport and mass outflow rates compared to their standard symmetric counterparts. It would therefore be worth investigating the conditions that lead to symmetry breaking, on which we will make a start in Part III. It would also be instructive to develop a semi-analytic model that can adequately model the properties of asymmetric discs in future work. Currently, switching the even-odd symmetry of the variables completely would yield the trivial result of zero net flux transport in our local models, as the transport from the bottom and top parts of the disc will cancel each other out. Modelling the flux transport meaningfully in such context therefore would require careful thought.

Future investigations should also seek to implement more realistic diffusivity profiles, such as those used in these simulations (Bai, 2017; Béthune et al., 2016, 2017). The flux transport mechanism reported in Suriano et al. (2018) is heavily dependent on the variation on the ambipolar diffusivity in the disc, and involves a time-dependent periodic flux concentration processes. This and other processes will have to be investigated through shearing box simulations that give us insight into how the disc develops over time before reaching equilibrium. We will begin working towards this goal through our more carefully calculated diffusivity profiles in Chapter 11, while acknowledging there are still many

uncertainties in the underlying processes affect the diffusivity parameters in protoplanetary discs.

Finally, it would be good to combine these local models into a global flux evolution framework, such as done by Guilet and Ogilvie (2014), Okuzumi et al. (2014) and Takeuchi and Okuzumi (2014). The main challenge resides in the fact that Hall/wind-driven flux transport requires knowledge of the disc surface toroidal field, while the models in the papers mentioned only required the calculation of the poloidal field structure which is more readily determined through the Biot-Savart law. Careful modelling of the global wind solution is required, and should be looked into in a future investigation. In the absence of a magnetic wind, the Hall effect (when $\eta_H(\mathbf{B}_z \cdot \Omega\mathbf{x}) > 0$) reduces the radially outward flux transport rate induced by Ohmic and/or ambipolar diffusion coupled with an inclined field. Hence we should expect the protoplanetary discs where the Hall effect is present, where the field is aligned with rotation, and where no outflow is launched, to settle into a more highly magnetised steady-state solution than those previously calculated.

To summarise, this Part represents an initial effort toward modelling flux transport in protoplanetary discs incorporating all three non-ideal effects, inclination of the large scale field, outflow and the presence of large-scale radial gradients. At present, we have focused on the local transport in the disc, with a range of parameters characterising the contribution from each effect, and in our semi-analytic models assumed a quasi-steady equilibrium state. Future work would need to address more fully the time-dependent aspect of disc evolution, and also consider the flux transport globally under more realistic physical parameters for better comparison and understanding to the results of present and future protoplanetary disc simulations.

Part III

Symmetries of magnetised discs and winds

Chapter 9

Introduction to symmetries of magnetic winds

An interesting aspect of protoplanetary disc magnetic winds brought out by Chapter 7 as well as by recent simulations in the literature is the symmetry of the disc and wind structure about the mid-plane. Traditional models of magnetised discs assumed an 'hourglass' symmetry of the magnetic field about the mid-plane (see Figure 9.1), where the poloidal field is purely vertical at the mid-plane and bends away from the star above and below. Shearing generates toroidal fields of opposite signs across the mid-plane, while the horizontal velocity components have the same signs on both sides of the disc, consistent with there being a net accretion flow. However, early local simulations of protoplanetary discs have shown that a 'slanted' symmetry state can also develop, where the poloidal field is slanted in one direction at the mid-plane, bending in opposite directions above and below the disc, and a significant toroidal field of a single sign also develops encompassing the whole disc (Bai and Stone, 2013a; Lesur et al., 2014). This slanted symmetry was later confirmed to occur not only in local simulations (which inherently do not distinguish between the radially inward and outward directions in relation to the star), but also in global simulations. The same features as the local slanted solution were observed in the disc region and extending to the lower atmosphere, before (in some cases) a kink occurs in the upper atmosphere bending the field in the half of the disc that is slanted towards the star back outwards (Bai, 2017; Béthune et al., 2017; Riols et al., 2020). In both local and global cases, the properties of the wind and the disc are significantly affected by which symmetry the solution takes. In the local scheme, a slanted symmetry solution implies no net accretion or magnetic flux transport because of a cancellation of the contributions from the upper and lower halves of the disc. For global solutions, even in cases where the field eventually bends back outwards from the star in the upper atmosphere, both the disc wind and accretion flow are significantly changed (becoming

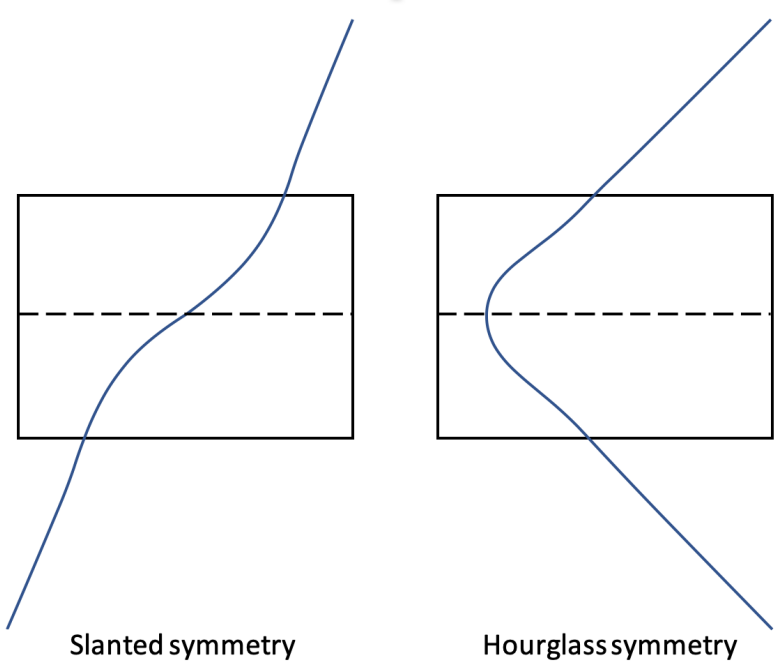

Fig. 9.1 Cartoon illustrating the two disc symmetries found in local simulations. The dotted line denotes the mid-plane, while the blue lines show the shapes of the poloidal magnetic field lines. These have also been found in global simulations.

highly one-sided), and the overall radial transport of vertical flux is also greatly affected (Bai, 2017; Béthune et al., 2017).

Thus far, there has been no agreed explanation for the development of the slanted symmetry state. Previous authors (Bai, 2017; Béthune et al., 2017) have invoked non-ideal MHD effects such as the Hall-shear instability (Kunz, 2008), which arises from the presence of Hall drift, to explain the development of the strong radial and toroidal net flux characteristic of the slanted solution. Others (Gressel et al., 2020) have suggested that it could be a manifestation of corrugation of the mid-plane by the vertical shear instability (VSI) (Urpin, 2003; Urpin and Brandenburg, 1998). However, settling to the slanted symmetry state was also observed in global simulations where Ohmic and ambipolar diffusion were the only non-ideal effects present (Gressel et al., 2020), and even in purely Ohmic (Rodenkirch et al., 2020) or ambipolar (Riols et al., 2020) discs. The latter simulation also uses a cooling timescale that prevents the growth of the VSI, thus ruling it out as necessary for the development of the slanted symmetry.

A mechanism that has been suggested to affect the disc wind configuration is the role of the MRI in the wind generation process (Ogilvie, 2012; Suzuki and Inutsuka, 2009; Suzuki et al., 2010). The MRI is a shear-induced instability which converts rotational energy in

the disc to magnetic energy by amplifying the horizontal fields (Balbus and Hawley, 1998). Lesur et al. (2013) first did a detailed investigation of the link between the MRI and magnetic winds using local simulations, and showed that large-scale channel modes could naturally produce steady outflows in the nonlinear regime. A further investigation by Riols et al. (2016) uncovered how these modes can also drive wind cycles with periodic outbursts in discs near the MRI marginal stability boundary. Since MRI channel modes naturally take either a slanted or hourglass symmetry about the mid-plane (Gammie and Balbus, 1994b; Latter et al., 2010; Sano and Miyama, 1999), they may also have a link to the wind configurations that we see in protoplanetary disc simulations. Past work on wind-MRI interactions has so far focused on the ideal MHD regime (Lesur et al., 2013) and much stronger fields (Riols et al., 2016) than are usually considered in protoplanetary discs (Guilet and Ogilvie, 2014; Wardle, 2007). In this Part, we aim to see if such interactions are also relevant in the non-ideal MHD weak field regime more suitable for modelling protoplanetary discs. We would like to find out to what extent large-scale MRI dynamics may influence the launching and configuration of magnetic disc winds, and how the wind in turn feeds back on the development of the MRI. Our ambition ultimately is to characterise and predict what disc symmetries and wind solutions may develop based on the different MRI modes being excited, and to provide a greater understanding into the development of the slanted symmetry steady wind seen in global simulations. We would also like to examine how factors such as disc magnetisation may affect the evolution and outcome of disc configurations.

For that purpose, we performed radially local 1D vertical shearing box simulations of stratified discs with a net vertical magnetic field using the PLUTO code. Although not all physical processess (such as turbulence) are present because of its 1D and local nature, the model is nevertheless sufficient to capture the large-scale channel modes we are after. Another advantage of a local model is that we can explore a much wider parameter space and run simulations for much longer than global ones, allowing us to access the long-term outcomes of the wind. Chapter 10 explores the case when only Ohmic resistivity is present, which simplifies the physics and is also relevant to the inner regions of protoplanetary discs where it is the dominant non-ideal effect. Chapter 11 extends the study to discs where all three non-ideal effects are present, and uses more realistic ionisation prescriptions to calculate their coefficients at different radii from the star. Each Chapter in this Part is self-contained, while a general conclusion summarising the results from both Chapters is presented in Chapter 12.

Chapter 10

Wind-MRI interactions: Ohmic resistivity only

As slanted symmetry profiles have been reported even in simulations with only Ohmic resistivity (Rodenkirch et al., 2020), we begin by restricting the non-ideal physics we consider in the same way, to identify the minimum ingredients required for the disc to adopt the different wind symmetries. While Hall drift and ambipolar diffusion also have significant impact on protoplanetary disc dynamics (Bai, 2015; Lesur et al., 2014), their anisotropic and nonlinear nature makes it much harder to isolate and evaluate their effects, and we relegate their study to the next Chapter. In fact, an Ohmic only regime may also be appropriate for the inner disc regions where it is significantly stronger than Hall drift and ambipolar diffusion (Bai, 2011; Wardle, 2007). Finally, we used targeted triggering of MRI modes through our initial conditions to better understand their effects on the wind topology. Using this approach, we examined whether the history of the disc is important to the intermediate and long term outcomes of the wind solution, and assessed the varying importance of MRI modes of different morphologies.

This Chapter is organised as follows: In Section 10.1, we describe the model and justify our use of the 1D local scheme. In Section 10.2, we explain our setup, particularly the tall boxes we used as well as our modelling of the non-ideal physics. Section 10.3 details the initial conditions we used for the targeted triggering of MRI modes, the different categories of wind solutions we found: cyclic, transitive and steady, as well as a brief description of their evolution and their dependence on disc parameters. In Sections 10.4, 10.5 and 10.6, we investigate and propose the mechanisms behind the cyclic and transitive states and saturation to the steady state wind respectively. We summarise our results in Section 10.7, and discuss how they relate to wind solutions found in other simulations and possible astrophysical applications.

10.1 Model and equations

We use the standard Cartesian local shearing-sheet description (Goldreich and Lynden-Bell, 1965) to investigate the behaviour of a radially local patch of the disc. The x, y and z coordinates represent the radial, azimuthal and vertical directions respectively. We assume that variables do not vary in the horizontal directions ($\partial/\partial x, \partial/\partial y = 0$), motivated by the laminar vertical 1D profiles found in both local (Bai, 2013) and global simulations (Bai, 2017; Bai and Stone, 2017). This assumption inevitably reduces the complex physics that may occur in a real disc, but may be sufficient to capture the essential mechanisms that influence wind launching.

For simplicity, we assume an isothermal disc with equation of state $p = c_{\rm s}^2\rho$, where $c_{\rm s}$ is the sound speed and is uniform in the domain. The system of equations governing the development of the density ρ, velocity $\mathbf{v}$ and magnetic field $\mathbf{B}$ under these approximations is then (Ogilvie, 2012)

$$\frac{\partial \rho}{\partial t} + \frac{\partial(\rho v_z)}{\partial z} = \varsigma(z,t), \tag{10.1}$$

$$\rho\left(\frac{\partial v_x}{\partial t} + v_z\frac{\partial v_x}{\partial z} - 2\Omega v_y\right) = \frac{\partial}{\partial z}\left(\frac{B_x B_z}{\mu_0} + \rho\nu\frac{\partial v_x}{\partial z}\right), \tag{10.2}$$

$$\rho\left(\frac{\partial v_y}{\partial t} + v_z\frac{\partial v_y}{\partial z} + \frac{1}{2}\Omega v_x\right) = \frac{\partial}{\partial z}\left(\frac{B_y B_z}{\mu_0} + \rho\nu\frac{\partial v_y}{\partial z}\right), \tag{10.3}$$

$$\rho\left(\frac{\partial v_z}{\partial t} + v_z\frac{\partial v_z}{\partial z}\right) = \rho g_z - \frac{\partial}{\partial z}\left(c_{\rm s}^2\rho + \frac{B_x^2 + B_y^2}{2\mu_0} - \frac{4}{3}\rho\nu\frac{\partial v_z}{\partial z}\right), \tag{10.4}$$

$$\frac{\partial B_x}{\partial t} = \frac{\partial}{\partial z}(v_x B_z - v_z B_x) + \frac{\partial}{\partial z}\left(\eta\frac{\partial B_x}{\partial z}\right), \tag{10.5}$$

$$\frac{\partial B_y}{\partial t} = -\frac{3}{2}\Omega B_x + \frac{\partial}{\partial z}(v_y B_z - v_z B_y) + \frac{\partial}{\partial z}\left(\eta\frac{\partial B_y}{\partial z}\right), \tag{10.6}$$

where η is the Ohmic diffusivity, and is allowed to vary with height, and ν is the kinematic viscosity. B_z is a constant parameter of the 1D model, because of flux conservation. We can define $H = c_s/\Omega$ as the standard hydrostatic scale-height of the disc, while our unit of time is given by Ω^{-1}. The source term $\varsigma(z,t)$ in the continuity equation represents an artificial mass injection that replenishes mass lost to the wind. In a real disc, this mass would be replenished by radial flows from neighbouring parts of the disc, but these depend on radial gradients and curvature effects that are not represented in the shearing sheet model. The various mass

replenishment schemes used in this paper are outlined in Section 10.2.2 and their effects on our results discussed in Section 10.3.4.

As noted in Riols et al. (2016), the shearing box gravity term $g_z = -\Omega^2 z$ is only appropriate when the vertical scales of interest are small compared to the disc radius. However, when $z \gg H$, this term actually completely suppresses vertical outflow from the box, as the gravitational potential well becomes infinite. We modify the vertical gravity in the same manner as Riols et al. (2016), taking into account the finite distance from the central object such that

$$g_z = -\frac{GMz}{(r_0^2+z^2)^{3/2}} = -\Omega^2 H \frac{\hat{z}}{(1+\delta^2\hat{z}^2)^{3/2}}, \tag{10.7}$$

where $\hat{z} \equiv z/H$ and $\delta = H/r_0$, with r_0 being the radial location from the star. Note that $\delta = 0$ brings us back to the standard shearing box gravity term, leading to the Gaussian hydrostatic density profile. When $0 < \delta < 1$, hydrostatic equilibrium is obtained by integrating with respect to z the z momentum equation,

$$\frac{\mathrm{d}\rho}{\mathrm{d}\hat{z}} = -\frac{\rho\hat{z}}{(1+\delta^2\hat{z}^2)^{3/2}}, \tag{10.8}$$

giving us a modified solution

$$\rho(z) = \rho_0 \exp\left[-\frac{1}{\delta^2}\left(1 - \frac{1}{\sqrt{1+\delta^2\hat{z}^2}}\right)\right], \tag{10.9}$$

where ρ_0 is the density at the mid-plane. Using binomial expansion, this solution can be shown to tend towards the standard Gaussian hydrostatic equilibrium when $\delta\hat{z} \ll 1$, in other words when $z \ll r_0$. When $z \to \infty$, $\rho(\infty)$ differs from the Gaussian solution by settling at a floor value of $\exp(-1/\delta^2)$ instead of vanishing to 0.

Similar modified gravity terms to ours have been used by other authors in both modelling accretion (Matsuzaki et al., 1997) and galactic discs (Kuijken and Gilmore, 1989). McNally and Pessah (2015) went a step further to include the effect of vertical shear for their globally vertical horizontally local model for accretion discs. Although a full treatment should in theory also account for the variation of the radial gravity term at large scale heights, as a simplification we assume that this is not important for the flow dynamics we are studying, and only apply the vertical gravity modifications in our 1D models. Recent observations of T-Tauri stars suggest that the typical δ for protoplanetary discs is between 0.03 and 0.2 (Andrews et al., 2009; Gräfe et al., 2013). Unless otherwise stated, we chose $\delta = 0.033$ in our simulations to represent a typical protoplanetary disc.

10.2 Numerical setup and parameters

10.2.1 Numerical code

We used the shearing box module of the astrophysical code PLUTO, developed by Mignone et al. (2007) (see Section 7.1 for more details). The fluxes here are computed by the HLLD Riemann solver unless otherwise stated, and we found no significant differences to our results when we varied the solver. Time stepping is done using a Runge-Kutta method of third order.

10.2.2 Boundary conditions and mass replenishment

Simulations are done for the whole vertical extent of the disc, with both sides of the disc mid-plane explicitly calculated. This is distinct from the approach of Riols et al. (2016), where symmetry was imposed with respect to the disc mid-plane and simulations were restricted to the upper half of the disc. Our approach allows us to explore geometries different from the classical hourglass symmetry wind-launching configuration, as discussed in the introduction. Local simulations (Bai, 2015; Bai and Stone, 2013a, 2014) found that discs may settle into the slanted symmetry, whether in the ideal MHD regime or not. Although such a configuration would not be physical at large z, as it would imply that one part of the field is bending towards the star, recent global simulations (Bai, 2017; Bai and Stone, 2017; Béthune et al., 2017; Gressel et al., 2020) have suggested that in certain radial locations such a symmetry is indeed adopted throughout the vertical extent of the disc region before field lines bend back in the normal manner away from the star further up in the atmosphere. Hence it will be useful to relax the symmetry assumptions of the solution to explore what factors contribute to the disc adopting a particular configuration.

Following Bai and Stone (2013a), we use an outflow boundary condition in the vertical directions that has zero vertical gradient for velocity and magnetic fields, while density is attenuated to account for vertical gravity. This attenuation significantly reduces the excitation of spurious artificial waves near the boundary. Lesur et al. (2013) noted that care is needed in implementing the boundary conditions for the magnetic field, as they found that using a zero vertical gradient condition prevented an outflow from being launched. However, this was not found to be the case in our simulations. An explanation for this may be that all the outflows in our simulations are super-Alfvénic, and therefore much less sensitive to the field configuration at the boundary than some of the sub-Alfvénic outflows they were investigating. Nevertheless, we ran simulations using both a vertical field boundary condition, and fixing the horizontal fields to finite values at the boundary, and found them to have negligible impact on our results.

In a global disc, radial redistribution of the material would replenish mass in a local patch that is lost to the wind. We mimic this in our local model by injecting mass near the mid-plane at each numerical time step. In the system of equations, this is equivalent to adding a source term in the mass conservation. We use the same source term as prescribed by Lesur et al. (2013),

$$\zeta(z,t) = \frac{2\dot{m}_i(t)}{\sqrt{2\pi}z_i} \exp\left(-\frac{z^2}{2z_i^2}\right), \tag{10.10}$$

where $\dot{m}_i(t)$ is the mass injection rate, and z_i controls the width of the region about the mid-plane where most of the mass replenishment occurs. For most simulations, we replenish the mass such that a constant disc surface density $\Sigma = \int_{-L_z}^{L_z} \rho \mathrm{d}z$ is maintained in time, but we also explored the effect of other schemes, described in Section 10.3.4. It is important to note though that such injection of mass breaks momentum conversation in the shearing box, as the mass is injected with the local velocity (injecting momentum so that the velocity stays the same), while it leaves the domain with a different velocity at the upper and lower boundaries. The loss of horizontal momentum from the box (including that from a torque exerted at the vertical boundaries by the Maxwell stress), drives a mean horizontal flow, which was interpreted by Riols et al. (2016) as the accretion flow for the x component, together with a small departure from Keplerian motion for the y component.

10.2.3 Box size and resolution:

As pointed out by previous authors (Fromang et al., 2013; Lesur et al., 2013), the choice of box size (which we label here as $2L_z$, with L_z being the maximum height above the mid-plane) and boundary conditions can have a strong effect on the wind solution obtained. This is especially the case when critical points of the wind flow (see definitions in Ogilvie (2012)) lie outside the simulation domain, allowing information to be propagated from the box boundaries back to the disc and affecting its behaviour. For the weak field strengths we consider in our simulations, the slow magnetosonic point and Alfvén point are always crossed within the box as long as $L_z \gg H$. However, like the simulations of Riols et al. (2016) and in line with other studies (Lesur et al., 2013), we are unable to find solutions that pass through the fast magnetosonic point. Hence it is possible that the vertical boundaries still have an effect on the nature of our wind solutions, although we find that the properties of our steady wind solutions converge with increasing box height, while the phenomenology of the wind behaviours is also independent of box size as long as $L_z \gg H$ (see Section 10.3.4).

Another cause of non-convergent wind properties with increasing box size in traditional shearing boxes is the nature of the standard shearing box gravity term being linear in z,

leading to the gas being trapped in an infinite potential well. This effect has largely been mitigated through the use of the modified gravity term we have adopted from Riols et al. (2016), and becomes negligible when $L_z/H > 1/\delta$, which in our case of $\delta = 0.033$ translates to $L_z > 30H$.

We mainly use two box sizes for our simulations. The first is a relatively 'small' box of $L_z = 12H$, while the second is a 'large' box with $L_z = 70H$. The latter is chosen as it satisfied the considerations outlined above with the exception of crossing the fast magnetosonic point for the parameter space we explore. However, running simulations in such tall boxes is costly, as they require a large number of grid points to resolve the dynamical features appropriately. We find that the phenomenological behaviour of the wind states in the tall box are the same even in much smaller boxes. Since our interest in this paper is in gaining an understanding into the mechanisms behind the generation of these wind states, rather than trying to predict the precise properties of real discs, we use the 'small' box simulations to further our exploration of the parameter space and their effects on disc behaviour.

For the $L_z = 12H$ small boxes, we use 200 grid points to resolve the mid-plane region $|z| < 2H$, while the two atmospheric regions $|z| > 2H$ are spanned by 500 points each. For large boxes with $L_z = 70H$, we also use 200 grid points to resolve the mid-plane region $|z| < 2H$, while the atmospheric regions $|z| > 2H$ have 2400 grid points each. The finer grid in the mid-plane region is motivated by small-scale structures that arise more naturally near the mid-plane. We vary the resolution to make sure that solutions are not drastically affected by the values we have chosen.

10.2.4 Physical parameters

The surface density in all simulations is fixed to be equivalent to that of a hydrostatic disc with mid-plane density $\rho_0 = 1$, which sets our unit of mass. We use units such that μ_0, c_s and Ω are set to 1. The magnetic field B_z, independent of z and t in the shearing box formulation, is derived from the mid-plane β_z (ratio of gas pressure to magnetic pressure),

$$\beta_0 \equiv \frac{2\mu_0 c_s^2 \rho_0}{B_z^2}, \tag{10.11}$$

which we set as a dimensionless parameter for the problem.

As we are primarily interested in investigating how the general shape of the diffusivity profile affects the phenomenology of the disc and wind, it is not necessary for us to solve the complex chemical networks to determine a precise profile for the resistivity. In a protoplanetary disc the resistivity is high near the mid-plane but much lower in the atmosphere, where the signficant ionisation due to FUV radiation and X-ray heating lead to near-ideal MHD

conditions. To mimic this situation, we use a simplified analytic η profile which has a fixed constant value in the disc mid-plane region, before decaying exponentially to a floor value in the atmosphere. Mathematically, this is given by

$$\eta = \begin{cases} \eta_0, & |z| < z_c, \\ (\eta_0 - \eta_\infty)\exp\left[-5(|z| - z_c)\right] + \eta_\infty, & |z| > z_c. \end{cases} \tag{10.12}$$

η_0 and η_∞ are the mid-plane and atmospheric diffusivity values respectively, while z_c sets the height at which the transition occurs. To estimate suitable values to use for our simulations, we used the ionisation model of Lesur et al. (2014) coupled with accounting for dust-enhanced recombination from Béthune and Latter (2020) (where the ionisation fraction further lowered by a factor of 10^2) to yield mid-plane η_0 values of 5.8 $H^2\Omega$ and $1.07 \cdot 10^{-2}$ $H^2\Omega$ at disc radii $R = 1$ and 5 AU respectively. Ionisation calculations (in the absence of FUV radiation) indicate an increase in the ionisation fraction, x_e, by a factor of between 10^2 and 10^4 from the mid-plane to the atmosphere at these radii (see figure 1 of Béthune and Latter (2020)). This in turn corresponds to a decrease of between 10^{-2} and 10^{-4} in the resistivity, which varies as x_e^{-1}. When FUV is included, this increases the ionisation fraction in the upper regions beyond $|z| = 4H$ even further to near ideal MHD conditions. For most simulations, we used $\eta_0 = 2\ H^2\Omega$, representative of the conditions in the inner disc, while we varied the floor value η_∞ from $1/200$ that of the mid-plane value (for most simulations), down to 0 to examine the effects of ideal MHD atmospheric conditions on the solutions we obtain. z_c is set to $2H$ for all simulations, which follows the ionisation depth for FUV photons estimated in Simon et al. (2015) for the $\eta_\infty = 0$ case, while this cut-off height also corresponds well with the ionisation profile of Béthune and Latter (2020) in the absence of FUV when the higher η_∞ value of 0.005 $H^2\Omega$ is used.

We mostly assume inviscid discs, motivated again by the laminar protoplanetary disc solutions recovered in local and global simulations. For simulations with large boxes ($L_z > 30H$), we found that strong numerical instabilities appear near the upper and lower boundaries in our steady wind solutions. In order to avoid these instabilities, we followed the prescription of Riols et al. (2016) by introducing a small, uniform dynamic viscosity $\rho\nu$, such that the kinematic viscosity $\nu \propto 1/\rho$ has the value 10^{-5} in the mid-plane but increases with $|z|$. We found that while the general shape of the solution is not changed significantly by this addition, numerical instabilities are indeed smoothed out when the viscosity is included. As noted in Riols et al. (2016), this prescription might also be physically relevant in the isothermal case, as ν can be estimated as the product of the thermal velocity and the mean free path, which scales as $1/\rho$ (Maxwell, 1866). For our runs with $L_z < 30H$ we used a zero viscosity treatment, while we only added the artificial viscosity for runs with $L_z > 30H$ as the solutions tend towards the steady state.

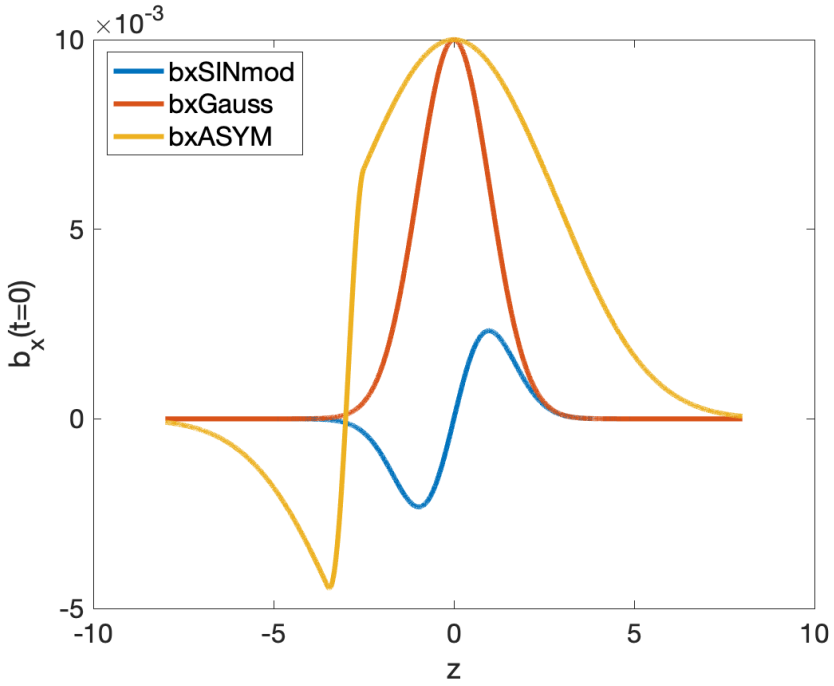

Fig. 10.1 Initial b_x profiles, see Section 10.3.1 for their analytic forms.

10.3 Categorisation of wind solutions

10.3.1 Initial conditions and obtaining a solution

It is not practical to initialise a simulation in a tall box with a small δ value from a hydrostatic equilibrium state, because the very low density in the atmosphere leads to a very high Alfvén speed that forces the time-step to be extremely small. We used two different methods to obtain wind solutions (which have much higher atmospheric densities than the hydrostatic state) in our extended boxes. The first loosely follows the prescription of Riols et al. (2016). We start with a medium box of size $L_z = 15$ and a high δ value of 0.33, which leads to a floor density of $1.028 \cdot 10^{-4}$ in the modified hydrostatic equilibrium. The disc is embedded in a vertical field of a strength corresponding to the value of β that we wish to investigate. Small random perturbations in the velocity profiles are then introduced, which are amplified by the MRI instability. As the wind solution develops, the density profile becomes more spread out, reaching above 10^{-3} at the boundaries. After the solution has reached steady state, we slowly reduce δ back to our desired value of 0.033, while we extend the size of the box gradually by uniform extrapolation of the boundary values, and allowing each model to settle into the new equilibrium wind solution. Using this method, we were able to obtain the slanted symmetry steady states described in Section 10.3.2. However, unlike in Riols et al. (2016), we did not

find that the wind solution bifurcates to a periodic outflow as the box size was increased beyond a certain height. Rather, solutions initiated with steady state profiles of smaller boxes always relaxed to the same type of steady state profiles, with converging wind properties.

The second method began with a medium box of size $L_z = 12$ and the desired δ value of 0.033. Again, we used a hydrostatic disc threaded by a vertical field as the initial condition, except this time we arbitrarily added a small fraction of the mid-plane density to the entire disc, to avoid the high Alfvén speeds that lead to impractically small time-steps in the atmosphere. For most simulations, a value of 10^{-4} in code units was chosen, motivated by the typical density measured by Riols et al. (2016) at their upper disc boundaries.

Instead of using random velocity perturbations, we started the simulations with three different profiles of B_x to examine the excitation of MRI modes of different symmetries, and its effect on the wind solutions obtained. The first, denoted 'bxSINmod', has the form

$$B_x(t=0) = 0.01 B_z \sin[k_z z] \exp(-z^2/2), \tag{10.13}$$

where $k_z = 2\pi/L_z$ is the wavenumber of a complete wave across the vertical domain, giving the initial profile an hourglass symmetry about the mid-plane. The second profile, 'bxGauss', explores perturbations with a slanted symmetry, and is simply a Gaussian function,

$$B_x(t=0) = 0.01 B_z \exp(-z^2/2). \tag{10.14}$$

The third, denoted 'bxASYM', explores the effect of starting with an asymmetric profile about the mid-plane but with an hourglass geometry in the atmosphere, motivated by the asymmetric steady state profiles observed in both local and global simulations (Bai, 2017; Bai and Stone, 2013a). It has the form

$$B_x(t=0) = 0.01 f(z) B_z \exp(-z^2/15), \tag{10.15}$$

where

$$f(z) = \begin{cases} -\cos(k_z(z+3.5)/2), & z < -3.5 \\ \cos(\pi(z+2.5)), & -3.5 < z < -2.5 \\ 1, & |z| < 2.5 \\ \cos(k_z(z-2.5)/2), & z > 2.5 \end{cases}. \tag{10.16}$$

A plot showing these initial B_x profiles is shown in Figure 10.1 (note the lower case 'b' denotes normalisation with respect to B_z).

Under these conditions, we found that solutions relax, depending on the initial conditions used, to one of two cyclical states that persist for 100s of orbits, before a growing mid-plane perturbation slowly transited the disc to the steady state profile of slanted symmetry obtained

using the first method. We restarted simulations from both the cyclic states and the slanted symmetry steady state in taller boxes with constant extrapolation to examine the effect of the extended vertical domain. We found that the same type of wind behaviour is retained, with the solution converging to an extended version of either the cyclic or slanted symmetry steady wind solutions of the smaller box runs. For the cyclic solutions, an eventual convergence to the steady wind solution is then again observed after a timescale of 100s of Ω^{-1}.

Note that the runs are named such that the numbers after 'b' denote the β_0 value, while the letter after the underscore denotes the initial b_x profile, with 'A' for 'bxASYM', 'S' for 'bxSINmod' and 'G' for 'bxGauss'. Unless otherwise labelled in the name, all runs have $\delta = 0.033$, $\hat{z}_i = 0.5$ and $L_z = 12H$. For example, **b1e5_S** has $\beta_0 = 10^5$ and is initiated from the 'bxSINmod' profile, while **b200_G** has $\beta_0 = 200$ and is initiated from the 'bxGauss' profile.

10.3.2 Phenomenology of wind solutions

In our simulations, the wind solutions obtained can be put into four general types: (i) a cyclic solution with hourglass (odd-z in $b_{x,y}$) symmetry about the mid-plane, (ii) a cyclic solution with slanted (even-z in $b_{x,y}$) symmetry about the mid-plane, (iii) a cyclic to steady wind transition state, and (iv) a steady wind solution with slanted (even-z in $b_{x,y}$) symmetry about the mid-plane. All four types of behaviour can be seen in the space-time plots of b_y in Figure 10.2. In general, simulations begun with a slanted symmetry initial condition (the 'bxGauss' profile) move into the slanted symmetry cyclic state, while those began with an hourglass symmetry initial condition (the 'bxSINmod' profile) settle into the odd symmetry cyclic state. Simulations started with the 'bxASYM' profile were found to settle into the hourglass symmetry cyclic state. After 100s of Ω^{-1}, a mid-plane perturbation exits these cyclic states through an intermediate and short-lived transition state to the slanted symmetry steady state. After that, no further qualitative changes were observed. Below, we give a more detailed description of the properties of each of the four states and their behaviour.

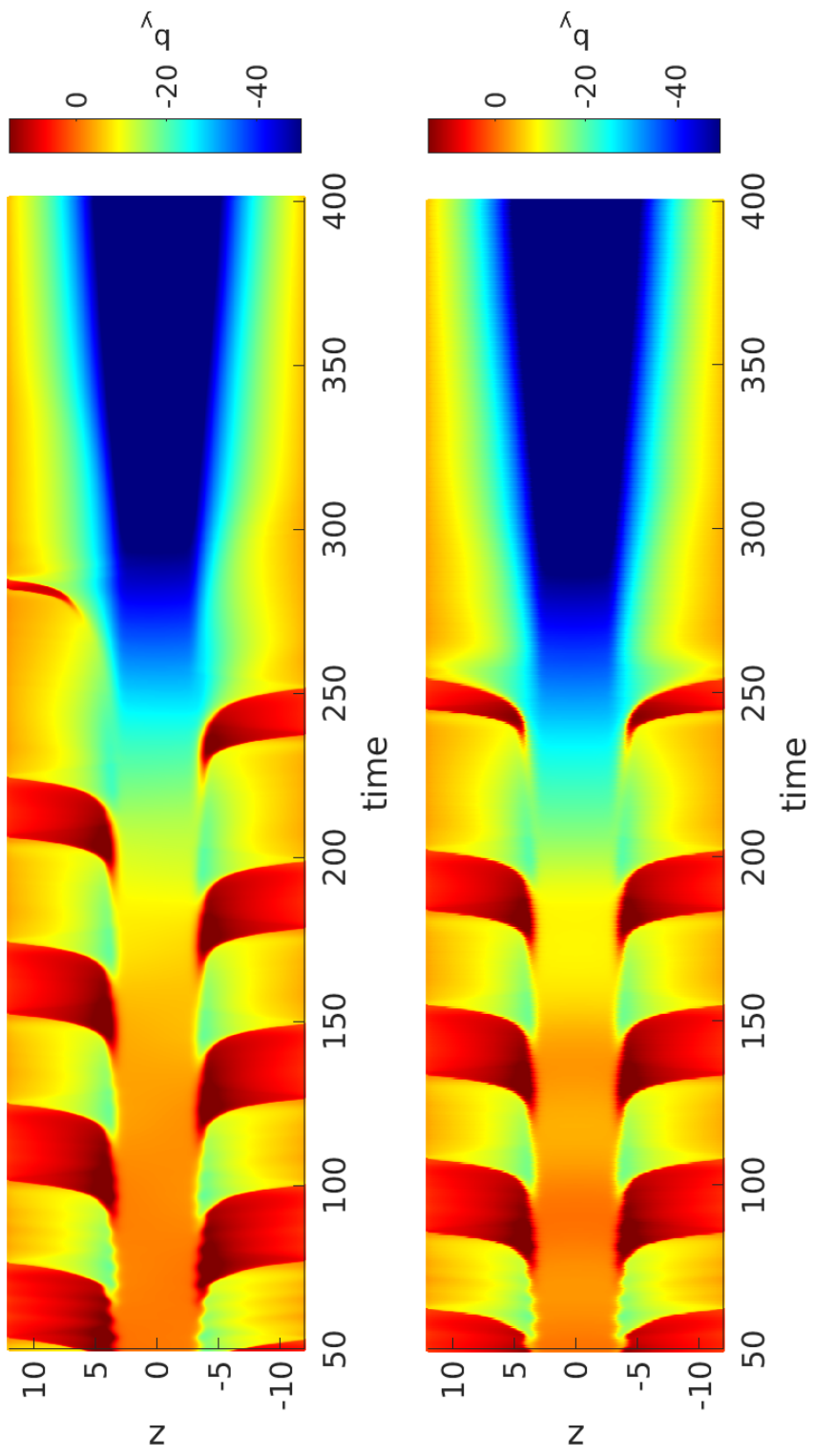

Fig. 10.2 Space-time plots of b_y for the situations where: (top) an hourglass symmetry cyclic state transits to the slanted symmetry steady state, and (bottom) a slanted symmetry cyclic state transits to the slanted symmetry steady state. The first 50 time units are not displayed as the runs are still in a chaotic transient phase with drastic variations that are strongly dependent on the particular initial conditions used. The runs depicted are **b1e5_A** and **b1e5_G** respectively.

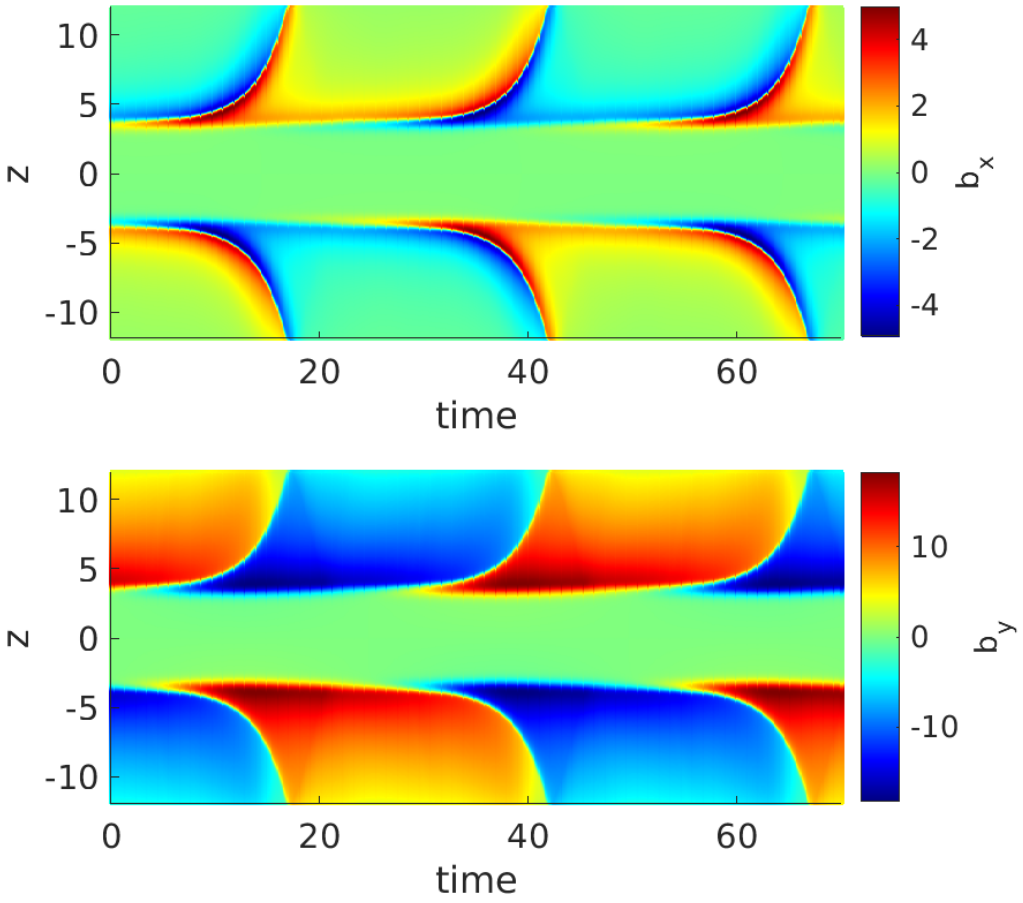

Fig. 10.3 Space-time plot of b_x (top) and b_y (bottom) for the hourglass symmetry cycles observed in run **b1e5_S**.

Hourglass symmetry cycles

The hourglass symmetry cycles are long-lived time-dependent states where horizontal magnetic fields b_x and b_y have opposite signs across the mid-plane, and the horizontal velocity fields v_x and v_y are even in z. As an example, we consider here the cyclic solutions obtained for run **b1e5_S**, with parameters $\beta_0 = 10^5$, $\delta = 0.033$, $\hat{z}_i = 0.5$, and initiated from the 'bxSINmod' profile. Figure 10.3 shows the space-time variation of the horizontal magnetic fields b_x and b_y, where the lower case b denotes that they have been normalised with respect to the vertical field strength. Owing to the hourglass symmetric nature of the solutions, we only describe the upper half of the disc where $z > 0$.

The period of the cycle is roughly equal to $50\Omega^{-1}$, i.e. eight orbital periods, and is divided equally into two half-cycles where the dynamics are identical with the exception of the horizontal magnetic and velocity fields being oppositely signed. The vertical outflow,

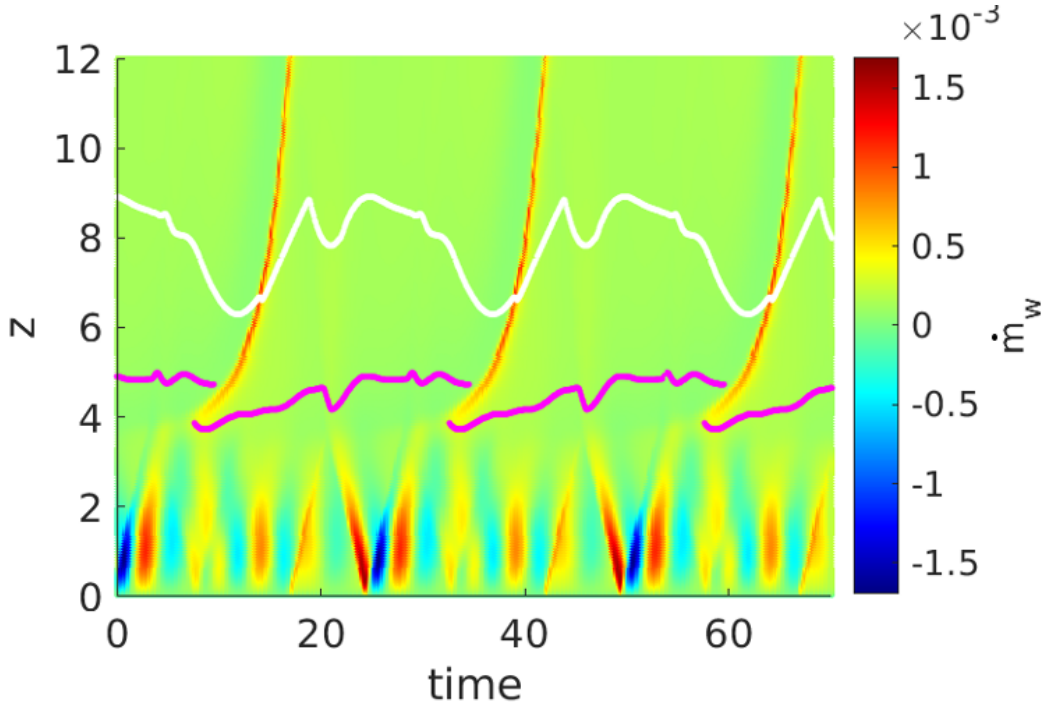

Fig. 10.4 Space-time plot of $\dot{m}_w$ for the hourglass symmetry cycles observed in run **b1e5_S**. The white line indicates the sonic point, while the magenta line marks the Alfvén point(s).

$\dot{m}_w$, defined as the average from the boundary at one side of the disc, is not affected by this change of sign, and repeats itself every half-cycle with a period of roughly $25\Omega^{-1}$. A strong and brief outburst roughly 6 times the quiescent value at the boundary marks the end of each half-cycle. We observe a slow and minute sinusoidal oscillation of the mid-plane horizontal fields about 0 with the same period as the overall cycle. The horizontal magnetic fields b_x and b_y are always anti-correlated with each other, and drive radial accretion or decretion flows by vertical transport of angular momentum through the $B_y B_z$ stress depending on the sign of the fields. Figure 10.4 shows the spatial variation and temporal evolution of the vertical outflow in time. The location z_{Az} of the Alfvén point, defined as the point above which v_z exceeds v_{Az}, fluctuates between $z = 4H$ and $z = 5H$. It is interesting to note here that z_{Az} is generally lower than the sonic point z_s, a consequence of the relatively weak-field regime explored in our simulations. The fast magnetosonic point is mostly approached at the simulation domain boundary, but sometimes crossing briefly occurs in the simulation domain though without significant impact, due to fluctuations in the b_x and b_y profiles as the outbursts pass through the atmosphere.

The quiescent stage outflow is largely steady, with $\dot{m}_w \sim 1.4 \times 10^{-4}$ in code units. In the atmospheric region $z \sim 3.8 - 7.5H$, the inclination of the poloidal field with respect to the vertical axis is significantly larger than the critical value of 30° (which is a necessary

but not sufficient criterion for a magneto-centrifugal outflow), allowing a steady wind to be launched from $z \sim 4H$ and gas to be accelerated along field lines by the magneto-centrifugal effect. The outflow is then further enhanced by the magnetic pressure gradient in the upper atmosphere before it leaves the box.

The outburst is initiated around $z \sim 4H$ at $t = 8\Omega^{-1}$, when b_x and b_y are both significantly growing in the same region and are about to reach their maximum field strengths in the half-cycle. The shape of the growing horizontal fields consists of a mid-plane region where they are flat and near zero, before developing into two peaks of opposite signs in quick succession beyond $z \sim 3H$. The peaks of b_x and b_y are then accelerated upwards out of the box, with the outburst following the point where the magnetic pressure gradient is greatest between the maximum and minimum peaks of b_x and b_y. This indicates that the gas parcel is pushed out of the box by the horizontal magnetic field peaks leaving the vertical domain. The outburst lasts for a duration of $\sim 3\Omega^{-1}$, and at its peak has $\dot{m}_w = 8.55 \times 10^{-4}$, up to 6 times the quiescent value. However, the amount of gas ejected per outburst, 7×10^{-4}, is still only a tiny fraction of the overall disc mass $\Sigma = 1$, and compares with 2.9×10^{-3} that is ejected over the longer quiescent interval between the outbursts. The peaks in b_x and b_y start decreasing in magnitude as they move beyond $z \sim 4.7H$. At this time, a peak of the same sign slowly develops behind the lower altitude peak at around $z \sim 4H$ which eventually becomes the higher altitude peak for the next outburst, while a peak of the opposite sign begins developing at $z \sim 3H$, becoming the new lower altitude peak. The next half-cycle then repeats the same dynamics, except the horizontal magnetic and velocity fields have now effectively switched signs compared with the previous half-cycle.

Slanted symmetry cycles

Like the hourglass symmetry cycles, these solutions are long-lived time-dependent states, but with b_x and b_y being even in z, while v_x and v_y are odd. In almost all properties, these cycles are identical to the hourglass symmetry cycles, with the b_x and b_y having small amplitudes and a nearly flat profile in the disc region ($|z| < 3H$), while in the atmosphere, cycles of outburst up to 6 times the mass flux of the quiescent steady outflow are driven by the same form of b_x and b_y peaks growing and moving up out of the vertical domain of the box. From Figure 10.2, we can see that the slanted and hourglass symmetry cycles under the same simulation parameters share the same period of around $50\Omega^{-1}$ for $\beta_0 = 10^5$, $\delta = 0.033$, $\hat{z}_i = 0.5$, and $L_z = 12$, a property which is also observed for other sets of simulation parameters. This suggests that the high diffusivity in the mid-plane region effectively cuts off magnetic communication between the upper and lower halves of the disc, and since these cycles are connected to and driven by the growth and movement of peaks in b_x and b_y, there

is (similar to Bai and Stone (2013a)) an equal chance of adopting either symmetry unless it is already set by the initial condition.

Cyclic to steady wind transition state

The hourglass and slanted symmetry cycles typically survive on a timescale of 100s of Ω^{-1}, with a weaker vertical field leading to a longer survival time. In fact, for runs initialised using 'bxSINmod' with $\beta_0 = 10^5$ and 10^6, the hourglass symmetry cyclic solutions show no sign of transitioning throughout the entire run time of the simulation up to $700\Omega^{-1}$. Transition to the intermediate state begins with a small mid-plane bulge in b_x which gets sheared into a corresponding mid-plane bulge of opposite sign in b_y. This bulge then grows slowly but exponentially in magnitude, as shown in Figure 10.5 for runs **b1e5_A** (solid lines) and **b1e5_G** (dashed lines). As long as the magnitude of the bulge in b_y is lower than that of the b_y peaks of the hourglass/slanted symmetry cycles, there is minimal effect of the growing mid-plane dynamics on the properties of the cyclic wind states, with both the magnitudes and periods of the cycles on the whole unaffected. However, once the mid-plane b_y has reached the magnitude of maximum wind cycle b_y peak strength, the period of the half-cycle lengthens or shortens if the sign of the mid-plane b_y is of the same or opposite sign of the higher altitude b_y peak respectively. The nature of the solution then changes to that of a steady wind over the next half-cycle, and the cycles stop. As in the case with the hourglass/slanted symmetry solutions, the mid-plane region disconnects the two sides of the disc, and each side of the disc effectively behaves independently from the other and interacts with mid-plane region individually.

Slanted symmetric steady state

For our simulations in Figure 10.2 with $\beta_0 = 10^5$, at around $t = 300\Omega^{-1}$, the exponential growth of the mid-plane b_x and b_y slows down, and a steady wind solution is reached by $t = 500\Omega^{-1}$. Throughout the saturation stage, the disc has a slanted symmetry with b_x and b_y even in z and of opposite signs, while v_x and v_y are odd in z. b_x and b_y have large amplitudes (> 1) and a flat profile near the mid-plane, but $\partial_z b_x, \partial_z b_y \neq 0$ at the z boundaries of the box. A plot showing the profile for $\beta_0 = 10^5$ is shown in Figure 10.6. b_x has amplitude maxima in the region where the b_x peaks are observed to start growing in the cyclic phase ($|z| \sim 3.15H$), while b_y has its amplitude maximum at the mid-plane. The flat mid-plane profiles of b_x and b_y may be attributed to the large diffusivities there suppressing bending of the field lines, while the absolute strength of the magnetic field at the mid-plane corresponds to $\beta = 7.95$. b_x and b_y in the atmosphere always tend towards zero as $|z|$ increases. The Alfvén point occurs

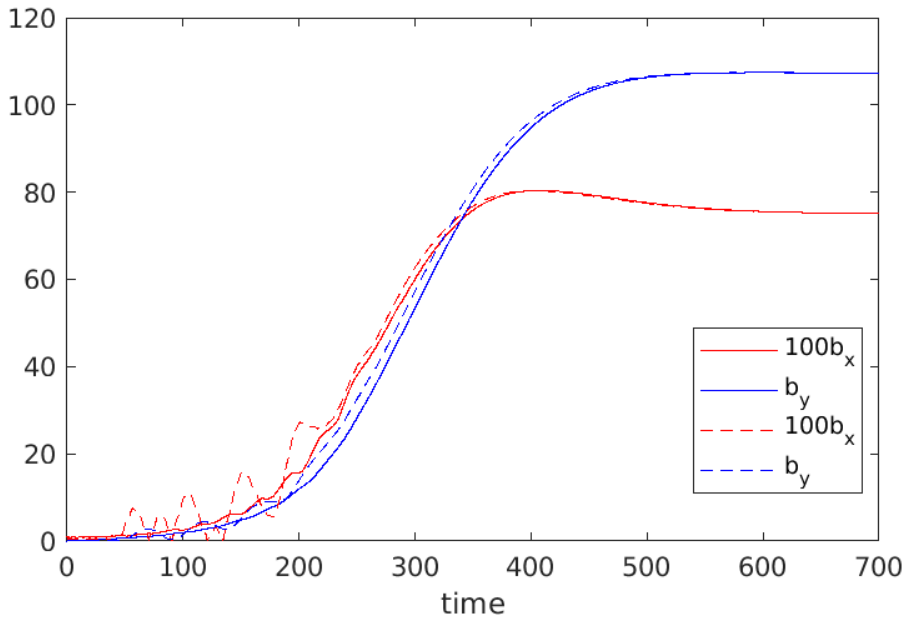

Fig. 10.5 Plot of mid-plane b_x (red) and b_y (blue) against time for **b1e5_A** (solid lines) and **b1e5_G** (dashed lines).

at around $|z| = 2.7H$, while the fast magnetosonic point is approached at the simulation domain boundary but not crossed. A strong, steady and slow wind of up to 10 times the $\dot{m}_w$ value of the quiescent state in the cyclic phase is launched.

10.3.3 Dependence on the vertical field

We varied the vertical field strength from $\beta_0 = 10^2$ to $\beta_0 = 10^6$ and examined its effect on both the cyclic state of hourglass symmetry, and its transition to the slanted symmetry steady wind solution.

Cyclic state

The variation of several key properties of the cyclic solution with β_0 are shown in Figure 10.7. For the cyclic states, as β_0 decreases, the mid-plane horizontal fields b_x and b_y become less flat, as the increased magnetisation allows a stronger current to flow there despite the higher resistivity. However, most of the bending still occurs above the region $|z| \sim 3H$, while the positions of the peaks as they grow are similarly located in the lower atmospheric region where η decreases dramatically to the atmospheric value. The period of the cycles generally shortens as the magnetisation is increased, although it reaches a minimum value at around $\beta_0 = 500$ beyond which the period increases slightly again. Both the outburst and

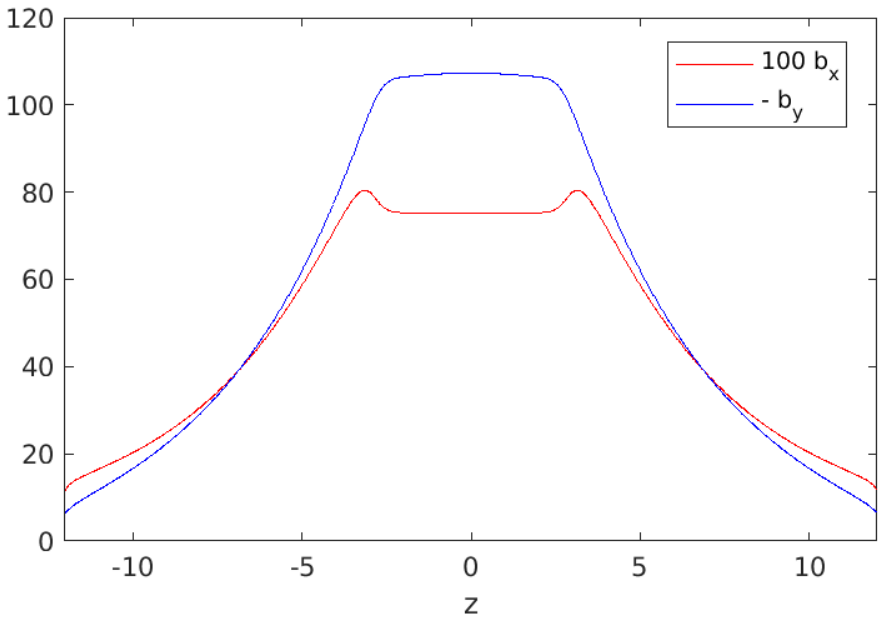

Fig. 10.6 Vertical profiles of b_x and b_y for the slanted symmetry steady state with $\beta_0 = 10^5$.

quiescent outflow strength increase as the magnetisation increases, and the vertical flow also becomes quicker with a lower sonic point. While the Alfvén point continues to vary within each half-cycle, the range of heights over which it varies stays roughly the same between $4H < |z| < 5H$ from $\beta_0 = 10^5$ to 5000, before drastically increasing and covering the whole simulation domain by $\beta_0 = 200$. The height from which the outburst is launched is always located at the lower atmosphere, although it decreases from $|z| \sim 4.7H$ to $|z| \sim 2.8H$ as the magnetisation is increased from $\beta_0 = 10^5$ to 200.

Transition state

For the transition to the slanted symmetry steady wind, an increase in field strength leads to less time spent in the cyclic state of hourglass symmetry, and a more rapid transition. Empirically, we find that the mid-plane b_x and b_y bulge initial growth rate satisfies the relation

$$\sigma \approx 10^{0.41} \cdot \beta_0^{-0.44}, \tag{10.17}$$

where σ is the growth rate measured before saturation flattens out the exponential growth profile. Figure 10.8 plots σ against β_0 and the empirical fit we are able to obtain. This roughly gives us $\sigma \propto B_z$, suggesting that the mid-plane growth mechanism is magnetic in nature. The tendency for more strongly magnetised discs to more rapidly transit to the slanted

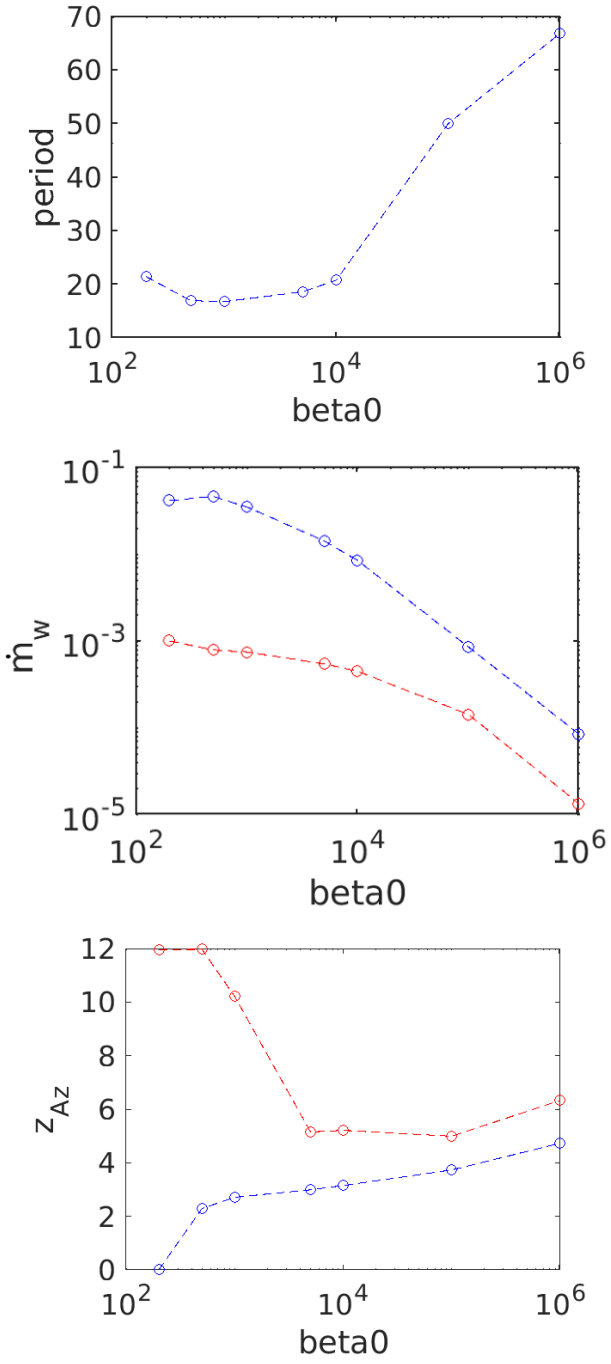

Fig. 10.7 Variation of wind properties with β_0 for the hourglass symmetry cycles. The left panel shows the period of the cycle. The middle panel shows the average quiescent outflow strength (red) and average outburst strength (blue). The right panel shows the minimum (blue) and maximum heights (red) of the Alfvén point(s) in the cycle.

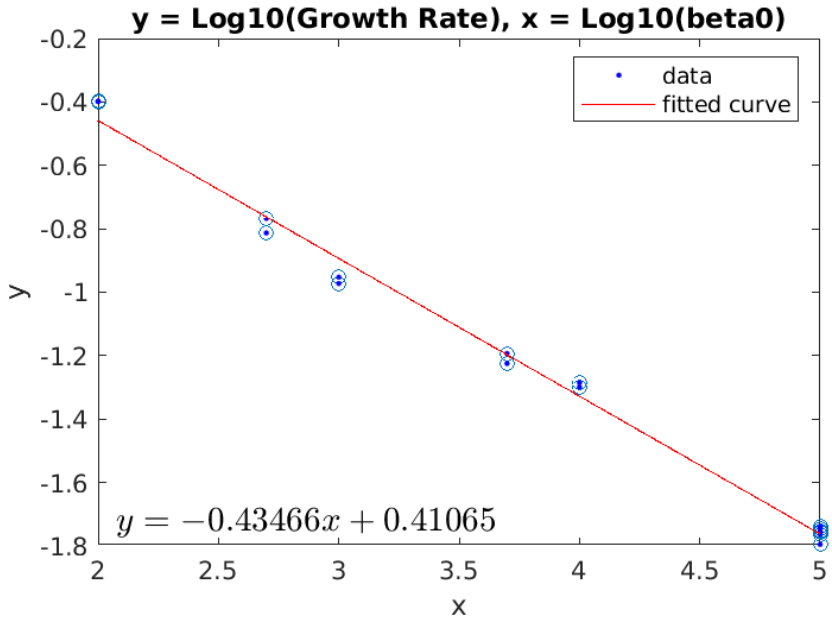

Fig. 10.8 Plot of log10 of exponential growth rate (y) against log10 of β_0 (x) with best fit line.

symmetry steady wind solution has been previously noted in the simulations of Bai and Stone (2013a), with the difference between our simulations being that they used more realistic diffusivity profiles, while ambipolar diffusion was also included. However, they did not examine the mechanism behind the transition, and only attributed it as possibly due to an increased difficulty in maintaining a strong current layer in the lower atmosphere (as seen in the cyclic stage with the b_x and b_y peaks) as the field strength is increased.

Steady wind

Finally, we examine the variation of the properties of the steady state slanted symmetry wind with disc magnetisation, which are plotted in Figure 10.9. The mass loss rate decreases with decreasing field strength and follows a power law of the form

$$\dot{m}_w \propto \beta_0^{-0.51}. \tag{10.18}$$

This is again similar to the relation obtained in Bai and Stone (2013a) for their slanted symmetry steady winds, where the index has a value of -0.54. Both of these values roughly give us $\dot{m}_w \propto B_z$, and again suggest that the vertical magnetic field still has a crucial role to play in the launching of the outflow despite being dominated by the horizontal fields in the wind-launch region. The value of the overall mid-plane β decreases slightly from 7.95 for $\beta_0 = 10^5$ to 1.15 for $\beta_0 = 10^2$, but its magnitude remains of order unity. The Alfvén point generally falls with magnetisation, and flattens off beyond $\beta_0 = 5000$ to $z_{Az} \sim 2.6H$.

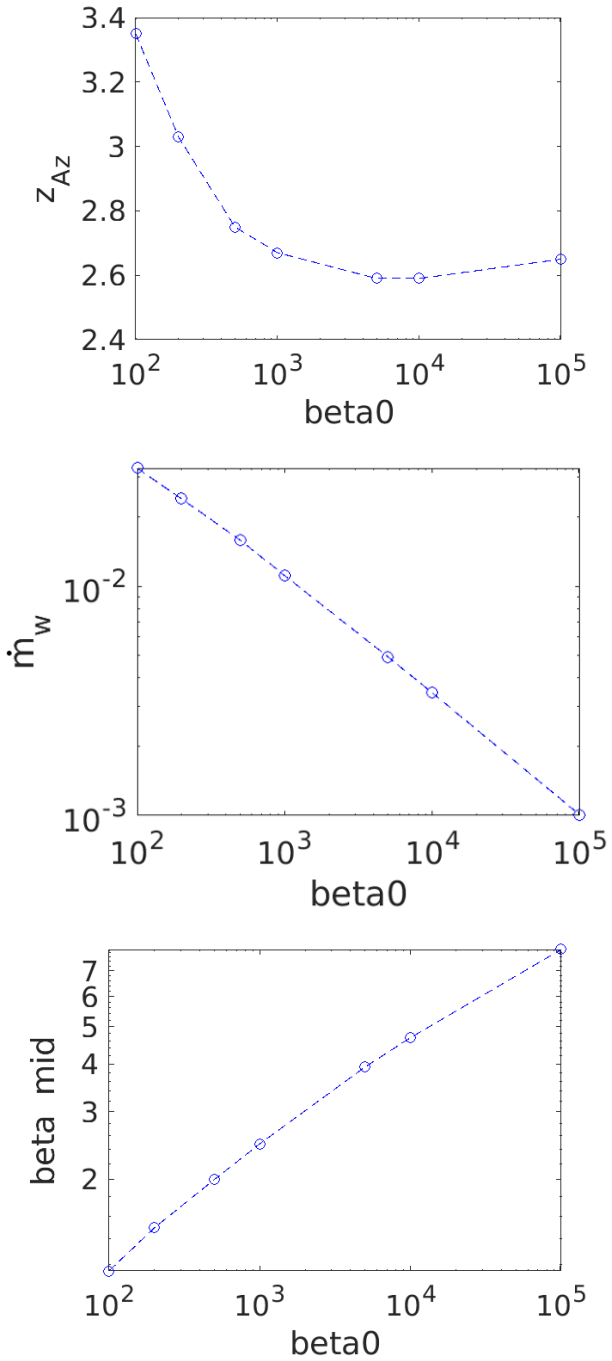

Fig. 10.9 Variation of wind properties with β_0 for the slanted symmetry steady state. Left: position of z_{Az}, middle: outflow strength $\dot{m}_w$, right: plasma β value taking into account all three magnetic field components at the mid-plane.

Table 10.1 Comparison between $L_z = 12H$ and $L_z = 70H$ runs. For the cycles, the lower $\dot{m}_w$ value is for the quiescent outflow, while the higher one is for the outburst, whereas the Alvén points indicate the range within which they vary.

Property	$12H$ cycles	$70H$ cycles	$12H$ steady	$70H$ steady
Period (Ω^{-1})	50	57.6	NA	NA
$\dot{m}_w$ (10^{-4})	1.4, 8.6	0.48, 5.3	10	6.02
z_{Az} (H)	[3.7, 5.0]	[3.6, 5.6]	2.65	$\tilde{3}$
$b_{x,\max}$	5.0	8.5	0.804	0.86
$b_{y,\max}$	18	23	107	121
β_{mid}	NA	NA	7.95	5.54

10.3.4 Robustness of the wind behaviour

Variation of box sizes

In order to confirm that our wind behaviour is not a result of our small box size of $L_z = 12H$, we also ran simulations for our $\beta_0 = 10^5$ simulations in boxes with $L_z = 70H$. We found that the same types of wind behaviour are preserved. A comparison of the key properties between runs at the two different scale heights is listed in Table 10.1.

For the hourglass symmetry cycles, we found that both periodicity and mass loss rate converge as box size is increased. Our $L_z = 70H$ cycles have a period of 57.6 Ω^{-1} compared with a period of 50 Ω^{-1} in our $L_z = 12H$ runs. Both the quiescent and outburst outflow strengths are slightly weaker in the taller box, which is expected as a larger box means a greater gravitational potential for the gas to overcome to escape from the box. The b_x and b_y peaks in the cycles are slightly increased in magnitude as L_z increases, and is probably because of the reduction of the escaping flux at the boundaries due to the smaller mass outflows (Suzuki et al., 2010). The overall cycle dynamics, including the relative positions of the wind launch point, the b_x and b_y peaks, and the variations of the Alfvén points, remain roughly the same.

For the transition state, the mid-plane bulge exponential growth rate converges as box size is increased and is only slightly modified, with $\sigma = 0.2$ for our $L_z = 70H$ runs, compared with $\sigma = 0.18$ for $L_z = 12H$.

The steady wind state shows similar trends in convergence to the cyclic state, with a slightly lower mass loss rate in the taller box as we would expect, and fractionally higher horizontal magnetic field strengths. Otherwise, there is no qualitative difference between the steady wind profile of the smaller box compared with the larger one.

Overall, the fact that most properties of our wind solutions were only slightly altered between our $L_z = 12H$ and $70H$ simulations justifies our usage of the more computationally

cost-friendly $L_z = 12H$ runs to explore the parameter space, and determine the mechanisms responsible for the different types of wind behaviour we have observed.

Mass replenishment

In order to check that the forms of the wind solution are independent of the mode of artificial mass injection, we used two different mass replenishment schemes: narrow and wide. The narrow scheme is the one used in our simulations unless otherwise stated, applying the source term of Lesur et al. (2013) and Riols et al. (2016), as presented in equation 10.10, with $z_i = 0.1$ such that mass is injected a narrow $|z| < 0.1H$ region about the mid-plane. The wide scheme, denoted 'mrw', injects mass in proportion to the local density instead, and was used in the simulations of Bai and Stone (2013a). For both injection schemes, mass replenished at each time-step is equivalent to the mass lost at the boundaries, so that the total mass of the disc is kept constant.

We found that while the four types of wind solutions still occur when we used the 'wide' scheme, there are small differences ($< 10\%$) to the locations of the $b_{x,y}$ peaks in both the cyclic phases and the slanted symmetry steady state. In general, their locations are higher up in the disc, which may reflect the fact that under the 'wide' scheme, the disc's density profile is more spread out than the 'narrow' scheme, as mass is injected at every point rather than simply the mid-plane region. This would then imply that the locations of the growth peaks are tied to the relative strength of the vertical field to the density at that point. Another small but notable difference between the 'wide' and 'narrow' schemes is in the cycle dynamics. In our runs for $\beta_0 = 10^5$, while the b_x and b_y peaks in the 'narrow' scheme are always monotonically moving away from the mid-plane, the peaks in the 'wide' scheme have a brief period of small oscillations of its position in the region $3H < |z| < 4.75H$ during which its growth rate also decreases and increases, before the same rapid acceleration out of the box occurs once they pass beyond $|z| \sim 4.75H$. Again, we attribute this difference to the fact that the 'wide' scheme artificially changes the density profile across the whole disc, and points to the sensitivity of the cycle mechanism to the density profile in the $3H < |z| < 4.75H$ region as the reason for the small oscillation in the b_x and b_y peaks' position. Both the mass loss rate and periodicity also only slightly altered by the 'wide' scheme and its effect is not significant.

To see whether the outburst behaviour is linked to the sudden increase in mass replenishment at those times, we did a run for our $\beta_0 = 10^5$ simulation in the cycle phase, where we set the mass replenishment to be constant in time instead. We found that cycle dynamics is unaffected by this change, which is not surprising given that even though the outbursts have significantly higher mass loss rates than the quiescent stage, they are still small when integrated in time compared with the total disc mass. We also did a few runs where there is

no mass replenishment at all, and found the cycles and periodic outburst behaviour to still persist in the absence of mass injection, and as long as the overall mass loss is not significant, there is no notable quantitative difference between the solutions.

Ideal MHD in the atmosphere

One caveat in our model with regard to mimicking real protoplanetary discs is in the diffusivity profile used. In particular, for most of our runs we lower the Ohmic diffusivity to be 0.5% that of the mid-plane value in the atmosphere, whereas one might argue that it would be more realistic to have ideal MHD due to the high FUV ionisation there. To test whether an ideal MHD atmosphere would make a difference to our results, we conducted four runs for our $\beta_0 = 10^5$ simulations, initialised from each of the four wind solution states, but with η_∞ set to 0.

We found that while the general dynamics of the cyclic states is not changed, the peaks in b_x and b_y become more pronounced, with $b_{x,\max} = 11.3$ and $b_{y,\max} = 23.2$ compared with $b_{x,\max} = 5.0$ and $b_{y,\max} = 18.0$ when $\eta_\infty = 0.005\eta_0$. The period of the cycles also becomes shorter, with $T = 20\Omega^{-1}$ instead of $T = 50\Omega^{-1}$ previously. The range of heights through which the Alfvén point moves also becomes lower, from $4H < |z| < 5.5H$ to $2.89H < |z| < 4.11H$, and a lower height above which the peaks will be significantly accelerated up out of the disc. The outburst becomes about 3 times stronger than in the more diffusive case, corresponding to the greater density of the lower launch point in the disc.

For our slanted symmetry steady state run, we observe almost no quantitative difference for the background steady state when $\eta_\infty = 0$. A very small (period of $73\Omega^{-1}$) perturbation in b_x sometimes occurs near the twin peaks at $|z| \sim 3H$, which gets rapidly advected upwards out of the disc, but is generally negligible compared with the profile.

Overall, this points to our simulation runs with the more diffusive atmosphere as still being able to capture the essential behaviour of the wind solutions as we would expect from the more realistic ideal MHD atmosphere. The more enhanced peaks in the ideal MHD atmosphere runs point towards the sensitivity of the mechanism behind the cyclic state to the resistivity profile of the disc, an effect which will be explored in greater detail in section 10.4.

Half disc simulations

We conducted a number of half disc simulations with $0 < z < L_z$ only where we enforced the traditional hourglass symmetry through equatorial symmetry conditions at the mid-plane, with $\rho(-z) = \rho(z)$, $v_{x,y}(-z) = v_{x,y}(z)$, $v_z(-z) = -v_z(z)$, $B_{x,y}(-z) = -B_{x,y}(z)$ and $B_z(-z) = B_z(z)$. Unsurprisingly, only hourglass symmetry cycles were recovered in this

regime, with the exact same properties as the ones in our full disc simulations. In cases where the growing mid-plane bulge rapidly disrupts the cyclic stage, we used data from these half disc simulations to analyse the behaviour of the cyclic phase.

10.4 Investigation of the wind cycle mechanism

In light of the various types of wind solutions recovered in our simulations, there are several questions we would like to address: What is the mechanism behind the wind cycles? What causes the transition from a cyclic wind to a steady one? Why is there a mid-plane bulge in b_x and b_y that grows exponentially, and what causes it to saturate in the slanted symmetry steady state? We begin in this section by investigating the wind cycle mechanism, while Section 10.5 discusses the transition from cycles to steady wind, and Section 10.6 addresses the growing mid-plane bulge and its saturation.

We present here a more detailed description and interpretation of the cyclic solutions based on the hourglass symmetry run obtained for $\beta_0 = 10^5$, $\delta = 0.033$, $z_i = 0.5H$. However, it should be noted that the same dynamics is also present across the cyclic solutions, and that the same mechanism is at work.

First, we analyse the region $3H < |z| < 4H$, where new b_x and b_y peaks are observed to grow at the beginning of each cycle. We hypothesise that this growth is a manifestation of an MRI mode, which becomes active in this region. It is a well known result that the MRI is largely suppressed by Ohmic diffusion when the Elsasser number

$$\Lambda \equiv \frac{v_{Az}^2}{\eta\Omega} \tag{10.19}$$

is smaller than 1 (Sano and Miyama, 1999). In the mid-plane region under the resistivity profile we have chosen, Λ at the mid-plane is of order 10^{-5}, and increases to only 10^{-3} at $z = 2H$, far too small for the MRI to be active. However, this changes dramatically at around $z \sim 3H$, where the diffusivity is rapidly reduced to its atmospheric value, coupled with a rapid decrease of the local density. At $z = 3H$, we have $\Lambda \approx 0.04$, but by $z = 3.9H$, Λ has reached 1, and continues to increase with height. We should therefore expect the MRI to cause growth of b_x and b_y as $|z|$ approaches $3.9H$, and a significant increase in growth rate when $|z|$ surpasses it, which is indeed what we observe in the behaviour of the peaks. We identify the relevant MRI modes as those with vertical mode number $n = 2$ or 3, in which the profiles of b_x and b_y each have a single node on each side of the mid-plane, the $n = 3$ mode also having a node at the mid-plane. These modes are usually discussed in the ideal MHD context, but given the mid-plane region is highly resistive, the node in the mid-plane for $n = 3$ is of less importance, because the mode is largely suppressed in this region. The

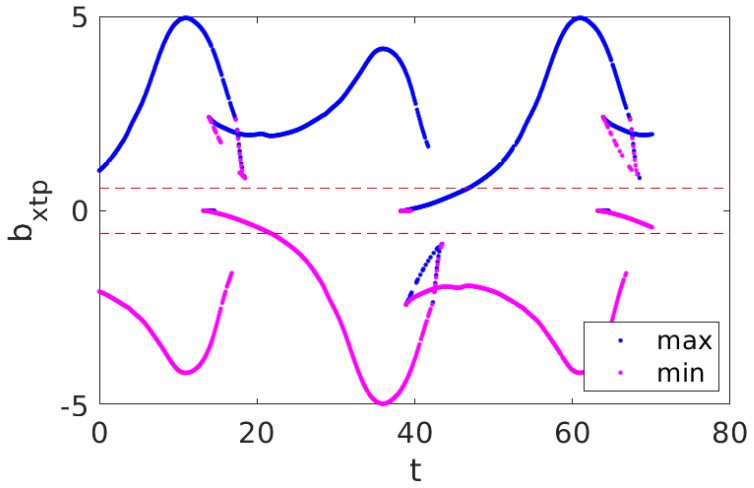

Fig. 10.10 Plot of b_x peaks strength against time. The blue line is for peaks that are maxima, while the magenta line is for peaks that are minima, and the analysis is done only for the upper half of the disc.

high mid-plane resistivity effectively shuts down communication between the two sides of the disc for this mode, allowing each side to have the further from mid-plane peak as either positive or negative, depending on the history of the half-disc profile. This may explain why the hourglass and slanted symmetry cycles share the same periodicity, as the MRI-dead mid-plane causes neighbouring modes of opposite symmetry (in particular the $n = 2$ and $n = 3$ modes) to become degenerate and share the same growth rate, and also to have the same eigenfunction and share the same mode shape, with the exception of the overall symmetry about the mid-plane. Figure 10.10 shows how the peaks of b_x, both primary and secondary, grow with time in the upper half of the disc over around one and a half cycles. By applying fits, we verified that the initial growth of these peaks is indeed exponential, with a measured growth rate $\sigma = 0.18$. However, as the peaks themselves rapidly reach saturation in the non-linear regime and are of the same order of magnitude as the background, we do not expect the modes to be recovered in a linear mode analysis, which ignores time-dependent terms and assumes a steady background.

Having established that the growth of the b_x and b_y peaks is mostly due to the $n = 2$ or 3 MRI mode, we now turn to examine what contributes to their saturation and eventual acceleration up out of the disc. The Alfvén point marks the height above which vertical advection dominates over MRI dynamics. We would therefore expect MRI modes excited above the Alfvén point to be rapidly advected out of the disc, preventing further growth. Figure 10.11 gives detailed space-time plots of the density (top), vertical velocity (middle) and vertical Alfvén velocity (bottom) over one half-cycle, with the Alfvén point(s) marked

with magenta dots. At the beginning of a half-cycle (which we define as after the previous outburst has been clearly emitted from the disc surface), the Alfvén point is at around $|z| = 4.5H$. A slow wind is present upwards of $|z| \sim 4.5H$, which is driven by the gradually weakening but nevertheless significant magnetic pressure gradient from b_y of the previous half-cycle. This weakening magnetic pressure gradient correspondingly leads to a lower vertical velocity in the slow wind region, and an overall small increase in height of the vertical Alfvén point.

As this is happening, the $n = 2$ or 3 mode is active at a lower height of around $z \sim 3.15H$, with a primary peak in b_x beginning to grow there of opposite polarity to the b_x profile in the upper atmosphere, which becomes the secondary peak of the mode. The corresponding b_y of opposite sign is generated through shearing of b_x. Figure 10.12 plots snapshots of the b_x and b_y profiles over the half-cycle, as well as the horizontal magnetic pressure proportional to $B_x^2 + B_y^2$. At the same time, the disc undergoes a slow expansion of its density profile, which we attribute to the disc moving back to hydrostatic equilibrium, having lost significant mass from the $|z| \sim 4H$ region in the previous outburst. This expansion slowly pushes the MRI mode further upwards into the atmosphere, while the background vertical velocity remains roughly constant. As the b_x and b_y peaks grow however, the node between adjacent peaks results in a magnetic pressure trap that begins to confine gas from the upper layers of the disc and move them higher up with the mode into the atmosphere. Eventually, by about $2/3$ of the way into the half-cycle, the increase in density in the lower atmosphere decreases the vertical Alfvén speed there so much that a second Alfvén point forms at a lower altitude of $z \sim 3.75H$ below the b_x and b_y peaks. As a result, advection now dominates the mode dynamics, accelerating the peaks upwards into the upper atmosphere and stopping their growth. As the MRI peaks are accelerated upwards, the large magnetic pressure dip between them continues to trap gas in that region, and moves it upwards out of the disc with the peaks. This then forms the outburst gas parcel that marks the end of the half-cycle as it leaves the simulation domain. Finally, with the loss of the gas parcel, the overall density profile is reduced back to the more compact state at the start. The half-cycle then repeats itself with the horizontal field variables taking values of the opposite polarity, and the old primary peak profile becomes the secondary peak of the new half-cycle.

10.4.1 Changes in the dynamics with increasing magnetisation

Here, we explain the changes in cycle dynamics with disc magnetisation described in Section 10.3.3 using our mechanism. Even for the strongest field strength we used of $\beta_0 = 200$, the Ohmic Elsasser number Λ is still very much < 1 in the mid-plane region, and only reaches the critical value of 1 for b_x and b_y peak growth at $|z| = 3.27H$. Hence the two sides of the

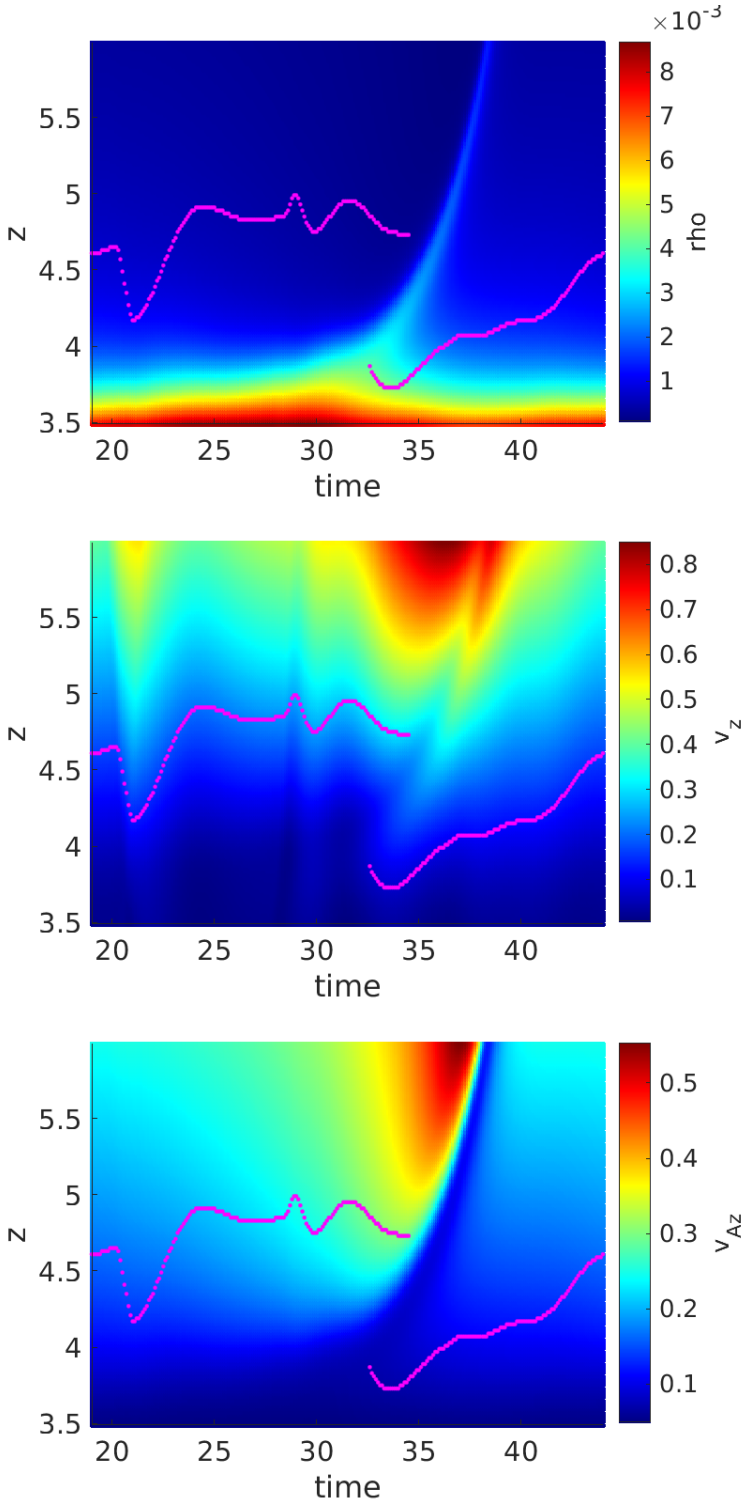

Fig. 10.11 Space-time plots zooming into the MRI-wind region in run **b1e5_S** over one half-cycle. The magenta lines plot the Alfvén point(s).

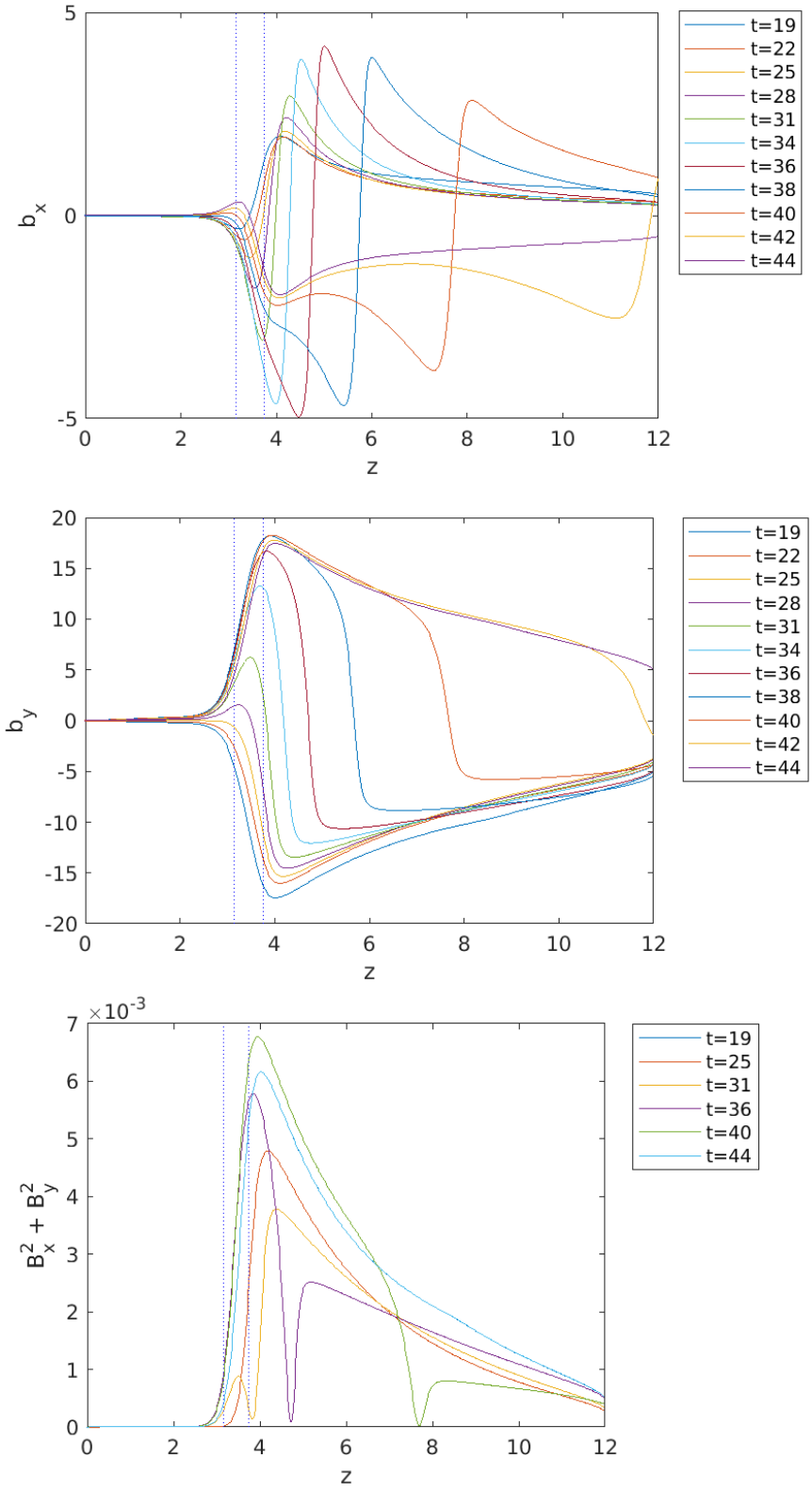

Fig. 10.12 Time snapshots of b_x (top), b_y (middle) and the horizontal magnetic pressure $B_x^2 + B_y^2$ (bottom) in run **b1e5_S** over one half-cycle. The two blue dotted lines in each plot mark the locations $z = 3.15H$ and $z = 3.75H$.

disc are still 'disconnected' from each other concerning the $n = 2$ or 3 MRI modes, and the peak growth mechanism driving the cycle dynamics continues to occur in the lower atmosphere. The period of the cycles is tied to how rapidly the $n = 2$ or 3 mode peaks grow sufficiently to trap gas in the disc surface layers and move them upwards to cause the occurrence of the second Alfvén point. Given a stronger vertical field, we would expect the growth rate of the mode to increase as long as the field is not so strong that the MRI is suppressed (Latter et al., 2010). Hence it is not surprising that the period of the cycles decreases as the magnetisation increases. The stronger vertical field also lowers the region in which $\Lambda > 1$, allowing the $n = 2$ or 3 mode peaks to develop lower in the disc where the density is higher, resulting in a stronger outflow in the outbursts. The outflow in the quiescent stage is enhanced slightly by the stronger magnetisation, as the horizontal fields are stronger and therefore can produce a steeper magnetic pressure gradient. Perhaps the greatest change to the cycle dynamics, as seen in Figure 10.7, is the range of heights that the Alfvén point traverses as the magnetisation is increased. We will address the issue of the maximum height the Alfvén point reaches in the next subsection, but we confirmed that the same mechanism is indeed at work in driving the cycles by observing that the outbursts are launched at the times when the second Alfvén point appears. The position of this Alfvén point does not necessarily matter, as long as it is lower than the b_x and b_y peaks, which is the case for all our simulations.

10.4.2 The absence of higher order modes

One question concerning our explanation of the cyclic state mechanism is why we only see the excitation of the $n = 2$ or 3 mode, while higher order modes are absent. For discs with $\beta_0 > 10^3$, we hypothesise that it is due to the generally low height ($|z| < 6H$) that the Alfvén point reaches even at its maximum in the cycle, thus higher order modes with multiple peaks, some of which would be located above this height, are advected rapidly out of the disc before any significant development. We confirmed this theory by repeating our runs in this regime from the cyclic state but with v_z arbitrarily set to 0 at each time-step. We see the rapid development of modes with multiple peaks in b_x and b_y in the upper atmosphere not present before, which quickly outgrow the original $n = 2$ or 3 mode peaks in the lower atmosphere. For discs with lower β_0, on the other hand, the Alfvén point varies over a much wider range, and reaches the box boundary and beyond for significant parts of each half-cycle. In these cases, we attribute the lack of higher order modes to the fact that they are shut down by the higher magnetisation, as seen in figure 2 of Lesur et al. (2013). We tested this hypothesis by again setting v_z to 0 for discs in the low β_0 regime, and confirming that the $n = 2$ or 3 modes in these cases are indeed the fastest growing modes.

10.4.3 Comparison with the cycle dynamics of Riols et al. (2016)

In the vertical 1D MHD simulations of Riols et al. (2016), they also observed the formation of wind cycles. These were mostly done in the ideal MHD regime, but were shown to be robust even in the presence of Ohmic resistivity. Here we would like to examine the differences between their work and ours, and why our wind cycle mechanism is distinct from the one proposed by Riols et al. (2016).

First, we note the very different magnetisation regimes that are considered in our papers. While their work focuses on a narrow range of strongly magnetised discs with $2.51 < \beta < 16$, ours explores a much more weakly magnetised regime of $10^2 < \beta < 10^6$. The corresponding strengths in the horizontal magnetic fields B_x and B_y mean that their discs are much more significantly compressed in certain phases of the cycle than ours, as indicated by the middle and bottom panels of their Figure 2. Consequently, while compression of the disc by the growing magnetic perturbations is the major cause of the shutting down of the MRI modes in their paper, our discs are still expanding when the MRI mode stops growing and is advected out of the disc. In a way, the MRI in our discs never truly shuts down, but rather, as one mode is advected out of the disc due to having crossed the Alfvén point, a new one develops in its place at a lower altitude and with the opposite polarity. Often this happens at the same time as the mode advection, hence making it difficult in our case to define when exactly a half-cycle ends or begins. In contrast, the cycles of b_x and b_y in the Riols et al. (2016) paper are always well separated in time, and the modes preserve the same sign across cycles. There is also a significant phase shift in time between the b_x and b_y maxima in the Riols cycles, whereas ours are always in phase.

Second, the nature of the outbursts themselves is significantly different. While ours are due to material trapped by the peaks of the magnetic perturbation being advected of the disc, forming a short, concentrated burst, theirs involves expansion of the disc atmosphere over a longer timescale pushing material out of the disc, forming a more spread out wind maximum.

Third, even though Riols et al. (2016) ran simulations with a resistive background, the values they used correspond to a minimum Λ of 1.7, which is not sufficient to significantly suppress the MRI. They also used a uniform diffusivity profile, and so would not have the situation as we do of a mid-plane region that effectively cuts off communication between the two sides of the disc, at least concerning the cycle dynamics.

To summarise, the cycles we recover here are significantly different from the ones found by Riols et al. (2016). Rather than compression-driven as in the Riols cycles, where a strong magnetic compression shuts down the MRI and its weakening then allows the disc to be MRI active again, our periodic cycles are rather advection-driven, where the rapid advecting of MRI modes out of the disc is the mechanism that prevents its further growth, and the

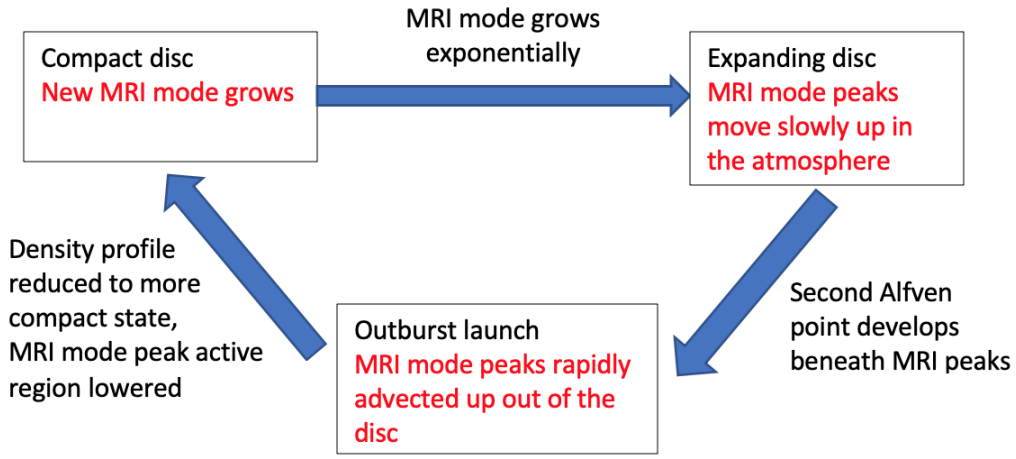

Fig. 10.13 A sketch of the proposed cycle mechanism. To be compared with figure 14 of Riols et al. (2016).

weakening of this advection allows the growth of the mode for the next half-cycle. Figure 10.13, which gives a sketch of our cycle mechanism, should be compared with figure 14 of Riols et al. (2016) to illustrate the differences between our cycles.

10.5 Mechanism for the transition to a steady wind of slanted symmetry

The aim of this section is to explain what causes the transition from a cyclic wind to a steady one of slanted symmetry. We do not address the origin of the mid-plane bulge itself, which we will examine in detail in the next section. The key questions we would like to answer are: Why does the final half-cycle where the horizontal fields of the atmosphere are of the same sign as the mid-plane bulge lengthen? What is the dynamics of the final shortened half-cycle and of the shutdown of the cycles?

We first recall our conclusion from the previous section that the cycles are primarily driven by the MRI combined with vertical advection, and that they depend on a delicate arrangement of the relative positions of the Alfvén points and the peaks of the fast growing $n = 2$ or 3 MRI mode in the atmospheric region. As noted in Section 10.3.2, the cycles pretty much continue as before until the magnitude of b_y of the growing mid-plane bulge is comparable to the maximum magnitude that is observed in the b_y peaks of the cycles. We now expand on why this is indeed a significant turning point in the disc dynamics from cycles to a steady wind, and how this transition occurs. To illustrate the dynamics of this process,

we focus on the transition as observed in the run **b1e5_G**, where $\beta_0 = 10^5$, $L_z = 12H$ and $\delta = 0.033$. The transition is from the slanted symmetry cyclic state to the slanted symmetry steady wind, but the same mechanism can also be individually applied to each half of the discs transiting from the hourglass symmetry cycles.

10.5.1 Lengthening of the final half-cycle of the same sign

First, we address the penultimate half-cycle where b_x and b_y begin with the same sign as the mid-plane bulge at $t = 205\ \Omega^{-1}$. The top two panels of Figure 10.14 shows time snapshots of the b_x and b_y profiles respectively. As in a normal half-cycle, new b_x and b_y peaks of opposite sign to the current state grow in the $|z| \sim 3.5H$ region of the more compact disc, becoming more visible from $t = 215$ to $t = 235$. At this stage in the cycle, we expect the disc to be expanding slowly from its more compact form by the gas pressure gradient, having lost mass in the wind launch region from the previous outburst. However, this time, as the peaks need to be connected to the mid-plane bulge, an additional magnetic pressure gradient, particularly from b_y, is formed at $|z| \sim 3.5H$, which expands a much larger portion of the disc with the growing mode. The disc, on the other hand, is prevented from just spreading out into the atmosphere by another magnetic pressure gradient with opposite sign just below the new b_x and b_y primary peaks. This results in a much more expanded disc than before, as can be seen by comparing the first panel of Figure 10.11 and Figure 10.15. The dramatic increase in the height of the disc surface (which we define to be where $\rho = 5 \times 10^{-3}$) leads to a much higher Alfvén point in the atmosphere despite its slow increase with respect with the disc surface as in a normal half-cycle. This is further enhanced by the extended time it takes for the new $n = 2$ or 3 peaks of opposite sign at the disc surface to gain sufficient strength to trap and move the gas parcel of the upper disc layers to cause the formation of the second Alfvén point beneath the peaks, as the mode peaks have to overcome the initial bias of opposing sign due to the mid-plane bulge. As a result, the half-cycle is lengthened, before the same outburst behaviour as the cyclic stage occurs due to advection once the second Alfvén point forms beneath the mode peaks.

10.5.2 Shutdown of the cycles

Having addressed the lengthening of the second last half-cycle, we now turn to the final shortened half-cycle and the shutdown of the cycles. As the disc returns to the more compact state at $t = 248\Omega^{-1}$, the new b_y peak that develops is now of the same sign as the mid-plane bulge, but is completely dwarfed by the mid-plane bulge strength. The b_x and b_y peaks fail to develop sufficiently to cause a node to appear between the primary and secondary

peaks. As a result, no magnetic pressure barrier develops to keep the disc from spreading out without check into the atmosphere. At the same time, a large magnetic pressure gradient, particularly from B_y due to connection of the profile with the now overwhelming mid-plane bulge, pushes gas in the disc upwards, dramatically altering the density profile as can be seen from $t = 248\Omega^{-1}$ onwards in Figure 10.15. This in turn causes a dramatic decrease of the Alfvén speed in both the lower and upper atmosphere due to the significant increase in density, and consequently the Alfvén point falls dramatically and becomes lower than the $n = 2$ or 3 MRI mode active region. The $n = 2$ or 3 mode which is responsible for driving the cycles is shut down, with the mid-plane bulge completely taking over the b_x and b_y profiles. The nature of the wind also changes to that of a slow wind launched from the disc by the magnetic pressure gradient of b_y.

10.6 Growing mid-plane bulge of the horizontal fields and its saturation

10.6.1 MRI linear stability analysis

To confirm our suspicion that the slowly but exponentially growing mid-plane horizontal fields are indeed a manifestation of the $n = 1$ MRI mode, we perform a normal mode analysis on the equations looking for axisymmetric modes with frequency ω. However, unlike the approach used in previous studies where simplifying assumptions are made about the background field variables, we allow for the background to take any values that form a valid disc solution, but not necessarily a steady state. The normal mode analysis solves the linearised equations, ignoring any time-dependence of the background state. The results should be meaningful if the background evolves sufficiently slowly, or perhaps if the variations (e.g. cyclic) in the background can be averaged over.

We assume the standard ansatz

$$\delta Q = \delta Q(z) \exp(-i\omega t) \tag{10.20}$$

for the perturbations, where Q denotes a generic field variable. The growth rate is then given by the imaginary part of ω, which we label as $\sigma \equiv \mathrm{Im}(\omega)$. The full set of linearised equations are listed in Appendix E. Since the mid-plane bulge in b_x and b_y grows on a significantly longer timescale (100s of Ω^{-1}) compared with the period of the wind cycles ($1 - 10\ \Omega^{-1}$), we attempt to account for the growth rate of the bulge by computing the linear mode of each snapshot of the simulation as the background, and averaging the growth rate computed over

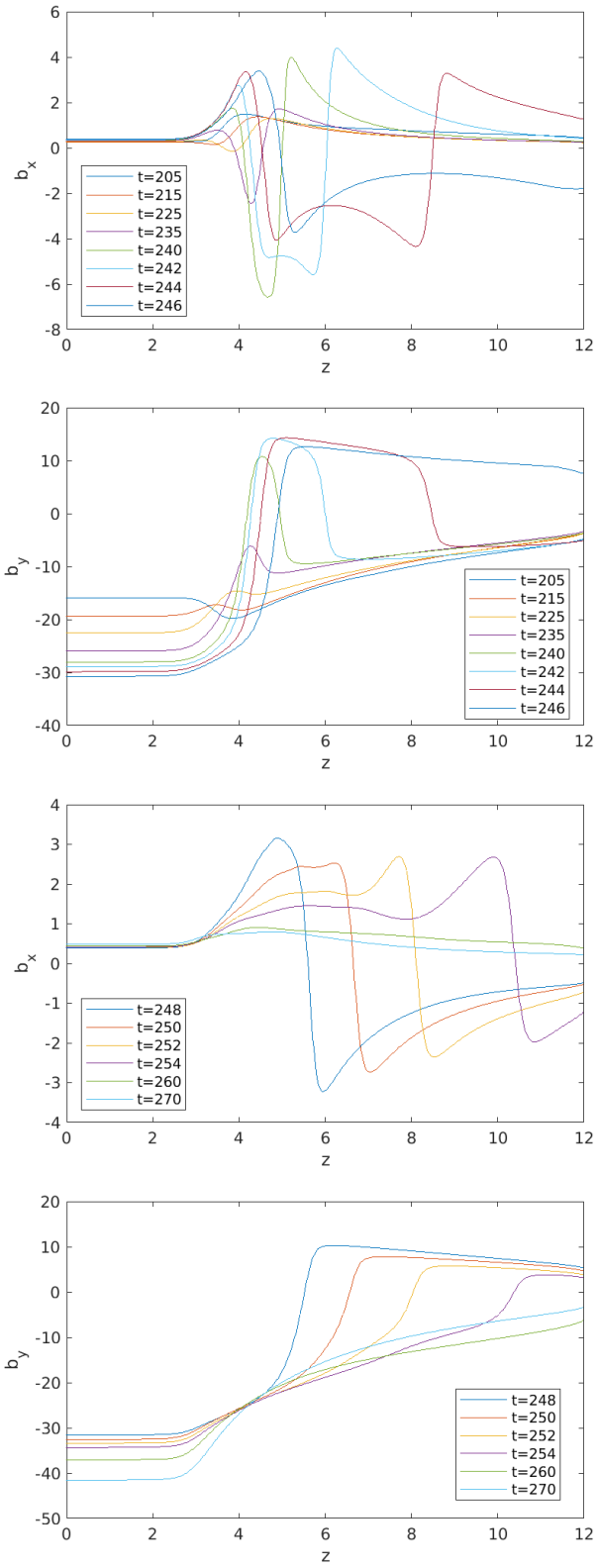

Fig. 10.14 b_x and b_y time snapshots over the transition in run **b1e5_G**. The top two plots depict the lengthening of the final half-cycle of the same sign as the bulge, while the bottom two plots depict the shutdown of the cycles.

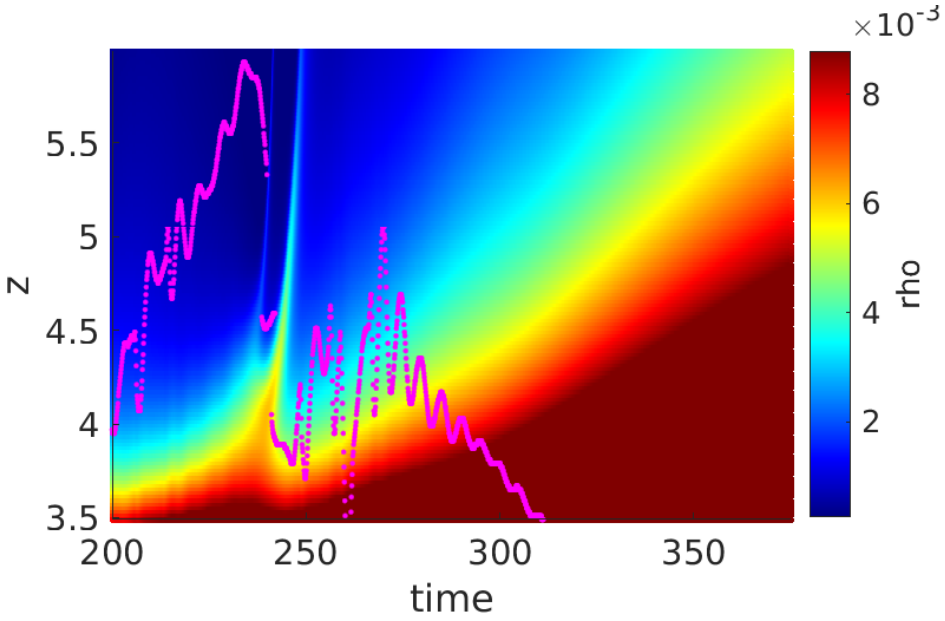

Fig. 10.15 Space-time plot of density zooming into the MRI-wind region in run **b1e5_G**. The magenta line depicts the Alfvén point.

the cycles to find the effective exponential growth rate that would be observed. Assuming that the mode growth has the form

$$f(t) \propto \exp\left[\gamma(t)\, t\right], \tag{10.21}$$

where $\gamma(t)$ is the instantaneous growth rate at a particular point in time, then it can be shown that the effective growth rate over the time period from t_1 to t_2 would be given by (see derivation in Appendix F)

$$\gamma_{\rm eff} = \frac{\int_{t_1}^{t_2} \gamma(t) \mathrm{d}t}{t_2 - t_1}. \tag{10.22}$$

To solve the system of equations, we used a pseudo-spectral method with a decomposition on Whittaker cardinal functions (i.e. sinc functions) (Boyd, 2001). The Whittaker functions naturally tend to 0 as $|z| \to \infty$. The equations were recast in terms of momenta $\delta\mathbf{m} \equiv \rho\,\delta\mathbf{v}$ instead of velocity $\delta\mathbf{v}$ to help with the convergence of solutions. In the case of the standard shearing box in the absence of an outflow, the magnetic fields are force-free in the low-density region at large $|z|$, and we would expect δB_x and δB_y to tend to 0. ρ would also tend to 0 following the isothermal Gaussian profile as $|z| \to \infty$, allowing us to use the momenta $\delta\mathbf{m}$ instead of velocity as suitable variables for the Whittaker basis. However, in our case, things are complicated not only by the presence of an outflow, but also the modified gravity. The density, ρ, no longer tends to 0 as $|z| \to \infty$, and we should not expect either $\mathbf{B}$ or $\mathbf{m}$ to tend

to 0 at the boundaries. Nevertheless, as we are applying the solver to the simulation region of $|z| < 12H$, ρ is still very small at the boundary and of the order 10^{-5}. Although $\delta\mathbf{B}$ and $\delta\mathbf{m}$ do not technically vanish exponentially in the regimes we study, our solver was able to yield consistent results as the resolution was increased. The full set of modified equations used in our pseudo-spectral method can be found in Appendix E.2. As we have not applied any simplifying assumptions such as $v_z = 0$ or a pure vertical B field, it is not possible to reduce the system of six equations (Equations (E.8) to (E.13)) into any simpler form, as is usually done in other studies of the MRI linear modes (Salmeron and Wardle, 2005; Sano and Miyama, 1999). We did, however, check that our solver yielded the same results as previous studies in these simplified regimes, as well as agreeing with the modes calculated in the vertical field only hydrostatic case using a simple shooting code solver, details of which can be found in Appendix E.3.

For most of our calculations, we used grids of 2201 and 2301 points over the domain $|z| < 12H$ to analyse data from our $L_z = 12H$ simulations. Using two different resolutions allows us to assess the convergence of solutions, and also flags up cases for exclusion when modes are obscured by numerical oscillations which may be excited in the pseudo-spectral method by using specific grid resolutions. Generally, the modes showed good convergence, and no qualitative difference was observed from further increases in resolution. In order to speed up the calculations and also allow the matrices to be computationally soluble, we used the assumption that modes take either a slanted or hourglass symmetry about the mid-plane, reducing the number of elements in each dimension by half. This condition arises naturally when the background field variables also adopt a slanted or hourglass symmetry about the mid-plane, but its validity is more dubious in the case when the background is asymmetric. Our linear analysis is therefore better suited to studying the cyclic states, the steady state solution, and the early/late stages of the asymmetric transition between the hourglass symmetry cyclic and the slanted symmetry steady state where there is great semblance to one of the symmetries, while our results for the middle of the asymmetric transition period should be treated with caution. It should be noted though that the transition from slanted symmetry cyclic to slanted symmetry steady state always preserves the slanted symmetry, and there should not be any symmetry concerns regarding our method of calculation in that case.

10.6.2 Direct analysis of the simulation states

Examining the cyclic states

As the mid-plane bulge begins its growth through amplifying perturbations of b_x and b_y in the cyclic states, we begin our investigation by applying our linear analysis directly to the

simulations by using data of our $L_z = 12H$ hourglass symmetry cycle run **b1e5_S** as the background disc. As we are primarily interested in whether the slow growing mid-plane mode can be understood through such analysis, we filtered out modes with an hourglass symmetry and only included the fastest growing mode with a slanted symmetry. However, it is interesting to note that the fastest growing modes obtained are almost exclusively of the slanted nature, with mode shapes resembling that of the growing mid-plane bulge observed. We attribute the lack of $n = 2$ or 3 modes to the rapidly changing dynamics of the cycles, which suggest that the modes are in the non-linear regime, and therefore not captured by our linear calculations. In order to remove modes obscured by rapid numerical oscillations, we compared results from two runs with different resolutions and only included modes whose growth rates differ by no more than 10%. We also applied a fast Fourier transform on the mode profiles and excluded modes dominated by extremely high frequencies.

We did both calculations where we inputted all the variables from our simulations as the background state for the linear analysis, as well as ones where only ρ, v_z and B_z are included and the other variables v_x, v_y, B_x and B_y are set to 0. The latter calculations, denoted with the suffix 'rhovz', are motivated by the observation in the previous section of the importance of outflow and change in density profile in affecting the growth of the magnetic fields. Isolating these variables allows us to examine to what extent they are responsible for the behaviour we find. Figure 10.16 shows the linearised growth rates calculated from the hourglass cycles in run **b1e5_S** where $\beta_0 = 10^5$. The blue curve is for calculations with all variables, denoted 'Full', while the orange curve is for the 'rhovz' case. They both vary periodically with the phase of the cycles, although apart from the decrease in magnitude from $t = 13\ \Omega^{-1}$ up to the end of the peak at $t = 22\ \Omega^{-1}$, both the behaviour and magnitude of the growth rates are notably different. It is interesting to note that the times when the 'Full' case yielded negligible growth rates for the slowly growing 'bulge' mode are when the b_x and b_y peaks of the $n = 2$ or 3 mode in the background are beginning to significantly grow again in the MRI active region of $3.15H < |z| < 4.75H$.

The shape of the modes in both the 'Full' and 'rhovz' calculations highly resembles the horizontal magnetic fields of the slanted symmetry steady state profile reached at the end of the simulations. Figure 10.17 shows the horizontal magnetic fields of one of the modes in the 'Full' calculation at $t = 22.2\Omega^{-1}$. Like the slanted symmetry steady state, the profile has δB_x peaks at $|z| \sim 3.15H$, and a significantly larger magnitude δB_y of the opposite sign in the mid-plane. We interpret the mode shape to be a result of the instability being active at $|z| \sim 3.15H$ leading to the b_x peaks there. The strong resistivity at the mid-plane causes the dense disc region to be linearly stable against the MRI, but the strong diffusion leaks the b_x flux from the MRI active surface layers to the disc, resulting in a significant net b_x

in the mid-plane region. This is similar to the mechanism described in Turner et al. (2007). Shearing of the b_x field then generates the large b_y that we see until saturation occurs.

When averaged using equation (10.22), the 'Full' calculations give an effective linear growth rate of $\gamma_{\text{eff}} = 0.0122$, while the 'rhovz' results give $\gamma_{\text{eff}} = 0.0155$. As we did not observe any mid-plane bulge growing in the run **b1e5_S** (see Section 10.3.2), this growth rate should be compared with the measured initial growth rate of $\sigma = 0.18$ in runs **b1e5_A** and **b1e5_G**. While the calculated growth rates are both slightly lower than the measured growths in the simulations, they are comparable and of the same order of magnitude. The difference in growth rates may be attributed to the effect of further changes in the background when the mid-plane bulge is already present and growing. Indeed, when we applied the linear mode solver using data from the runs **b1e5_A** and **b1e5_G** as background discs, we obtained closer values of $\gamma_{\text{eff}} = 0.0192$ (Full), 0.0200 (rhovz) and $\gamma_{\text{eff}} = 0.0185$ (Full), 0.0143 (rhovz) respectively. This strongly suggests that the mid-plane bulge is indeed the result of a slow MRI mode of slanted symmetry growing on top of the cyclic state background.

Robustness in behaviour across magnetisations

We also repeated the same analysis for simulations with different β_0, the results of which are plotted in Figure 10.20. As can be seen, the calculated linear growth rate and its trend with β_0 closely follows that of the measured initial growth rates. This suggests that the mid-plane bulge growth is indeed a manifestation of the MRI across the different field strengths investigated.

Progression to the slanted symmetry steady state

In order to investigate the saturation mechanism, we applied the linear growth rate calculations to our full disc runs beginning in the cyclic stage (mostly hourglass), right up to them reaching the slanted symmetry steady states. Figure 10.18 shows a moving average of the growth rates (over $20\Omega^{-1}$) calculated from **b1e4_G** and **b1e5_G**, with blue denoting the results for the 'Full' scheme and orange for 'rhovz'. We found that they all follow the same pattern. The linear growth rate varies in magnitude periodically with the cycles in the cyclic stage but with a moving average γ_{eff} value close to the measured growth rate at those times. As the disc goes through the transition and the cycles shut down, the linear growth rate begins to gradually decrease in magnitude. During this time, the mid-plane bulge is also observed to slow down in its growth. Upon saturation to the slanted symmetry steady state, the largest linear growth rate becomes negative. While the 'Full' and 'rhovz' calculations have notable differences in the cyclic stage though yielding similar γ_{eff} (see section 10.6.2), their growth

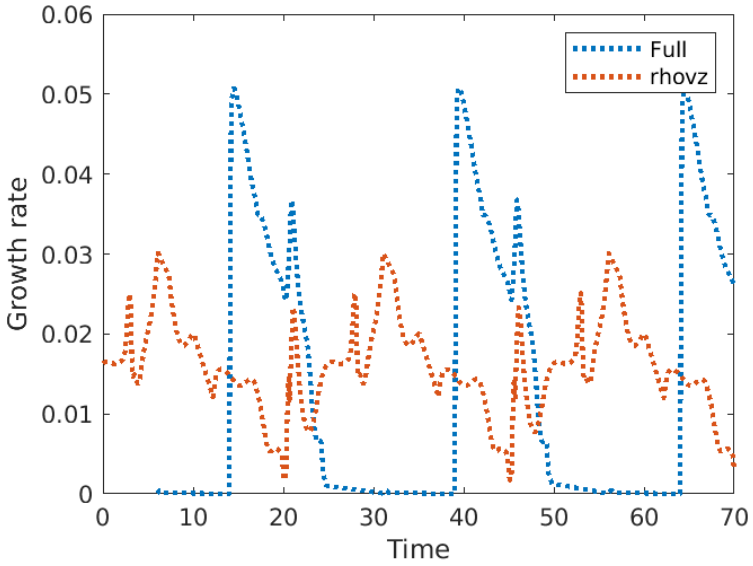

Fig. 10.16 MRI growth rates obtained using linear analysis on the background fields of the hourglass symmetry cycles in run **b1e5_S**. The blue dotted line is for full background, while the orange dotted line is when only ρ, v_z and the background vertical field are included.

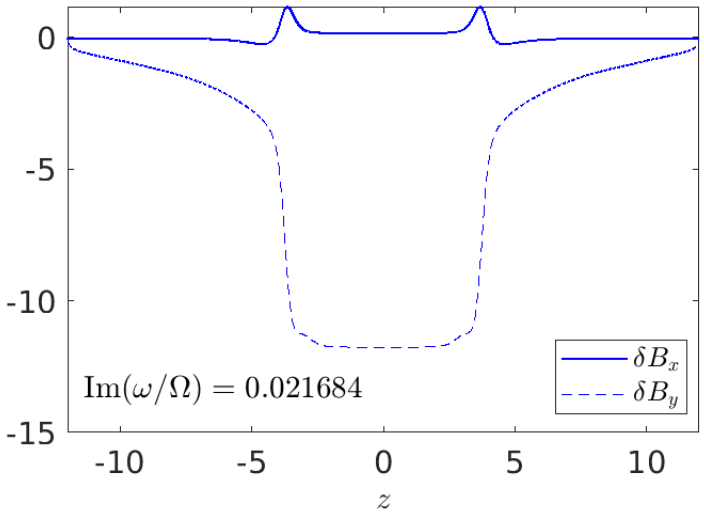

Fig. 10.17 Mode at $t = 22.2\Omega^{-1}$ calculated from **b1e5_S** using the 'Full' scheme.

rates converge as the cycles shut down and the slanted symmetry steady state is reached. The rate of convergence is quickest for simulations with stronger magnetic fields ($\beta_0 \leq 10^4$). This suggests that for discs threaded by strong magnetic fields, the slowing of the growth of the mid-plane bulge and its eventual saturation are mostly due to the changes in the density profile and outflow, whereas in the case of weak magnetic fields, the mid-plane b_y also has a significant effect in slowing the growth of the MRI. The eventual saturation however is still maintained by the density and outflow modifications, as shown by the convergence of the two curves as steady state is reached.

The significance of a large b_y in suppressing the mid-plane bulge growth rate was noted in the local dispersion analysis of the MRI by Sano and Miyama (1999). In section 3.2 (see also Figures 5 and 6) of their paper, they showed that the maximum growth rate is decreased as B_ϕ (equivalent to our B_y) is increased. They explained this effect by pointing out that the toroidal field acts as a magnetic pressure on the axisymmetric perturbations, suppressing the unstable growth. This effect was found to be significant when the azimuthal Alfvén speed, $v_{Ay} = |B_y|/\sqrt{\mu_0 \rho}$, becomes faster than the sound speed. Figure 10.19 plots the profiles of v_{Ay} in the slanted symmetry steady states for our runs with different β_0. As is clearly shown, the v_{Ay} values are of order unity when compared with the sound speed, with only a small decrease in magnitude as the magnetisation decreases, with the disc region v_{Ay} becoming slightly lower than the sound speed at around $\beta_0 = 10^3$. This suggests that B_y should indeed have a significant impact in suppressing MRI growth for the range of magnetisations considered. On the other hand, steady state runs with higher magnetisations (lower β_0) have higher mass outflows and likewise greater changes in their density profiles (to preserve mass conservation). We therefore hypothesise that the greater mass outflow and corresponding flattening of the density profile also has an effect of suppressing the mid-plane MRI growth, and is the dominant mechanism for saturation in the low β_0 cases.

10.6.3 The significance of density modification, outflow and azimuthal magnetic field on the MRI

To assess the importance of outflow, density profile modification, and the azimuthal field in suppressing the $n = 1$ mode of the MRI, we used a simplified model where we ignored the physics of wind-launching, and the backgrounds are comprised of analytic profiles governed by easy to interpret parameters. For the density, we used a profile of the form

$$\rho = \rho_0 \exp\left(-z^2/2\right) + \rho_1 \left(\frac{|z|}{1+z^2}\right), \tag{10.23}$$

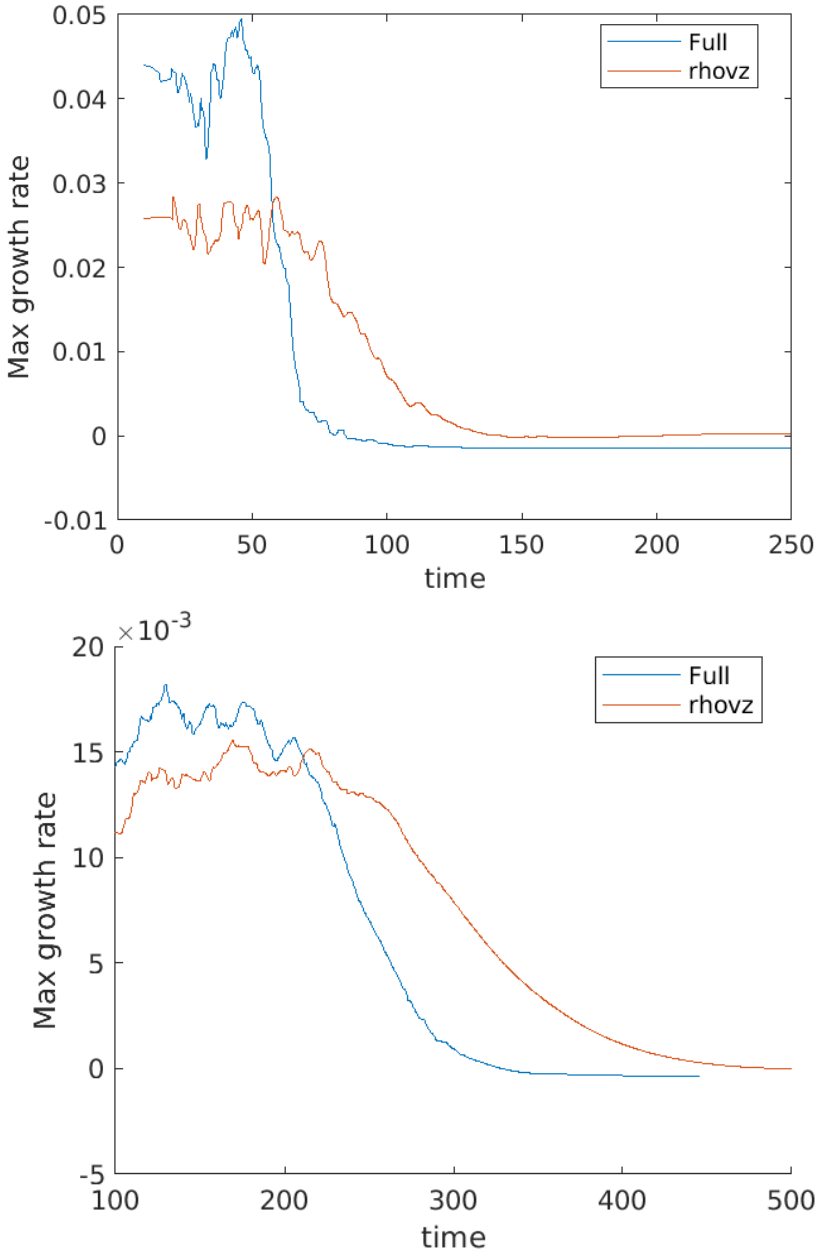

Fig. 10.18 Plots of linear growth rate against time, calculated from **bt1e4_G** (top) and **bt1e5_G** (bottom).

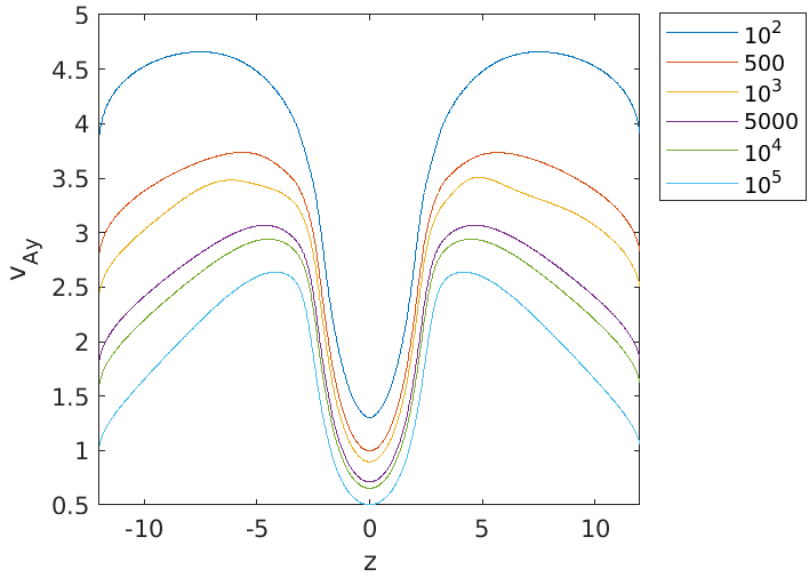

Fig. 10.19 Vertical profiles of the azimuthal Alfvén speed (in units of the sound speed) for runs with different β_0, as indicated by the legend.

where ρ_0 and ρ_1 are parameters governing the normalisation of the density and the flattening out of the hydrostatic Gaussian density profile due to an outflow respectively. We keep $\rho_0 = 1$ for all our runs so that as before the magnetisation of the disc is set through varying B_z, while the larger the value of ρ_1, the more flattened the profile becomes. The vertical velocity is calculated through

$$|\rho v_z| = \dot{m}_w = \text{constant}, \tag{10.24}$$

where $\dot{m}_w$ is the outflow rate and is one of our input parameters. It can then be shown in our model that, for $|z| \gg 1$,

$$\rho \sim \frac{\rho_1}{|z|}, \tag{10.25}$$

and

$$v_z \sim \frac{\dot{m}_w}{\rho_1} z. \tag{10.26}$$

The vertical magnetic field strength B_z is set by the β_0 parameters as before, and we used the same resistivity profile with $\eta_0 = 2$ and $\eta_\infty = 0.01$ as in most of our runs. For the azimuthal field, we set the value of B_y such that v_{Ay}, which we use as the input parameter, is always constant, and is given by

$$B_y = \sqrt{v_{Ay}\rho}. \tag{10.27}$$

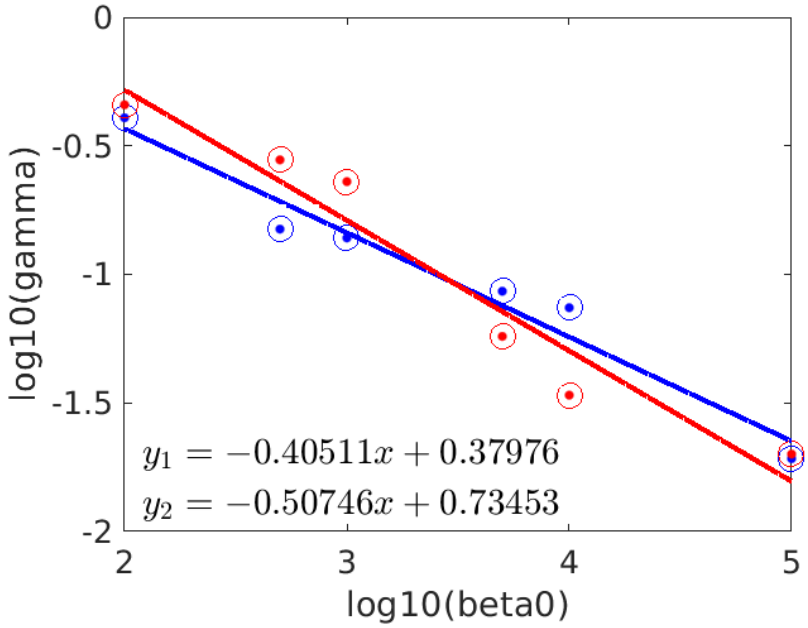

Fig. 10.20 Plots of log of the time-averaged effective linear growth rate, γ, against $\log(\beta_0)$. Blue is for the case when all variables from the simulations are included as the background, while red is for when only ρ and v_z and B_z from the simulations are included, and all other variables are set to 0. The growth rates are calculated from full disc simulation runs. The blue and red lines, whose equations are given by y_1 and y_2 respectively, are the best fit lines for the 'Full' and 'rhovz' results. This plot is to be compared with Figure 10.8 of the growth rates observed in the simulations.

All other field variables are set to 0, and we ignore any additional physics that might be operating in the disc. After the linear calculation, in most cases we extract the $n = 1$ mode by restricting our result to the highest growth rate mode of the slanted symmetry, which we also checked to corresponds to the expected form of a mode with no nodes. When we reduced $\dot{m}_w$ to 0 however, we found that for high β_0 discs, the highest growth rate mode of slanted symmetry is no longer the $n = 1$ mode as before. This is in agreement with the calculations of Latter et al. (2010), who showed that as disc magnetisation is weakened, the highest growth rate mode moves from the $n = 1$ mode to higher order modes. However, for the background disc parameters relevant to our study of the saturation to the slanted wind state (particularly the condition that $z_{Az} < 4H$), the $n = 1$ mode is always the fastest growing mode.

Our results are plotted in Figure 10.21 in the following manner. Each dot corresponds to a result from a different background profile, with the $\log_{10}$ of the linear growth rate calculated shown by its colour. Each vertical column of dots has the same set of parameters with the exception of the mass outflow, which is indicated by the vertical coordinate of the Alfvén point of the background profile, with a lower Alfvén point corresponding to a larger mass outflow. The vertical columns are grouped horizontally in clusters according to their β_0 values of $10^2, 10^3, 10^4$ and 10^5. The top plot has clusters of three columns for each β_0 value, where ρ_1 varies in the order 0.0005, $0.005, 0.05$ from left to right, with v_{Ay} kept at 0 for all these runs. The bottom plot has clusters of five columns for each β_0 value, where v_{Ay} varies in the order $0, 0.1, 0.5, 0.8, 1$ from left to right, while ρ_1 is always 0.0005 for these runs. Figure 10.22 plots the variation of the background azimuthal field, characterised by v_{Ay}, against the magnetisation, characterised by β_0. The growth rate of the fastest growing mode is indicted by its colour, but is not necessarily the $n = 1$ mode, as discussed above. The columns in the triplet for each β_0 value correspond from left to right to the three density modifications of $\rho_1 = 0.0005, 0.005$ and 0.05, while $\dot{m}_w$ is set to 0 indicating no outflow for these calculations.

Effect of density modification

We begin by examining the effect of modifying the density distribution. As the density profile becomes flatter with a larger ρ_1 (moving across the columns within each triplet in the top plot of Figure 10.21), the linear growth rate of the $n = 1$ mode decreases for almost all outflow strengths and disc magnetisations explored. The only exception is the case when there is a large v_{Ay} and no outflow present. We attribute the general trend to the decrease in the Ohmic Elsasser number Λ in the atmospheric regions as the density profile becomes flatter, since $\Lambda \propto 1/\rho$. This is turn extends the region over which the quenching effect of Ohmic resistivity

on the MRI is significant, lowering the overall growth rate. We can see this reflected in the mode shapes as δB_x and δB_y vanish at the boundaries less rapidly from the central bulge as ρ_1 is increased. Generally, the effect of density modification corresponds to a 10-fold decrease in the linear growth rate when the density in the atmosphere is increased 100-fold. This most likely is a significant contributing factor to the shutdown of the $n = 1$ MRI mode in the slanted wind, as the atmospheric density does experience a roughly 100-fold increase in the simulations compared with that of the cyclic state at all the magnetisations explored. However, Figure 10.22 shows us that in the absence of outflow and an azimuthal field, a significant linear growth rate of $\mathcal{O}(0.1)$ still remains, so density modification alone is not sufficient to account for the saturation of the steady wind.

Effect of outflow

The presence of an outflow drastically reduces the linear growth rate when the Alfvén point z_{Az} is lowered beyond $|z| \sim 3.15H$. This corresponds to a strong and dense wind launched from the lower atmosphere below the δB_x peaks of the $n = 1$ mode, which we suggested back in section 10.6.2 when coupled with diffusion of the horizontal field to the mid-plane may be responsible for driving the mode development. Hence, once z_{Az} is lowered below the peaks, we expect vertical outward advection of the MRI mode to dominate, shutting down the MRI completely, which is indeed what we find. The behaviour of the MRI when a weaker wind is present such that $z_{Az} > 4H$ in our background configuration is less clear, and there are indications that under certain conditions, such as when $\beta_0 = 10^3$ and $\rho_1 = 0.005$ (2nd column of the 2nd cluster from the left of the top plot of Figure 10.21), as the wind weakens, there may be a brief shutdown of the $n = 1$ mode before its growth rate is restored to its high no-outflow value (Figure 10.22). However, as the Alfvén points in the saturation phase of our simulations is always below $|z| = 4H$, we can conclude that a strong outflow ($z_{Az} < 3.15H$) induced advection of the $n = 1$ mode does have a critical effect of its eventual shutdown. The rapid decrease of the growth rate to 0 as $z_{Az} < 3.15H$ is also most prominent for more highly magnetised (lower β_0) discs, a result which is in line with the generally higher Alfvén points we found for the saturated slanted winds for lower β_0 discs.

Effect of azimuthal field

Finally, we examine the effect of azimuthal field strength. As v_{Ay} increases from 0 to 1 (left to right in each cluster of five columns in the bottom plot of Figure 10.21), in the majority of cases, the growth rate is abruptly and rapidly reduced to 0 as v_{Ay} increases beyond 0.8. There is a limited range of intermediate outflow strengths (where $3H < z_{Az} < 4H$) when the

quenching effect of the azimuthal field on the MRI is less significant, particularly for the more highly magnetised discs. However, for the parameters that most closely resemble the saturated states of our simulations, the effect of $v_{Ay} \sim 1$ is indeed significant in contributing to the shutdown of the MRI. This, coupled with our analysis in Section 10.6.2, suggests that the saturation mechanism is largely a combination of vertical advective damping from the outflow, and a large azimuthal field strength in quenching axisymmetric perturbations.

10.7 Discussion and astrophysical implications

10.7.1 Summary of the results

By using radially local 1D vertical resistive shearing box simulations in the parameter regime relevant to protoplanetary discs, we have found wind solutions which go through three stages of development: cyclic, transitive and slanted symmetry steady winds, the last of which bears great resemblance to the slanted winds seen in other local and global simulations. We have assessed, in particular, the importance of large-scale MRI channel modes in driving these wind states. Figure 10.13 shows the mechanism we proposed to be responsible for the cyclic state, which is driven by periodic excitation of the $n = 2$ or 3 MRI channel mode, coupled with advective eviction when the Alfvén point falls below the mode peaks. We have shown that the mid-plane bulge which eventually causes the transition to the steady wind is a result of a much slower growing $n = 1$ MRI mode, and the transition occurs when the mid-plane B_y value is larger than the maximum peak B_y strength in the cyclic stage. Saturation of the growing bulge to the steady state wind of slanted symmetry occurs due to both a combination of advective damping from the strong wind, and suppression of the instability from a large toroidal field. We also found that a more magnetised disc would speed up the process of transition and saturation to the steady wind through our parameter study, and confirmed the robustness of our results by varying both the box size and mass replenishment schemes.

10.7.2 Connection of our results with other MRI-driven wind simulations

The first implication of our results is in understanding the essential ingredients for the development of the slanted wind observed in both local (Bai, 2013; Lesur et al., 2014) and global simulations (Bai, 2017; Béthune et al., 2017; Gressel et al., 2020; Riols et al., 2020; Rodenkirch et al., 2020). We have shown that it is the result of a slowly growing $n = 1$ MRI mode, characterised by a mid-plane bulge in B_x and B_y. This bulge eventually flips the disc

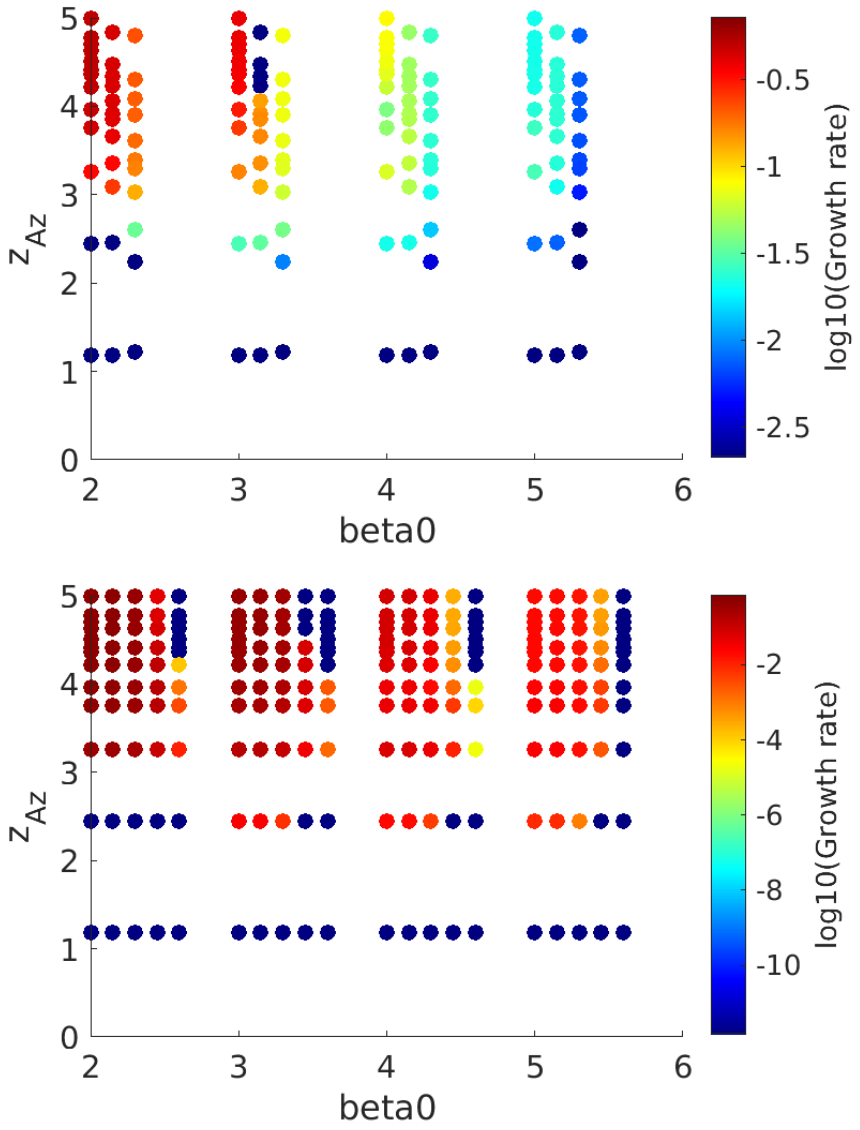

Fig. 10.21 Plots of log10 of the linear growth rate with β_0 of the background profile varying horizontally taking the values $10^2, 10^3, 10^4, 10^5$, and z_{Az} varying vertically. The top plot has $v_{Ay} = 0$ for all data points, while each triplet of columns with the same β_0 value has $\rho_1 = 0.0005, 0.005$ and 0.05 from left to right. The bottom plot fixes $\rho_1 = 0.0005$ for all data points, while each quintet of columns with the same β_0 value has $v_{Ay} = 0, 0.1, 0.5, 0.8, 1$ from left to right.

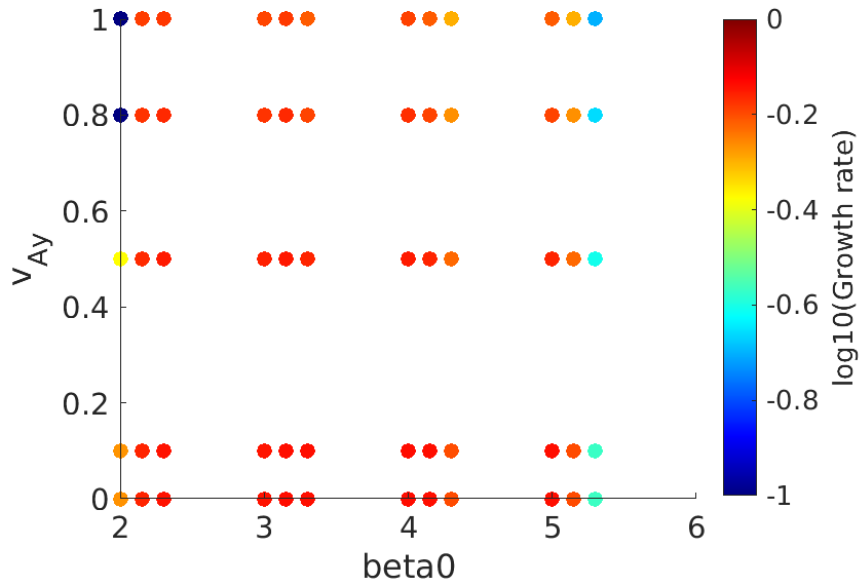

Fig. 10.22 Plot of log10 of the fastest linear growth rate (not necessarily the $n = 1$ mode) with β_0 of the background profile varying horizontally taking the values $10^2, 10^3, 10^4, 10^5$, and v_{Ay} varying vertically. Each triplet of columns with the same β_0 value has $\rho_1 = 0.0005, 0.005$ and 0.05 from left to right.

symmetry from the traditional hourglass configuration to the slanted wind, shutting down other MRI modes that may be present via advective damping from the dense low-Alfvén point winds launched. This process seems to only require the presence of a strongly diffusive mid-plane region, which forces all higher order modes than the $n = 1$ one to be localised in the disc lower atmosphere or above. These modes are in turn are shut down as the Alfvén point falls below those regions, allowing the slower $n = 1$ mode to grow and eventually dominate the profile. Therefore, we should expect all discs with highly Ohmic diffusive mid-plane regions to eventually settle into the slanted state regardless of its history, which is in line with what has been reported by certain authors in global simulations (Béthune et al., 2017; Riols et al., 2020). In particular, the simulations of Béthune et al. (2017) showed a convergence to the slanted profile on a timescale of 100s of Ω^{-1} (see their Figure 23), which is in agreement with the timescales we have found in our study. Our parameter study suggests that we should expect lower β_0 discs (i.e. discs with higher magnetisations) to be more prone and quicker to develop the slanted symmetry wind state. This is also noted in other local simulations (Bai and Stone, 2013a), while figure 31 of Béthune et al. (2017) also appears to indicate the same trend. It would be interesting for future global simulations to explore this in more detail as the parameter space is further expanded and simulations are run for longer periods of time.

The periodic outbursts observed in our cyclic stage are reminiscent of cyclic outbursts found in other local simulations (Fromang et al., 2013; Riols et al., 2016; Suzuki and Inutsuka, 2009; Suzuki et al., 2010). Similar to our cycles, the cycles in their simulations show a strong correlation between development of the horizontal magnetic fields and the outburst behaviour, suggesting that horizontal magnetic fields are involved in the cyclic launching mechanism. As we have already discussed in Section 10.4.3, our outbursts are different in nature and mechanism from those of Riols et al. (2016), which is most likely due to our lower field strengths and the dead-zone resistivity profile we used. There are greater similarities in both the outburst strength, period and launch region between our results and those of Suzuki et al. (2010), which also used a dead-zone profile over and $\beta_0 = 10^6$, but over a much smaller box size ($L_z = 4H$). Their simulations were done in 3D, and it was noted that their disc winds were partly driven by the breakup of channel flows triggered by the MRI in the lower atmosphere, although they did not do a detailed analysis of the mechanism as we have done here. This confirms that even though are our simulations are in 1D, they are nevertheless able to capture one of the key behaviours that may be responsible for driving periodic outbursts. We are also able to conduct simulations for longer and with lower β_0 values than Suzuki et al. (2010), hence showing that the slanted symmetry state would eventually take over and change the wind behaviour, which was hinted at in their snapshots by the slightly slanted fields at the mid-plane, but were not fully developed to the extent that the cycles would be shut down and morph into the slanted steady wind, due to both their shorter run time and the very high β_0 value they used. Outburst behaviour was also observed in the initial stages of the Ohmic-only global simulations of Rodenkirch et al. (2020) before settling of the disc to the slanted symmetry wind state, and it would be interesting to investigate to what extent the cyclic outburst behaviour we uncovered is also present in global discs.

It is also worth comparing our 1D resistive shearing box calculations with simulations where other non-ideal MHD effects are present. Notably, the simulations of Bai and Stone (2013a) showed no periodic wind solutions despite similar parameter regimes to us in resistivity and field strength ($\beta_0 = 10^6 - 10^3$). We attribute this difference to the presence of ambipolar diffusion in their lower atmosphere (absent in ours), which may have stemmed the growth of the $n = 2$ or 3 MRI mode peaks in b_x and b_y before they are strong enough to modify the density profile sufficiently to cause the occurrence of a second Alfvén point beneath the peaks to drive the outbursts. The slanted wind profiles in Bai and Stone (2013a) also have a longer and quasi-steady transition state, where a strong current layer is maintained at $z \sim 3H$ for about 100 orbits, before a full slanted wind solution is recovered. Again, we attribute this difference to the presence of ambipolar diffusion in their simulations, which would have altered the shapes and growth rates of the MRI channel modes. Simulations

where the Hall effect is also included (Bai, 2014, 2015; Lesur et al., 2014; Simon et al., 2015) showed that its presence may enhance the development of a mid-plane azimuthal magnetic field and progression to the slanted wind state, depending on which polarity the Hall term has with respect to the vertical field. All this shows that the additional of other non-ideal effects presents a wide parameter space for exploration which could have significant enhancements and changes to our Ohmic only picture, and will be investigated in the next Chapter.

Chapter 11

Magnetic wind symmetries - full non-ideal MHD generality

The previous chapter examined the effect of an Ohmic dead-zone in the vertical profile of a radially local patch of the disc on the symmetries of the magnetic wind solutions that develop. Through the use of a simple analytic profile that mimics the resistive dynamics of the inner disc ($R \sim 1$ AU), we revealed a wealth of behaviour from wind cycles to the eventual adjustment of the disc to the slanted symmetry.

In this chapter, we extend our investigation to full non-ideal MHD generality, as well as using more realistic semi-analytic prescriptions for the ionisation profiles at different disc radii.

11.1 Computing the non-ideal MHD coefficients

As noted in Section 2.4.3, there is great uncertainty in the ionisation profile present in protoplanetary discs. Many of the considerations that factor into its calculation are still poorly constrained by observations. We describe here two schemes used in the literature by Lesur et al. (2014) and Béthune and Latter (2020), which we roughly follow to give a sense of how the underlying model affects the results obtained, and to provide a means of comparing our results to those previously obtained by other authors.

11.1.1 Disc models

We begin by considering the underlying disc models that describe the temperature and surface density variation with radius. From here onwards, we denote the model following Lesur et al.

(2014) by the abbreviation 'L14', while 'BL20' denotes the model following Béthune and Latter (2020).

Surface density profile

Both L14 and BL20 use the radial surface density of the minimum mass Solar nebula model (MMSN; Hayashi (1981)), where

$$\Sigma(R) = 1700(R/1\text{ au})^{-3/2}\text{ g cm}^{-2}, \tag{11.1}$$

and R is the cylindrical radial distance from the star. The MMSN is a protoplanetary disc with the minimum amount of solids required to account for the planets of the Solar system. Although the model by Hayashi (1981) is the most widely used in literature, it is by no means an agreed quantity, and depends sensitively on assumptions about the dust and gas composition of the disc as well as dynamical processes in the formation of planets such as planet migration (Crida, 2009). Chiang and Laughlin (2013) used 1,925 exoplanets observed by *Kepler* to produce a minimum mass extrasolar nebular that is roughly twice as dense as the MMSN and with a slightly steeper exponent of -1.6, while Desch (2007)'s calculation resulted in a model that is 10 times denser than that of Hayashi (1981). Recent surveys on the other hand point towards shallower surface density profiles $\Sigma \sim r^{-1/2}$ (Andrews and Williams, 2007; Tazzari et al., 2017). While large uncertainties remain in both observations of disc masses and ages (Bergin and Williams, 2017) as well as in the theoretical modelling, the MMSN model we use facilitates easier comparison with earlier works, and its steeper profile allows us to capture a broad enough range of disc conditions to compensate for the lack of clear information on actual protoplanetary discs.

Temperature profile

For the temperature profile, we treat the disc as locally isothermal at each radius throughout its vertical extent.

L14 follows the prescription given by Hayashi (1981)'s MMSN model with

$$T(R) = 280(R/1\text{ au})^{-1/2}\text{ K}. \tag{11.2}$$

This is calculated by assuming that the gaseous disc is almost everywhere transparent to the Solar visible radiation, but not to Solar UV.

BL20 assumes the disc to be a blackbody in equilibrium with heating from the central star. Using the Sun as a typical star, the surface temperature of the disc is then given by

$$T_{\text{bb}}(R) = T_{\odot}\left(\frac{R_{\odot}}{R}\right)^{1/2}\left(\frac{H}{R}\right)^{1/4}, \tag{11.3}$$

where $R_\odot = 6.957 \times 10^{10}$ cm is the Solar radius, and the surface temperature of the star is taken to be $T_\odot = 5777$ K. The mid-plane temperature in Béthune and Latter (2020) is generally higher by a factor of $\mathcal{O}(1)$ to the disc surface temperature, with a slightly different radial scaling. However, in our BL20 model, we used $T_{\rm bb}$ as the temperature of the whole vertical portion of the disc of our isothermal model. The passive opening angle of the disc is given by (see Dullemond (2000) for its derivation)

$$\frac{H}{R} = \left(\frac{k_B T_\odot \sqrt{R_\odot R}}{M_r m_u G M_\odot} \right)^{4/7}, \tag{11.4}$$

where H is the pressure scale-height, $k_{\rm B}$ is Boltzmann's constant, $M_r = 2.353$ is the mean molecular weight of the gas for a prescribed Solar composition, m_u the atomic mass unit, and $M_\odot = 1.989 \times 10^{33}$ g the mass of the Sun.

Density profile

Assuming hydrostatic balance in the vertical direction, the initial disc has an isothermal Gaussian profile about the mid-plane:

$$\rho = \rho_0(R) \exp(-z^2/2H^2), \tag{11.5}$$

where $H(R) \equiv c_s/\Omega$ is the isothermal scale height.

In the majority of L14 simulations, we used a constant aspect ratio $\varepsilon \equiv H/R = 0.05$, following Béthune et al. (2017). The mid-plane density is then calculated from the relation $\Sigma = \sqrt{2\pi}\rho_0 H$, giving us

$$\rho_0(R) = 9.07 \times 10^{-10} \left(\frac{R}{1 \text{ au}} \right)^{-5/2} \text{ g cm}^{-3}. \tag{11.6}$$

In this case, the local sound speed is artificially imposed by the disc aspect ratio profile and the gravitational potential of the central star.

For a more self-consistent calculation, the sound speed should be calculated through the ideal gas equation and the temperature profile,

$$c_s = \sqrt{\frac{k_B T}{M_r m_u}}. \tag{11.7}$$

The disc aspect ratio is then given by

$$\varepsilon \equiv \frac{H}{R} = \frac{1}{R\Omega} \sqrt{\frac{k_B T}{M_r m_u}}, \tag{11.8}$$

which for a Sun-like star and the MMSN temperature and surface density profiles gives us

$$\varepsilon \equiv \frac{H}{R} = 0.0334 \left(\frac{R}{1 \text{ au}} \right)^{1/4}, \tag{11.9}$$

$$\rho_0(R) = 1.4 \times 10^{-9} \left(\frac{R}{1 \text{ au}} \right)^{-11/4} \text{ g cm}^{-3}. \tag{11.10}$$

It should therefore be noted that the density profile of our L14 discs has a slightly shallower decrease of mid-plane density ρ_0 with radius than that used in Lesur et al. (2014) and Simon et al. (2015), which follows the more consistent treatment. However, over the range of radii ($5 - 100$ AU) considered in our simulations, this should not too drastically affect the comparison of our results[1].

For BL20, we use Equation (11.4) for our disc aspect ratio. Following the same calculation, we arrive at a mid-plane density relation of

$$\rho_0(R) = 3.89 \times 10^{-10} \left(\frac{R}{1 \text{ au}} \right)^{-39/14} \text{ g cm}^{-3}, \tag{11.11}$$

giving us a steeper mid-plane density profile than L14.

11.1.2 Ionisation profile

To calculate our diffusivities, we use a semi-analytic ionisation prescription. For simplicity, the vertical ionisation profile is assumed to be constant throughout the simulation, although in real discs changes would be expected from the mixing of species through fluid movement. Our ionisation prescription is based on the same framework as that used in Lesur et al. (2014) and Béthune and Latter (2020), where the ionisation fraction x_e is treated as a balance between local ionisation and recombination rates. We consider a dust-free environment with 75% hydrogen and 25% helium.

We consider contributions from stellar X-rays (Igea and Glassgold, 1999), cosmic rays and radioactive decay to the local ionisation in the following manner.

X-ray ionisation

For L14 runs, X-ray ionisation due to 3 keV photons is computed using the model of Bai and Goodman (2009):

$$\begin{aligned} \frac{\zeta_X^{\text{eff}}}{L_X/10^{29} \text{ erg s}^{-1}} \left(\frac{R}{1 \text{ au}} \right)^{2.2} = \; & \zeta_1 [e^{-(N_{H1}/N_1)^\alpha} + e^{-(N_{H2}/N_1)^\alpha}] \\ & + \zeta_2 [e^{-(N_{H1}/N_2)^\beta} + e^{-(N_{H2}/N_2)^\beta}], \end{aligned} \tag{11.12}$$

where $N_{H1,2}$ is the column density of hydrogen nuclei vertically above and below the point of interest, and L_X is the luminosity of the central star, which is assumed to be 10^{30} erg s^{-1}.

[1] At 5 AU and 10 AU, our model gives $\rho_0 = 1.62 \times 10^{-11}$ g cm^{-3} and $\rho = 9.07 \times 10^{-15}$ g cm^{-3} respectively, compared with $\rho_0 = 1.67 \times 10^{-11}$ g cm^{-3} and $\rho = 4.43 \times 10^{-15}$ g cm^{-3} of the more consistent model.

The constants in the equation are: $\zeta_1 = 6.0 \times 10^{-12}$ s^{-1}, $N_1 = 1.5 \times 10^{21}$ cm^{-2}, $\alpha = 0.4$, $\zeta_2 = 1.0 \times 10^{-15}$ s^{-1}, $N_2 = 7.0 \times 10^{23}$ cm^{-2} and $\beta = 0.65$. The first exponential represents attenuation of X-ray photons by absorption, while the second exponential incorporates a contribution from scattering. The column densities of hydrogen nuclei are calculated by

$$N_{H1,2} = \Sigma_{1,2}/M_r \times 0.75/m_u, \tag{11.13}$$

where $\Sigma_{1,2}$ are the column mass densities above and below the point of interest.

For BL20 runs, we use the fit of Gressel et al. (2015) (first term of their equation 4) for better comparison to the Béthune and Latter (2020) results. The X-ray ionisation rate here is based on a similar analysis to Bai and Goodman (2009), and is given by:

$$\zeta_X = 10^{-15}\ \text{s}^{-1} \left[\exp\left(-\left(\frac{\Sigma_1}{\Sigma_{\text{sc}}} \right)^{\alpha} \right) + \exp\left(-\left(\frac{\Sigma_2}{\Sigma_{\text{sc}}} \right)^{\alpha} \right) \right] R^{-2}, \tag{11.14}$$

where $\Sigma_{1,2}$ are the same as in (11.13), and the shape coefficients are $\Sigma_{\text{sc}} = 7 \times 10^{23}$ cm^{-2}, and $\alpha = 0.65$ for scattered X-rays. We do not further enhance the incident X-ray flux by a factor of 5 as done in Gressel et al. (2015).

Cosmic rays and radioactive decay

For both cosmic rays and radioactive decay, we use the same method for both L14 and BL20 runs, and cosmic rays are assumed to penetrate the disc vertically from both sides.

Ionisation from cosmic rays is given by

$$\zeta_{\text{cr}} = \zeta_0 \left[\exp\left(-\Sigma_1/96\ \text{g cm}^{-2}\right) + \exp\left(-\Sigma_2/96\ \text{g cm}^{-2}\right) \right], \tag{11.15}$$

with $\zeta_0 = 10^{-17}$ s^{-1} (Umebayashi and Nakano, 1981).

Radioactive decay is regarded as contributing a constant rate of ionisation of

$$\zeta_{\text{rad}} = 10^{-19}\ \text{s}^{-1} \tag{11.16}$$

(Umebayashi and Nakano, 2009).

Ionisation fraction and FUV contribution

Following Lesur et al. (2014), we balance the total ionisation rate ζ from the sum of the contributions with dissociative recombination in a metal- and dust-free environment (Fromang et al., 2002; Gammie, 1996):

$$x_e = \sqrt{\frac{\zeta}{n_n \alpha_{\text{dr}}}} + x_{\text{FUV}}, \tag{11.17}$$

where $\alpha_{\rm dr} = 3 \times 10^{-6}\ T^{-1/2}$ cm^2 s^{-1} is the dissociative recombination rate coefficient for molecular ions, n_n is the neutral number density given by $\rho/M_r m_u$, and $x_{\rm FUV}$ is an additional contribution from FUV ionisation from the star.

Stellar FUV is known to ionise carbon and sulphur in the uppermost layers of the disc, and can lead to ionisation fractions as high as 10^{-4} for a penetration depth of up to 10^{-2} g cm^{-3} (Perez-Becker and Chiang, 2011). FUV ionisation is estimated by

$$x_{\rm FUV} = 2 \times 10^{-5} \Bigg(\exp\left[-(\Sigma_1/0.03\ \text{g cm}^{-2})^4\right] + \exp\left[-(\Sigma_2/0.03\ \text{g cm}^{-2})^4\right] \Bigg), \tag{11.18}$$

following the rough model of Lesur et al. (2014).

Figure 11.1 plots the ionisation fraction at selected radii for the L14 and BL20 models, and can be compared with figure 1 of Lesur et al. (2014) and figure 1 of Béthune and Latter (2020) respectively.

11.1.3 Diffusivities calculation

Ohmic, Hall and ambipolar diffusivities are calculated in the absence of dust grains from the ionisation fraction using expressions from the multi-fluid approximation (Balbus and Terquem, 2001; Wardle, 2007) (see Section 2.4.1). We convert them from SI units to the CGS units used in the PLUTO code, which gives us:

$$\eta_O = \frac{c^2 m_e}{4\pi e^2} \frac{n}{n_e} \langle \sigma v \rangle_e, \tag{11.19}$$

$$\eta_H = \frac{Bc}{e n_e \sqrt{4\pi}}, \tag{11.20}$$

$$\eta_A = \frac{B^2}{\gamma_i \rho \rho_i}, \tag{11.21}$$

where

$$\langle \sigma v \rangle_e = 8.28 \times 10^{-9} \left(\frac{T}{100\ \text{K}} \right)^{0.5} \text{cm}^3\ \text{s}^{-1} \tag{11.22}$$

is the electron-neutral collision rate (Draine et al., 1983), ρ_i is the ion mass density,

$$\gamma_i = \frac{\langle \sigma v \rangle_i}{m_{\rm n} + m_{\rm i}}, \tag{11.23}$$

with

$$\langle \sigma v \rangle_i = 1.3 \times 10^{-9}\ \text{cm}^3\ \text{s}^{-1} \tag{11.24}$$

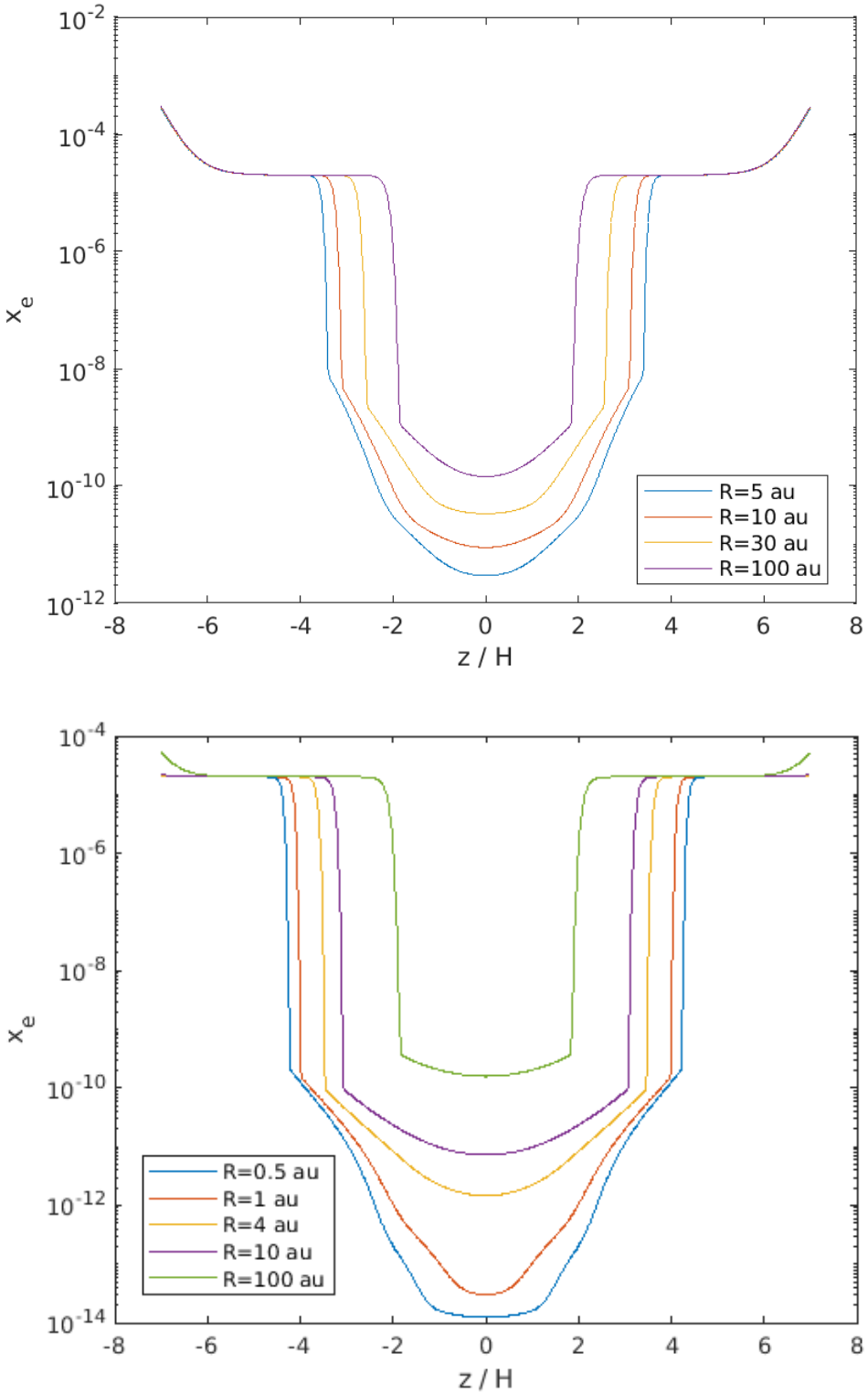

Fig. 11.1 Vertical profiles of ionisation fraction x_e for the L14 (top) and BL20 (bottom) models at selected radii (see legends).

being the ion-neutral collision rate (Draine, 2011), and m_n and m_i are the average masses of the neutrals and ions respectively. From Balbus and Terquem (2001), the dominant ion of interest will generally be the once-ionised potassium K^+ with a mean ion mass of $m_\mathrm{i} = 39 m_\mathrm{p}$, where $m_\mathrm{p} = 1.6726 \times 10^{-24}$ g, while the neutral mass is given by $m_\mathrm{n} = M_r m_u$.

Our model is unable to account for thermal ionisation in the hot corona, with the upper layers of protoplanetary discs at 1 AU likely heated by X-rays to temperatures of up to ~ 8000 K (Aresu et al., 2011). Under such conditions, the gas can be effectively modelled in ideal MHD limit, especially with respect to the MRI. We mimic this by following Lesur et al. (2014) in arbitrarily multiplying our diffusivities by a constant factor of $\exp\left(-0.01/\Sigma_{1,2}\ \mathrm{g\ cm^{-2}}\right)$ when $\Sigma_{1,2} \leq 0.01\ \mathrm{g\,cm^{-2}}$, leading to the expected ideal MHD conditions in the upper atmosphere.

There is great uncertainty about the abundance and distribution of dust grains and/or metals in protoplanetary discs, and their inclusion can alter the ionisation fraction, and consequently the diffusivities, by several orders of magnitude (Lesur, 2020). We follow Béthune and Latter (2020) in their simple way of accounting for the dust-enhanced recombination rate by artificially reducing the ionisation fraction by a constant factor of 10^{-2} for runs where we are mimicking a dusty disc.

11.2 Method

11.2.1 Framework

We used a similar set up of 1D vertical stratified shearing-box approximation with modified vertical gravity to that described in Section 10.1. The box is centred on a radially local patch at radius R, and rotates with the disc at the Keplerian angular velocity $\Omega \equiv \Omega_\mathrm{K}(R)$. We assume an isothermal disc with equation of state $p = c_s^2 \rho$, and take viscosity to be zero everywhere.

The governing equations are the same as those in Section 10.1 with the exception of the induction equation, where we now include all three non-ideal MHD terms. The x and y components are then given by:

$$\begin{aligned}\frac{\partial B_x}{\partial t} = \frac{\partial}{\partial z}\left(v_x B_z - v_z B_x\right) &+ \frac{\partial}{\partial z}\left(\eta \frac{\partial B_x}{\partial z}\right) \\ &+ \frac{\partial}{\partial z}\left(\frac{\eta_H}{B} B_z \frac{\partial B_y}{\partial z}\right) \\ &+ \frac{\partial}{\partial z}\left(\frac{\eta_A}{B^2}\left[(B_x^2 + B_z^2)\frac{\partial B_x}{\partial z} + B_x B_y \frac{\partial B_y}{\partial z}\right]\right)\end{aligned} \tag{11.25}$$

and

$$\frac{\partial B_y}{\partial t} = -\frac{3}{2}\Omega B_x + \frac{\partial}{\partial z}\left(v_y B_z - v_z B_y\right) + \frac{\partial}{\partial z}\left(\eta \frac{\partial B_y}{\partial z}\right) - \frac{\partial}{\partial z}\left(\frac{\eta_H}{B} B_z \frac{\partial B_x}{\partial z}\right) + \frac{\partial}{\partial z}\left(\frac{\eta_A}{B^2}\left[B_x B_y \frac{\partial B_x}{\partial z} + (B_y^2 + B_z^2)\frac{\partial B_y}{\partial z}\right]\right), \tag{11.26}$$

where $B = \sqrt{B_x^2 + B_y^2 + B_z^2}$ is the total magnetic field strength.

For the modified gravity term in Equation (10.4), we have

$$g_z = -\frac{GMz}{(R^2 + z^2)^{3/2}} = -\Omega^2 H \frac{\hat{z}}{(1 + \delta^2 \hat{z}^2)^{3/2}}, \tag{11.27}$$

where $\hat{z} \equiv z/H$ and $\delta = H/R$. A fully consistent treatment would set δ to be equal to ε, the disc aspect ratio. We use the consistent treatment for all our BL20 runs, but note that most of our L14 runs had a fixed δ value of 0.033, giving us a slightly slower drop-off in gravitational potential than would be the case in a more self-consistent treatment.

11.2.2 Implementation of diffusivities

We implemented the diffusivities in PLUTO by approximating the ionisation fraction profiles calculated in Section 11.1.3 using analytic forms obtained through `Matlab` 's fitting algorithm. The Gaussian, Fourier and Sine models of up to the 8th order are used for this purpose. The analytic form that best fits the values of the actual profile is selected, and care is taken to made sure that the resulting profile is symmetrical about the mid-plane. While this is not as accurate as implementing the diffusivities through a lookup table, it is easier to code, and the great uncertainties in the literature about the ionisation profiles render the errors through our approximation insignificant for our purpose of gauging the general behaviour of discs. Figure 11.2 displays example Elsasser number profiles given by

$$\Lambda_{O,H,A} = \frac{B^2}{\eta_{O,H,A}\rho\Omega} \tag{11.28}$$

of the diffusivities for the L14 and BL20 runs approximated this way for discs with $\beta_0 = 10^3$ at the beginning of the simulations. It should be noted that only the initial Λ_A profile is independent of the vertical field strength, while the initial Λ_O profile is $\propto \beta_0^{-1}$, and $\Lambda_H \propto \beta_0^{-1/2}$. As we increase β_0 between simulations, the initial Λ_O and Λ_H will therefore decrease accordingly. Since the Elsasser number profiles are sensitive to both the overall field strength as well as the density profile, they change as the discs settle into different

configurations. The initial profiles are useful for predicting the initial behaviour of the discs as perturbations grow, but the saturation into different states require more careful analysis of the profiles as they evolve.

11.2.3 Set-up

We used the same outflow boundary conditions and mass replenishment scheme as in Section 10.2.2, where we took z_i the mass injection width to be $0.1H$.

We also followed Section 10.2.3 in our box size and resolution, using the 'small' box where $L_z = 12H$, with 200 grid points for $|z| < 2H$, and 500 points each for the two atmospheric regions where $|z| > 2H$.

The Lesur-modified shearing box module of PLUTO (see Mignone et al. (2007) and also Section 7.1) is once again employed to solve the full non-ideal MHD equations. To ensure compatibility with the Hall MHD module, fluxes are computed by the modified HLL solver. Time stepping is done using a Runge-Kutta method of third order.

11.2.4 Physical parameters and initial conditions

We used the same definition of β_0 as in Section 10.2.4, as well as the same prescription of the density profile such that the initial mid-plane density $\rho_0 = 1$ in the simulations. We ran simulations at $\beta_0 = 10^3, 10^4, 10^5$ for each disc profile at different radii for the two ionisation profiles used. A selection of runs have either Hall or ambipolar diffusion arbitrarily switched off to isolate the effects they may have on the disc evolution, while both the aligned and anti-aligned configurations for the Hall effect are explored. Some runs also have the ionisation fraction reduced by a factor of 100 to mimic a disc profile with significant dust content. To extend our investigation on the impact of initial conditions on the outcome of the solutions into the full non-ideal MHD regime, we use the 'bxSINmod' and 'bxGauss' profiles of B_x as described in Section 10.3.1 as initial conditions for the different runs done. We ran most simulations up to $t = 1000\Omega^{-1}$, although for some we ran up to $t = 2000\Omega^{-1}$ to be confident of the long term outcome of the system, especially when it was clear that the solution was still transitioning to a different state at $t = 1000\Omega^{-1}$.

Our simulations are named in the following way: the first letter denotes the ionisation scheme used to calculate the diffusivity profiles, with 'L' for the L14 scheme and 'B' for the BL20 scheme. This is followed by the letter 'R' and a numeric showing the radius at which the ionisation profile is calculated. The letter 'b' then follows with another numeric, where $3, 4, 5$ denotes that the simulation is run with $\beta_0 = 10^3, 10^4, 10^5$ respectively. Runs where the Hall effect or ambipolar diffusion is turned off then has 'H0' or 'A0' following respectively,

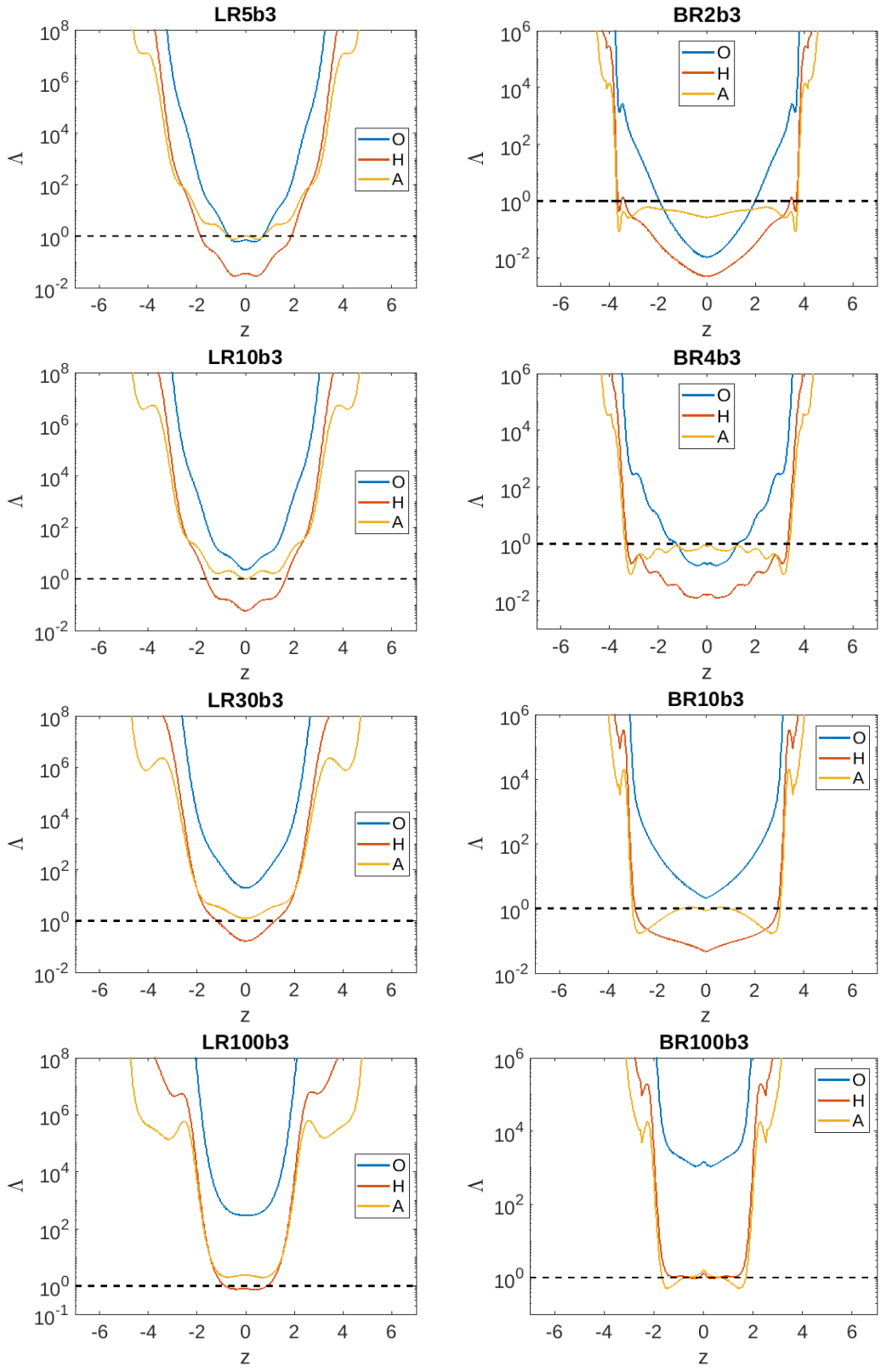

Fig. 11.2 Elsasser number profiles at the beginning of the simulations indicated in the titles of each plot where $\beta_0 = 10^3$. Blue, red and yellow lines are for Λ_O, Λ_H and Λ_A respectively.

whereas runs where the Hall effect is in the aligned or anti-aligned configuration has 'H+' or 'H-' following respectively. In cases where we reduce the ionisation fraction by a factor of 100, we add on 'r2' to the end of the first part of the name string. Finally, names of runs initiated with the 'bxSINmod' profile end with 'S', while those initiated with the 'bxGauss' profile end with 'G'. As an example, the run BR10b3H+A0r2S denotes a simulation done at $R = 10$ AU of the BL20 ionisation profile, with $\beta_0 = 10^3$, an aligned configuration for the Hall term, an arbitrarily removed ambipolar diffusion, a reduction by a factor of 100 in the ionisation fraction everywhere, and an initial condition of the 'bxSINmod' profile in b_x.

11.3 Results

11.3.1 Separation in behaviour between discs and winds

Compared with the simulations of the previous Chapter, our simulations here with full non-ideal MHD and more realistic diffusivity profiles exhibit a much wider range of behaviour than the four wind states uncovered there. One key difference between the simulations here and the purely Ohmic simulations there is a more prominent separation of solutions into a slowly varying and in some cases steady state 'disc' part near the mid-plane, and a rapidly varying 'wind' part beyond a certain number of scale heights from the mid-plane, where wind cycles of a similar nature to those of Chapter 10 are observed. In a way, such a separation is also present for our solutions in Chapter 10, as the wind cycles there are only launched beyond a certain number of scale heights, while the mid-plane region is slowly varying and has b_x and b_y near zero due to the high level of Ohmic resistivity there. The main difference in this Chapter is that rather than simply having a near vertical magnetic field in the disc region, with the only change brought about by the slowly growing $n = 1$ bulge mode that causes the whole disc-wind system to eventually transit to the slanted steady state, the disc solutions here exhibit a much wider variety of behaviour that may or may not transit to the slanted steady state, while the wind cycles also appear to operate rather independently of the disc solution, and may even continue after the disc section has reached a slanted steady state. We begin our discussion by describing the broad categories of disc solutions uncovered in our simulations here, before moving on to discuss the wind part, the various parameters that affect the behaviour of the disc-wind system, and how our previous work is both related to and superseded by our work here.

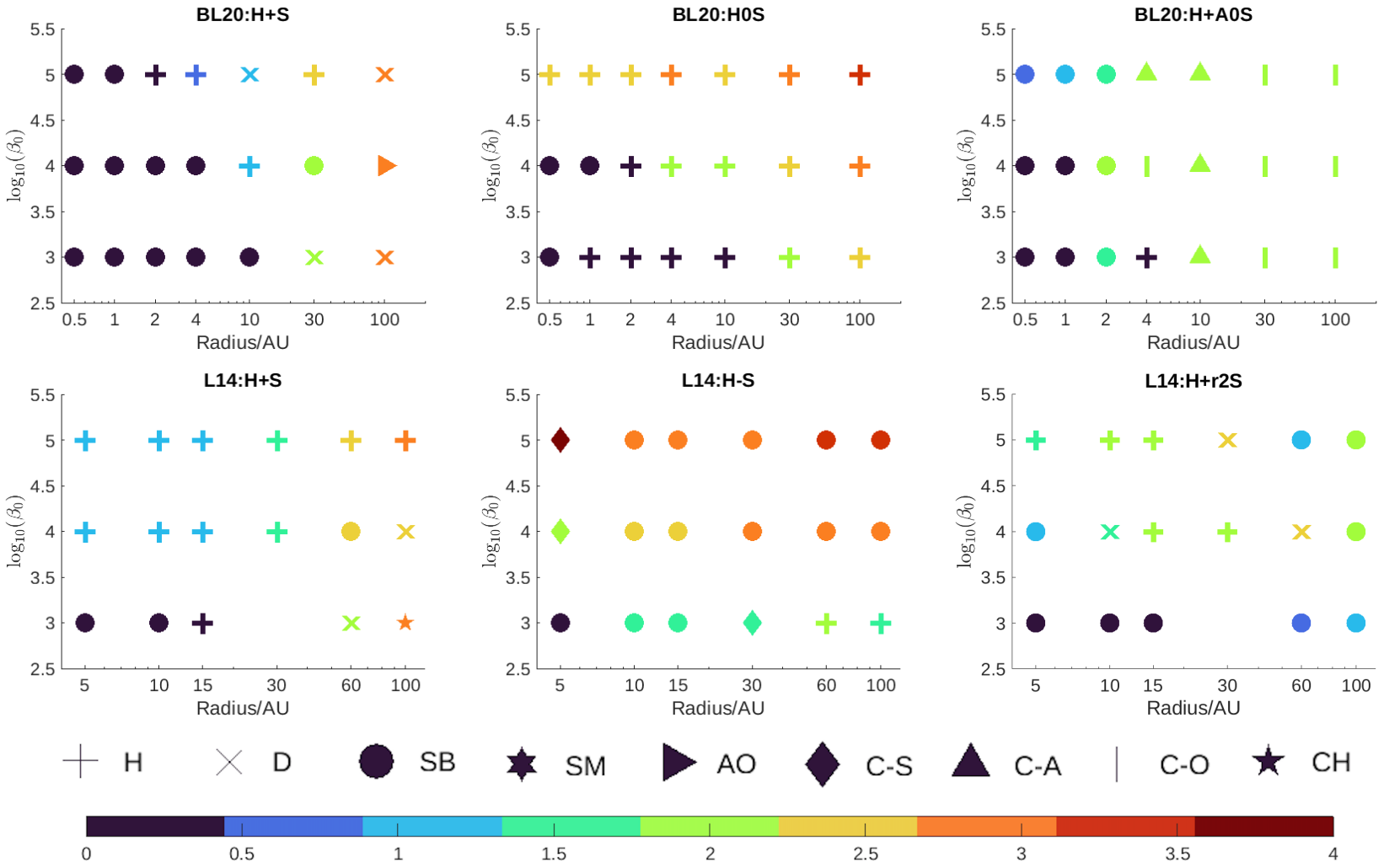

Fig. 11.3 Plots showing the types of solutions we obtained under different disc models. The title of each plot gives the disc model used, followed by modifications to the diffusivity profiles and the initial condition after the colon using the same nomenclature as for labelling the runs (see second paragraph of Section 11.2.4). The x axis denotes the radius in the disc model used, while the y axis denotes the $\log_{10}$ value of the vertical magnetic plasma beta value. Marker symbols denote different types of solutions of the 'disc' portion, with labels corresponding to those described in Section 11.3.2, while the colour represents a measure of the strength of the wind cycles in the atmospheric regions. An explanation of the scale is given in the first paragraph of Section 11.3.2.

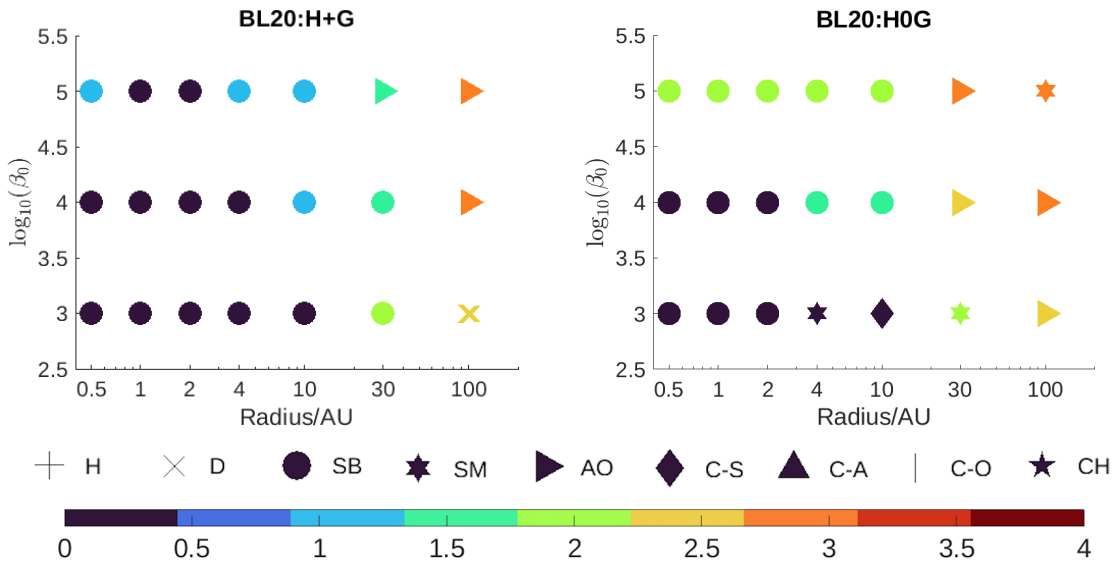

Fig. 11.4 Same as Figure 11.3, except here all the runs are initialised with the 'bxGauss' profile.

11.3.2 Phenomenology of disc solutions

In this section, the subsection titles give the names of the types of disc solutions obtained, followed in brackets by the abbreviations used to label them in the plots of Figures 11.3 and 11.4. Figures 11.3 and 11.4 plot the disc type (indicated by the marker symbol) and the strength of the wind cycles in the wind part of the solutions (indicated by the marker colour) against disc radii on the x axis, and $\log_{10}(\beta_0)$ on the y axis. The disc model, implementation of the non-ideal MHD effects and initial conditions are given by the title of each plot. The wind cycle strength scale is defined by the amplitude of b_x and b_y of the cycles compared with their maximum amplitude in the disc solution, with 0 indicating no wind cycles present, 1 indicating that the wind cycle amplitude is less than 50% of the disc profile amplitude, 2 when the wind cycle amplitude is roughly the same as the disc profile amplitude, 3 for when the wind cycle amplitude exceeds 150% of the disc profile amplitude, and 4 for when the wind cycle amplitude is more than 10 times that of the disc profile amplitude.

Hourglass steady discs (H)

First, we have the classic hourglass steady disc solution, with $b_x(z) = -b_x(-z)$ and $b_y(z) = -b_y(-z)$, accompanied by a strong current layer at the mid-plane. An example of this configuration as a persistent disc solution is shown in the space-time diagram of b_y for the disc BR10b4H+S in the top left panel of Figure 11.5, particularly from $t = 200\Omega^{-1}$ onwards. In some cases, the mid-plane current layer may experience small oscillations about $z = 0$, but

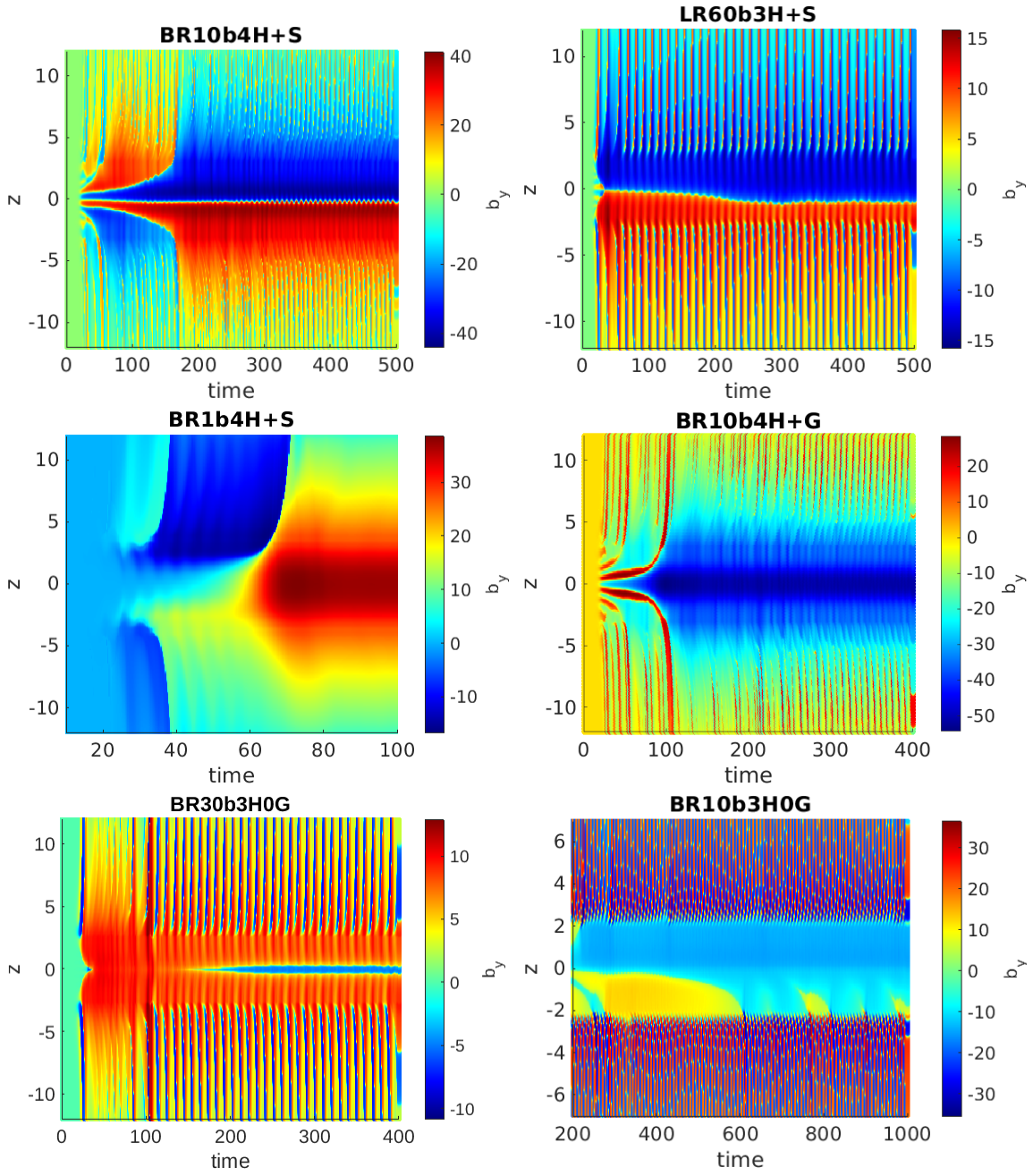

Fig. 11.5 Space-time plots of b_y to demonstrate the phenomenology of disc solutions discussed in Section 11.3.2. The title of each plot indicates the simulation it depicts. The disc types depicted from top left to bottom right reading first across and then down are as follows: hourglass steady (H), displaced hourglass steady (D), slanted steady mid-plane bulge (SB) with no wind cycles, same as previous but with small wind cycles, slanted steady with multiple bends (SM), and asymmetric one-sided varying (AO) discs.

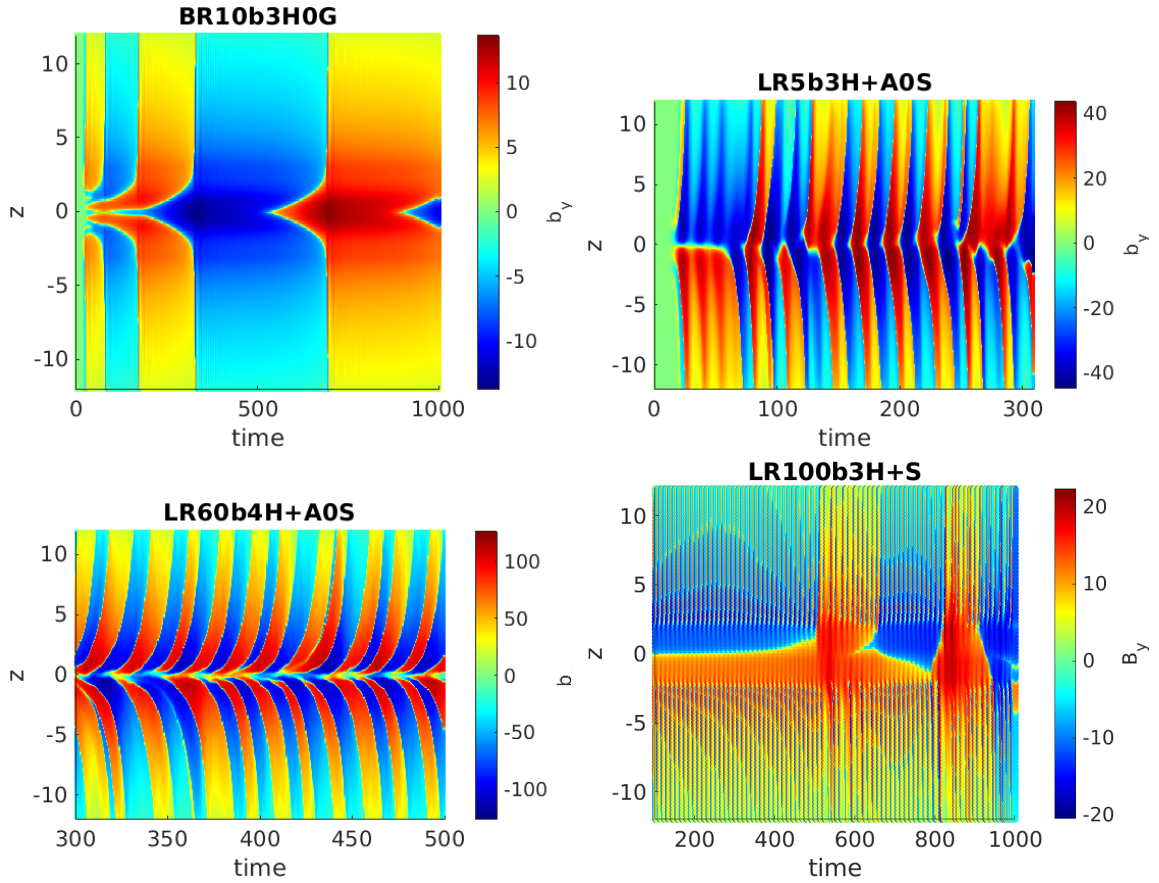

Fig. 11.6 Space-time plots of b_y to demonstrate the phenomenology of disc solutions discussed in Section 11.3.2. The title of each plot indicates the simulation it depicts. The disc types depicted from top left to bottom right reading first across and then down are as follows: slanted cyclic (C-S), alternating cyclic (C-A), overlapping cyclic (C-O), and chaotic (CH) discs.

they are insufficient to expel it from the mid-plane region. These oscillations have the same period as the wind cycles in the 'wind' region (in this case $|z| > 3H$) of the system, and may be a result of the wind cycles in the atmospheric regions modifying the disc configuration in a minor way.

Displaced hourglass steady discs (D)

Next, we have the displaced hourglass steady disc solution, where the disc portion of the solution initially settles into the classic hourglass configuration, but the strong current layer gradually moves away from the mid-plane, and eventually settles one or two scale heights away from the disc. The resulting long term configuration in the disc is asymmetric, but we call it 'displaced hourglass' to reflect both its evolutionary history, as well as the fact that the solution resembles that of an hourglass one except with the current layer displaced to one side of the disc. The top right panel of Figure 11.5 shows an example of such a solution, taken from the run LR60b3H+S. The displaced hourglass steady solution is settled by about $t = 300\Omega^{-1}$, and persists without any major changes. Like the hourglass steady solution of BR10b4H+S discussed previously, there are small oscillations of the current layer and the disc solution in z that are the result of wind cycles in the atmospheric regions. The wind cycles are however unchanged in periodicity and strength between the disc being in the hourglass steady state and the displaced hourglass steady state.

Slanted steady mid-plane bulge discs (SB)

We move on to the slanted steady mid-plane bulge solution, which is the same as the slanted steady state described in Chapter 10, and is characterised by a mid-plane bulge in b_x and b_y resembling the $n = 1$ mode of the MRI. The left panel of the second row of Figure 11.5 shows the disc BR1b4H+S settling into this configuration after $t = 85\Omega^{-1}$. In most cases, discs with this solution also shut down the wind cycles in the atmosphere, like in the solutions of Chapter 10. However, there are also cases, such as BR10b4H+G (right panel of the second row of Figure 11.5), where small cycles continue to exist in the upper atmospheres without drastically affecting the slanted steady solution in the bulk of the disc.

Slanted steady multiple-bend discs (SM)

The slanted steady mid-plane bulge solution is however not the only slanted steady configuration uncovered in our simulations. We also found slanted steady solutions characterised by two sharp bends and changes of signs in b_x and b_y on both side of the mid-plane, such as that of BR30b3H0G depicted in the left plot of the third row of Figure 11.5 from $t = 250\Omega^{-1}$

onwards. These solutions only occur for simulations initiated with the 'bxGauss' initial condition, and where Hall drift is arbitrarily switched off, or is set to be in the anti-aligned configuration. The slanted steady multiple-bend solutions then persist for the remainder of the simulations, with varying degrees of wind cycles in the 'wind' region beyond $|z| > 3H$.

Asymmetric one-sided varying discs (AO)

The final disc configuration of a nearly steady nature is the asymmetric one-sided varying solution, which is characterised by the solution from $t = 600\Omega^{-1}$ onwards of BR10b3H0G on the bottom right plot of Figure 11.5. This configuration is usually evolved from an hourglass steady disc which has its mid-plane current layer slowly expelled from the disc over 100s of Ω^{-1}. The disc portion then settles into a slanted-like asymmetric configuration, but with occasional variations in b_x and b_y driving outbursts on the side of the disc from which the mid-plane current layer was expelled. The overall behavioural pattern of the state remains similar indefinitely, and has a clear separation from the much more rapid wind cycles in the 'wind' region.

Slanted cyclic discs (C-S)

Our next disc type, depicted by the top left plot of Figure 11.6, has a different nature from the ones so far discussed. Here, the disc alternates between slanted steady mid-plane bulge states of opposite signs, with the transition initiated by a growing mid-plane dip in the b_x and b_y profiles that eventually takes over as the new mid-plane bulge, and changes the sign of the overall configuration. The time period between flips is of order 100s of Ω^{-1}, and the pattern steadily repeats itself after it has been established. We call this disc type the slanted cyclic disc to reflect the cyclical nature of the flips between slanted bulge states of opposite sign.

Alternating cyclic discs (C-A)

The next two states are distinctive from the others in that they affect the whole solution, and it is no longer meaningful to talk about a divide between a slowly varying mid-plane 'disc' portion and a separate fast-varying 'wind' portion. Rather, the whole solution takes on a wind-like nature, with rapid variation in b_x and b_y on the order of $1-10$s of Ω^{-1}. Both types are found only in discs where either ambipolar diffusion is arbitrarily set to zero, or where the Hall effect is in the anti-aligned configuration. The first, depicted by the top right panel of Figure 11.6, we call the alternating cyclic disc. The solution alternates in a random fashion between what looks like an hourglass state, such as at $t = 110\Omega^{-1}$ and $t = 280\Omega^{-1}$, and what appears to be a more slanted configuration.

Overlapping cyclic discs (C-O)

The second type we call overlapping cyclic discs, and an example of this solution is depicted in the bottom left panel of Figure 11.6. Here, the solution takes the same form as the wind cycles of Chapter 10, except the launching region is at or very near the mid-plane, and the launching of the next wind cycle begins while the previous wind cycle is still in the simulation domain being advected outwards. The upper and lower halves of the disc behave semi-independently, with the phases showing signs of matching up but also at times showing discrepancies.

Chaotic discs (CH)

Finally, we have the chaotic discs, so named because the disc portion follows no set pattern in its evolution. An example of this is depicted in the bottom right plot of Figure 11.6 from $t = 500\Omega^{-1}$ onwards. These solutions still demonstrate a clear separation in timescale from the faster-varying 'wind' portion further from the mid-plane. They are usually found at large radii and for more highly magnetised discs.

11.3.3 Dependence on non-ideal MHD effects and vertical magnetic field strength

Both BL20 and L14 models show similar trends in the dependence of solutions on disc radius, which sets the profiles of the non-ideal MHD effects, and vertical magnetisation used. This shows us that the small differences between the two disc models generally do not affect the overall trends in disc behaviour. In the following discussion, we will refer only to the sets of simulations displayed in Figures 11.3 and 11.4, and note that corresponding sets of simulations of the other disc profile show the same trends.

Strength of wind cycles in the 'wind' region

First, we note that when we talk of wind cycle strength in this Section, we are not talking about its absolute strength in launching mass outflows, but rather its relative strength in driving outbursts compared with the outflows that are launched from the configurations of the generally steadier 'disc' region. For the 'C-A' and 'C-O' solutions where the whole disc behaves like the wind region, we attribute a wind cycle strength of 2 to indicate that the outflow strengths of the two regions are the same.

The height from the mid-plane beyond which wind cycles may be present decreases with increasing radius, and corresponds well to the height at which the Elsasser profiles of the disc

rapidly increase in magnitude (see Figure 11.2). This suggests that the separation of solutions to 'disc' and 'wind cycles' portions is largely due to the shape of the diffusivity profiles, which in turn are determined by ionisation processes in the disc. The 'disc' portion generally has $\Lambda_O < 1$ for $R < 10$ AU and $\Lambda_A \lesssim 1$ for $R \lesssim 100$ AU, leading to suppression of the MRI near the mid-plane, and the possibility of settling into (quasi-)steady states. The 'wind' portion on the other hand has near ideal MHD conditions, and depending on the level of magnetisation can be highly unstable to the MRI. When we switched off ambipolar diffusion in the BL20:H+A0S runs, discs with $R \geq 10$ AU notably no longer have the disc-wind separation, as Ohmic resistivity alone is not enough to enforce the suppression of the MRI in the 'disc' region for those radii. The whole system then takes on the nature of a wind cycle, as represented by the 'C-A' and 'C-O' states.

The ambipolar Elsasser number in general remains at low values much further away from the mid-plane than the Ohmic Elsasser number, and the high ambipolar diffusivity in the lower atmosphere is likely to be responsible for shutting down the wind cycles in some of the slanted steady discs of the BL20:H0+S runs compared with the wind cycles of the slanted steady discs of the BL20:H+A0S runs at the same radii and magnetisations. The presence of the Hall effect in the positive configuration also helps with the shutting down of cycles in the wind region (compare the runs of BL20:H+S with BL20:H0S). This is in line with the result from Chapters 5 and 6 that Hall drift in the positive configuration contributes to the stabilisation of the MRI with respect to the threshold requirement for marginal stability. Switching the Hall configuration from positive to negative on the other hand increases the presence of wind cycles (compare L14:H+S results to those of L14:H-S), and may be attributed to the destabilising effect the negative Hall configuration has on the system.

Generally, switching of the configuration in the 'disc' portion between different long-term states does not alter much the strength of the wind cycles. This is evidenced by comparing data from BL20:H+S and BL20:H0S in Figure 11.3 with those from BL20:H+G and BL20:H0G respectively in Figure 11.4, and noting the similarity in wind-cycle strength despite the different profiles in the 'disc' portion. We also checked that the cycles had similar absolute strengths in their outbursts across the two sets of data. Hence cycle dynamics is largely independent of the solution in the disc portion, and is rather dependent on the underlying diffusivity profile determined from the disc model. In the previous Chapter, we concluded that the shutting down of wind cycles in the 'wind' region is largely due to the large outflow rate produced by the mid-plane bulge profile of the saturated slanted steady state, which may seem to contradict the results we have here. However, there is one crucial difference our discs have to those of Chapter 10, in that the hourglass steady solutions we

have here in the 'disc' portion also launch strong outflows, and have maximum values in b_x and b_y that are similar in strength to their slanted mid-plane bulge steady counterpart. Therefore, different long term configurations of the 'disc' portion under the same diffusivity parameters have similar contributions to the dampening or shutting down of the wind-cycles from their outflow rates, leading to wind-cycles of similar relative and absolute strength in the 'wind' regions.

Across all our simulations, the strength of wind cycles generally increases with increasing radius and β_0 within each disc model. Discs in the positive Hall configuration with $R \leq 15$ AU at $\beta_0 = 10^3$ and with $R \leq 4$ AU at $\beta_0 = 10^4$ have no wind cycles at all and are overall steady. The trend of increasing wind cycle strength with increasing radius can be attributed to the overall increase in the profiles of Λ_O and Λ_A, as the disc becomes more ionised further away from the star, resulting in weaker η_O and η_A profiles that act less to quench the MRI. As wind cycles are driven by a delicate balance between MRI mode growth and advective eviction (see Section 10.4), slowing of the former by lower Λ_O or Λ_A values could lead to shutting down of the cycles in less highly ionised discs at smaller radii, and advection expels the modes from the box before they are sufficiently strong to modify the disc profile.

The increase in relative strength of wind cycles with decreasing vertical magnetisation of the disc on the other hand is harder to explain. We speculate that it may be due to a stronger field shutting down the growth of MRI in the wind region. However, we also note that where wind cycles are present, runs with higher β_0 have wind cycles with longer periods than those with lower β_0. This suggests that lower β_0 leads to higher growth rates of the MRI which drive the wind cycles more rapidly in discs where wind cycles exist. These opposing trends may be due to two competing effects that affect that growth rates of the MRI modes that drive the wind cycles, with a sufficiently strong field quenching the modes completely, while too weak a field would lead to smaller growth rates.

Type of solution in the 'disc' region initiated with the 'bxSINmod' profile

For discs initiated with 'bxSINmod' where all three non-ideal effects are present in the positive Hall configuration, the type of solution found for the long term state of the 'disc' region shifts from slanted mid-plane bulge steady solutions at lower radii and higher magnetisations, to hourglass steady, and eventually displaced steady or asymmetric one-sided solutions as we move to larger radii and lower magnetisations. The greater susceptibility to the slanted mid-plane bulge steady state for disc slices at lower radii is likely to be due to the higher levels of Ohmic diffusivity near the mid-plane, which lends less support for a strong current layer in the mid-plane region present in any hourglass-like configurations, but rather eventually expels it, transitioning it to a more slanted-like configuration. As disc

radius increases, the dominant 'diffusive' non-ideal effect in the 'disc' region switches from Ohmic to ambipolar diffusion (see Figure 11.2). Ambipolar diffusion, as we shall investigate in Section 11.4, naturally supports the formation of strong current layers, a result that was first noted by Brandenburg and Zweibel (1994). We speculate that this is one of the reasons for discs at larger radii to be able to retain an hourglass steady or displaced hourglass steady state in the 'disc' region for long periods of time and resist transition to the slanted mid-plane bulge steady state. On the other hand, the trend of having more hourglass steady discs at lower magnetisations is most likely due to the much slower rate at which the mid-plane bulge in b_x and b_y grows (similar to the discussion on the transition state in Section 10.3.3), leading to much longer survival of the hourglass state. Given that in our idealised set-up we initialised the 'bxSINmod' runs with a perfectly hourglass state, it would take a long time for a very slowly growing mode to amplify numerical effects that would break the original symmetry of the disc. Indeed, some of our hourglass steady disc solutions at $\beta_0 = 10^5$ do show a strong current layer with ever-increasing, albeit small departures from the mid-plane, which we speculate will continue to increase and move the current layer out of the disc if the simulation is run for much longer. We also note that, as we shall show later in Section 11.4, ambipolar diffusion can support the formation of sharper current layers when no vertical field is present than when a strong vertical field is there. This might be another factor that contributes to less vertically magnetised discs being more likely to retain hourglass steady states with sharp mid-plane current layers than more highly magnetised ones.

When the Hall effect is switched off compared with the positive configuration, discs are more likely to take an hourglass steady configuration than a slanted steady one (compare BL20:H0S runs to BL20:H+S). We attribute the tendency towards more slanted solutions of the positive Hall case to the HSI, which is active in this configuration amplifying the horizontal magnetic fields, leading to sharper current layers that are less sustainable in discs with strongly Ohmic diffusive mid-planes. The HSI may have also increased the growth rate of the $n = 1$ bulge mode in b_x and b_y which is responsible for the transition to slanted steady states in at least some of the discs at lower radii (see Section 11.3.4), increasing the likelihood of a disc being in the slanted configuration by the end of our run time. When the Hall polarity is switched from positive to negative on the other hand, disc portions at all radii and magnetisations have an even greater tendency to take on slanted states (compare L14:H+S solutions with L14:H-S in Figure 11.5) and also have much smaller horizontal magnetic fields (compare the horizontal magnetic field profiles of LR10b3H+S and LR10b3H-S in the left hand plot of Figure 11.7). The negative feedback loop of the negative Hall configuration (see Section 2.5.3 and the bottom half of Figure 2.7) weakens the horizontal magnetic fields, causing b_y to take smaller values in the mid-plane 'disc' regions where the Hall effect is

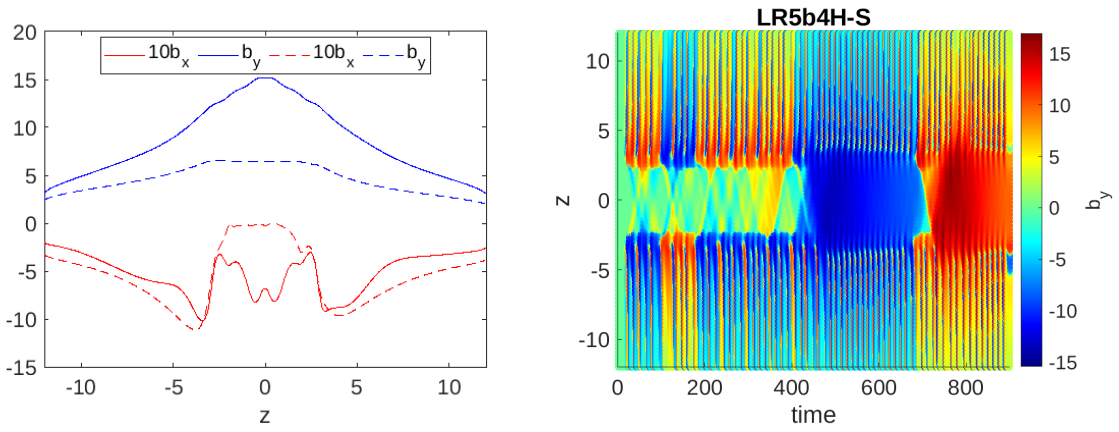

Fig. 11.7 Left: b_x (red) and b_y (blue) profiles of the runs LR10b3H+S (solid lines) and LR10b3H-S (dashed lines) at $t = 948.4\Omega^{-1}$. The profiles are largely steady in time with small variations that do not change their overall shape. Right: space-time plot of b_y for run LR5b4H-S.

strongest than would be generated by shearing of b_x in the normal MRI. The b_x profile also takes on near zero values in the mid-plane regions. We note that b_x and b_y can be of the same sign in parts of the mid-plane regions, possibly due to the ion-cyclotron instability (ICI) generating b_y from b_x of the same sign. Discs with a negative Hall polarity are also generally more unstable than discs with a positive polarity, or where the Hall effect is not present at all, and some of the slanted solutions take on more of a cyclic nature, such as in the right-hand plot of Figure 11.7.

Finally, when we reduced the disc ionisation by a factor of 100 for discs with all three non-ideal effects in the positive Hall configuration to mimic the effect of dust, we find that solutions generally take on a slightly more slanted nature, but with the general trends discussed unaffected (compare L14:H+S results with L14:H+r2S). This is likely to be due to less ionised discs being more diffusive, so providing less support for the strong mid-plane current layer in hourglass configurations. This shows that dusty discs are more likely to take the slanted configuration than hourglass discs, but the overall trends in variation with radius and magnetisation are unaffected.

Type of solution in the ‘disc’ region initiated with the ‘bxGauss’ profile

When discs are initiated with the ‘bxGauss’ profile, the vast majority of solutions of the BL20:H+G and BL20:H0G disc models settle into slanted-like states, with discs at lower radii ($R \lesssim 10$ AU) generally taking the slanted mid-plane bulge steady state. This shows that the long term state of a solution is strongly dependent on the history of the disc profile, and is more inclined toward a slanted state than an hourglass one. Some of the BL20:H0G discs at

larger radii settled into slanted multiple-bend states rather than the traditional mid-plane bulge configuration. This may be due to the dominance of ambipolar diffusion in the mid-plane region over Ohmic diffusion at larger radii allowing strong current layers that are present in the slanted multiple-bend state to be supported. At $R \geq 30$ AU, discs become less steady and may take the more variable asymmetric one-sided solution rather than slanted steady configurations, which can be attributed to the reduced significance of all non-ideal MHD effects at large radii.

11.3.4 Nature of the transition

A key question for our full non-ideal MHD investigation in this Chapter is whether the $n = 1$ mid-plane bulge MRI mode is still valid for transitioning discs from hourglass states to slanted steady states, as occurred in the solutions of the previous Chapter. We find that this is generally still true for discs at small radii ($R \lesssim 2$ AU) where the mid-plane has sufficient Ohmic resistivity to suppress other MRI modes in this region. At larger radii, we find that while the bulge growth mechanism is still at work, the evolution of the mid-plane is also influenced by other factors.

The mid-plane bulge MRI growth-induced transition of discs at small radii is verified by confirming that the growth of the mid-plane values of b_x and b_y is indeed exponential, with similar saturation to those found in Chapter 10. The top left plot of Figure 11.8 shows the mid-plane values of b_x and b_y plotted over time for the run BR0p5b3H+S, which can be compared in form to Figure 10.5. The initial growth fits perfectly with an exponential of the form $\exp(\sigma t)$ for both b_x and b_y, with $\sigma = 0.496$ and 0.493 respectively (see bottom plots of Figure 11.8) agreeing with each other to a high degree of precision. We find that discs which transit to slanted mid-plane bulge steady states in BL20:H+S discs satisfy similar properties up to $R = 2$ AU, while discs up to $R = 10$ AU in both BL20:H+S and L14:H+S discs also have similarly shaped growths of mid-plane b_x and b_y in time, but with ever-increasing departures from pure exponential growth in the early stages, and increasing spikes in b_x and b_y in the saturation stage of the solution. This can be seen in the top right plot of Figure 11.8 for the disc BR4b3H+S. For discs that end up in the slanted steady state at or beyond $R = 30$ AU, the mid-plane b_x and b_y values may even end up oppositely signed to their initial direction of increase. We take this to imply that as we move to disc slices at higher radii, there are additional factors at work that are transitioning the disc away from hourglass symmetry to slanted symmetry, and that the slowly growing mid-plane bulge MRI mode characteristic of discs with high levels of Ohmic resistivity near the mid-plane is no longer the only or dominant mechanism in causing the transition. The precise identification of these additional factors is beyond the scope of this Thesis, but may be linked with the nonlinear

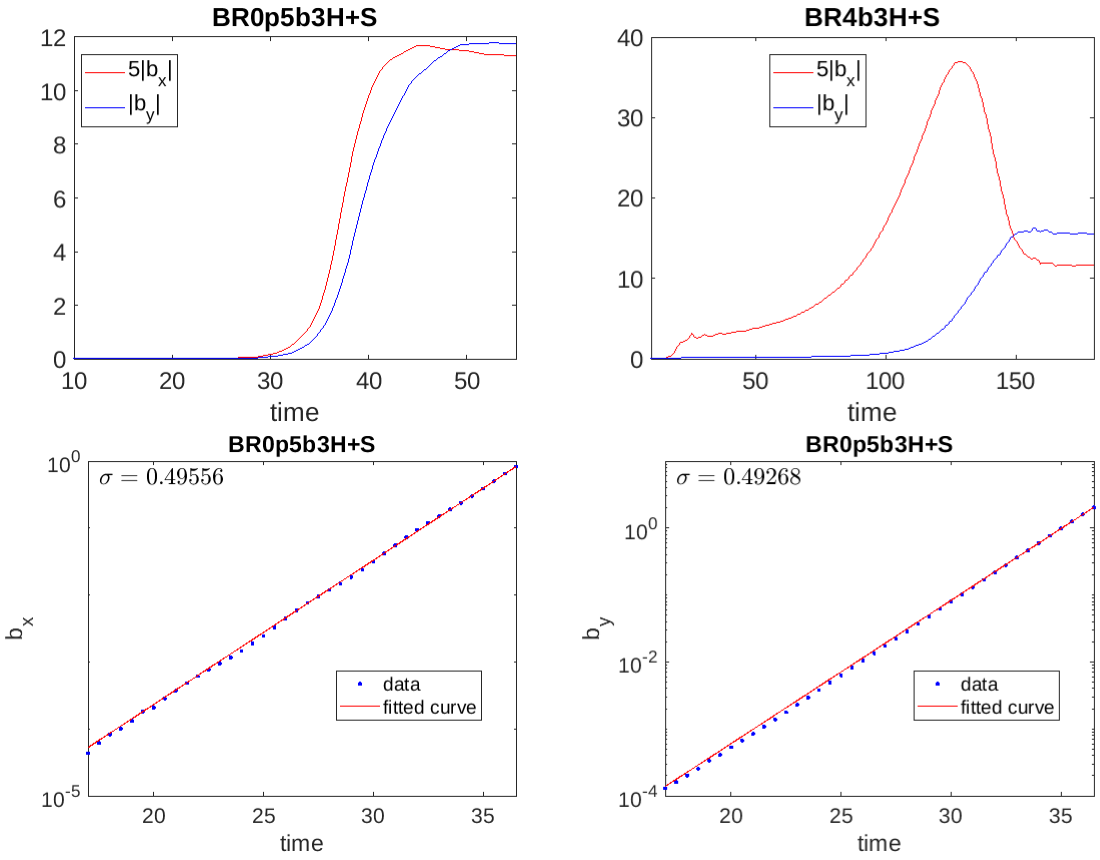

Fig. 11.8 Plots of mid-plane b_x (red) and b_y (blue) against time for BR0p5b3H+S (top left) and BR4b3H+S (top right). Bottom plots shows the exponential fits for b_x (left) and b_y (right) for BR0p5b3H+S between $t = 17$ and $36.5\Omega^{-1}$.

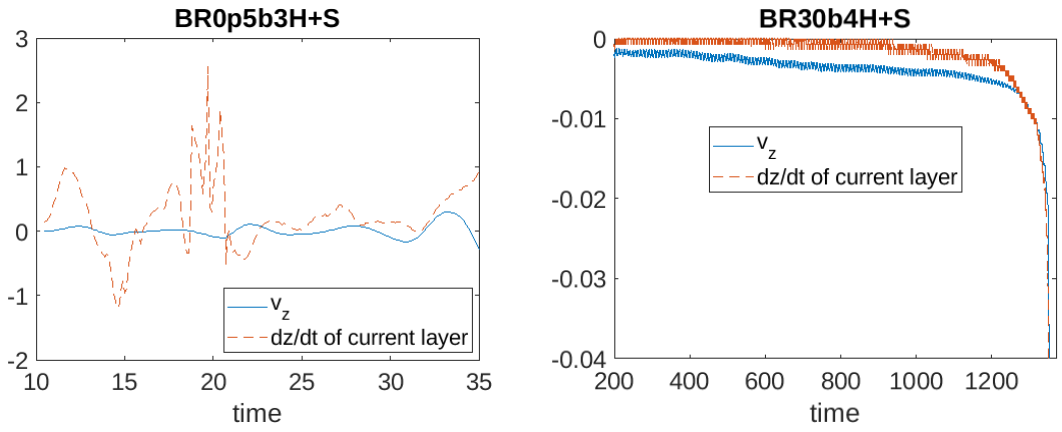

Fig. 11.9 Plots of v_z at the position of the strong current layer originally at the mid-plane (blue) and $\mathrm{d}z/\mathrm{d}t$ of the same current layer (red dashed) against time for discs BR0p5b3H+S (left) and BR30b4H+S (right).

and anisotropic nature of Hall drift and ambipolar diffusion that dominate the 'disc' portion in the limit of large radii.

We also verified that the movement of the strong current layer away from the mid-plane in the early stages is not purely due to vertical advection by the outflow by computing $\mathrm{d}z/\mathrm{d}t$ of the position of the current layer and comparing it with v_z of that location at the same time. Two examples of this are shown in Figure 11.9 for two different discs' current layers that were originally at the mid-plane. While there is a strong correspondence between v_z at and $\mathrm{d}z/\mathrm{d}t$ of the current layer once it has moved beyond a certain distance from the mid-plane (e.g. from $t = 1300\Omega^{-1}$ onwards in the right-hand plot of Figure 11.9), where it probably crossed the Alfvén point and its motion then became dominated by vertical advection, there is significant difference in the early stages of its journey, suggesting that other effects, perhaps the growth of MRI modes or the presence of non-ideal effects, are responsible for shifting the position of the current layer in addition to vertical advection.

11.4 Analysis of the ambipolar diffusion-supported current layer

One of the key factors identified in the previous Section that could affect how likely an hourglass steady configuration is to exist is the ability of ambipolar diffusion to support the formation of sharp current layers near the mid-plane of the disc.

Brandenburg and Zweibel (1994) investigated the formation of sharp structures around magnetic nulls (where $B_x = B_y = 0$) using a 1D vertical incompressible model with no

vertical magnetic field, uniform density and only the presence of ambipolar diffusion. They also neglected the effect of shear. They found that ambipolar diffusion has a self-focussing effect, forming current layers that scale like $z^{-2/3}$, where z is the vertical displacement from the null point. We follow their analysis but include both a vertical magnetic field and Ohmic diffusion to see what their effect on the solution may be. The induction equation that we need to solve can be rewritten in the form:

$$\partial_t \mathbf{B} = \nabla \times (\mathbf{u} \times \mathbf{B} + \mathbf{u}_{\rm AD} \times \mathbf{B} - \eta_O \nabla \times \mathbf{B}), \tag{11.29}$$

where

$$\mathbf{u}_{\rm AD} = \frac{\eta_A}{\mu_0 |\mathbf{B}|^2} (\nabla \times \mathbf{B}) \times \mathbf{B} \tag{11.30}$$

is the ion-neutral drift velocity. The magnetic field is given by $\mathbf{B} = (B_x(z,t), B_y(z,t), B_z)$, and we rewrite the horizontal components in terms of a complex number as $\mathscr{B} \equiv B_x + iB_y$. We also introduce the ambipolar factor $D_A^{-1} = \eta_A / \mu_0 |\mathbf{B}|^2$.

We follow the procedure in Brandenburg and Zweibel (1994) in assuming that the density is uniform (such that $\partial_z D_A = 0$) and that we have hydrostatic equilibrium so that $\mathbf{u} = 0$. We also assume that Λ_A and η_O are uniform in the domain considered. These assumptions are reasonable if the thickness of the current layer is small compared to the vertical scale height. The induction equation would then only have non-zero entries in the x and y components of the form:

$$\begin{aligned} \partial_t \mathbf{B} = \; & D_A \nabla \times ([(\nabla \times \mathbf{B}) \times \mathbf{B}] \times \mathbf{B}) - \eta_O \nabla \times (\nabla \times \mathbf{B}) \\ = \; & D_A \begin{pmatrix} \left(B_z^2 + \dfrac{\eta_O}{D_A} \right) \partial_z^2 B_x + \partial_z (B_x^2 \partial_z B_x + B_x B_y \partial_z B_y) \\ \left(B_z^2 + \dfrac{\eta_O}{D_A} \right) \partial_z^2 B_y + \partial_z (B_y^2 \partial_z B_y + B_x B_y \partial_z B_x) \\ \\ 0 \end{pmatrix}, \end{aligned} \tag{11.31}$$

which can be rewritten as

$$\partial_t \mathscr{B} = D_A \left[\left(B_z^2 + \frac{\eta_O}{D_A} \right) \partial_z^2 \mathscr{B} + \partial_z \left(\frac{\mathscr{B}}{2} \partial_z |\mathscr{B}|^2 \right) \right]. \tag{11.32}$$

We can see at this point that the inclusion of a vertical magnetic field has the same kind of effect on the solution as including Ohmic resistivity, which we know from Zweibel and Brandenburg (1997) resists the formation of ambipolar diffusion-induced sharp current layers. We should therefore expect a strong vertical magnetic field to similarly resist the sustaining of sharp current structures by ambipolar diffusion in our simulations.

To obtain a steady state solution, we need to set $\partial_t \mathscr{B} = 0$. Integrating (11.32), we obtain:

$$\frac{K}{D_A} = \left(B_z^2 + \frac{\eta_O}{D_A} \right) \partial_z \mathscr{B} + \frac{\mathscr{B}}{2} \partial_z |\mathscr{B}|^2, \tag{11.33}$$

where K is the constant of integration. The solution when $B_z = \eta_O = 0$ is $\mathscr{B} \propto |z|^{1/3}$, with infinite current density at $z = 0$. The inclusion of a non-zero first term of the right-hand side of Equation 11.33 when either B_z or $\eta_O \neq 0$ on the other hand does not permit the appearance of any infinite currents in the solution for non-zero values of D_A, and therefore places a limit on the sharpness of the current layer.

11.5 Discussion and relation to other works

It is worth comparing the trends uncovered in our results with the trends identified in other simulations, such as those of Lesur et al. (2014) where all three non-ideal effects (OHA) are included for discs at $R = 1 - 10$ AU, or Simon et al. (2015) which extends their work to discs up to $R = 100$ AU.

Lesur et al. (2014) found that all their OHA discs exhibited slanted symmetry in their saturated states, while we find that our $R \leq 10$ AU discs do settle into the slanted symmetry if initiated with the slanted 'bxGauss' profile, but may remain at the steady hourglass configuration when initiated with the hourglass 'bxSINmod' profile for discs at higher radii and lower magnetisations. The difference in our results may be due to the fact that the Lesur et al. (2014) simulations are in 3D, and therefore can admit a wider variety of MRI modes in the initial stages of the simulation that are otherwise limited by our 1D vertical model. Although their simulations eventually settle into largely laminar states, the symmetry breaking elements introduced by the MRI modes in the early stages would have sowed the seeds for the disc to transit to the more stable slanted symmetry within the run time. The results of Lesur et al. (2014) also only show wind cycles of the kind observed in the 'wind' region of our simulations for their Ohmic resistive-only discs, at which point the solutions largely resemble those uncovered in Chapter 10. However, no significant wind cycles were observed for their discs where Hall and ambipolar diffusion are also present, while for the same range of radii considered, we do find small wind cycles in the upper atmospheric regions of our $\beta_0 = 10^4 - 10^5$ discs. The difference here may be due to the fact our wind cycles for these discs are launched from $|z| > 5H$, whereas the boxes used in the Lesur et al. (2014) only extended up to $6H$ on either side of the mid-plane. Otherwise, our solutions do resemble the form of solution displayed in the figures of Lesur et al. (2014), and agree with their analysis that the inclusion of the Hall effect in the positive configuration leads

to more likely formation of a strong azimuthal magnetic field in the disc mid-plane which increases the vertical scale-height of the disc and launches strong steady outflows, while a negative Hall polarity would have the opposite effect, leading to a pronounced bimodality with respect to the Hall configuration in the solution profile for discs at $R \leq 10$ AU. We also find that ambipolar diffusion has a stabilising effect on the solution up to a larger scale-height of $z \sim 5H$ for $R \lesssim 10$ AU discs, in agreement with their result that inclusion of ambipolar diffusion reduces the surface activity of the discs.

At larger radii ($R \geq 10$ AU), we found that discs with ambipolar diffusion-dominated profiles can exhibit steady outflows with hourglass symmetry at $|z| > 3.5H$ with a strong off-midplane current layer (e.g. our LR60b3H+S run). The form of these solutions is similar to some of the solutions of Bai and Stone (2013b) for their ambipolar diffusion-dominated discs, and lends support to the claim that ambipolar diffusion may be responsible for retaining a strong current layer in the 'disc' portion of the solution, rather than advection out of the simulation domain and transition to full slanted symmetry.

The more variable slanted-cyclic solutions we found for some of our L14:H-S runs fit in well with the findings of Simon et al. (2015) that a negative Hall configuration can lead to unstable solutions, which in the case of their 3D simulations led to bursts of turbulent stress in the region $R \sim 5 - 10$ AU. Unlike their simulations though, our 1D runs do not permit the non-axisymmetric HSI modes which they identify as the source of the large-amplitude variability they observed. We therefore conjecture that an axisymmetric Hall instability, such as the ICI, is also at work in destabilising solutions when the Hall effect is in the negative configuration. Similar to Simon et al. (2015), we find that the importance of the Hall polarity on the solution decreases as we go to higher radii, with discs becoming more prone to take hourglass or displaced hourglass steady configurations as ambipolar diffusion becomes the dominant non-ideal MHD effect governing disc evolution.

Chapter 12

Conclusion to Part III

In this Part, we have investigated various factors that may impact on the overall symmetry of the magnetic disc-wind solution in a vertical slice of a protoplanetary disc through 1D radially local shearing box simulations. We began by examining the purely Ohmic case with a prescribed resistivity profile that is large in the mid-plane, characteristic of what we would expect in the inner disc. We then implemented all three non-ideal effects through more realistic ionisation calculations, and surveyed the types of disc and wind solutions obtained over a wide range of radii and magnetisation.

Overall, we found that both the evolution and the final state of solutions are highly dependent on three factors: the diffusivity profile of the disc, the vertical magnetisation, and the history of the disc profile. They can be summarised as follows:

- High levels of non-ideal MHD effects in the mid-plane region separate solutions into 'disc' regions which vary on a long timescale ($\mathscr{O}(10) - \mathscr{O}(100)\Omega^{-1}$), and 'wind' regions beyond a certain distance from the mid-plane, which have more rapidly varying ($\mathscr{O}(1) - \mathscr{O}(10)\Omega^{-1}$) periodic wind cycles.

- The wind cycles are driven by periodic excitation of the $n = 2$ or 3 MRI channel mode coupled with advective eviction when the Alfvén point falls below the mode peaks, and result in the cyclic states identified in Chapter 10 that can be either hourglass or slanted owing to the degeneracy of the $n = 2$ and 3 MRI modes when the strong diffusivities of the mid-plane region cut off communication between the two sides of the disc.

- A much slower growing ($\mathscr{O}(10) - \mathscr{O}(1000)\Omega^{-1}$) $n = 1$ MRI channel mode with mid-plane bulge in b_x and b_y is also present, and may take over the profile of the 'disc' portion and transition it to a slanted mid-plane bulge steady state, similar to the slanted steady wind solutions observed in other local and global simulations.

- The evolution and long-term state of the 'disc' portion is highly dependent on the history of its profile. An hourglass initial condition leads to it first settling into a (quasi-)steady hourglass state, before possible transition to the slanted steady state depending on the vertical magnetisation and diffusivity profile. A slanted initial condition on the other hand almost always leads to a slanted symmetry long-term state.

- Strong Ohmic resistivity near the mid-plane leads to the 'disc' region about the mid-plane initially taking on a near vertical magnetic field profile with b_x and $b_y \approx 0$.

- Strong Hall drift in the positive configuration near the mid-plane leads to amplification of the horizontal fields by the HSI. Amplification of horizontal fields that have initially settled into the hourglass configuration may cause it to transition into the slanted wind state owing to the limited ability of a highly resistive mid-plane to sustain strong currents. This may be one of the factors contributing to more slanted-steady final disc configurations for discs with positive Hall polarity.

- Strong Hall drift in the negative configuration about the mid-plane leads to the opposite effect of dampening the amplitude of the horizontal fields since the operation of the HSI is now reversed. We also found that the disc region is rendered less stable, which we speculate to be caused by the operation of the ICI. Discs with negative Hall polarity usually settle into slanted wind solutions with smaller mid-plane bulges in b_x and b_y than their positive Hall polarity counterparts.

- Strong ambipolar diffusivity near the mid-plane encourages the formation of sharp current layers in the mid-plane region, leading to longer or permanent survival of the 'disc' solution in an hourglass or displaced hourglass steady state.

- Stronger vertical magnetisation in general leads to a greater tendency to transition to slanted states for the long-term. It also leads to a weakening (relative to the outflow launched from the 'disc' region) or complete shutting down of the wind cycles in the 'wind' region.

- Discs with negligible levels of Ohmic resistivity and marginally stable levels of Hall and ambipolar diffusivity, such as those at large radii ($R \gtrsim 60$ AU), generally have less stable profiles than those with higher levels of all three non-ideal diffusivities. This is in line with our results from Part II concerning the contribution of non-ideal MHD effects to the overall stability of the system.

With the disc models we used, our results overall point to a picture of protoplanetary discs where, when the Hall effect is present in the positive configuration, the disc symmetry

would start off at small radii ($R \lesssim 10$ AU) in a slanted mid-plane bulge configuration with small cyclical outbursts in the atmosphere, before moving to more hourglass-like configurations with increasing levels of outbursts, and perhaps even breaking into turbulence in the atmospheric regions, as we move to large radii ($R \gtrsim 30$ AU). On the other hand, protoplanetary discs in a negative Hall configuration would also start off in the slanted mid-plane bulge configuration at small radii ($R < 5$ AU), before undergoing 'bursts' of turbulent activity at the mid-plane at small to intermediate radii ($R \sim 5-10$ AU). It would then return to the slanted symmetry but with much stronger wind cycles at intermediate radii ($R \sim 15-30$ AU), before moving towards more hourglass configurations at large radii ($R > 100$ AU). In the positive Hall configuration, a larger magnetic field would lead to a greater tendency of disc slices to settle into more slanted-like solutions, whereas for the negative Hall configuration, it appears that their effect may be opposite in supporting more hourglass-like configurations.

One area of interest for future investigations is a more precise description of how the transition of the disc to the slanted or asymmetric one-sided wind state impacts on the accretion and radial transport of poloidal magnetic flux in the disc. By nature of the slanted symmetry, a disc with such configuration cannot (at least in the local model) support a net radial steady state transport of matter or poloidal magnetic flux, as contributions from the two sides cancel out. Global simulations (Bai, 2017; Béthune et al., 2017; Gressel et al., 2020; Riols et al., 2020), as well as our simulations in Chapter 7, have also shown that such symmetry may lead to a reduction in both overall accretion and flux transport rate, and may even cause the disc wind and accretion stream to be restricted to one hemisphere only. Since the slanted symmetry steady state is more easily reached when the local B_z flux is strong, it may contribute to an automatic shut-down mechanism for the flux transport when the local build-up of B_z flux becomes too strong and the disc transitions to the slanted state. This in turn, could have an interplay with the magnetic wind driven ring formation mechanism recently uncovered by Riols and Lesur (2019); Riols et al. (2020), which assumes the wind to already have the slanted symmetry in the more highly magnetised gap regions. A future study probing the importance of the transition to the slanted wind state for the working of this mechanism, as well as the long term radial transport of vertical flux, would be needed to address these questions.

Finally, the periodic outbursts observed in our solutions show that MRI-wind outburst cycles could in theory operate in the protoplanetary disc regime, and may be linked to the time variability observed in some protoplanetary discs (Bary et al., 2009; Muzerolle et al., 2009; Wisniewski et al., 2008). However, the simplified 1D radially local nature of our study does not allow us to form any firm conclusion on the possible link between our cycles and

observations. Future work will need to be done with better informed disc ionisation profiles, as well as addressing the problem in the global simulations, to ascertain if such connections exist.

Part IV

Conclusion

Chapter 13

Conclusion

In this Thesis, we have examined the role a large-scale magnetic field plays in the structure and evolution of protoplanetary discs. We looked at how non-ideal MHD effects arising from disc microphysics in the form of Ohmic, Hall and ambipolar diffusivities impact on the evolution of the long-term radial transport of the large-scale magnetic field threading the disc. We also investigated the different factors that contribute to the overall configuration of the large scale magnetic field and the accompanying dynamics of a radially local vertical slice of the disc. Our work has shed light on the importance of effects arising from coupling between locally determined non-ideal MHD effects and globally determined disc properties such as the inclination of the disc surface magnetic field in driving global flux transport. We have also identified the local disc profile, the history of the disc and the triggering of specific MRI modes as crucial factors that influence the long term configuration of the disc slice, and whether we should expect outburst behaviour in the atmosphere.

Our work utilised the property uncovered in recent global simulations that protoplanetary discs are likely to be laminar due to the presence of non-ideal MHD effects, and therefore can be modelled by local vertical slices at different radial locations. Using this approach, we were able to isolate and determine the different factors and mechanisms that contribute to flux transport and disc configuration in radially local patches. In reality, disc slices are all interconnected, forming a continuum from the inner to the outer disc, and global effects are likely to have an important role in determining their properties. We have attempted to include an element of this in our Thesis by inputting global gradients as a parameter in some of our models. However, to obtain a full picture of protoplanetary disc dynamics under the influence of magnetic fields, we ultimately require a global approach where all such effects are included self-consistently. Our work paves the way towards the realisation of such a model by identifying the key factors on a local scale that must be included in the development of a global framework, and extends the work of previous authors in our

understanding of the interplay between magnetic fields and disc dynamics in the conditions unique to protoplanetary discs.

Appendix A

Stability of an uniform density disc with Hall drift and Ohmic resistivity

We examine the stability of the disc profiles and their variation with both diffusivity parameters and the degree of magnetisation. The wavenumber for a given set of disc parameters is

$$k^2 = \frac{2q\Omega^2\rho_0}{B_z^2}\left[1+\rho_0^2\frac{\eta_O^2\kappa^2}{B_z^4}\left(\frac{1}{1+\rho_0\tilde{\eta}_H\kappa^2/2\Omega B_z}\right)+\rho_0\frac{2\tilde{\eta}_H\Omega}{B_z}\right]^{-1}. \tag{A.1}$$

Marginal stability requires $k_{\rm crit} = \pi/2H$. If $k < (>)\, k_{\rm crit}$, then the solution would be (un)stable to the MRI. We used the density, ρ, as a measure of degree of magnetisation, as we have done before in Chapter 5. However, it is no longer meaningful to relate ρ to β in the incompressible regime. Instead, we can see that ρ_0 is related to the dimensionless magnetisation parameter μ through

$$\sqrt{\rho} = \frac{B_z}{\sqrt{2}H\Omega}\frac{1}{\mu}. \tag{A.2}$$

In the Keplerian case and setting $|B_z| = H = \Omega = 1$, this reduces to

$$\rho = \frac{1}{2\mu^2}, \tag{A.3}$$

and conversely

$$\mu = \pm\sqrt{\frac{1}{2\rho}}, \tag{A.4}$$

with $+(-)$ for the case when B_z is (anti-)aligned with Ω. Hence we can see that a high (low) ρ would indicate a low (high) degree of magnetisation in the disc.

When Ohmic resistivity is non-zero, we found that the behaviour of k with ρ_0 fall into four sub-regimes (see Figure A.1) depending on whether the rotation is aligned or anti-aligned with the field (or equivalently whether η_H is positive or negative), and on whether Ohmic or Hall diffusive effects are dominant. The criterion for Ohm (Hall) dominated regimes is given by

$$\eta_O > \ (<) \ \frac{1}{2}|\tilde{\eta}_H|B_z. \tag{A.5}$$

Without loss of generality, we describe the sub-regimes in the case when B_z is always aligned with Ω, and change to sign of η_H to reflect the change in polarity. The plots in Figure A.1 are related to Figure 5.4 in that the point(s) of critical stability marked by the red lines in former appear as points on the intersection between the relevant curve and the $f(\mu) = 0$ line in the latter. In Figure A.1, solutions to k below $k_{\rm crit}$ (marked by a horizontal red line) are stable, while solutions above the line are unstable.

$\eta_H > 0$, Ohm dominated regime

Here, k has only one turning point in the plot (see Figure A.1a). The largest possible k value is found at this turning point, which occurs at

$$\rho_{\rm max} = \frac{B_z^2}{\kappa(\eta_O - \tilde{\eta}_H B_z \kappa/2\Omega)}. \tag{A.6}$$

The corresponding value of $k_{\rm max}$ can then be calculated. If $k_{\rm max} < k_{\rm crit}$, then all magnetisations are stable. If $k_{\rm max} > \pi/2H$, unstable solutions exist. The limiting wavenumber value at zero magnetisation is given by

$$k(\rho \to \infty) = \sqrt{\frac{\tilde{\eta}_H B_z}{4q\Omega^3(\eta_O^2 + \tilde{\eta}_H^2 B_z^2)}}. \tag{A.7}$$

If this value is larger than $k_{\rm crit}$, then unstable magnetisations are contained in the region

$$\rho_0 > \rho_{\rm crit}, \tag{A.8}$$

where $\rho_{\rm crit}$ is the density corresponding to $k = k_{\rm crit}$. If $k(\rho \to \infty) < k_{\rm crit}$, then there are two values of ρ_0 at which marginal stability can occur. The unstable magnetisations are then contained in the region between the two critical values:

$$\rho_{\rm crit,\ lower} < \rho_0 < \rho_{\rm crit,\ upper}. \tag{A.9}$$

$\eta_H > 0$, Hall dominated regime

In this case, the k versus ρ plot no longer has a turning point (see Figure A.1b). The largest possible k value is found at zero magnetisation, when $\rho \to \infty$, which is given by the same expression as equation (A.7). If $k(\rho \to \infty) > k_{\text{crit}}$, then unstable solutions exist for $\rho_0 > \rho_{0,\text{crit}}$. Otherwise, the disc is stable for all magnetisations.

$\eta_H < 0$, Ohm dominated regime

The change in polarity causes $k^2 < 0$ at low magnetisations (large ρ), yielding complex unstable modes of k (see Figure A.1c). As in the $\eta_H > 0$ Ohm dominated case, the largest possible k value is found at the turning point. This occurs at the same value as that given by equation (A.6), with its corresponding k_{max} value. Again, if $k_{\text{max}} < k_{\text{crit}}$, then all magnetisations are stable. If $k_{\text{max}} > k_{\text{crit}}$, then unstable solutions can exist. The ρ value at which $k = 0$ is given by:

$$\rho_{0,k=0} = -\frac{2\Omega B_z}{\tilde{\eta}_H \kappa^2}, \tag{A.10}$$

and is always $> \rho_{0,\text{tp}}$. Hence there are always two solutions to marginal stability, and the unstable region occurs when

$$\rho_{\text{crit, lower}} < \rho_0 < \rho_{\text{crit, upper}}. \tag{A.11}$$

$\eta_H < 0$, Hall dominated regime

In this regime, the value of k^2 has two asymptotes in its variation with ρ, and there are always two solutions for marginal stability (see Figure A.1d). The values of ρ at which the asymptotes occur are at

$$\rho_{\text{asym}\pm} = \frac{2\Omega B_z^2}{-\kappa(\tilde{\eta}_H B_z \kappa \pm 2\eta_O \Omega \kappa)}. \tag{A.12}$$

Graphically, one marginally stable state must be between the two asymptotes, while the other must be when $\rho > \rho_{\text{asymp}+}$.

Hall only case

When Ohmic resistivity is set to zero, the condition $E_y' = 0$ forces B_y'' to also be zero, and B_y is no longer linked to B_x through η_O as before. The value of k for B_x however, can still be calculated using equation (5.39). There would be no overall flux transport. Since B_y' is

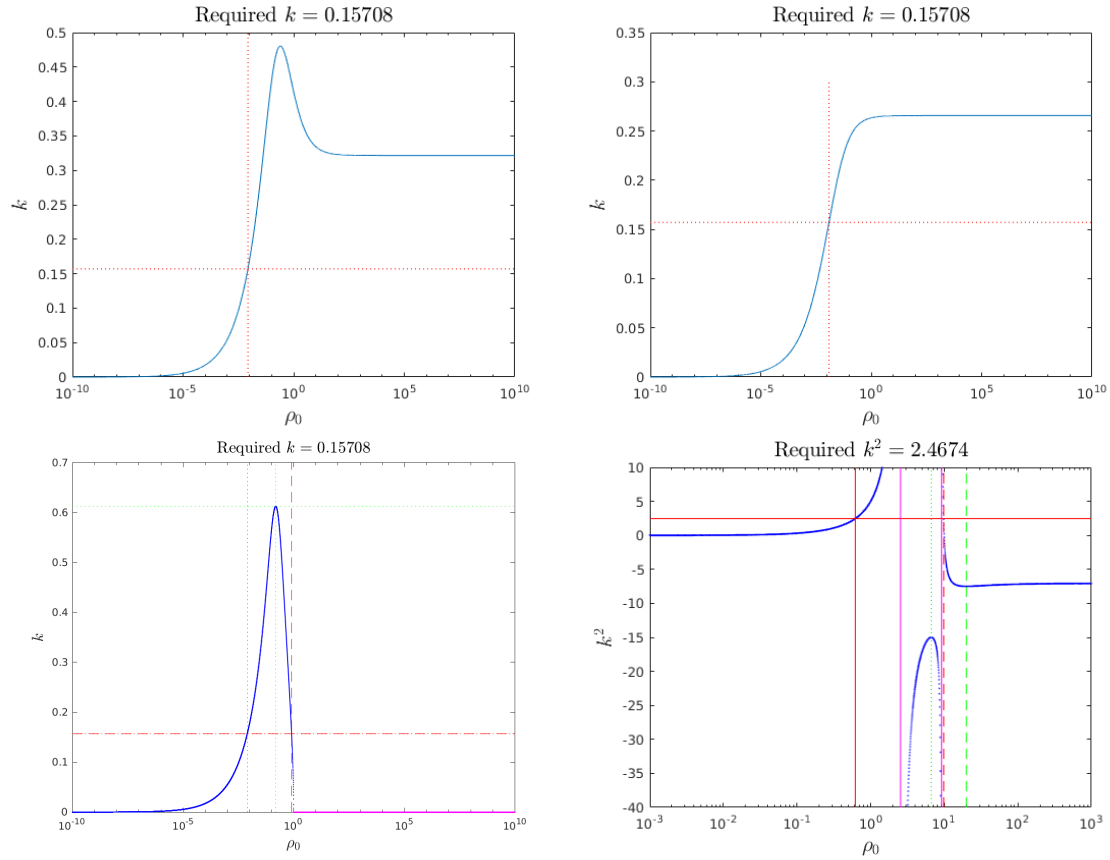

Fig. A.1 k or k^2 vs. ρ (denoted ρ_0 here) are plotted (blue) in the various regimes. Red horizontal dotted/dashed lines indicate the k value for marginal stability, while the corresponding vertical lines show the ρ value at which this occurs. Purple lines indicate either asymptotes (vertical) or regions where the solution is complex (horizontal). For the bottom plots, the green lines mark out where the various turning points are. *Top left (a):* $\eta_H > 0$, Ohm dominated case ($\eta_O = 5, \tilde{\eta}_H = 2$). *Top right (b):* $\eta_H > 0$, Hall dominated case ($\eta_O = 5, \tilde{\eta}_H = 20$). *Bottom left (c):* $\eta_H < 0$, Ohm dominated case ($\eta_O = 5, \tilde{\eta}_H = -2$). *Bottom right (d):* $\eta_H < 0$, Hall dominated case ($\eta_O = 5, \tilde{\eta}_H = -20$). For (a)−(c), disc surface $z_{\text{end}} = 10$, while (d) has $z_{\text{end}} = 1$, hence the different values of k required for marginal stability to occur (displayed in the title of each plot).

a constant, we require it to also be zero, as $B_y' \neq 0$ would imply a magnetic torque on the disc exterior. The k^2 vs. ρ plots would be of the same form as that of the Hall dominated regime cases in the limit of $\eta_O \to 0$. For the negative polarity case ($\eta_H < 0$) case, we can find the positions of the asymptotes on the graph by setting the expression within the square brackets of equation (5.39) to zero. When expressed in the Hall strength parameter x, they correspond to the points when $x = -1, -4$, with unphysical complex k solutions occuring when x is between those two values. This is in agreement with the result found in the pure Hall anaylsis of Balbus and Terquem (2001).

Appendix B

Linearised equations for marginal stability analysis

The equations I seek to linearise are

$$\rho' = c_s^{-2}[-\rho\Omega^2 z + J_x B_y - J_y B_x], \tag{B.1}$$

$$B_x' = \mu_0 J_y, \tag{B.2}$$

$$B_y' = -\mu_0 J_x, \tag{B.3}$$

$$E_x' = -\frac{3}{2}\Omega B_x. \tag{B.4}$$

$$E_y' = 0. \tag{B.5}$$

Let the following be a perturbation from the equilibrium solution

$$\begin{aligned} \rho &= \rho_{eq} + \Delta\rho \\ B_x &= B_{x,eq} + \Delta B_x \\ B_y &= B_{y,eq} + \Delta B_y \\ E_x &= E_{x,eq} + \Delta E_x \\ E_y &= E_{y,eq} + \Delta E_y \end{aligned} \tag{B.6}$$

The linearised equations are then

$$\Delta\rho' = c_s^{-2}[-\Delta\rho\Omega^2 z + \Delta J_x B_y + J_x \Delta B_y - \Delta J_y B_x - J_y \Delta B_x], \tag{B.7}$$

$$\Delta B_x' = \mu_0 \Delta J_y, \tag{B.8}$$

$$\Delta B_y' = -\mu_0 \Delta J_x, \tag{B.9}$$

$$\Delta E_x' = -\frac{3}{2}\Omega \Delta B_x. \tag{B.10}$$

$$\Delta E_y' = 0. \tag{B.11}$$

For an induction equation of the form

$$\mathbf{E} + \mathbf{v} \times \mathbf{B} = C_O \mathbf{J} + C_H \mathbf{J} \times \mathbf{B} - C_A (\mathbf{J} \times \mathbf{B}) \times \mathbf{B}, \tag{B.12}$$

we have

$$\begin{pmatrix} J_x \\ \\ J_y \end{pmatrix} = \frac{1}{\rho^2 \det(\mathbf{R})} \mathbf{M} \begin{pmatrix} E_x \\ \\ E_y \end{pmatrix}, \tag{B.13}$$

where

$$\begin{aligned} \rho^2 \det(\mathbf{R}) =& [C_O + C_A(B_z^2 + B_y^2)][C_O + C_A(B_z^2 + B_x^2)]\rho^2 \\ &+ [(C_H B_z - C_A B_x B_y)\rho + (2\Omega)^{-1} B_z^2][(C_H B_z + C_A B_x B_y)\rho + 2\Omega^{-1} B_z^2] \end{aligned} \tag{B.14}$$

and

$$\mathbf{M} = \begin{pmatrix} [C_O + C_A(B_z^2 + B_x^2)]\rho^2 & (-C_H B_z + C_A B_x B_y)\rho^2 - \dfrac{\rho B_z^2}{2\Omega} \\ \\ (C_H B_z + C_A B_x B_y)\rho^2 + \dfrac{2\rho B_z^2}{\Omega} & [C_O + C_A(B_z^2 + B_y^2)]\rho^2. \end{pmatrix} \tag{B.15}$$

Then the current perturbations from equilibrium are given by

$$\begin{pmatrix} \Delta J_x \\ \\ \Delta J_y \end{pmatrix} = \frac{-\Delta(\rho^2 \det(\mathbf{R}))}{(\rho^2 \det(\mathbf{R}))^2} \mathbf{M} \begin{pmatrix} E_x \\ \\ E_y \end{pmatrix} + \frac{\Delta \mathbf{M}}{\rho^2 \det(\mathbf{R})} \begin{pmatrix} E_x \\ \\ E_y \end{pmatrix} + \frac{\mathbf{M}}{\rho^2 \det(\mathbf{R})} \begin{pmatrix} \Delta E_x \\ \\ \Delta E_y \end{pmatrix}, \tag{B.16}$$

where

$$\begin{aligned}
\Delta(\rho^2 \det(\mathbf{R})) = &\left(-\rho_0^2 C_{\mathrm{A0}} B_{\mathrm{x0}} B_{\mathrm{y0}} + \rho_0^2 B_z C_{\mathrm{H0}} + \frac{\rho_0 B_z^2}{2\Omega}\right) \\
&(\rho_1 C_{\mathrm{A0}} B_{\mathrm{x0}} B_{\mathrm{y0}} + \rho_0 C_{\mathrm{A0}} B_{\mathrm{x0}} B_{\mathrm{y1}} \\
&+ \rho_0 C_{\mathrm{A0}} B_{\mathrm{x1}} B_{\mathrm{y0}} + \rho_0 C_{\mathrm{A1}} B_{\mathrm{x0}} B_{\mathrm{y0}} + \rho_1 B_z C_{\mathrm{H0}} + \rho_0 B_z C_{\mathrm{H1}}) \\
&+ \left(\rho_0 C_{\mathrm{A0}} B_{\mathrm{x0}} B_{\mathrm{y0}} + \rho_0 B_z C_{\mathrm{H0}} + \frac{2B_z^2}{\Omega}\right) \\
&\left(-2\rho_0\rho_1 C_{\mathrm{A0}} B_{\mathrm{x0}} B_{\mathrm{y0}} - \rho_0^2 C_{\mathrm{A0}} B_{\mathrm{x0}} B_{\mathrm{y1}} - \rho_0^2 C_{\mathrm{A0}} B_{\mathrm{x1}} B_{\mathrm{y0}}\right. \\
&\qquad \left. - \rho_0^2 C_{\mathrm{A1}} B_{\mathrm{x0}} B_{\mathrm{y0}} + 2\rho_0\rho_1 B_z C_{\mathrm{H0}} + \rho_0^2 B_z C_{\mathrm{H1}} + \frac{\rho_1 B_z^2}{2\Omega}\right) \\
&+ \rho_0^2 \left(\left(C_{\mathrm{A0}} B_{\mathrm{y0}}^2 + C_{\mathrm{A0}} B_z^2 + C_{\mathrm{O0}}\right)\right. \\
&\qquad \left(2C_{\mathrm{A0}} B_{\mathrm{x0}} B_{\mathrm{x1}} + C_{\mathrm{A1}} B_{\mathrm{x0}}^2 + C_{\mathrm{A1}} B_z^2 + C_{\mathrm{O1}}\right) \\
&\qquad + \left(C_{\mathrm{A0}} B_{\mathrm{x0}}^2 + C_{\mathrm{A0}} B_z^2 + C_{\mathrm{O0}}\right) \\
&\qquad \left.\left(2C_{\mathrm{A0}} B_{\mathrm{y0}} B_{\mathrm{y1}} + C_{\mathrm{A1}} B_{\mathrm{y0}}^2 + C_{\mathrm{A1}} B_z^2 + C_{\mathrm{O1}}\right)\right) \\
&+ 2\rho_1\rho_0 \left(C_{\mathrm{A0}} B_{\mathrm{x0}}^2 + C_{\mathrm{A0}} B_z^2 + C_{\mathrm{O0}}\right)\left(C_{\mathrm{A0}} B_{\mathrm{y0}}^2 + C_{\mathrm{A0}} B_z^2 + C_{\mathrm{O0}}\right),
\end{aligned} \tag{B.17}$$

$$\begin{aligned}
\Delta M_{11} = \; &\rho_0^2 \left(2C_{\mathrm{A0}} B_{\mathrm{y0}} B_{\mathrm{y1}} + C_{\mathrm{A1}} B_{\mathrm{y0}}^2 + C_{\mathrm{A1}} B_z^2 + C_{\mathrm{O1}}\right) \\
&+ 2\rho_1\rho_0 \left(C_{\mathrm{A0}} B_{\mathrm{y0}}^2 + C_{\mathrm{A0}} B_z^2 + C_{\mathrm{O0}}\right),
\end{aligned} \tag{B.18}$$

$$\begin{aligned}
\Delta M_{12} = \; &2\rho_0\rho_1 C_{\mathrm{A0}} B_{\mathrm{x0}} B_{\mathrm{y0}} + \rho_0^2 C_{\mathrm{A0}} B_{\mathrm{x0}} B_{\mathrm{y1}} + \rho_0^2 C_{\mathrm{A0}} B_{\mathrm{x1}} B_{\mathrm{y0}} + \rho_0^2 C_{\mathrm{A1}} B_{\mathrm{x0}} B_{\mathrm{y0}} \\
&- 2\rho_0\rho_1 B_z C_{\mathrm{H0}} - \rho_0^2 B_z C_{\mathrm{H1}} - \frac{\rho_1 B_z^2}{2\Omega},
\end{aligned} \tag{B.19}$$

$$\begin{aligned}
\Delta M_{21} = \; &2\rho_0\rho_1 C_{\mathrm{A0}} B_{\mathrm{x0}} B_{\mathrm{y0}} + \rho_0^2 C_{\mathrm{A0}} B_{\mathrm{x0}} B_{\mathrm{y1}} + \rho_0^2 C_{\mathrm{A0}} B_{\mathrm{x1}} B_{\mathrm{y0}} \\
&+ \rho_0^2 C_{\mathrm{A1}} B_{\mathrm{x0}} B_{\mathrm{y0}} + 2\rho_0\rho_1 B_z C_{\mathrm{H0}} + \rho_0^2 B_z C_{\mathrm{H1}} + \frac{2\rho_1 B_z^2}{\Omega},
\end{aligned} \tag{B.20}$$

$$\begin{aligned}
\Delta M_{22} = \; &\rho_0^2 \left(2C_{\mathrm{A0}} B_{\mathrm{y0}} B_{\mathrm{y1}} + C_{\mathrm{A1}} B_{\mathrm{y0}}^2 + C_{\mathrm{A1}} B_z^2 + C_{\mathrm{O1}}\right) \\
&+ 2\rho_1\rho_0 \left(C_{\mathrm{A0}} B_{\mathrm{y0}}^2 + C_{\mathrm{A0}} B_z^2 + C_{\mathrm{O0}}\right),
\end{aligned} \tag{B.21}$$

with the subscript 0 terms being the values of the variables and diffusivities of the equilibrium solution profile, and subscript 1 terms are the first order deviation of the Δ terms of the perturbation from equilibrium.

Appendix C

Pseudo-spectral method

We have a system of N linear differential equations with variables $v_1(z), v_2(z), \cdots, v_N(z)$ dependent on coordinate z. In operator form, the equations can be written in matrix form on a grid in z of size M as:

$$\mathscr{L}\mathrm{X} = \mathrm{S}, \tag{C.1}$$

where $\mathscr{L}$ is the $NM \times NM$ matrix operator acting on the NM column vector of variables in z space, and S is the NM column vector of source terms.

The matrix $\mathscr{L}$ is arranged as:

$$\mathscr{L} = \begin{pmatrix} \mathscr{L}_{1,v_1} & \mathscr{L}_{1,v_2} & \cdots & \mathscr{L}_{1,v_N} \\ \mathscr{L}_{2,v_1} & & & \\ \vdots & & & \\ \mathscr{L}_{N,v_1} & \cdots & & \mathscr{L}_{N,v_N} \end{pmatrix}, \tag{C.2}$$

where the first part of the subscript denote the equation it is describing, while the second part denotes the variable on which it is acting. Each $\mathscr{L}_{n,v_n}$ is a $M \times M$ matrix.

The vector of variables is arranged as:

$$\mathrm{X} = \begin{pmatrix} v_1(z) \\ \downarrow \\ v_2(z) \\ \downarrow \\ \vdots \\ v_N(z) \\ \downarrow \end{pmatrix}. \tag{C.3}$$

Likewise, S is arranged as

$$S = \begin{pmatrix} f_1(z) \\ \downarrow \\ f_2(z) \\ \downarrow \\ \vdots \\ f_N(z) \\ \downarrow \end{pmatrix}, \tag{C.4}$$

where $f_n(z)$ denotes the source term dependent on z of the n^{th} equation.

C.1 Solving the eigenvalue problem (with no source terms)

We want to solve

$$\mathscr{L}\mathrm{X} = (\mathscr{L}_{\text{base}} + \sigma\mathscr{L}_{\sigma})\mathrm{X} = 0, \tag{C.5}$$

where $\mathscr{L}_{\text{base}}$ is the operator with all σ terms removed, and $\mathscr{L}_{\sigma}$ is the σ only terms of the operator.

We can then rearrange the equation so that

$$\mathscr{L}_{\text{base}}\mathrm{X} = -\sigma\mathscr{L}_{\sigma}\mathrm{X}, \tag{C.6}$$

and

$$(-\mathscr{L}_{\sigma}^{-1}\mathscr{L}_{\text{base}})\mathrm{X} = \sigma\mathrm{X}, \tag{C.7}$$

which in other words is an eigenvalue problem for the matrix $-\mathscr{L}_{\sigma}^{-1}\mathscr{L}_{\text{base}}$.

Appendix D

Mathematical derivation of analytic models for analysing GO model

D.1 Analytic model Ohmic diffusion only

This section follows the same procedures as Section 4.1 of Guilet & Ogilvie (2012). We assume constant Ohmic diffusivity throughout the disc.

Passive field regime

$\beta \to \infty$ and the equations become:

$$-2u_\phi = \frac{3}{2} + D_H - D_{\nu\Sigma} + \left(\frac{3}{2} - D_H\right)\zeta^2, \tag{D.1}$$

$$u_r = 0, \tag{D.2}$$

$$\eta_O \partial_\zeta^2 b_r = 0, \tag{D.3}$$

$$-\eta_O \partial_\zeta^2 b_\phi - \partial_\zeta u_\phi + \frac{3}{2} b_r = 0. \tag{D.4}$$

The azimuthal velocity can then be written as:

$$u_\phi = u_{\phi 0} + u_{\phi 2}\zeta^2, \tag{D.5}$$

$$u_{\phi 0} = -\frac{1}{2}\left(\frac{3}{2} + D_H - D_{\nu\Sigma}\right), \tag{D.6}$$

$$u_{\phi 2} = \frac{1}{2}\left(D_H - \frac{3}{2}\right). \tag{D.7}$$

From (D.3), and the boundary condition $b_r(0) = 0$, we can deduce that:

$$b_r = b_{r1}\zeta. \tag{D.8}$$

We can then find b_ϕ by substituting (D.5) and (D.8) into (D.4), giving us:

$$\partial_\zeta^2 b_\phi = \frac{1}{\eta_O}\left(-2u_{\phi 2} + \frac{3}{2}b_{r1}\right)\zeta. \tag{D.9}$$

This, with the boundary condition $b_\phi(0) = 0$, has the solution

$$b_\phi = \frac{1}{6\eta_O}\left(-2u_{\phi 2} + \frac{3}{2}b_{r1}\right)\zeta^3 + b_{\phi 1}\zeta. \tag{D.10}$$

The flux transport in this region is given by Equation (82):

$$u_\Psi = \eta_O(\partial_\zeta b_r - D_B). \tag{D.11}$$

Force-free regime

$\beta \ll 1$, nothing can compensate the Lorentz force resulting in force-free magnetic fields with current parallel to the field lines. The equations become:

$$\partial_\zeta b_r = D_B, \tag{D.12}$$

$$\partial_\zeta b_\phi = 0, \tag{D.13}$$

$$\partial_\zeta u_r = 0, \tag{D.14}$$

$$-\partial_\zeta u_\phi + \frac{3}{2}b_r = 0. \tag{D.15}$$

For our case where the field is almost vertical, the radial and azimuthal currents vanish. Diffusive effects no longer have any importance, and:

$$\partial_\zeta b_\phi = 0, \tag{D.16}$$

$$\partial_\zeta b_r - D_B = 0. \tag{D.17}$$

With our boundary conditions at infinity, we find that throughout the force-free region:

$$b_\phi = \pm b_{\phi s}, \tag{D.18}$$

$$b_r = \pm b_{rs} + D_B\zeta, \tag{D.19}$$

where $\pm$ stands for the sign of ζ.

For the azimuthal velocity, substituting (D.19) and (D.18) to (D.15):

$$u_\phi = \frac{3}{2}\left(b_{rs}|\zeta| + \frac{D_B}{2}\zeta^2\right) + u'_{\phi 0}, \tag{D.20}$$

where $u'_{\phi 0}$ is an integration constant to be determined.

From Equation (82), the radial velocity is equal to the flux transport velocity and is a constant:

$$u_r = u_\Psi. \tag{D.21}$$

Two-zone model

The height at which the magnetic pressure is equal to the thermal pressure is given by:

$$\zeta_B = \sqrt{\ln\left(\frac{2}{\pi}\beta_0^2\right)}. \tag{D.22}$$

We assume that for $\zeta < \zeta_B$ we have a 'passive field', and for $\zeta > \zeta_B$, we have a 'force-free field'. We neglect the thickness of the transition where β is of order unity, and determine proper boundary conditions at $\zeta = \zeta_B$. Four conditions are needed to constrain the four unknowns.

Two boundary conditions can be obtained from the analysis of the induction equation. Using (D.11), (D.8) and (D.10) at $\zeta = 0$, we obtain:

$$u_\Psi = \eta_O\left[\partial_\zeta\left(b_{r1}\zeta\right) - D_B\right] = \eta_O\left(b_{r1} - D_B\right). \tag{D.23}$$

The azimuthal component of the induction is more complicated because b_r acts as a source term. We integrate between two heights ζ_1 and ζ_2 to get:

$$\left[\eta_O\partial_\zeta b_\phi + u_\phi\right]_{\zeta_1}^{\zeta_2} = \frac{3}{2}\int_{\zeta_1}^{\zeta_2} b_r \mathrm{d}\zeta. \tag{D.24}$$

We can use this relation between ζ_B^- and ζ_B^+ to connect the two regions. We neglect the width of the intermediate region, so the RHS of the equation vanishes. This is equivalent to the condition that horizontal electric field components are continuous across the boundary. Including the force-free conditions that $\partial_\zeta b_r(\zeta_B^+) = D_B$ and $\partial_\zeta b_\phi(\zeta_B^+) = 0$, we obtain:

$$u_\phi(\zeta_B^+) - u_\phi(\zeta_B^-) = \eta_O\partial_\zeta b_\phi(\zeta_B^-). \tag{D.25}$$

The other two boundary conditions come from assuming that the magnetic field does not vary significantly at the transition between the two regions:

$$b_r(\zeta_B^-) = b_r(\zeta_B^+) = b_{rs} + D_B\zeta_B, \tag{D.26}$$

$$b_\phi(\zeta_B^-) = b_\phi(\zeta_B^+) = b_{\phi s}. \tag{D.27}$$

The radial magnetic field profile in the passive-field region is then given by:

$$b_r(\zeta) = b_{r1}\zeta = \left[\frac{b_{rs}}{\zeta_B} + D_B\right]\zeta. \tag{D.28}$$

While the azimuthal magnetic field profile in the passive-field region is:

$$b_\phi = \frac{1}{6\eta_O}\left(-2u_{\phi 2} + \frac{3}{2}b_{r1}\right)\zeta^3 + b_{\phi 1}\zeta. \tag{D.29}$$

where

$$b_{r1} = \frac{b_{rs}}{\zeta_B} + D_B, \tag{D.30}$$

$$b_{\phi 1} = \frac{b_{\phi s}}{\zeta_B} - \frac{1}{6\eta_O}\left(-2u_{\phi 2} + \frac{3}{2}b_{r1}\right)\zeta_B^2. \tag{D.31}$$

The azimuthal velocity field in the passive-field region is given by (D.5), while in the force-free field region we use (D.25) to find:

$$u_\phi = \frac{3}{2}\left(b_{rs}|\zeta| + \frac{D_B}{2}\zeta^2\right) + u'_{\phi 0}, \tag{D.32}$$

$$u'_{\phi 0} = \eta_O \partial_\zeta b_\phi(\zeta_B^-) + u_\phi(\zeta_B^-) - \frac{3}{2}\left(b_{rs}|\zeta_B| + \frac{D_B\zeta_B^2}{2}\right). \tag{D.33}$$

To calculate the flux transport, we evaluate the gradients of the horizontal magnetic fields in the passive-field region:

$$\partial_\zeta b_r^- = \frac{b_{rs}}{\zeta_B} + D_B, \tag{D.34}$$

$$\partial_\zeta b_\phi^- = \frac{1}{3\eta_O}\left(-2u_{\phi 2} + \frac{3}{2}b_{r1}\right)\zeta^2 + b_{\phi 1}. \tag{D.35}$$

This gives us the flux transport velocity as:

$$u_\Psi = \eta_O \frac{b_{rs}}{\zeta_B}. \tag{D.36}$$

This shows us that the Ohm term can drive flux transport given the presence of an inclination in the poloidal field to the vertical. A large scale radial magnetic gradient also contributes to flux transport.

D.2 Approximate analytic model when $\eta_H \gg \eta_O$

We follow the same procedure as Appendix D.1 but with η_H included.

Purely hydrodynamic, $\beta \to \infty$ [Passive field]

The equations become:

$$-2\tilde{u}_\phi = \frac{3}{2} + D_H - D_{v\Sigma} + \left(\frac{3}{2} - D_H\right)\zeta^2, \tag{D.37}$$

$$\tilde{u}_r = 0, \tag{D.38}$$

$$\partial_\zeta\left(\eta_O \partial_\zeta b_r\right) + \partial_\zeta\left(\eta_H \partial_\zeta b_\phi\right) = D_B \partial_\zeta\left(\eta_O\right), \tag{D.39}$$

$$\partial_\zeta\left(\tilde{\eta}_H \partial_\zeta b_r\right) - \partial_\zeta\left(\tilde{\eta}_O \partial_\zeta b_\phi\right) - \partial_\zeta u_\phi + \frac{3}{2} b_r = D_B \partial_\zeta \tilde{\eta}_H. \tag{D.40}$$

From (D.37), we can write

$$u_\phi = u_{\phi 0} + u_{\phi 2}\zeta^2, \tag{D.41}$$

$$u_{\phi 0} = -\frac{1}{2}\left(\frac{3}{2} + D_H - D_{v\Sigma}\right), \tag{D.42}$$

$$u_{\phi 2} = \frac{1}{2}\left(D_H - \frac{3}{2}\right). \tag{D.43}$$

Assuming constant diffusivities, we have:
(D.39):

$$\eta_O \partial_\zeta^2 b_r + \eta_H \partial_\zeta^2 b_\phi = 0, \tag{D.44}$$

(D.40):

$$\eta_H \partial_\zeta^2 b_r - \eta_O \partial_\zeta^2 b_\phi - 2u_{\phi 2}\zeta + \frac{3}{2} b_r = 0. \tag{D.45}$$

We find B_r via (D.45)$\times\eta_H$ + (D.44) $\times\eta_O$, which after some rearrangement gives us:

$$\partial_\zeta^2 b_r + \frac{3}{2}\left(\frac{\eta_H}{\eta_O^2 + \eta_H^2}\right) b_r = 2u_{\phi 2}\left(\frac{\eta_H}{\eta_O^2 + \eta_H^2}\right)\zeta. \tag{D.46}$$

This can be solved as a second order ODE using standard techniques:

$$b_{r,\mathrm{CF}} = B_1 \cos(\kappa\zeta) + B_2 \sin(\kappa\zeta), \tag{D.47}$$

$$\kappa = \sqrt{\frac{3}{2}\left(\frac{\eta_H}{\eta_O^2+\eta_H^2}\right)}, \tag{D.48}$$

$$b_{r,\mathrm{PI}} = \frac{4}{3}u_{\phi 2}\zeta, \tag{D.49}$$

$$b_{r,\mathrm{GS}} = b_{r,\mathrm{CF}} + b_{r,\mathrm{PI}}. \tag{D.50}$$

Applying midplane boundary conditions, we obtain $B_1 = 0$. Hence,

$$b_r(\zeta) = B_2 \sin(\kappa\zeta) + \frac{4}{3}u_{\phi 2}\zeta, \tag{D.51}$$

$$u_{\phi 2} = \frac{1}{2}\left(D_H - \frac{3}{2}\right). \tag{D.52}$$

Note that when $\eta_H = 0$, $\partial_\zeta^2 b_r = 0$, and

$$b_r = b_{r1}\zeta, \tag{D.53}$$

where b_{r1} is a constant to be determined.

We find B_ϕ via (D.44)$\times\eta_H$ − (D.45)$\times\eta_O$, which after rearranging gives us:

$$\partial_\zeta^2 b_\phi = \frac{3}{2}B_2\left(\frac{\eta_O}{\eta_O^2+\eta_H^2}\right)\sin(\kappa\zeta). \tag{D.54}$$

When $\eta_O \neq 0$, $\eta_H = 0$:

$$\partial_\zeta^2 b_\phi = 0, \tag{D.55}$$

$$b_\phi(\zeta) = b_{\phi 1}\zeta. \tag{D.56}$$

When $\eta_O, \eta_H \neq 0$:

$$b_\phi = -B_2\frac{\eta_O}{\eta_H}\sin(\kappa\zeta) + b_{\phi 1}\zeta. \tag{D.57}$$

As $\eta_H \to 0$, $\kappa \to 0$ but the limit is such that $b_\phi \to \pm\infty$.

The flux transport in this region is given by Equation (82):

$$u_\Psi = \eta_O(\partial_\zeta b_r - D_B) + \eta_H\partial_\zeta b_\phi. \tag{D.58}$$

Force-free magnetic field

By the same arguments outlined in Appendix D.1, we have:

$$\partial_\zeta b_\phi = 0, \tag{D.59}$$

$$\partial_\zeta b_r - D_B = 0. \tag{D.60}$$

With our boundary conditions at infinity, we find that throughout the force-free region:

$$b_\phi = \pm b_{\phi s}, \tag{D.61}$$

$$b_r = \pm b_{rs} + D_B \zeta, \tag{D.62}$$

where $\pm$ stands for the sign of ζ.

The absence of a current means that the magnetic field cannot diffuse. Velocity is dtermined by the fact that the fluid is frozen into the magnetic field lines.

For the azimuthal velocity, substituting (D.62) and (D.61) to Equation (64) and integrating over ζ:

$$u_\phi = \frac{3}{2}\left(b_{rs}|\zeta| + \frac{D_B}{2}\zeta^2\right) - D_B\eta_H + u'_{\phi 0}. \tag{D.63}$$

The radial velocity is equal to the flux transport velocity and is a constant:

$$u_r = u_\Psi. \tag{D.64}$$

Two-zone model

The height at which the magnetic pressure is equal to the thermal pressure is given by:

$$\zeta_B = \sqrt{\ln\left(\frac{2}{\pi}\beta_0^2\right)}. \tag{D.65}$$

We make the same assumptions and follow through the argument of Appendix D.1 to determine the boundary conditions at $\zeta = \zeta_B$ to connect the two zones.

Two boundary conditions can be obtained from the analysis of the induction equation. Using (D.58), (D.51) and (D.57) at $\zeta = 0$, we obtain:

$$u_\Psi = \eta_O\left[\frac{4}{3}u_{\phi 2} - D_B\right] + \eta_H b_{\phi 1}. \tag{D.66}$$

The azimuthal component of the induction is more complicated because b_r acts as a source term. We integrate between two heights ζ_1 and ζ_2 to get:

$$\left[\eta_O \partial_\zeta b_\phi + \eta_H (D_B - \partial_\zeta b_r) + u_\phi\right]_{\zeta_1}^{\zeta_2} = \frac{3}{2}\int_{\zeta_1}^{\zeta_2} b_r \mathrm{d}\zeta. \tag{D.67}$$

We use this relation between ζ_B^- and ζ_B^+ to connect the two regions and neglect the width of the intermediate region, so the RHS of the equation vanishes. The force-free condition gives us $\partial_\zeta b_r(\zeta_B^+) = D_B$ and $\partial_\zeta b_\phi(\zeta_B^+) = 0$. Hence,

$$u_\phi(\zeta_B^+) - u_\phi(\zeta_B^-) = \eta_O \partial_\zeta b_\phi(\zeta_B^-) - \eta_H \partial_\zeta b_r(\zeta_B^-). \tag{D.68}$$

The two other conditions come from the two components of the equation of motion. Assuming that the magnetic field does not vary significantly at the transition between the two regions:

$$b_r(\zeta_B^-) = b_r(\zeta_B^+) = b_{rs} + D_B \zeta_B, \tag{D.69}$$

$$b_\phi(\zeta_B^-) = b_\phi(\zeta_B^+) = b_{\phi s}. \tag{D.70}$$

The radial magnetic field profile in the passive-field region is given by:

$$b_r(\zeta) = B_2 \sin(\kappa\zeta) + \frac{4}{3} u_{\phi 2} \zeta, \tag{D.71}$$

where

$$B_2 = \frac{b_{rs} + \left(D_B - \frac{4}{3}u_{\phi 2}\right)\zeta_B}{\sin(\kappa\zeta_B)}, \tag{D.72}$$

The azimuthal magnetic field profile in the passive-field region is:

$$b_\phi = -B_2 \frac{\eta_O}{\eta_H} \sin(\kappa\zeta) + b_{\phi 1}\zeta. \tag{D.73}$$

The azimuthal velocity field in the passive-field region is given by (D.41), while in the force-free field region it is:

$$u_\phi = \frac{3}{2}\left(b_{rs}|\zeta| + \frac{D_B}{2}\zeta^2\right) - D_B\eta_H + u'_{\phi 0}, \tag{D.74}$$

$$\begin{aligned} u'_{\phi 0} = {} & \eta_O \partial_\zeta b_\phi(\zeta_B^-) - \eta_H \partial_\zeta b_r(\zeta_B^-) + u_\phi(\zeta_B^-) \\ & - \frac{3}{2}\left(b_{rs}|\zeta_B| + \frac{D_B \zeta_B^2}{2}\right) + D_B \eta_H. \end{aligned} \tag{D.75}$$

The gradients of the horizontal magnetic fields in the passive-field region are:

$$\partial_\zeta b_r^- = B_2 \kappa \cos(\kappa\zeta) + \frac{4}{3} u_{\phi 2}, \tag{D.76}$$

$$\partial_\zeta b_\phi^- = -B_2 \kappa \frac{\eta_O}{\eta_H} \cos(\kappa\zeta) + b_{\phi 1}. \tag{D.77}$$

The flux transport is then explicitly calculated as:

$$u_\Psi = \eta_H \frac{b_{\phi s}}{\zeta_B} + \eta_O \frac{b_{rs}}{\zeta_B}. \tag{D.78}$$

D.3 Ohmic diffusion only incorporating effects from the intermediate transition region

Here, we assume intermediate region to the thin, and concentrate only on the D_B, b_{rs} and $b_{\phi s}$ source terms (neglecting Keplerian and Hydrodynamic source terms).

The density profile around ζ_B is approximated by:

$$\tilde{\rho} \simeq \frac{1}{2\beta_0} \exp(-\zeta_B x), \tag{D.79}$$

where $x \equiv \zeta - \zeta_B$. The intermediate region where $\beta \sim 1$ has a typical thickness of $x \sim 1/\zeta_B$, and our assumption of a thin transition is valid if $\zeta_B^2 \gg 1$.

The differential system is then rewritten as:

$$-2\tilde{u}_\phi - 2\mathrm{e}^{\zeta_B x} \partial_\zeta b_r = -2\mathrm{e}^{\zeta_B x} D_B, \tag{D.80}$$

$$\frac{1}{2}\tilde{u}_r - 2\mathrm{e}^{\zeta_B x} \partial_\zeta b_\phi = 0, \tag{D.81}$$

$$\partial_\zeta \left[\tilde{\eta}_O \left(\partial_\zeta b_r - D_B\right) + u_r\right] = 0, \tag{D.82}$$

$$\partial_\zeta \left(\tilde{\eta}_O \partial_\zeta b_\phi + u_\phi\right) = \frac{3}{2} b_r. \tag{D.83}$$

We integrate between two heights ζ_1 and ζ_2 to get:

$$\left[\eta_O \partial_\zeta b_\phi + u_\phi\right]_{\zeta_1}^{\zeta_2} = \frac{3}{2} \int_{\zeta_1}^{\zeta_2} b_r \mathrm{d}\zeta. \tag{D.84}$$

As before, we use this relation between ζ_B^- and ζ_B^+ to connect the two regions, neglecting the width of the intermediate region, so the RHS of the equation vanishes. The force-free condition is also employed where $\partial_\zeta b_r(\zeta_B^+) = D_B$ and $\partial_\zeta b_\phi(\zeta_B^+) = 0$. Hence,

$$u_\phi(\zeta_B^+) - u_\phi(\zeta_B^-) = \eta_O \partial_\zeta b_\phi(\zeta_B^-) - \eta_H \partial_\zeta b_r(\zeta_B^-). \tag{D.85}$$

and

$$\begin{aligned} u_\Psi &= u_r + \eta_O(\partial_\zeta b_r - D_B) \\ &= -\eta_O D_B. \end{aligned} \tag{D.86}$$

Thus,

$$u_r = u_\Psi - \eta_O(\partial_x b_r - D_B), \tag{D.87}$$

$$u_\phi = \Delta u_\phi - \eta_O \partial_x b_\phi, \tag{D.88}$$

where $\Delta u_\phi = u_\phi(\zeta_B^+) - u_\phi(\zeta_B^-) = \eta_O \partial_\zeta b_\phi(\zeta_B^-)$.

We substitute these relations into (D.80) and (D.81):

$$\eta_O \partial_x b_\phi - \mathrm{e}^{\zeta_B x}(\partial_x b_r - D_B) = \Delta u_\phi, \tag{D.89}$$

$$\eta_O(\partial_x b_r - D_B) + 4\mathrm{e}^{\zeta_B x}\partial_x b_\phi = u_\Psi. \tag{D.90}$$

We can treat them as simultaneous equations in $\partial_x b_r - D_B$ and $\partial_x b_\phi$:

$$-\mathrm{e}^{\zeta_B x}(\partial_x b_r - D_B) + \eta_O \partial_x b_\phi = \Delta u_\phi, \tag{D.91}$$

$$\eta_O(\partial_x b_r - D_B) + 4\mathrm{e}^{\zeta_B x}\partial_x b_\phi = u_\Psi. \tag{D.92}$$

We find $\partial_x b_r$ via (D.92)$\times\eta_O$−(D.91)$\times 4\mathrm{e}^{\zeta_B x}$, which after rearranging gives:

$$\partial_x b_r = D_B + \frac{\eta_O u_\Psi - 4\mathrm{e}^{\zeta_B x}\Delta u_\phi}{\eta_O^2 + 4\mathrm{e}^{2\zeta_B x}}. \tag{D.93}$$

We find $\partial_x b_\phi$ via (D.91)$\times\eta_O$−(D.92)$\times\mathrm{e}^{\zeta_B x}$, which after rearranging gives:

$$\partial_x b_\phi = \frac{\eta_O \Delta u_\phi + \mathrm{e}^{\zeta_B x} u_\Psi}{\eta_O^2 + 4\mathrm{e}^{2\zeta_B x}}. \tag{D.94}$$

Integrating over x, we compute the jump in b_r across the intermediate region if $\mathrm{e}^{\zeta_B x} \gg 1$:

$$\begin{aligned} & b_r(x) - b_r(-x) \\ &\simeq 2D_B x \\ &\quad + \frac{1}{\zeta_B}\frac{u_\Psi}{\eta_O} \cdot \left\{ 2\zeta_B x - \frac{1}{2}\ln\left(\frac{4}{\eta_O^2}\mathrm{e}^{2\zeta_B x}\right) \right\} \\ &\quad - \frac{\pi}{\zeta_B}\frac{\Delta u_\phi}{\eta_O}. \end{aligned} \tag{D.95}$$

The jump condition is thus:

$$\Delta b_r = -\frac{\pi}{\eta_O}\frac{\Delta u_\phi}{\zeta_B} - \ln\left(\frac{2}{\eta_O}\right)\frac{u_\Psi}{\eta_O\zeta_B}. \tag{D.96}$$

Doing the same for b_ϕ, we have:

$$\begin{aligned} & b_\phi(x) - b_\phi(-x) \\ & \simeq \frac{1}{\zeta_B}\left\{\frac{\Delta u_\phi}{\eta_O}\right\}\cdot\left\{2\zeta_B x - \frac{1}{2}\ln\left(\frac{4}{\eta_O^2}\mathrm{e}^{2\zeta_B x}\right)\right\} \\ & \quad + \frac{\pi}{\zeta_B}\frac{u_\Psi}{4\eta_O}. \end{aligned} \tag{D.97}$$

The jump condition is thus:

$$\Delta b_\phi = \frac{4\pi}{\eta_O}\frac{u_\Psi}{\zeta_B} - \ln\left(\frac{2}{\eta_O}\right)\frac{\Delta u_\phi}{\eta_O\zeta_B}. \tag{D.98}$$

These new boundary conditions can be injected into the two zone model such that

$$b_r(\zeta_B^-) = b_r(\zeta_B^+) - \Delta b_r, \tag{D.99}$$

$$b_\phi(\zeta_B^-) = b_\phi(\zeta_B^+) - \Delta b_\phi. \tag{D.100}$$

Hence for b_r, we have

$$b_{r1}\zeta_B = \frac{\pi}{\eta_O}\frac{\Delta u_\phi}{\zeta_B} + \ln\left(\frac{2}{\eta_O}\right)\frac{u_\Psi}{\eta_O\zeta_B} + b_{rs} + D_B\zeta_B. \tag{D.101}$$

After some algebra, we obtain

$$\begin{aligned} b_{r1} = & \frac{1}{\zeta_B\left(1-\dfrac{\pi}{2\eta_O}\right) - \dfrac{1}{\zeta_B}\ln\left(\dfrac{2}{\eta_O}\right)} \\ & \times\left\{\frac{\pi b_{\phi s}}{\zeta_B^2} + b_{rs} + D_B\left[\zeta_B - \frac{1}{\zeta_B}\ln\left(\frac{2}{\eta_O}\right)\right]\right\}. \end{aligned} \tag{D.102}$$

For b_ϕ, we obtain

$$\begin{aligned} b_{\phi 1} = & \left[\zeta_B - \ln\left(\frac{2}{\eta_O}\right)\frac{1}{\zeta_B}\right]^{-1} \\ & \times\left[b_{\phi s} - \frac{\pi(b_{r1}-D_B)}{4\zeta_B} - \frac{1}{4\eta_O}b_{r1}\zeta_B^3\right. \\ & \left. \quad + \ln\left(\frac{2}{\eta_O}\right)\frac{\zeta_B}{\eta_O}\left[\frac{3}{4}b_{r1})\right]\right] \end{aligned} \tag{D.103}$$

Under these new conditions, the flux transport is:

$$u_\Psi = \eta_O\left[\partial_\zeta\left(b_{r1}\zeta\right) - D_B\right], \tag{D.104}$$

$$u_\Psi = \eta_O\left(b_{r1} - D_B\right). \tag{D.105}$$

D.4 Ideal MHD case

The equations become:

$$-2u_\phi - \frac{1}{\beta_0\tilde{\rho}}\partial_\zeta b_r = \frac{3}{2} + D_H - D_{\nu\Sigma} + \left(\frac{3}{2} - D_H\right)\zeta^2 - \frac{D_B}{\beta_0\tilde{\rho}}, \tag{D.106}$$

$$\frac{1}{2}u_r - \frac{1}{\beta_0\tilde{\rho}}\partial_\zeta b_\phi = 0, \tag{D.107}$$

$$\partial_\zeta u_r = 0, \tag{D.108}$$

$$-\partial_\zeta u_\phi + \frac{3}{2}b_r = 0. \tag{D.109}$$

u_r and b_ϕ form a closed system through (D.107) and (D.108). u_ϕ and b_r form a separate closed system through (D.106) and (D.109).

From (D.108), we have constant radial velocity:

$$u_r(\zeta) = \text{constant}. \tag{D.110}$$

The azimuthal momentum balance gives us an error function profile for b_ϕ:

$$b_\phi = \frac{\beta_0 u_r}{2}\int_0^\zeta \rho(\zeta)\mathrm{d}\zeta. \tag{D.111}$$

If $b_\phi \to b_{\phi s}$ as $\zeta \to \infty$, we have:

$$u_r = \frac{b_{\phi s}}{\beta_0}\frac{2}{\int_0^\infty \rho\mathrm{d}\zeta}. \tag{D.112}$$

For the Gaussian profile we are using, $\int_0^\infty \rho\mathrm{d}\zeta = 1/2$, so

$$u_r = 4\cdot\frac{b_{\phi s}}{\beta_0}. \tag{D.113}$$

We can see that a larger magnetic field strength (lower β_0) leads to a larger radial outflow, while a larger magnetic torque (larger $b_{\phi s}$) also brings about the same result. The flux transport is simply given by the radial velocity:

$$u_\Psi = u_r. \tag{D.114}$$

Appendix E

Linear expansion of the equations on a general background

E.1 Linearised equations for Ohmic only case

We study the behaviour of the MRI modes using a linear expansion of the perturbations on top of a general background assumed to vary on a longer timescale. In the local approximation the governing equations are

$$\rho(\partial_t v_x + v_z D v_x - 2\Omega v_y) = B_z D B_x, \tag{E.1}$$

$$\rho\left(\partial_t v_y + v_z D v_y + \frac{1}{2}\Omega v_x\right) = B_z D B_y, \tag{E.2}$$

$$\rho(\partial_t v_z + v_z D v_z) = -\rho\Omega^2 z - Dp - B_y D B_y - B_x D B_x, \tag{E.3}$$

$$\partial_t \rho + \rho D v_z + v_z D\rho = 0, \tag{E.4}$$

$$\partial_t B_x = B_z D v_x - v_z D B_x - B_x D v_z + (D\eta)(D B_x) + \eta D^2 B_x + f_x(\eta_H, \eta_A), \tag{E.5}$$

$$\partial_t B_y = -\frac{3}{2}\Omega B_x - v_z D B_y - B_y D v_z + B_z D v_y + (D\eta)(D B_y) + \eta D^2 B_y + g_y(\eta_H, \eta_A), \tag{E.6}$$

where I have used units such that $\mu_0 = 1$, $\mathbf{v}$ is the departure from steady Keplerian rotation, and $f_x(\eta_H, \eta_A)$ and $g_y(\eta_H, \eta_A)$ are the contributions from Hall and ambipolar terms to the x and y components of the induction equation respectively, which we set to zero for in this part of the analysis. In a 1D vertically stratified shearing box, only the "Ω effect" due to shear is present in the term $-\frac{3}{2}\Omega B_x \mathbf{e}_y$. Using the ansatz

$$\delta Q = \delta Q(z)\exp(-i\omega t) \tag{E.7}$$

for perturbations δQ, and using the notation $D \equiv \partial/\partial z$, the linearised equations are

$$\begin{aligned} &-\rho v_z D\delta v_x + B_z D\delta B_x \\ &\qquad = B_z (DB_x)\frac{\delta\rho}{\rho} - i\omega\rho\,\delta v_x - 2\rho\Omega\delta v_y + \rho(Dv_x)\delta v_z, \end{aligned} \tag{E.8}$$

$$\begin{aligned} &-\rho v_z D\delta v_y + B_z D\delta B_y \\ &\qquad = B_z (DB_y)\frac{\delta\rho}{\rho} + \frac{1}{2}\rho\Omega\delta v_x - i\omega\rho\,\delta v_y + \rho(Dv_y)\delta v_z, \end{aligned} \tag{E.9}$$

$$\begin{aligned} &D\delta p + \rho v_z D\delta v_z + B_x D\delta B_x + B_y D\delta B_y \\ &\qquad = (Dp + B_y DB_y + B_x DB_x)\frac{\delta\rho}{\rho} + \rho(i\omega - Dv_z)\delta v_z \\ &\qquad\quad - (DB_x)\delta B_x - (DB_y)\delta B_y, \end{aligned} \tag{E.10}$$

$$v_z D\delta\rho + \rho D\delta v_z = (i\omega - Dv_z)\delta\rho - (D\rho)\delta v_z, \tag{E.11}$$

$$\begin{aligned} &\eta D^2\delta B_x + B_z D\delta v_x - B_x D\delta v_z - (v_z - D\eta)D\delta B_x \\ &\qquad = (DB_x)\delta v_z - (i\omega - Dv_z)\delta B_x, \end{aligned} \tag{E.12}$$

$$\begin{aligned} &-\eta D^2\delta B_y - B_z D\delta v_y + B_y D\delta v_z + (v_z - D\eta)D\delta B_y \\ &\qquad = -(DB_y)\delta v_z - \frac{3}{2}\Omega\delta B_x + (i\omega - Dv_z)\delta B_y. \end{aligned} \tag{E.13}$$

We have six equations and six unknowns:

$$\delta\rho, \delta v_x, \delta v_y, \delta v_z, \delta B_x, \delta B_y, \tag{E.14}$$

and one eigenvalue,

$$\omega. \tag{E.15}$$

This is therefore a complete system of equations for obtaining a solution in combination with boundary conditions and an arbitrary normalisation condition.

E.2 Recasting into operator form for pseudospectral analysis

As described in Section 10.6.1, it is more useful to use $m_{x,y,z}$ than $\delta v_{x,y,z}$ to encourage convergence when using Whittaker functions. The corresponding changes are given by

$$\delta v_{x,y,z} \to \frac{1}{\rho}\delta m_{x,y,z}. \tag{E.16}$$

Recasting the equations in operator form (using isothermal equation of state with $c_s^2 = 1$):

$$-B_z(DB_x)\frac{\delta\rho}{\rho} + \left[v_z\left(\frac{D\rho}{\rho} - D\right) + i\omega\right]\delta m_x + 2\Omega\delta m_y - (Dv_x)\delta m_z + B_z D\delta B_x = 0, \tag{E.17}$$

$$-B_z(DB_y)\frac{\delta\rho}{\rho} - \frac{1}{2}\Omega\delta m_x + \left[v_z\left(\frac{D\rho}{\rho} - D\right) + i\omega\right]\delta m_y - (Dv_y)\delta m_z + B_z D\delta B_y = 0, \tag{E.18}$$

$$\left[D - \frac{1}{\rho}(D\rho + B_y DB_y + B_x DB_x)\right]\delta\rho + \left[v_z\left(D - \frac{D\rho}{\rho}\right) - i\omega + Dv_z\right]\delta m_z + (B_x D + DB_x)\delta B_x + (B_y D + DB_y)\delta B_y = 0, \tag{E.19}$$

$$(v_z D - i\omega + Dv_z)\delta\rho + D\delta m_z = 0, \tag{E.20}$$

$$\eta\rho D^2\delta B_x + B_z\left(D - \frac{D\rho}{\rho}\right)\delta m_x + \left[B_x\left(-D + \frac{D\rho}{\rho}\right) - DB_x\right]\delta m_z + \left[(-v_z + D\eta)\rho D + \rho(i\omega - Dv_z)\right]\delta B_x = 0, \tag{E.21}$$

$$-\eta\rho D^2\delta B_y + B_z\left(-D + \frac{D\rho}{\rho}\right)\delta m_y + \left[B_y\left(D - \frac{D\rho}{\rho}\right) + DB_y\right]\delta m_z + \frac{3}{2}\rho\Omega\delta B_x + \left[(v_z - D\eta)\rho D + (-i\omega + Dv_z)\rho\right]\delta B_y = 0. \tag{E.22}$$

E.3 Simplied regime: reduced equations and the shooting method

In the limit, $v_z, B_x, B_y, \delta v_z = 0$, we obtain:

$$B_z D\delta B_x = -i\omega\rho\,\delta v_x - 2\rho\Omega\delta v_y, \tag{E.23}$$

$$B_z D\delta B_y = \frac{1}{2}\rho\Omega\delta v_x - i\omega\rho\,\delta v_y, \tag{E.24}$$

$$0 = (Dp)\frac{\delta\rho}{\rho} - D\delta p, \tag{E.25}$$

$$0 = i\omega\delta\rho, \tag{E.26}$$

$$\eta D^2\delta B_x + B_z D\delta v_x + (D\eta)D\delta B_x = -i\omega\delta B_x, \tag{E.27}$$

$$-\eta D^2\delta B_y - B_z D\delta v_y - (D\eta)D\delta B_y = -\frac{3}{2}\Omega\delta B_x + i\omega\delta B_y. \tag{E.28}$$

Notice that if a mode exists, $\delta\rho = 0$, hence we only have four equations effectively.

Using an isothermal equation of state, and units such as $c_s^2 = 1$, this becomes

$$D\delta B_x = -i\omega\frac{\rho}{B_z}\delta v_x - 2\frac{\rho}{B_z}\Omega\delta v_y, \tag{E.29}$$

$$D\delta B_y = \frac{1}{2}\frac{\rho}{B_z}\Omega\delta v_x - i\omega\frac{\rho}{B_z}\delta v_y, \tag{E.30}$$

$$\eta D^2\delta B_x + B_z D\delta v_x + (D\eta)D\delta B_x = -i\omega\delta B_x, \tag{E.31}$$

$$\eta D^2\delta B_y + B_z D\delta v_y + (D\eta)D\delta B_y = \frac{3}{2}\Omega\delta B_x - i\omega\delta B_y. \tag{E.32}$$

We can further express δv_x and δv_y in terms of $D\delta B_x$ and $D\delta B_y$:

$$\delta v_x = \frac{1}{\Omega^2 - \omega^2}\left(\frac{B_z}{\rho}\right)\left(-i\omega D\delta B_x + 2\Omega D\delta B_y\right), \tag{E.33}$$

$$\delta v_y = -\frac{1}{\Omega^2 - \omega^2}\left(\frac{B_z}{\rho}\right)\left(\frac{\Omega}{2}D\delta B_x + i\omega D\delta B_y\right). \tag{E.34}$$

Substituting this into the second order equations, we get:

$$\begin{aligned}\eta D^2\delta B_x + \frac{v_{Az}^2}{\Omega^2 - \omega^2}\Bigg(& -i\omega D^2\delta B_x + 2\Omega D^2\delta B_y \\ & - \frac{D\rho}{\rho}\left[-i\omega D\delta B_x + 2\Omega D\delta B_y\right]\Bigg) \\ & + (D\eta)D\delta B_x = -i\omega\delta B_x,\end{aligned} \tag{E.35}$$

$$\begin{aligned}\eta D^2\delta B_y - \frac{v_{Az}^2}{\Omega^2 - \omega^2}\Bigg(& \frac{\Omega}{2}D^2\delta B_x + i\omega D^2\delta B_y \\ & - \frac{D\rho}{\rho}\left[\frac{\Omega}{2}D\delta B_x + i\omega D\delta B_y\right]\Bigg) \\ & + (D\eta)D\delta B_y = \frac{3}{2}\Omega\delta B_x - i\omega\delta B_y.\end{aligned} \tag{E.36}$$

Using the same definitions as Sano & Miyama, where

$$\sigma = (\Omega^2 - \omega^2)\frac{\eta}{v_{Az}^2} - i\omega, \tag{E.37}$$

$$\begin{aligned}\mathscr{S} = &\left[i\omega\frac{D\rho}{\rho} + \frac{(\Omega^2-\omega^2)}{v_{Az}^2}D\eta\right]D\delta B_x \\ &- 2\Omega\frac{D\rho}{\rho}D\delta B_y + i\omega\frac{(\Omega^2-\omega^2)}{v_{Az}^2}\delta B_x,\end{aligned} \tag{E.38}$$

$$\begin{aligned}\mathscr{T} = &\frac{\Omega}{2}\frac{D\rho}{\rho}D\delta B_x + \left[i\omega\frac{D\rho}{\rho} + \frac{(\Omega^2-\omega^2)}{v_{Az}^2}D\eta\right]D\delta B_y \\ &- \frac{(\Omega^2-\omega^2)}{v_{Az}^2}\left[\frac{3}{2}\Omega\delta B_x + i\omega\delta B_y\right],\end{aligned} \tag{E.39}$$

the equations are recast as

$$\sigma D^2\delta B_x + 2\Omega D^2\delta B_y = -\mathscr{S}, \tag{E.40}$$

$$-\frac{\Omega}{2}D^2\delta B_x + \sigma D^2\delta B_y = -\mathscr{T}. \tag{E.41}$$

This gives us finally

$$D^2\delta B_x = \frac{-\sigma\mathscr{S} + 2\Omega\tau}{\Omega^2+\sigma^2}, \tag{E.42}$$

$$D^2\delta B_y = \frac{-(\Omega/2)\mathscr{S} - \sigma\tau}{\Omega^2+\sigma^2}, \tag{E.43}$$

which reproduces the results of Sano and Miyama (1999), and can easily be solved for δB_x and δB_y using the shooting method via standard techniques.

E.4 Inclusion of Hall and ambipolar terms

We now consider the contributions from Hall and ambipolar terms to the linearised equations. To simplify some of the expressions, we use $\tilde{\eta}_H = \eta_H/|\mathbf{B}|$ and $\tilde{\eta}_A = \eta_A/|\mathbf{B}|^2$. The terms $f_x(\eta_H,\eta_A)$ and $g_y(\eta_H,\eta_A)$ are:

$$\begin{aligned}f_x(\eta_H,\eta_A) = \; &\tilde{\eta}_H(D^2B_y)B_z + (D\tilde{\eta}_H)DB_yB_z \\ &+ \tilde{\eta}_A\{(D^2B_x)B_z^2 + (D^2B_yB_y + [DB_y]^2 + D^2B_xB_x + 2[DB_x]^2)B_x \\ &\quad + (DB_yB_y)DB_x\} \\ &+ (D\tilde{\eta}_A)[DB_xB_z^2 + (DB_yB_y + DB_xB_x)B_x],\end{aligned} \tag{E.44}$$

$$\begin{aligned} g_y(\eta_H,\eta_A) = & -\tilde{\eta}_H D^2 B_x B_z - (D\tilde{\eta}_H) D B_x B_z \\ & + \tilde{\eta}_A [D^2 B_y B_z^2 + (D^2 B_y B_y + 2[DB_y]^2 + D^2 B_x B_x + [DB_x]^2) B_y \\ & \quad + (DB_x B_x) DB_y] \\ & + (D\tilde{\eta}_A)[DB_y B_z^2 + (DB_y B_y + DB_x B_x) B_y]. \end{aligned} \tag{E.45}$$

The inclusion of Hall and ambipolar effects only affects the x and y components of the induction equation, and so we include them in the linearised equations by inserting the relevant linearised components $f_{\rm lin}(\eta_H,\eta_A)$ and $g_{\rm lin}(\eta_H,\eta_A)$ into them respectively, giving us

$$\begin{aligned} & \eta D^2 \delta B_x + B_z D\delta v_x - B_x D\delta v_z - (v_z - D\eta) D\delta B_x + f_{\rm lin}(\eta_H,\eta_A) \\ & \qquad = (DB_x)\delta v_z - (i\omega - Dv_z)\delta B_x, \end{aligned} \tag{E.46}$$

$$\begin{aligned} & \eta D^2 \delta B_y + B_z D\delta v_y - B_y D\delta v_z - (v_z - D\eta) D\delta B_y + g_{\rm lin}(\eta_H,\eta_A) \\ & \qquad = (DB_y)\delta v_z + \frac{3}{2}\Omega \delta B_x - (i\omega - Dv_z)\delta B_y. \end{aligned} \tag{E.47}$$

where

$$\begin{aligned} f_{\rm lin}(\eta_H,\eta_A) = & \ \delta\tilde{\eta}_H (D^2 B_y) B_z + \tilde{\eta}_H (D^2 \delta B_y) B_z \\ & + (D\delta\tilde{\eta}_H) DB_y B_z + (D\tilde{\eta}_H) D\delta B_y B_z \\ & + \delta\tilde{\eta}_A [(D^2 B_x) B_z^2 + (D^2 B_y B_y + [DB_y]^2 + D^2 B_x B_x \\ & \qquad + 2[DB_x]^2) B_x + (DB_y B_y) DB_x] \\ & + \tilde{\eta}_A [(D^2 \delta B_x) B_z^2 \\ & \quad + (D^2 \delta B_y B_y + D^2 B_y \delta B_y + 2DB_y D\delta B_y \\ & \qquad + D^2 \delta B_x B_x + D^2 B_x \delta B_x + 4DB_x D\delta B_x) B_x \\ & \quad + (D^2 B_y B_y + [DB_y]^2 + D^2 B_x B_x + 2[DB_x]^2)\delta B_x \\ & \quad + D\delta B_y B_y DB_x + DB_y \delta B_y DB_x + DB_y B_y D\delta B_x] \\ & + (D\delta\tilde{\eta}_A)[DB_x B_z^2 + (DB_y B_y + DB_x B_x) B_x] \\ & + (D\tilde{\eta}_A)[D\delta B_x B_z^2 \\ & \qquad + (D\delta B_y B_y + DB_y \delta B_y + D\delta B_x B_x + DB_x \delta B_x) B_x \\ & \qquad + (DB_y B_y + DB_x B_x)\delta B_x]. \end{aligned} \tag{E.48}$$

$$
\begin{aligned}
g_{\text{lin}}(\eta_H,\eta_A) = \; & -\delta\tilde{\eta}_H D^2 B_x B_z - \tilde{\eta}_H D^2 \delta B_x B_z \\
& - (D\delta\tilde{\eta}_H) D B_x B_z - (D\tilde{\eta}_H) D\delta B_x B_z \\
& + \delta\tilde{\eta}_A [D^2 B_y B_z^2 + (D^2 B_y B_y + 2[DB_y]^2 \\
& \qquad + D^2 B_x B_x + [DB_x]^2) B_y + (DB_x B_x) DB_y] \\
& + \tilde{\eta}_A [D^2 \delta B_y B_z^2 \\
& \qquad + (D^2 \delta B_y B_y + D^2 B_y \delta B_y + 4DB_y D\delta B_y \\
& \qquad\qquad + D^2 \delta B_x B_x + D^2 B_x \delta B_x + 2DB_x D\delta B_x) B_y \\
& \qquad + (D^2 B_y B_y + 2[DB_y]^2 + D^2 B_x B_x + [DB_x]^2)\delta B_y \\
& \qquad + D\delta B_x B_x DB_y + DB_x \delta B_x DB_y + DB_x B_x D\delta B_y] \\
& + (D\delta\tilde{\eta}_A)[DB_y B_z^2 + (DB_y B_y + DB_x B_x) B_y] \\
& + (D\tilde{\eta}_A)[D\delta B_y B_z^2 \\
& \qquad + (D\delta B_y B_y + DB_y \delta B_y + D\delta B_x B_x + DB_x \delta B_x) B_y \\
& \qquad + (DB_y B_y + DB_x B_x)\delta B_y].
\end{aligned}
\tag{E.49}
$$

Note that $\delta Q\cdots$ is implicitly included in $\delta\tilde{\eta}_{H,A}$ while $DQ\cdots$ is incorporated in $D\tilde{\eta}_{H,A}$.

E.4.1 Vertical magnetic field only background

In the case where the background magnetic field is purely vertical and uniform, $B_x, B_y = 0$. Hence we can simplify the additional linear terms to:

$$
f_{\text{lin}} = \left[\tilde{\eta}_A B_z^2 D^2 + (D\tilde{\eta}_A) B_z^2 D\right] \delta B_x + \left[\tilde{\eta}_H B_z D^2 + (D\tilde{\eta}_H) B_z D\right] \delta B_y. \tag{E.50}
$$

$$
g_{\text{lin}} = \left[-\tilde{\eta}_H B_z D^2 - (D\tilde{\eta}_H) B_z D\right] \delta B_x + \left[\tilde{\eta}_A B_z^2 D^2 + (D\tilde{\eta}_A) B_z^2 D\right] \delta B_y. \tag{E.51}
$$

We can also revert back to normal diffusivities, as $\tilde{\eta}_H = \eta_H / B_z$ and $\tilde{\eta}_A = \eta_A / B_z^2$, giving us:

$$
f_{\text{lin}} = \left[\eta_A D^2 + (D\eta_A) D\right] \delta B_x + \left[\eta_H D^2 + (D\eta_H) D\right] \delta B_y. \tag{E.52}
$$

$$
g_{\text{lin}} = \left[-\eta_H D^2 - (D\eta_H) D\right] \delta B_x + \left[\eta_A D^2 + (D\eta_A) D\right] \delta B_y. \tag{E.53}
$$

In this limit, it is worth noting that ambipolar diffusivity has the same effect on the system as Ohmic resistivity.

Appendix F

Calculating the average exponential growth

The linear MRI analysis yielded a varying growth rate, the average effect of which may be able to explain the slow exponential increase we observe in the mid-plane b_x and b_y values. We need a suitable average to see its effective exponential growth over one cycle.

In the constant exponential growth rate model:

$$f(t) = A\exp(\gamma t), \tag{F.1}$$

such that

$$\frac{1}{f}\frac{\mathrm{d}f}{\mathrm{d}t} = \gamma. \tag{F.2}$$

But now, suppose that $B(t)$ is a varying function with time, then

$$\frac{1}{f}\frac{\mathrm{d}f}{\mathrm{d}t} = \gamma(t). \tag{F.3}$$

We integrate the equation

$$\int_{f(t_1)}^{f(t_2)} \frac{\mathrm{d}f'}{f'} = \int_{t_1}^{t_2} \gamma(t)\ \mathrm{d}t, \tag{F.4}$$

and obtain

$$\ln\left(\frac{f(t_2)}{f(t_1)}\right) = \int_{t_1}^{t_2} \gamma(t)\ \mathrm{d}t. \tag{F.5}$$

Hence

$$f(t_2) = f(t_1)\exp\left[\int_{t_1}^{t_2} \gamma(t)\ \mathrm{d}t\right] = f(t_1)\exp\left[\gamma_{\mathrm{eff}}(t_2 - t_1)\right], \tag{F.6}$$

and the effective growth rate over the time period is

$$\gamma_{\mathrm{eff}} = \frac{\int_{t_1}^{t_2} \gamma(t)\ \mathrm{d}t}{t_2 - t_1}. \tag{F.7}$$

The numerator of γ_{eff} can be found through numerical integration.

References

ALMA Partnership, Brogan, C. L., Pérez, L. M., Hunter, T. R., Dent, W. R. F., Hales, A. S., Hills, R. E., Corder, S., Fomalont, E. B., Vlahakis, C., Asaki, Y., Barkats, D., Hirota, A., Hodge, J. A., Impellizzeri, C. M. V., Kneissl, R., Liuzzo, E., Lucas, R., Marcelino, N., Matsushita, S., Nakanishi, K., Phillips, N., Richards, A. M. S., Toledo, I., Aladro, R., Broguiere, D., Cortes, J. R., Cortes, P. C., Espada, D., Galarza, F., Garcia-Appadoo, D., Guzman-Ramirez, L., Humphreys, E. M., Jung, T., Kameno, S., Laing, R. A., Leon, S., Marconi, G., Mignano, A., Nikolic, B., Nyman, L. A., Radiszcz, M., Remijan, A., Rodón, J. A., Sawada, T., Takahashi, S., Tilanus, R. P. J., Vila Vilaro, B., Watson, L. C., Wiklind, T., Akiyama, E., Chapillon, E., de Gregorio-Monsalvo, I., Di Francesco, J., Gueth, F., Kawamura, A., Lee, C. F., Nguyen Luong, Q., Mangum, J., Pietu, V., Sanhueza, P., Saigo, K., Takakuwa, S., Ubach, C., van Kempen, T., Wootten, A., Castro-Carrizo, A., Francke, H., Gallardo, J., Garcia, J., Gonzalez, S., Hill, T., Kaminski, T., Kurono, Y., Liu, H. Y., Lopez, C., Morales, F., Plarre, K., Schieven, G., Testi, L., Videla, L., Villard, E., Andreani, P., Hibbard, J. E., and Tatematsu, K. (2015). The 2014 ALMA Long Baseline Campaign: First Results from High Angular Resolution Observations toward the HL Tau Region. *ApJ*, 808(1):L3.

Andrews, S. M. (2020). Observations of Protoplanetary Disk Structures. *ARA&A*, 58:483–528.

Andrews, S. M., Rosenfeld, K. A., Kraus, A. L., and Wilner, D. J. (2013). The Mass Dependence between Protoplanetary Disks and their Stellar Hosts. *ApJ*, 771(2):129.

Andrews, S. M. and Williams, J. P. (2007). High-Resolution Submillimeter Constraints on Circumstellar Disk Structure. *ApJ*, 659(1):705–728.

Andrews, S. M., Wilner, D. J., Hughes, A. M., Qi, C., and Dullemond, C. P. (2009). Protoplanetary Disk Structures in Ophiuchus. *ApJ*, 700(2):1502–1523.

Aresu, G., Kamp, I., Meijerink, R., Woitke, P., Thi, W. F., and Spaans, M. (2011). X-ray impact on the protoplanetary disks around T Tauri stars. *A&A*, 526:A163.

Armitage, P. J. (2015). Physical processes in protoplanetary disks. *arXiv e-prints*, page arXiv:1509.06382.

Bai, X.-N. (2011). Magnetorotational-instability-driven Accretion in Protoplanetary Disks. *ApJ*, 739:50.

Bai, X.-N. (2013). Wind-driven Accretion in Protoplanetary Disks. II. Radial Dependence and Global Picture. *ApJ*, 772(2):96.

Bai, X.-N. (2014). Hall-effect-Controlled Gas Dynamics in Protoplanetary Disks. I. Wind Solutions at the Inner Disk. *ApJ*, 791:137.

Bai, X.-N. (2015). Hall Effect Controlled Gas Dynamics in Protoplanetary Disks. II. Full 3D Simulations toward the Outer Disk. *ApJ*, 798(2):84.

Bai, X.-N. (2016). Towards a Global Evolutionary Model of Protoplanetary Disks. *ApJ*, 821:80.

Bai, X.-N. (2017). Global Simulations of the Inner Regions of Protoplanetary Disks with Comprehensive Disk Microphysics. *ApJ*, 845:75.

Bai, X.-N. and Goodman, J. (2009). Heat and Dust in Active Layers of Protostellar Disks. *ApJ*, 701(1):737–755.

Bai, X.-N. and Stone, J. M. (2013a). Local Study of Accretion Disks with a Strong Vertical Magnetic Field: Magnetorotational Instability and Disk Outflow. *ApJ*, 767:30.

Bai, X.-N. and Stone, J. M. (2013b). Wind-driven Accretion in Protoplanetary Disks. I. Suppression of the Magnetorotational Instability and Launching of the Magnetocentrifugal Wind. *ApJ*, 769(1):76.

Bai, X.-N. and Stone, J. M. (2014). Magnetic Flux Concentration and Zonal Flows in Magnetorotational Instability Turbulence. *ApJ*, 796:31.

Bai, X.-N. and Stone, J. M. (2017). Hall Effect-Mediated Magnetic Flux Transport in Protoplanetary Disks. *ApJ*, 836:46.

Bai, X.-N., Ye, J., Goodman, J., and Yuan, F. (2016). Magneto-thermal Disk Winds from Protoplanetary Disks. *ApJ*, 818(2):152.

Balbus, S. A. (2011). *Magnetohydrodynamics of Protostellar Disks*, pages 237–282.

Balbus, S. A. and Hawley, J. F. (1991). A powerful local shear instability in weakly magnetized disks. I - Linear analysis. II - Nonlinear evolution. *ApJ*, 376:214–233.

Balbus, S. A. and Hawley, J. F. (1998). Instability, turbulence, and enhanced transport in accretion disks. *Reviews of Modern Physics*, 70:1–53.

Balbus, S. A. and Hawley, J. F. (2003). *Numerical Simulations of MHD Turbulence in Accretion Disks*, volume 614, pages 329–348.

Balbus, S. A. and Terquem, C. (2001). Linear Analysis of the Hall Effect in Protostellar Disks. *ApJ*, 552:235–247.

Bary, J. S., Leisenring, J. M., and Skrutskie, M. F. (2009). Variations of the 10 μm Silicate Features in the Actively Accreting T Tauri Stars: DG Tau and XZ Tau. *ApJ*, 706(1):L168–L172.

Beckwith, S. V. W., Sargent, A. I., Chini, R. S., and Guesten, R. (1990). A Survey for Circumstellar Disks around Young Stellar Objects. *AJ*, 99:924.

Benisty, M., Juhasz, A., Boccaletti, A., Avenhaus, H., Milli, J., Thalmann, C., Dominik, C., Pinilla, P., Buenzli, E., Pohl, A., Beuzit, J. L., Birnstiel, T., de Boer, J., Bonnefoy, M., Chauvin, G., Christiaens, V., Garufi, A., Grady, C., Henning, T., Huelamo, N., Isella, A., Langlois, M., Ménard, F., Mouillet, D., Olofsson, J., Pantin, E., Pinte, C., and Pueyo, L. (2015). Asymmetric features in the protoplanetary disk MWC 758. *A&A*, 578:L6.

Bergin, E. A. and Williams, J. P. (2017). *The Determination of Protoplanetary Disk Masses*, volume 445, page 1.

Bertrang, G. H. M., Flock, M., and Wolf, S. (2017). Magnetic fields in protoplanetary discs: from MHD simulations to ALMA observations. *MNRAS*, 464(1):L61–L64.

Béthune, W. and Latter, H. (2020). Electric heating and angular momentum transport in laminar models of protoplanetary disks. *arXiv e-prints*, page arXiv:2003.13263.

Béthune, W., Lesur, G., and Ferreira, J. (2016). Self-organisation in protoplanetary discs. Global, non-stratified Hall-MHD simulations. *A&A*, 589:A87.

Béthune, W., Lesur, G., and Ferreira, J. (2017). Global simulations of protoplanetary disks with net magnetic flux. I. Non-ideal MHD case. *A&A*, 600:A75.

Biersteker, J. B., Weiss, B. P., Heinisch, P., Herčik, D., Glassmeier, K.-H., and Auster, H.-U. (2019). Implications of Philae Magnetometry Measurements at Comet 67P/Churyumov-Gerasimenko for the Nebular Field of the Outer Solar System. *ApJ*, 875(1):39.

Bjerkeli, P., van der Wiel, M. H. D., Harsono, D., Ramsey, J. P., and Jørgensen, J. K. (2016). Resolved images of a protostellar outflow driven by an extended disk wind. *Nature*, 540(7633):406–409.

Blandford, R. D. and Payne, D. G. (1982). Hydromagnetic flows from accretion discs and the production of radio jets. *MNRAS*, 199:883–903.

Blundell, S. and Blundell, K. (2009). *Concepts in Thermal Physics*. Oxford University Press.

Boyd, J. (2001). *Chebyshev and Fourier Spectral Methods Second Edition (Revised)*. Dover.

Brandenburg, A., Nordlund, A., Stein, R. F., and Torkelsson, U. (1995). Dynamo-generated Turbulence and Large-Scale Magnetic Fields in a Keplerian Shear Flow. *ApJ*, 446:741.

Brandenburg, A. and Zweibel, E. G. (1994). The Formation of Sharp Structures by Ambipolar Diffusion. *ApJ*, 427:L91.

Chiang, E. and Laughlin, G. (2013). The minimum-mass extrasolar nebula: in situ formation of close-in super-Earths. *MNRAS*, 431(4):3444–3455.

Cho, J. and Lazarian, A. (2007). Grain Alignment and Polarized Emission from Magnetized T Tauri Disks. *ApJ*, 669(2):1085–1097.

Christiaens, V., Casassus, S., Perez, S., van der Plas, G., and Ménard, F. (2014). Spiral Arms in the Disk of HD 142527 from CO Emission Lines with ALMA. *ApJ*, 785(1):L12.

Clarke, C. and Carswell, B. (2014). *Principles of Astrophysical Fluid Dynamics*.

Cleeves, L. I., Adams, F. C., Bergin, E. A., and Visser, R. (2013). Radionuclide Ionization in Protoplanetary Disks: Calculations of Decay Product Radiative Transfer. *ApJ*, 777(1):28.

Cleeves, L. I., Bergin, E. A., Qi, C., Adams, F. C., and Öberg, K. I. (2015). Constraining the X-Ray and Cosmic-Ray Ionization Chemistry of the TW Hya Protoplanetary Disk: Evidence for a Sub-interstellar Cosmic-Ray Rate. *ApJ*, 799(2):204.

Crida, A. (2009). Minimum Mass Solar Nebulae and Planetary Migration. *ApJ*, 698(1):606–614.

Crutcher, R. M. (2012). Magnetic Fields in Molecular Clouds. *ARA&A*, 50:29–63.

Currie, T. and Sicilia-Aguilar, A. (2011). The Transitional Protoplanetary Disk Frequency as a Function of Age: Disk Evolution In the Coronet Cluster, Taurus, and Other 1-8 Myr Old Regions. *ApJ*, 732(1):24.

D'Alessio, P., Calvet, N., and Hartmann, L. (1997). The Structure and Emission of Accretion Disks Irradiated by Infalling Envelopes. *ApJ*, 474(1):397–406.

D'Alessio, P., Cantö, J., Calvet, N., and Lizano, S. (1998). Accretion Disks around Young Objects. I. The Detailed Vertical Structure. *ApJ*, 500(1):411–427.

Desch, S. J. (2004). Linear Analysis of the Magnetorotational Instability, Including Ambipolar Diffusion, with Application to Protoplanetary Disks. *ApJ*, 608:509–525.

Desch, S. J. (2007). Mass Distribution and Planet Formation in the Solar Nebula. *ApJ*, 671(1):878–893.

Donati, J. F., Hébrard, E., Hussain, G. A. J., Moutou, C., Malo, L., Grankin, K., Vidotto, A. A., Alencar, S. H. P., Gregory, S. G., Jardine, M. M., Herczeg, G., Morin, J., Fares, R., Ménard, F., Bouvier, J., Delfosse, X., Doyon, R., Takami, M., Figueira, P., Petit, P., Boisse, I., and MaTYSSE Collaboration (2015). Magnetic activity and hot Jupiters of young Suns: the weak-line T Tauri stars V819 Tau and V830 Tau. *MNRAS*, 453(4):3706–3719.

Dong, R., Liu, S.-y., Eisner, J., Andrews, S., Fung, J., Zhu, Z., Chiang, E., Hashimoto, J., Liu, H. B., Casassus, S., Esposito, T., Hasegawa, Y., Muto, T., Pavlyuchenkov, Y., Wilner, D., Akiyama, E., Tamura, M., and Wisniewski, J. (2018). The Eccentric Cavity, Triple Rings, Two-armed Spirals, and Double Clumps of the MWC 758 Disk. *ApJ*, 860(2):124.

Draine, B. T. (2011). *Physics of the Interstellar and Intergalactic Medium*.

Draine, B. T., Roberge, W. G., and Dalgarno, A. (1983). Magnetohydrodynamic shock waves in molecular clouds. *ApJ*, 264:485–507.

Dullemond, C. P. (2000). Are passive protostellar disks stable to self-shadowing? *A&A*, 361:L17–L20.

Dullemond, C. P. and Dominik, C. (2004). The effect of dust settling on the appearance of protoplanetary disks. *A&A*, 421:1075–1086.

Ercolano, B. and Pascucci, I. (2017). The dispersal of planet-forming discs: theory confronts observations. *Royal Society Open Science*, 4(4):170114.

Evans, C. R. and Hawley, J. F. (1988). Simulation of Magnetohydrodynamic Flows: A Constrained Transport Model. *ApJ*, 332:659.

Fedele, D., van den Ancker, M. E., Henning, T., Jayawardhana, R., and Oliveira, J. M. (2010). Timescale of mass accretion in pre-main-sequence stars. *A&A*, 510:A72.

Ferraro, V. C. A. (1937). The non-uniform rotation of the Sun and its magnetic field. *MNRAS*, 97:458.

Flaherty, K. M., Hughes, A. M., Rose, S. C., Simon, J. B., Qi, C., Andrews, S. M., Kóspál, Á., Wilner, D. J., Chiang, E., Armitage, P. J., and Bai, X.-n. (2017). A Three-dimensional View of Turbulence: Constraints on Turbulent Motions in the HD 163296 Protoplanetary Disk Using DCO^+. *ApJ*, 843(2):150.

Flaherty, K. M., Hughes, A. M., Rosenfeld, K. A., Andrews, S. M., Chiang, E., Simon, J. B., Kerzner, S., and Wilner, D. J. (2015). Weak Turbulence in the HD 163296 Protoplanetary Disk Revealed by ALMA CO Observations. *ApJ*, 813(2):99.

Frank, A., Ray, T. P., Cabrit, S., Hartigan, P., Arce, H. G., Bacciotti, F., Bally, J., Benisty, M., Eislöffel, J., Güdel, M., Lebedev, S., Nisini, B., and Raga, A. (2014). Jets and Outflows from Star to Cloud: Observations Confront Theory. In Beuther, H., Klessen, R. S., Dullemond, C. P., and Henning, T., editors, *Protostars and Planets VI*, page 451.

Fromang, S. (2013). MRI-driven angular momentum transport in protoplanetary disks. In Hennebelle, P. and Charbonnel, C., editors, *EAS Publications Series*, volume 62 of *EAS Publications Series*, pages 95–142.

Fromang, S., Latter, H., Lesur, G., and Ogilvie, G. I. (2013). Local outflows from turbulent accretion disks. *A&A*, 552:A71.

Fromang, S. and Stone, J. M. (2009). Turbulent resistivity driven by the magnetorotational instability. *A&A*, 507:19–28.

Fromang, S., Terquem, C., and Balbus, S. A. (2002). The ionization fraction in α models of protoplanetary discs. *MNRAS*, 329(1):18–28.

Fu, R. R., Lima, E. A., and Weiss, B. P. (2014). No nebular magnetization in the Allende CV carbonaceous chondrite. *Earth and Planetary Science Letters*, 404:54–66.

Gammie, C. F. (1996). Layered Accretion in T Tauri Disks. *ApJ*, 457:355.

Gammie, C. F. and Balbus, S. A. (1994a). Quasi-Global Linear Analysis of a Magnetized Disc. *MNRAS*, 270:138.

Gammie, C. F. and Balbus, S. A. (1994b). Quasi-Global Linear Analysis of a Magnetized Disc. *MNRAS*, 270:138.

Ginski, C., Stolker, T., Pinilla, P., Dominik, C., Boccaletti, A., de Boer, J., Benisty, M., Biller, B., Feldt, M., Garufi, A., Keller, C. U., Kenworthy, M., Maire, A. L., Ménard, F., Mesa, D., Milli, J., Min, M., Pinte, C., Quanz, S. P., van Boekel, R., Bonnefoy, M., Chauvin, G., Desidera, S., Gratton, R., Girard, J. H. V., Keppler, M., Kopytova, T., Lagrange, A. M., Langlois, M., Rouan, D., and Vigan, A. (2016). Direct detection of scattered light gaps in the transitional disk around HD 97048 with VLT/SPHERE. *A&A*, 595:A112.

Goldreich, P. and Lynden-Bell, D. (1965). II. Spiral arms as sheared gravitational instabilities. *MNRAS*, 130:125.

Goodman, J. and Xu, G. (1994). Parasitic instabilities in magnetized, differentially rotating disks. *ApJ*, 432:213–223.

Gräfe, C., Wolf, S., Guilloteau, S., Dutrey, A., Stapelfeldt, K. R., Pontoppidan, K. M., and Sauter, J. (2013). Vertical settling and radial segregation of large dust grains in the circumstellar disk of the Butterfly Star. *A&A*, 553:A69.

Gressel, O., Ramsey, J. P., Brinch, C., Nelson, R. P., Turner, N. J., and Bruderer, S. (2020). Global Hydromagnetic Simulations of Protoplanetary Disks with Stellar Irradiation and Simplified Thermochemistry. *arXiv e-prints*, page arXiv:2005.03431.

Gressel, O., Turner, N. J., Nelson, R. P., and McNally, C. P. (2015). Global Simulations of Protoplanetary Disks With Ohmic Resistivity and Ambipolar Diffusion. *ApJ*, 801(2):84.

Guan, X. and Gammie, C. F. (2009). The Turbulent Magnetic Prandtl Number of MHD Turbulence in Disks. *ApJ*, 697:1901–1906.

Guilet, J. and Ogilvie, G. I. (2012). Transport of magnetic flux and the vertical structure of accretion discs - I. Uniform diffusion coefficients. *MNRAS*, 424:2097–2117.

Guilet, J. and Ogilvie, G. I. (2013). Transport of magnetic flux and the vertical structure of accretion discs - II. Vertical profile of the diffusion coefficients. *MNRAS*, 430:822–835.

Guilet, J. and Ogilvie, G. I. (2014). Global evolution of the magnetic field in a thin disc and its consequences for protoplanetary systems. *MNRAS*, 441:852–868.

Hawley, J. F., Gammie, C. F., and Balbus, S. A. (1995). Local Three-dimensional Magnetohydrodynamic Simulations of Accretion Disks. *ApJ*, 440:742.

Hawley, J. F., Gammie, C. F., and Balbus, S. A. (1996). Local Three-dimensional Simulations of an Accretion Disk Hydromagnetic Dynamo. *ApJ*, 464:690.

Haworth, T. J., Clarke, C. J., and Owen, J. E. (2016). Rapid radiative clearing of protoplanetary discs. *MNRAS*, 457(2):1905–1915.

Hayashi, C. (1981). Structure of the Solar Nebula, Growth and Decay of Magnetic Fields and Effects of Magnetic and Turbulent Viscosities on the Nebula. *Progress of Theoretical Physics Supplement*, 70:35–53.

Henriksen, R. N. and Rayburn, D. R. (1971). Relativistic stellar wind theory: ' Near'zone solutions. *MNRAS*, 152:323.

Hernández, J., Calvet, N., Briceño, C., Hartmann, L., Vivas, A. K., Muzerolle, J., Downes, J., Allen, L., and Gutermuth, R. (2007). Spitzer Observations of the Orion OB1 Association: Disk Census in the Low-Mass Stars. *ApJ*, 671(2):1784–1799.

Heyvaerts, J., Priest, E. R., and Bardou, A. (1996). Magnetic Field Diffusion in Self-consistently Turbulent Accretion Disks. *ApJ*, 473:403.

Hu, Z. and Bai, X.-N. (2021). Dust Transport in Protoplanetary Disks with Wind-driven Accretion. *MNRAS*.

Huang, J., Andrews, S. M., Pérez, L. M., Zhu, Z., Dullemond, C. P., Isella, A., Benisty, M., Bai, X.-N., Birnstiel, T., Carpenter, J. M., Guzmán, V. V., Hughes, A. M., Öberg, K. I., Ricci, L., Wilner, D. J., and Zhang, S. (2018). The Disk Substructures at High Angular Resolution Project (DSHARP). III. Spiral Structures in the Millimeter Continuum of the Elias 27, IM Lup, and WaOph 6 Disks. *ApJ*, 869(2):L43.

Igea, J. and Glassgold, A. E. (1999). X-Ray Ionization of the Disks of Young Stellar Objects. *ApJ*, 518:848–858.

Ilgner, M. and Nelson, R. P. (2006). On the ionisation fraction in protoplanetary disks. I. Comparing different reaction networks. *A&A*, 445(1):205–222.

Ji, H., Burin, M., Schartman, E., and Goodman, J. (2006). Hydrodynamic turbulence cannot transport angular momentum effectively in astrophysical disks. *Nature*, 444(7117):343–346.

Johansen, A., Blum, J., Tanaka, H., Ormel, C., Bizzarro, M., and Rickman, H. (2014). The Multifaceted Planetesimal Formation Process. In Beuther, H., Klessen, R. S., Dullemond, C. P., and Henning, T., editors, *Protostars and Planets VI*, page 547.

Kant, I. (1755). *Universal Natural History and Theory of the Heavens*.

Kataoka, A., Muto, T., Momose, M., Tsukagoshi, T., Fukagawa, M., Shibai, H., Hanawa, T., Murakawa, K., and Dullemond, C. P. (2015). Millimeter-wave Polarization of Protoplanetary Disks due to Dust Scattering. *ApJ*, 809(1):78.

Kataoka, A., Okuzumi, S., and Tazaki, R. (2019). Millimeter-wave Polarization Due to Grain Alignment by the Gas Flow in Protoplanetary Disks. *ApJ*, 874(1):L6.

Kley, W. and Nelson, R. P. (2012). Planet-Disk Interaction and Orbital Evolution. *ARA&A*, 50:211–249.

Königl, A., Salmeron, R., and Wardle, M. (2010). Wind-driving protostellar accretion discs - I. Formulation and parameter constraints. *MNRAS*, 401:479–499.

Kuijken, K. and Gilmore, G. (1989). The mass distribution in the galactic disc -II. Determination of the surface mass density of the galactic disc near the Sun. *MNRAS*, 239:605–649.

Kunz, M. W. (2008). On the linear stability of weakly ionized, magnetized planar shear flows. *MNRAS*, 385:1494–1510.

Kunz, M. W. and Balbus, S. A. (2004). Ambipolar diffusion in the magnetorotational instability. *MNRAS*, 348:355–360.

Kunz, M. W. and Lesur, G. (2013). Magnetic self-organization in Hall-dominated magnetorotational turbulence. *MNRAS*, 434:2295–2312.

Lada, C. J. (1987). Star formation: from OB associations to protostars. In Peimbert, M. and Jugaku, J., editors, *Star Forming Regions*, volume 115, page 1.

Latter, H. N., Fromang, S., and Gressel, O. (2010). MRI channel flows in vertically stratified models of accretion discs. *MNRAS*, 406:848–862.

Latter, H. N., Lesaffre, P., and Balbus, S. A. (2009). MRI channel flows and their parasites. *MNRAS*, 394:715–729.

Lesur, G. (2020). Magnetohydrodynamics of protoplanetary discs. *arXiv e-prints*, page arXiv:2007.15967.

Lesur, G., Ferreira, J., and Ogilvie, G. I. (2013). The magnetorotational instability as a jet launching mechanism. *A&A*, 550:A61.

Lesur, G., Kunz, M. W., and Fromang, S. (2014). Thanatology in protoplanetary discs. The combined influence of Ohmic, Hall, and ambipolar diffusion on dead zones. *A&A*, 566:A56.

Lesur, G. and Longaretti, P.-Y. (2009). Turbulent resistivity evaluation in magnetorotational instability generated turbulence. *A&A*, 504:309–320.

Lesur, G. and Ogilvie, G. I. (2010). On the angular momentum transport due to vertical convection in accretion discs. *MNRAS*, 404(1):L64–L68.

Leung, P. K. C. and Ogilvie, G. I. (2019). Local semi-analytic models of magnetic flux transport in protoplanetary discs. *MNRAS*, 487(4):5155–5174.

Leung, P. K. C. and Ogilvie, G. I. (2020). Wind-MRI interactions in local models of protoplanetary discs - I. Ohmic resistivity. *MNRAS*, 498(1):750–770.

Lovelace, R. V. E., Rothstein, D. M., and Bisnovatyi-Kogan, G. S. (2009). Advection/Diffusion of Large-Scale B Field in Accretion Disks. *ApJ*, 701:885–890.

Lubow, S. H., Papaloizou, J. C. B., and Pringle, J. E. (1994). Magnetic field dragging in accretion discs. *MNRAS*, 267:235–240.

Lubow, S. H. and Spruit, H. C. (1995). Magnetic interchange instability in accretion disks. *ApJ*, 445:337–347.

Luhman, K. L., Allen, P. R., Espaillat, C., Hartmann, L., and Calvet, N. (2010). The Disk Population of the Taurus Star-Forming Region. *ApJS*, 186(1):111–174.

Lynden-Bell, D. (1996). Magnetic collimation by accretion discs of quasars and stars. *MNRAS*, 279(2):389–401.

Lynden-Bell, D. (2003). On why discs generate magnetic towers and collimate jets. *MNRAS*, 341(4):1360–1372.

Manara, C. F., Fedele, D., Herczeg, G. J., and Teixeira, P. S. (2016). X-Shooter study of accretion in Chamaeleon I. *A&A*, 585:A136.

Manara, C. F., Testi, L., Natta, A., Rosotti, G., Benisty, M., Ercolano, B., and Ricci, L. (2014). Gas content of transitional disks: a VLT/X-Shooter study of accretion and winds. *A&A*, 568:A18.

Matsuzaki, T., Matsumoto, R., Tajima, T., and Shibata, K. (1997). *Three Dimensional MHD Simulations of Parker Instability in Differentially Rotating Disk*, volume 121 of *Astronomical Society of the Pacific Conference Series*, page 766.

Maxwell, J. C. (1866). *Proc. R. Soc.*, 15, 14.

McNally, C. P. and Pessah, M. E. (2015). On Vertically Global, Horizontally Local Models for Astrophysical Disks. *ApJ*, 811(2):121.

Mignone, A., Bodo, G., Massaglia, S., Matsakos, T., Tesileanu, O., Zanni, C., and Ferrari, A. (2007). PLUTO: A Numerical Code for Computational Astrophysics. *ApJS*, 170(1):228–242.

Morse, T. E. (1963). Energy and Momentum Exchange between Nonequipartition Gases. *The Physics of Fluids*.

Muzerolle, J., Flaherty, K., Balog, Z., Furlan, E., Smith, P. S., Allen, L., Calvet, N., D'Alessio, P., Megeath, S. T., Muench, A., Rieke, G. H., and Sherry, W. H. (2009). Evidence for Dynamical Changes in a Transitional Protoplanetary Disk with Mid-Infrared Variability. *ApJ*, 704(1):L15–L19.

Najita, J., Carr, J. S., and Mathieu, R. D. (2003). Gas in the Terrestrial Planet Region of Disks: CO Fundamental Emission from T Tauri Stars. *ApJ*, 589:931–952.

Nelson, R. P., Gressel, O., and Umurhan, O. M. (2013). Linear and non-linear evolution of the vertical shear instability in accretion discs. *MNRAS*, 435(3):2610–2632.

Nolan, C. A., Salmeron, R., Federrath, C., Bicknell, G. V., and Sutherland, R. S. (2017). Centrifugally driven winds from protostellar accretion discs - I. Formulation and initial results. *MNRAS*, 471:1488–1505.

Norman, C. and Heyvaerts, J. (1985). Anomalous magnetic field diffusion during star formation. *A&A*, 147:247–256.

O'dell, C. R. and Wen, Z. (1994). Postrefurbishment Mission Hubble Space Telescope Images of the Core of the Orion Nebula: Proplyds, Herbig-Haro Objects, and Measurements of a Circumstellar Disk. *ApJ*, 436:194.

Ogilvie, G. I. (1997). The equilibrium of a differentially rotating disc containing a poloidal magnetic field. *MNRAS*, 288:63–77.

Ogilvie, G. I. (1998). Waves and instabilities in a differentially rotating disc containing a poloidal magnetic field. *MNRAS*, 297:291–314.

Ogilvie, G. I. (1999). Nonlinear Fluid Dynamics of Warped Discs. In Sellwood, J. A. and Goodman, J., editors, *Astrophysical Discs - an EC Summer School*, volume 160 of *Astronomical Society of the Pacific Conference Series*, page 61.

Ogilvie, G. I. (2012). Jet launching from accretion discs in the local approximation. *MNRAS*, 423:1318–1324.

Ogilvie, G. I. (2016). Astrophysical fluid dynamics. *Journal of Plasma Physics*, 82(3):205820301.

Ogilvie, G. I. and Livio, M. (2001). Launching of Jets and the Vertical Structure of Accretion Disks. *ApJ*, 553:158–173.

Okuzumi, S., Takeuchi, T., and Muto, T. (2014). Radial Transport of Large-scale Magnetic Fields in Accretion Disks. I. Steady Solutions and an Upper Limit on the Vertical Field Strength. *ApJ*, 785:127.

Owen, J. E., Clarke, C. J., and Ercolano, B. (2012). On the theory of disc photoevaporation. *MNRAS*, 422(3):1880–1901.

Padovani, M., Ivlev, A. V., Galli, D., and Caselli, P. (2018). Cosmic-ray ionisation in circumstellar discs. *A&A*, 614:A111.

Pandey, B. P. and Wardle, M. (2012). Magnetorotational instability in magnetic diffusion dominated accretion discs. *MNRAS*, 423:222–235.

Paris, J. B. and Ogilvie, G. I. (2018). A local model of warped magnetized accretion discs. *MNRAS*, 477:2406–2418.

Pérez, L. M., Carpenter, J. M., Andrews, S. M., Ricci, L., Isella, A., Linz, H., Sargent, A. I., Wilner, D. J., Henning, T., Deller, A. T., Chandler, C. J., Dullemond, C. P., Lazio, J., Menten, K. M., Corder, S. A., Storm, S., Testi, L., Tazzari, M., Kwon, W., Calvet, N., Greaves, J. S., Harris, R. J., and Mundy, L. G. (2016). Spiral density waves in a young protoplanetary disk. *Science*, 353(6307):1519–1521.

Perez-Becker, D. and Chiang, E. (2011). Surface Layer Accretion in Conventional and Transitional Disks Driven by Far-ultraviolet Ionization. *ApJ*, 735(1):8.

Petersen, M. R., Julien, K., and Stewart, G. R. (2007a). Baroclinic Vorticity Production in Protoplanetary Disks. I. Vortex Formation. *ApJ*, 658(2):1236–1251.

Petersen, M. R., Stewart, G. R., and Julien, K. (2007b). Baroclinic Vorticity Production in Protoplanetary Disks. II. Vortex Growth and Longevity. *ApJ*, 658(2):1252–1263.

Pinte, C., Dent, W. R. F., Ménard, F., Hales, A., Hill, T., Cortes, P., and de Gregorio-Monsalvo, I. (2016). Dust and Gas in the Disk of HL Tauri: Surface Density, Dust Settling, and Dust-to-gas Ratio. *ApJ*, 816(1):25.

Polygiannakis, J. M. and Moussas, X. (2001). A review of magneto-vorticity induction in Hall-MHD plasmas. *Plasma Physics and Controlled Fusion*, 43(2):195–221.

Pringle, J. E. and King, A. (2007). *Astrophysical Flows*.

Rafikov, R. R. (2016). Protoplanetary Disk Heating and Evolution Driven by Spiral Density Waves. *ApJ*, 831(2):122.

Reed, B. C. (2018). A compact general expression for momentum exchange in elastic collisions. *American Journal of Physics*.

Regev, O. and Umurhan, O. M. (2008). On the viability of the shearing box approximation for numerical studies of MHD turbulence in accretion disks. *A&A*, 481:21–32.

Riols, A. and Lesur, G. (2019). Spontaneous ring formation in wind-emitting accretion discs. *A&A*, 625:A108.

Riols, A., Lesur, G., and Menard, F. (2020). Ring formation and dust dynamics in wind-driven protoplanetary discs: global simulations. *arXiv e-prints*, page arXiv:2006.01194.

Riols, A., Ogilvie, G. I., Latter, H., and Ross, J. P. (2016). Magnetorotationally driven wind cycles in local disc models. *MNRAS*, 463(3):3096–3112.

Rodenkirch, P. J., Klahr, H., Fendt, C., and Dullemond, C. P. (2020). Global axisymmetric simulations of photoevaporation and magnetically driven protoplanetary disk winds. *A&A*, 633:A21.

Rothstein, D. M. and Lovelace, R. V. E. (2008). Advection of Magnetic Fields in Accretion Disks: Not So Difficult After All. *ApJ*, 677:1221–1232.

Sakurai, T. (1985). Magnetic stellar winds: a 2-D generalization of the Weber-Davis model. *A&A*, 152:121–129.

Salmeron, R., Königl, A., and Wardle, M. (2011). Wind-driving protostellar accretion discs - II. Numerical method and illustrative solutions. *MNRAS*, 412:1162–1180.

Salmeron, R. and Wardle, M. (2005). Magnetorotational instability in protoplanetary discs. *MNRAS*, 361:45–69.

Salmeron, R. and Wardle, M. (2008). Magnetorotational instability in protoplanetary discs: the effect of dust grains. *MNRAS*, 388:1223–1238.

Sano, T. and Miyama, S. M. (1999). Magnetorotational Instability in Protoplanetary Disks. I. On the Global Stability of Weakly Ionized Disks with Ohmic Dissipation. *ApJ*, 515(2):776–786.

Schartman, E., Ji, H., Burin, M. J., and Goodman, J. (2012). Stability of quasi-Keplerian shear flow in a laboratory experiment. *A&A*, 543:A94.

Shakura, N. I. and Sunyaev, R. A. (1973). Reprint of 1973A&A....24..337S. Black holes in binary systems. Observational appearance. *A&A*, 500:33–51.

Simon, J. B., Lesur, G., Kunz, M. W., and Armitage, P. J. (2015). Magnetically driven accretion in protoplanetary discs. *MNRAS*, 454:1117–1131.

Spitzer, L. (1962). *Physics of Fully Ionized Gases*.

Spruit, H. C. (1996). Magnetohydrodynamic jets and winds from accretion disks. In Wijers, R. A. M. J., Davies, M. B., and Tout, C. A., editors, *NATO Advanced Science Institutes (ASI) Series C*, volume 477 of *NATO Advanced Science Institutes (ASI) Series C*, pages 249–286.

Spruit, H. C. (2010). Theory of Magnetically Powered Jets. In Belloni, T., editor, *Lecture Notes in Physics, Berlin Springer Verlag*, volume 794 of *Lecture Notes in Physics, Berlin Springer Verlag*, page 233.

Spruit, H. C., Stehle, R., and Papaloizou, J. C. B. (1995). Interchange instability in and accretion disc with a poloidal magnetic field. *MNRAS*, 275:1223–1231.

Suriano, S. S., Li, Z.-Y., Krasnopolsky, R., and Shang, H. (2017). Rings and gaps produced by variable magnetic disc winds and avalanche accretion streams - I. Axisymmetric resistive MHD simulations. *MNRAS*, 468:3850–3868.

Suriano, S. S., Li, Z.-Y., Krasnopolsky, R., and Shang, H. (2018). The formation of rings and gaps in magnetically coupled disc-wind systems: ambipolar diffusion and reconnection. *MNRAS*, 477:1239–1257.

Suriano, S. S., Li, Z.-Y., Krasnopolsky, R., Suzuki, T. K., and Shang, H. (2019). The formation of rings and gaps in wind-launching non-ideal MHD discs: three-dimensional simulations. *MNRAS*, 484:107–124.

Suzuki, T. K. and Inutsuka, S.-i. (2009). Disk Winds Driven by Magnetorotational Instability and Dispersal of Protoplanetary Disks. *ApJ*, 691(1):L49–L54.

Suzuki, T. K., Muto, T., and Inutsuka, S.-i. (2010). Protoplanetary Disk Winds via Magnetorotational Instability: Formation of an Inner Hole and a Crucial Assist for Planet Formation. *ApJ*, 718(2):1289–1304.

Swedenborg, E. (1734). *Latin: Opera Philosophica et Mineralia (English: Philosophical and Mineralogical Works)*.

Takeuchi, T. and Okuzumi, S. (2014). Radial Transport of Large-scale Magnetic Fields in Accretion Disks. II. Relaxation to Steady States. *ApJ*, 797:132.

Tang, Y.-W., Guilloteau, S., Dutrey, A., Muto, T., Shen, B.-T., Gu, P.-G., Inutsuka, S.-i., Momose, M., Pietu, V., Fukagawa, M., Chapillon, E., Ho, P. T. P., di Folco, E., Corder, S., Ohashi, N., and Hashimoto, J. (2017). Planet Formation in AB Aurigae: Imaging of the Inner Gaseous Spirals Observed inside the Dust Cavity. *ApJ*, 840(1):32.

Tang, Y. W., Guilloteau, S., Piétu, V., Dutrey, A., Ohashi, N., and Ho, P. T. P. (2012). The circumstellar disk of AB Aurigae: evidence for envelope accretion at late stages of star formation? *A&A*, 547:A84.

Tazaki, R., Lazarian, A., and Nomura, H. (2017). Radiative Grain Alignment In Protoplanetary Disks: Implications for Polarimetric Observations. *ApJ*, 839(1):56.

Tazzari, M., Testi, L., Natta, A., Ansdell, M., Carpenter, J., Guidi, G., Hogerheijde, M., Manara, C. F., Miotello, A., van der Marel, N., van Dishoeck, E. F., and Williams, J. P. (2017). Physical properties of dusty protoplanetary disks in Lupus: evidence for viscous evolution? *A&A*, 606:A88.

Teague, R., Bae, J., Huang, J., and Bergin, E. A. (2019). Spiral Structure in the Gas Disk of TW Hya. *ApJ*, 884(2):L56.

Teitler, S. (2011). Global Self-similar Protostellar Disk/Wind Models. *ApJ*, 733:57.

Turner, N. J., Sano, T., and Dziourkevitch, N. (2007). Turbulent Mixing and the Dead Zone in Protostellar Disks. *ApJ*, 659(1):729–737.

Umebayashi, T. and Nakano, T. (1981). Fluxes of Energetic Particles and the Ionization Rate in Very Dense Interstellar Clouds. *PASJ*, 33:617.

Umebayashi, T. and Nakano, T. (2009). Effects of Radionuclides on the Ionization State of Protoplanetary Disks and Dense Cloud Cores. *ApJ*, 690(1):69–81.

Urpin, V. (2003). A comparison study of the vertical and magnetic shear instabilities in accretion discs. *A&A*, 404:397–403.

Urpin, V. and Brandenburg, A. (1998). Magnetic and vertical shear instabilities in accretion discs. *MNRAS*, 294(3):399–406.

van Ballegooijen, A. A. (1989). Magnetic Fields in the Accretion Disks of Cataclysmic Variables. In Belvedere, G., editor, *Accretion Disks and Magnetic Fields in Astrophysics*, volume 156, page 99.

Vlemmings, W. H. T., Lankhaar, B., Cazzoletti, P., Ceccobello, C., Dall'Olio, D., van Dishoeck, E. F., Facchini, S., Humphreys, E. M. L., Persson, M. V., Testi, L., and Williams, J. P. (2019). Stringent limits on the magnetic field strength in the disc of TW Hya. ALMA observations of CN polarisation. *A&A*, 624:L7.

Wardle, M. (1997). Magnetically-Driven Winds from Protostellar Disks. In Wickramasinghe, D. T., Bicknell, G. V., and Ferrario, L., editors, *IAU Colloq. 163: Accretion Phenomena and Related Outflows*, volume 121 of *Astronomical Society of the Pacific Conference Series*, page 561.

Wardle, M. (1999). The Balbus-Hawley instability in weakly ionized discs. *MNRAS*, 307:849–856.

Wardle, M. (2007). Magnetic fields in protoplanetary disks. *Ap&SS*, 311:35–45.

Wardle, M. and Koenigl, A. (1993). The structure of protostellar accretion disks and the origin of bipolar flows. *ApJ*, 410:218–238.

Wardle, M. and Ng, C. (1999). The conductivity of dense molecular gas. *MNRAS*, 303:239–246.

Wardle, M. and Salmeron, R. (2012). Hall diffusion and the magnetorotational instability in protoplanetary discs. *MNRAS*, 422:2737–2755.

Williams, J. P. and Cieza, L. A. (2011). Protoplanetary Disks and Their Evolution. *ARA&A*, 49(1):67–117.

Wisniewski, J. P., Clampin, M., Grady, C. A., Ardila, D. R., Ford, H. C., Golimowski, D. A., Illingworth, G. D., and Krist, J. E. (2008). The HD 163296 Circumstellar Disk in Scattered Light: Evidence of Time-Variable Self-Shadowing. *ApJ*, 682(1):548–558.

Wurster, J. (2017). *Physical and Artificial Resistivity (in smoothed particle magnetohydrodynamics)*. 1st Phantom Users Workshop, Monash University.

Wurster, J. (2021). Do we need non-ideal magnetohydrodynamic to model protostellar discs? *MNRAS*, 501(4):5873–5891.

Zhu, Z. and Stone, J. M. (2018). Global Evolution of an Accretion Disk with a Net Vertical Field: Coronal Accretion, Flux Transport, and Disk Winds. *ApJ*, 857:34.

Zweibel, E. G. and Brandenburg, A. (1997). Current Sheet Formation in the Interstellar Medium. *ApJ*, 478(2):563–568.